Classification of Pedestrian Streams: From Empirics to Modelling

Jakob Cordes

JÜLICH
Forschungszentrum

Classification of Pedestrian Streams: From Empirics to Modelling

Jakob Cordes

I don't mind diving into the crowd. I love the crowd as I love the sea. Not to be engulfed by or lost in it but to sail it like a solitary pirate, seeming to follow it's rhythm but finding my own when the current breaks or dissipates. Like the sea a crowd is invigorating. My thoughts come to me in the street even those that concern my work.

Éric Rohmer, L'Amour l'après-midi (1972)

Abstract

Pedestrian streams are ubiquitous, but very diverse. Classifying them is critical in practice for crowd management but also for the organization and validation of models. As far as an empirical classification is concerned, a robust method is still lacking. But also in terms of a theoretical description, a large number of models coexist with an ill-defined range of applicability. In this thesis, these problems are addressed in two ways. First, by studying crowds in their one-dimensional limit, namely Single-File motion, which allows for a better understanding of conceptual problems in models. Second, by drawing inspiration from fluid dynamics, where dimensionless numbers such as the Reynolds number help to classify flows.

Single-File motion exhibits interesting collective effects, such as stop-and-go waves, which are validation benchmarks for any agent-based modeling approach of traffic systems. We investigate different classes of models by examining the influence of different parameters, including time-gap, anticipation time, and reaction time - sometimes revealing surprising connections between well-known modeling approaches.

Then the wide range of phenomena encountered in crowds is organized by introducing two dimensionless numbers rooted in psychological and biomechanical considerations: the Intrusion number based on the preservation of personal space and the Avoidance number based on the anticipation of collisions. Using an extensive data set we show that these two numbers delineate regimes in which different variables characterize the crowd's arrangement, namely, Euclidean distances at low Avoidance number and times-to-collision at low Intrusion number. Based on these results, a fairly general perturbative expansion of the individual pedestrian dynamics around the non-interacting state is performed. Simulations confirm that this expansion performs well in its expected regime of applicability. This is also relevant for the larger class of agent-based crowd models as their equations of motion typically depend on variants of the Intrusion number or the Avoidance number. Simulations show that the occurrence of the Intrusion number and Avoidance number in these models limits their range of applicability to specific regimes of crowd motion.

Contents

Symbols

N	number of agents	
$\boldsymbol{r}_i = (x_i, y_i)$	position of agent i	m
$\boldsymbol{v}_i$	velocity of agent i	m/s
$\boldsymbol{a}_i$	acceleration of agent i	m/s^2
$\boldsymbol{v}_{\text{des},i}$	desired velocity of agent i	m/s
$\boldsymbol{e}_{\text{des},i} = \boldsymbol{v}_{\text{des},i}/|\boldsymbol{v}_{\text{des},i}|$	desired orientation of agent i	
$v_{\text{des},i} = |\boldsymbol{v}_{\text{des},i}|$	desired speed of agent i	m/s
$v_{\max}$	maximum speed	m/s
ℓ	diameter of disc-shaped agents	m
$\ell_{\min}$	minimal diameter of disc-shaped agents	m
$\mathcal{N}_i$	neighbourhood of agent i	
$\boldsymbol{r}_{ij}$	vector pointing from i to j	m
$r_{ij} = |\boldsymbol{r}_{ij}|$	Euclidean distance between centers of i and j	m
r_{soc}	social distance	m
$\mathcal{I}n_{ij}$	intrusion between i and j	
$\mathcal{I}n_i = \sum_{j \in \mathcal{N}_i} \mathcal{I}n_{ij}$	intrusion of i	
$\mathcal{I}n$	averaged Intrusion number	
τ_{ij}	time-to-collision between i and j	s
$\tau_i = \min_{j \neq i} \tau_{ij}$	minimal time-to-collision of i	s
τ_0	desired time-to-collision	s
$\mathcal{A}v_{ij} = \tau_0/\tau_{ij}$	avoidance between i and j	
$\mathcal{A}v_i = \sum_{j \in \mathcal{N}_i} \mathcal{A}v_{ij}$	avoidance of i	
$\mathcal{A}v$	averaged Avoidance number	
T_{ij}	time-gap between i and j	s

$T_i = \min_{j \neq i} T_{ij}$	minimal time-gap of i	s
T	desired time-gap	s
$\mathcal{T}_{ij} = T/T_{ij}$	risk-of-following of i to j	
$\mathcal{T}_i = \sum_{j \in \mathcal{N}_i} \mathcal{T}_{ij}$	risk-of-following of i	
$\mathcal{T}$	averaged Risk-of-Following number	
$v_{ij} = -dr_{ij}/dt$	rate of approach between i and j	m/s
τ_R	reaction or relaxation time	s
τ_A	anticipation time	s
δt	(numerical) update time	s
α, β, γ	varying model parameters	

Chapter 1

Introduction

Systems studied in physics range from the smallest time and length scales, e.g., the dynamics of electrons within attoseconds, up to the largest structures observed in the universe as in cosmology. While particle physics is concerned with individual particles, condensed matter physics studies various unexpected behaviours that emerge from large assemblies of atoms. This is just a glimpse of the variety of systems encountered within the realms of physics. Despite their differences, traditionally, the common ground has been that physics is associated with the study of the inanimate world. However, as of now, physics of living systems has fully emerged as its own field of physics, alongside the more traditional branches mentioned above [1].

An important contribution of physics to the study of biological systems has, for example, been the reveal of the double-helix structure of the DNA in the 50s with the help of X-ray diffraction [2]. However, new experimental methods allow, for instance, to track the dynamics of single molecules in cells [3]. Novel methods, like these, helped to unveil the dynamic, stochastic, and emergent nature typically present in biological systems [4]. Such questions are addressed within the vivid field of active matter, which studies emergent behaviour of large assemblies of self-propelled particles, i.e., systems inherently far away from equilibrium [5]. Active matter includes systems across various length scales ranging from microscopic, such as bacteria that consume ATP and use its energy to self-propel to macroscopic such as birds which can form mesmerising flocks. Obviously, bacteria are 'dump' whereas large animals have a complex perceptional and self-regulating apparatus, thus, the term *smart active matter* has been proposed to describe the latter [6]. Crowds may be categorized as such.

Despite this, the study of pedestrians and crowds does not originate in biological systems but features a quite different history and touches upon various disciplines. With regard to the human locomotion, the bipedal gait, anatomical studies date back to the early

19th century [7]. In biomechanics, human gait is still actively studied and, for example, the analysis of human gait serves as a method to diagnose various diseases [8]. Within sociology and psychology, crowds have been studied since the late 19th century [9], often characterizing crowds as violent and without rationality. Later that view has been corrected by emphasizing that cooperative and rational behaviour is present in crowds [10]. Nonetheless, such connotations still persist, for instance, the term 'panic' is widely used to describe crowd crushes - often incorrectly blaming the victims instead of criticizing inadequate planning [11].

Such practical questions originate in safety engineering which has been most influential for the emergence of the field, at least from the perspective of physics. Logistical issues when organizing large-scale events must have been relevant for human societies for centuries. One of the earliest reports on a crowd crush dates back to the mid 19th century, where a fire in the theatre of Karlsruhe has claimed many victims due to limited and blocked emergency exits [12]. Events as such have led to the development of safety regulations for buildings in Germany around that time. Even though rules of thumb must have been used by safety engineers long before, the first systematic and quantitative examination of the topic was only published in the 1970s [13]. While around that time the first agent-based model for crowds has been proposed [14], it only sparked a larger interest, particularly within the physics community, twenty years later with the proposal of the Floor-Field model [15] and the Social-Force model [16]. The topic held relevance, also in the public's mind, due to tragic crowd crushes around the world [17]. This has led to numerous quantitative investigations of crowds both experimentally in which the positions of each pedestrian in a crowd is tracked and theoretically through the proposal of new, mostly agent-based, models.

Thereby, the understanding of crowds has greatly improved allowing, for instance, to put building regulations on a more solid empirical footing. Several collective phenomena of self-organization have been identified and analyzed quantitatively, such as lane and stripe formation [18, 19], rotors in crowds [20] or clogging at bottlenecks [21] often serving as corner stones for the validation of agent-based models [22]. Similar models are also employed commercially to ensure a safer planning and, recently, an ISO norm has been published to regularize the use of such models [23].

Despite these advancements, a zoo of models co-exist [24–27] and the realm of applicability of each is ill-defined. Often new models are defined in an *ad-hoc* way without proper justification nor substantial improvements in their dynamics. But also empirically the classification of crowds remains unsatisfactory. In my thesis, I will try to address these problems in two ways. In the first chapter we will 'zoom in' and simplify the system by

considering the one-dimensional limit of crowds, namely single-file motion. Then we will 'zoom out' and take the broad array of crowd phenomena into account.

When modelling human behaviour one is confronted with numerous, untraceable degrees of freedom. This 'curse of dimensionaility' is typically handled by representing pedestrians as disks moving in the 2d plane, neglecting, for instance, the bipedal gait or complex cognitive processes. This is partly justified by focusing on the macroscopic and statistical properties of the system instead of trying to capture the behaviour of individuals correctly. Despite these simplifications, the corresponding models are quite complicated, for instance, not allowing for an analytical treatment. Therefore, we will begin by examining *single-file motion*, where individuals move in a line without overtaking. This represents a significant simplification of pedestrian dynamics, particularly in terms of theoretical description, as it allows for the study of models in their one-dimensional limit.

This scenario bears resemblance to car traffic on a single-lane road, for which many models have been proposed. We will adopt these approaches and pay attention to their interconnections by scrutinizing the influence of different time-scales, namely time-gap, anticipation time, and reaction time. These models can capture the essential properties of single-file motion, the fundamental diagram and stop-and-go waves, reasonably well in particular if noise included. Besides, in the one-dimensional limit conceptual problems can be identified more readily than in complex two-dimensional scenarios. This will allow us to point out problems in two other model classes, namely force-based models and time-to-collision based models which are both popular approaches when modelling pedestrian crowds. This will be examined in chapter 3.

However, as mentioned above, pedestrian dynamics encompass a broad spectrum of scenarios which are at least two-dimensional. Thus, before aiming at a theoretical description it is prudent to organize the multitude encountered here. Typically, the crowd's density is used to delineate different regimes, for instance the levels of service defined by Fruin for crowds [28, 29]. Each level is marked by a dominant behavior: (un)avoidable contact, necessity to change gait, possibility to turn around, etc. and it has been argued that as the density changes crowd dynamics should be controlled by distinct laws [30]. However, the watersheds between the regimes are arbitrary. Even from a practical standpoint, for safety assessments, crowds at similar densities may present contrasted characters and risk profiles. Consider the difference between a densely packed, but static audience in a concert hall and people vying for escape in an emergency evacuation [17]. Recently, yearning for a better classification of these scenarios, it was proposed to gauge congestion on the basis of a dimensionless number related to the vorticity of the velocity field, instead of the density [31]. This quantity is practically relevant, notably for

safety issues, but gives no insight into the determinants of pedestrian dynamics at the microscale.

We will draw inspiration from fluid dynamics, where dimensionless numbers like the Reynolds number help classify flows. Starting with psychological considerations of pedestrian behavior, we will introduce the dimensionless Intrusion and Avoidance numbers, which quantify the intrusions into the pedestrians' personal spaces and the imminency of the collisions that they face, respectively. Their averages over the crowd define dimensionless parameters that delineate regimes of crowd flows intuitively and empirically. These regimes are found to differ markedly with regard to their 'self-organized' structure, i.e., the variables that characterize the crowds' arrangement. This empirical analysis is carried out in chapter 4.

These distinct types of arrangements, depending on the regime, contribute to making the delineation of regimes useful, especially from a modelling perspective. It will allow us to perform a perturbative analysis of the agent-based dynamics around the non-interacting situation. This will yield different models each tied closely to a specific regime of crowd flows. In particular, we will verify that the corresponding models can and can only be applied in the regime they have been derived for. While in chapter 5 the focus is put on these perturbative models, the discussion has bearing on the broader category of agent-based models: their equations of motion often hinge on variants of either the intrusion variable or the avoidance variable and thereby limiting their range of applicability to the associated regime; a detailed inspection of this broader model category is conducted in chapter 6.

The dissertation can be divided into two parts that can be read separately, especially chapter 3 on the one hand and chapters 4, 5, and 6 on the other hand. I strongly encourage the reader to read chapters 4, 5, and 6 one after the other, as I hope this will give you the most complete picture. In particular, the buildup, starting from psychological considerations that allow an empirical classification, which leads to the derivation of agent-based models closely related to models known in the literature, is, in my opinion, one of the main strengths of this manuscript. While the general background is described in chapter 2 most methods are introduced within the text when actually needed.

Chapter 2

Theoretical Background

Before presenting the results of this dissertation, let us introduce some genral concepts and findings in pedestrian dynamics. We will start by looking at a single pedestrian and its properties related to perception, biomechanics, and psychology. Our main focus, however, lies in assemblies of many pedestrians, i.e., crowds. Such a system of 'interacting particles' endorses a description in the framework of statistical physics. However, unlike, say, a system of interacting spins as in the Ising model, pedestrians are active, self-propelling entities. Accordingly, crowds cannot reach thermodynamic equilibrium, which is characteristic of systems studied in the field of active matter. After discussing some general properties of active matter, we will introduce the basic quantitative measures used to describe crowds, i.e., velocity, density, and flow. Furthermore, we will give a short overview of the main (collective) phenomena encountered in crowds. Finally, we will discuss some aspects of modelling pedestrian crowds.

2.1   The Pedestrian

A pedestrian is a human moving on foot in a publicly accessible area [32]. Even though walking is an every day activity which literally happens 'on the move', it is a complex process: Based on the perceptions of the sensory system, the central nervous system (CNS) contracts or relaxes the muscles. Thereby, the CNS coordinates the limps in order to initiate movement and to keep balance, cf. the simplified picture in Fig. 2.1.

In the sensory system, the proprioceptors are sensory receptors in muscles and joints that provide information about body position and movement. The visual system is the physiological basis to see, i.e., to detect and process light. The vestibular system (in the inner ear), combined with the other senses, creates a sense of balance and orientation.
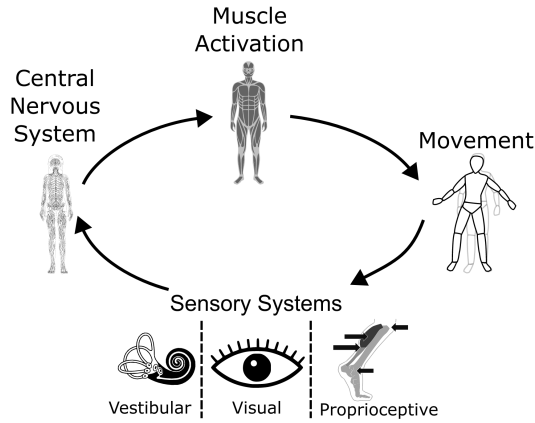
FIGURE 2.1: Simplified diagram of the human postural control loop used to stabilize body posture and to coordinate body movement. Figure taken from [34].

The information of the sensory system is processed and interpreted by the CNS, which includes the brain. This allows to represent the external state (our enviroment) and an internal state (position of limbs but also, for instance, the desire to go somewhere). According to the external and internal state, the CNS generates motor commands which are send to the muscular system. These commands are executed by contracting and relaxing the relavant muscles which results in movement of the corresponding limbs. This coordination gives rise to the human to locomotion (e.g., walking) that is facilitated by friction between the feet and the ground. Through evolution and learning this control loop can reach a great level of precision, as exemplified by professional long-jumpers who, at high speeds, strike the take-off boards at the precision of centimetres [33].

2.2 The Crowd

This work is occupied with the description of *crowds* which are simply defined as an aggregation of pedestrians [32]. From the perspective of physics, a crowd can be described as an interacting many particle system. It consists of elementary entities, the pedestrians, which interact with each other. The way the crowd flows, with all its collective phenomena, emerges from these interactions. Thus, it is natural to apply ideas and concepts from statistical physics to study crowds. However, in contrast to classical problems in statistical physics we are dealing with entities that posess the ability to move on their own, i.e., to self-propel. The ability to self-propel is constitutive, not only for crowds, but also for various systems which are described as *active matter*. Apart from crowds,

active matter includes assemblies of bacteria, nanomotors, or microswimmers but also flocks of birds or schools of fish [35].

For some systems out of equilibrium an equilibrium steady-state exists and, after some thermalization period, the system will reach it. If the system is sufficiently close to its equilibrium state, it can be described using linear response theory. The equilibrium steady-state itself fulfills detailed balance, time-reversal symmetry, and the probabilities of its configurations are given by the Gibbsian form. All of these properties are broken in truely non-equilibrium systems. These systems may only reach a non-equilibrium steady-state, which is characterized by a non-zero flux. One can further distuingish between active systems and systems in which energy is injected through the boundaries. In the latter, a current is maintained by an external drive, such as an electrical wire carrying an electrical current or charged colloids driven by an external field. Active systems, on the other hand, are persistently out of equilibrium because the elementary entities locally consume energy. This entails that no global symmetry is enforced by an external field, but the agents move individually according to their preferred motion [36].

In practice, the description of crowds by means of statistical physics supposes that most of the complex properties of the individual pedestrians, which we have indicated in Section 2.1, can be neglected - as long as one is only interested in the statistical and 'macroscopic' properties of the system. This typically implies that pedestrians are represented as disks, occupying a certain area, that navigate in the 2d plane. This is also reflected in the empirical data, which usually consists of 2d trajectory data, obtained by tracking the heads of people. Of course, at certain instances more realistic representations may be needed such as elliptical body shapes, which allow to take shoulder rotation into consideration. Accordingly, the shoulder movement has recently been tracked in experiments [37]. Apart from that, actual mechanical interactions become relevant in very dense crowds. Here, other experimental methods such as pressure sensors or 'X-Sense' suits give detailled information about the contact forces and the complete body posture of pedestrians, respectively. This allows, for instance, to investigate the propagation of pushes [38] or stepping strategies in dense crowds [39]. Let us, however, start by summarizing the well established findings in pedestrian dynamics, starting with the basic quantitative measures employed to describe crowds.

2.2.1   Density, Velocity and Flow

The three most important quantities to measure in crowds are *density*, *velocity* and *flow*. While the velocity is straightforward to define and to calculate, there are several ways to

define a density in crowds. Regarding the flow, there are some subtleties in its calculation which we will briefly discuss below.

In general terms, the density is given by the number of people N located in an area A, i.e.,

$$\rho = \frac{N}{A}. \tag{2.1}$$

This defines a *global density*, taking as the area, for example, the experimental site and counting the people inside this area.

The definition in Eq. (2.1) is however not well suited to describe a *local density*, as there is no strict separation of scales between the entity and the assembly. This problem is usually circumvented by either a Voronoi tesselation [40], where the inverse of the area corresponds to the local density, or by using Gaussian Kernels for each pedestrian. For details with regard to the exact definition or implementation refer to [41].

The *flow J* states how many people cross a fixed location of a facility per time. Typically it is defined as a scalar quantity by only considering the flow perpendicular to a line [42]. It can be calculated simply by counting the number of people that pass, for example, through a line in a corridor, and dividing by the measurement time T, i.e.,

$$J = \frac{N}{T}. \tag{2.2}$$

It is also directly related to the time Δt_{ii+1} between two consecutive people i and $i+1$ crossing that line, in particular $J = 1/\langle \Delta t \rangle$. To obtain a quantity independent of the length of the line b, a specific flow is defined as

$$J_S = \frac{J}{b}, \tag{2.3}$$

which gives the number of pedestrians per unit time and length that passes the corresponding cross section. The specific flow can also be calculated via the *Hydrodynamic* relation, i.e.,

$$J_S = \rho v, \tag{2.4}$$

where v is the average speed of the pedestrians.[1] Note that, the average speed in Eq. (2.4) is typically calculated as an average over space, whereas Eq. (2.2) involves an average over time. Thus, the influence of fast pedestrians is underestimated in the former which can lead to considerable differences between the two methods [42].

---

[1]In the case of single-file motion, typically a line density is defined by dividing the number of agents N that are located on a specific line-segment by the length L of this segment. In the case of a line density ρ, the hydrodynamic relation yields the flow J per unit time instead of the specific flow.

The relation of how the mean speed changes with density is called the *fundamental diagram*. Through the hydrodynamic relation Eq. (2.4), there exist three different representations of the fundamental diagram, namely $J_S(\rho)$, $v(\rho)$, and $J_S(v)$. Loosely speaken, the fundamental diagram can be described as follows: at small densities, there are few interactions and everyone moves with their desired velocity, the system is in a *free-flow* state and the flow increases lineraly with the density. At some density the maximum flow is reached (the *capacity*). Beyond that critical density, mean velocity and flow decrease with increasing density. The system is in a *congested* state.

As the fundamental diagram is a central quantity for planning and designing pedestrian facilities, many studies have been focused on determining its exact shape. Despite this, certain essential questions are still not agreed on, i.e., at which density the capacity is reached, how large is the capacity, and at which density will the flow go to zero [42]. These differences can partly be traced back to several factors, for instance between different cultures or different levels of motivation [43–45]. Furthermore, the exact method to calculate the fundamental diagram, especially regarding the definition of the flow, can have a large influence on the fundamental diagram [29, 46]. We will discuss the fundamental diagram of single-file motion again in chapter 3.

2.2.2 Self-Organization in Crowds

In crowds, several collective effects and self-organization phenomena have been observed. These 'macroscopic' effects, on the level of the crowd, arise through the 'microscopic' interactions between the individual pedestrians. Consequently, these phenomena are well suited to validate agent-based models. In the following, I will try to provide a concise overview of the main phenomena and its properties. For a detailed description and quantitative results refer to the corresponding references.

Lane and Stripe Formation In bidirectional flows, i.e., if two crowds move through the same facility in opposite directions, multiple unidirectional lanes will typically emerge. An exemplaric snapshot is depicted in the left of Fig. 2.2. Through the formation of lanes the number of interactions is reduced and a more comfortable flow is achieved. Depending on multiple factors, like boundary conditions and density, the system can form few, thick, and stable lanes or multiple, thin, and rather short-living lanes. Multiple studies investigated lane formation experimentally [18, 47, 48] and theoretically [15, 19, 49].

The formation of lanes in two-component active flows has been observed in various contexts, for instance in mixtures of oppositely charged colloids driven by an external field [50]. Lanes seems to emerge from many different kinds of interactions and, accordingly,

FIGURE 2.2: On the left, a snapshot of bidirectional flow where four lanes have formed [18]. The color of the hats indicates the direction of motion (i.e., red from left to right and yellow from right to left). On the right, cross flow with two stripes [52].

most pedestrian models can replicate its basic features. At high densities, however, many models end up in grid-locks [49, 51]. This has not been observed in experiments yet which investigated bidirectional flows up to densities of $3.5/m^2$ [52]. To avoid the formation of grid-locks in models, the importance of anticipation has been emphasized [49]. Experimentally it was also shown that (mutual) anticipation leads to a faster formation of lanes [18].

A related phenomenon is the formation of stripes that occur, for example, if two crowds intersect each other at a crossing [19]. See Fig. 2.2 on the right for an exemplaric snapshot.

Bottleneck: Jamming, Clogging and Oscillations   Apart from crowd flows through corridors (uni- or bidirectional) and crossings (multidirectional), bottlenecks are essential to understand the crowds' motion. Especially for practical purposes such as evacuations of large (high-rise) buildings. The term bottleneck is defined as a physical obstacle that has a lower capacity than the sorrounding enviroment [32], for instance a narrowing of a corridor (e.g., doors) or stairs.

As long as the inflow is less than the capacity of the bottleneck, the system remains in a *free-flow* state, where the inflow equals the flow through the bottleneck. However, if the inflow surpasses the capacity of the bottleneck, it leads to an accumulation of individuals in front of the bottleneck, resulting in *congestion* or *jamming*. At such instances, the density decreases within and behind the bottleneck compared to the density in front of it, as illustrated in Fig. 2.3 (*right*) and discussed in [53].

In the congested regime, especially when the crowd is highly motivated to get through the bottleneck, the pedestrians' bodies can form structures that obstruct the flow (*clogging*). These structures, if viewed from above, typically resemble semi-circular, self-stabilizing
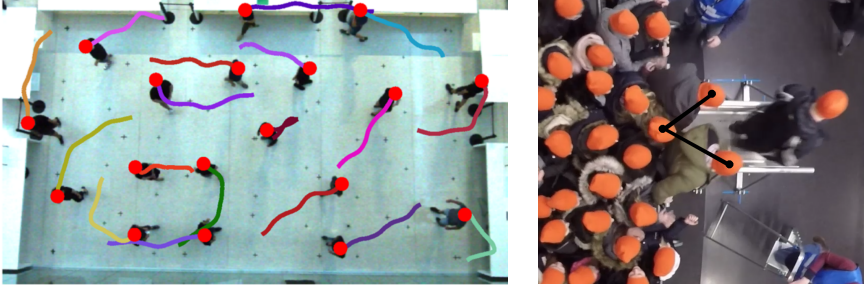
FIGURE 2.3: On the left, a snapshot of a crowd forming a counter-clockwise vortex, taken from [20]. The colored tails show the last 2s of the trajectory. On the right, a short living clog at a bottleneck where a force chain is indicated by the black line [61].

shapes, so-called *arches* as indicated by the black line in Fig. 2.3 (*right*). Clogging and the formation of arches has not only been investigated for pedestrians (cf. [54, 55]) but also for sheeps [56] and granular systems [57]. While for crowds clogs are only short-living, in granular systems arches can permanently block the flow. In such cases, adding vibrations to the system can prevent the formation of permanent clogs [58]. Similarly for pedestrian models, the formation of unrealistic permanent clogs is a frequent problem which can be solved by adding noise [59].

Related to the formation of clogs, simulations suggested that as the crowd tries to pass a bottleneck faster (e.g. due to a higher urgency to exit), the evacuation time increases [60]. While this *faster-is-slower* effect has been verfied empirically under some experimental conditions [21], the contrary (a '*faster-is-faster*' effect) has been observed in other studies [61].

Other collective effects observed at bottlenecks are the *Zipper-Effect*, related to the linear dependency of the bottleneck's capacity on its width [25]. Furthermore, if two crowds approach the bottleneck from both sides these will spontaneously organize such that the two crowds pass through the bottleneck in *oscillations*, where at each turn a handful of people passes the bottleneck [25].

Density Waves   Crowds at high density can exhibit density fluctuations which are quasiperiodic in space and time. These have been observed in real crowds, e.g., on the Jamarat Bridge in Makkah [62] but also experimentally for single-file motion, e.g., [46].

In single-file motion, these density waves consist of a high density part, in which people have a speed close to zero, and another region of lower density in which people are still able to move, so called *stop-and-go* waves. Interestingly, these have some similarities and differences with regard to the formation of traffic jams in vehicular traffic, which we will discuss in more detail in chapter 3. The related phenomenon of phase separation has

been observed in various systems, for example band-formation by charged colloids [50] or in flocking models [63].

Fluctuations in density also occur in critical and dangerous situations as it has been reported for the tragic crowd crush at the Love Parade in Duisburg [64]. In regions of increased density, people can be lifted and loose their contact to the ground. At the same time, the pressure on the chest increases which can cause people to faint. As soon as the density decreases, this can induce falling. These 'holes', where people have fallen onto the ground, pull in people from the sorrounding area as the pressure from that side is reduced [64].

Rotors Another collective phenomenon in crowds is the spontanuous formation of circular motion if there is no desired direction [20] with an exemplaric snapshot shown in Fig. 2.3 (*left*). Similar phenomena of vortex formation have been observed is other active systems, such as confined bacteria [65] or the milling of fish [66]. For crowds these vortices show a characteristic counter-clockwise rotation. The reason behind this 'symmetry breaking' is yet unknown [67].

2.2.3   Modelling of Crowds

At many instances it is not possible, due to ethical or financial reasons, to perform experiments. For instance, when planning large-scale buildings like a stadium, one might want to investigate the influence of certain elements on the overall evacuation time. Such hypothetical scenarios can be tested with models. Apart from practical questions like these, models are crucial to understand crowds, especially from a physics perspective. For instance, with help of a minimal model one might be able to identify the mechanisms that are essential to explain the core-features of certain collective phenomena.

A model might be rather abstract, for instance a network where each node represents a certain area within a facility. The nodes are connected with links that feature a certain (empirically measured) capacity [68]. On the other hand, agent-based models refer to each individual seperately and assign them fairly complex and possibly heterogeneous behaviours. To get a handle on the variety of models, several classifications have been proposed. Let us discuss two of these classificaction schemes below.

The first important classification distinguishes different time-scales of pedestrian behaviour, which are shown in Fig. 2.4 and have been introduced by [69, 70]. On the longest relevant time-scale, i.e., the *strategic level*, pedestrians choose certain activities that they want to perform, e.g., going shopping to a number of stores. At the *tactical*
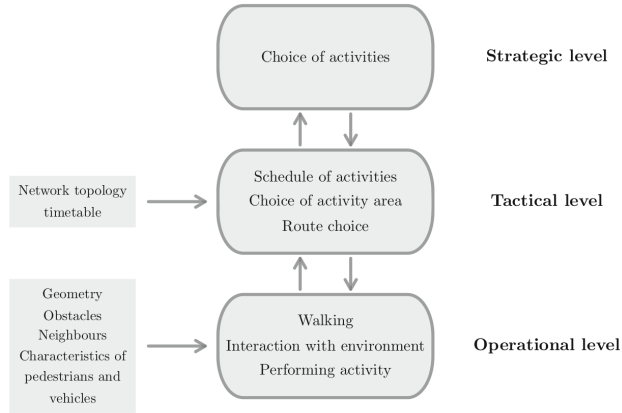
FIGURE 2.4: The three different levels of modelling pedestrian dynamics, following [69, 70]. Figure taken from [25]
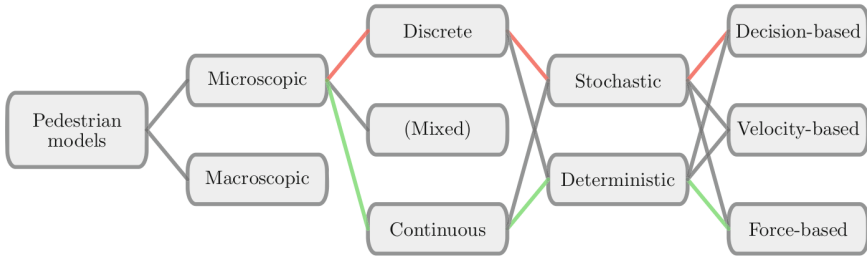
FIGURE 2.5: Classification of pedestrian models following [29]. The green and the red 'path' indicates two types of models which are most frequently encountered. Figure taken from [25].

level, these activities would be scheduled and a certain route is chosen, for instance, based on the current level of crowding. The shortest time-scale is described by the *operational level*, at which the actual walking dynamics is determined, e.g., avoiding an approaching person by stepping to the side. While some models exist for the tactical level, such as those describing route choice behavior, the strategic level is almost exclusively treated as an external input to models. Most models aim at describing the operational level.

At the operational level, models can be further classified according to the scheme depicted in Fig. 2.5 which is based on [29]. In *macrocopic* models, the crowd is treated as a continuum by utilising continuity equations and conservation laws, cf. [71, 72]. In contrast to this, most models are *microscopic* (agent-based) models that refer to each agent individually.

Within microscopic models, one can further distinguish between *discrete* and *continuous* models. In the former, space, time, and the variables that characterize the internal state

of each agent are integers. In the latter they are real numbers and the corresponding model is typically formulated in terms of differential equations. Some models are *mixed*, for instance, the optimal steps model [73] is continuous in space but discrete in time, taking as a time step the actual steps people take.

One can further distinguish between *stochastic* and *deterministic* models. In the latter the state of the systems is determined by the dynamics and the initial conditions at any time. In the former stochastic elements add uncertainties to the system. This stochasticity might be added as probabilities in the decisions that agents take, reflecting our imperfect knowledge of such complex processes. On the other hand, it can also be included as a (white or correlated) noise which is added to the variables of state for each agent.

Finally, it is distinguished between *velocity-based*, *accelaration-based* (or *force-based*), and *decision-based* models. In velocity-based and accelaration-based models, the agents are treated as particles subjected interactions with the external enviroment, e.g., repulsions from neighboring agents, which determine their velocity or acceleration, respectively. Acceleration-based models are typically described by second-order differential equations often using analogies with Newtonian mechanics ('forces'). Velocity-based models, on the other hand, are described by first-order differential equations. In decision-based models the focus is put on the decision processes of the agents by assigning specific rules to each of them.

Not all combinations of the different factors are equally likely. So much so that two typical types of microscopic models are highlighted in Fig. 2.5. On the one hand, there are Cellular Automata models which are discrete, stochastic, and decision based (indicated by red). A typical model out of that class is the floor-field model [15], in which the space is divided into discrete cells. Each pedestrian occupies one of these cells and their decisions are modelled by transition probabilities to one of the neighboring cells. On the other hand, as indicated in green in Fig. 2.5, there are continuous, deterministic, and accelaration-based models, as represented by the Social-Force model [60]. In these kind of models, pedestrians are particles subjected to different 'forces' which are superimposed onto each other. The most important factors are a 'driving force' and a repulsive 'social force'. For more detailed information refer to the reviews of pedestrian models and the references therein [24–27, 74]. Throughout this dissertation, specifically in chapters 3 and 6, we will disucss numerous models that have been proposed to describe crowds. Thereby we will limit ourselves to microscopic models that are continuous in space and typically continuous in time as well.

An important aspect with regard to modeling is, of course, how to assess the realism of these models, i.e., their *validation*. Answering this question can be tricky when modeling

human behaviour. While in traditional theories in physics quantitative agreement is decisive, here the somewhat vague notion of 'similarity' is considered, which always shows some context dependency [75].

The validation of pedestrian models helds practical relevance in the context of commercial software which is employed to test potentially dangerous situations. To this end, a guideline has been proposed which consists of mostly qualitative test-cases which models need to pass [76]. Similarly, an ISO norm has been published which puts more emphasis on quantitative aspects [23]. In a scientific context, the occurence of the collective phenomena and the fundamental diagram are essential to assess the realism of a model [25]. This can be done in a qualitative fashion (e.g., 'the model reproduces lane-formation'), semi-quantitative, for instance, by comparing the flow-density relationship, or by defining a measure that quantifies the similarity [77, 78]. Often models are not proposed to describe pedestrian dynamics in every conceivable situation but in order to understand a certain 'target-phenomenon'. Accordingly, the corresponding models are only checked to reproduce the key features of the specific phenomenon. We will discuss some aspects (and frequent problems) with regard to the validation of pedestrian models in chapter 6.

Chapter 3

Single-File Motion

Human behavior within crowds is generally complex, leading to different collective phenomena. Several key principles of the individual behavior are widely agreed on. Pedestrians naturally occupy a certain volume or area, actively pursuing their objectives while maintaining a safe distance to others. Moreover, pedestrians anticipate changes in their environment and base their decisions on this [79].

The way these principles are conceptualized, however, differ notably between the plethora of agent-based models that have been suggested to describe pedestrian dynamics [25, 26, 80]. Crowds may be described in terms of (social) forces [16], cellular automata [15] or by an optimal velocity which is chosen according to the surroundings [81].

Our aim is to organize the zoo of models for pedestrian dynamics systematically. Focusing solely on models continuous in time and space, we have classified them into three categories based primarily on the variables that characterize the interactions between pedestrians. These categories are Force-based models, Optimal Velocity models, and Velocity Obstacles which are associated with Euclidean spacings, time-gap, and time-to-collision, respectively.

Before delving into the wide array of phenomena observed in crowds, we will begin by examining *single-file motion*, where individuals move in a line without overtaking. This represents a significant simplification of pedestrian dynamics, particularly in terms of theoretical description, as it allows for the study of models in their one-dimensional limit. Moreover, the interaction is primarily restricted to the nearest neighbor in front, and route choice behavior, relevant in many crowd scenarios, being fully negligible. Consequently, this scenario bears resemblance to car traffic on a single-lane road, enabling the application of ideas from models for vehicular traffic. These simplifications facilitate

the identification of conceptual problems more readily than in complex two-dimensional scenarios.

Another important reason for focusing on single-file motion is that many experiments have been conducted and the essential properties of pedestrian single-file motion are relatively well understood. This allows a much more straightforward comparison between models and experiments.

We will commence with a concise overview of the primary findings concerning pedestrian single-file motion, particularly focusing on the emergence of stop-and-go waves and the fundamental diagram. The starting point of our theoretical investigation will be the popular class of force-based models. These models, however, not only grapple with conceptual issues associated with the analogy to Newtonian forces, but also have difficulties in accurately replicating key features of single-file motion.

Therefore, we will introduce models rooted in vehicular traffic, known as *car-following* models, which have a long history and include quite different models. Our focus will be on *Optimal Velocity* models, wherein we demonstrate their derivation from a first principle based on the time-gap. Introducing more nuanced behaviors such as finite reaction time and anticipation will spawn a whole family of models, revealing interconnections between established models. Through stability and scaling analysis, alongside numerical simulations, we will illustrate that this class of models can reasonably capture the essential characteristics of single-file pedestrian motion.

Lastly, we will delve into Velocity Obstacle models, where the time-to-collision, which quantifies the temporal 'distance' to an anticipated collision, governs interactions between agents. Despite the proven accuracy of TTC in describing crowds in certain scenarios [82], we find that in the context of single-file motion, the TTC falls short in capturing its primary features.

This chapter is based on findings that have been published in [83, 84].

3.1   Empirical Findings

Let us quickly recapitulate the main empirical findings regarding single-file motion. For a more extensive review on the different concepts and the numerous experiments that have been conducted refer to the corresponding citations.
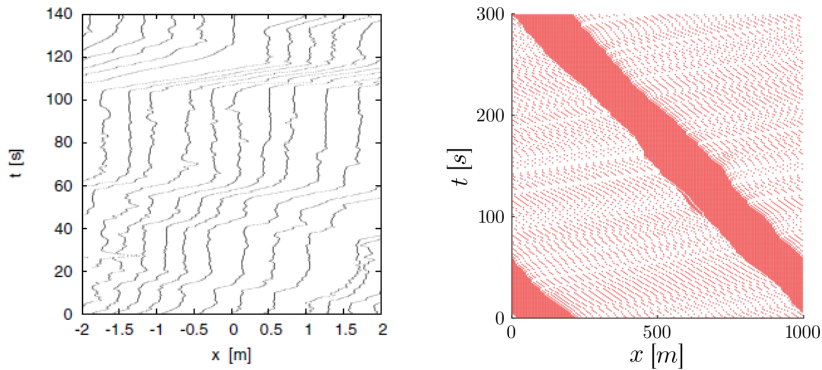
FIGURE 3.1: Left: Stop-and-go waves in trajectories from a single-file experiment with $N = 70$ pedestrians (figure taken from [46]); Right: Trajectories showing phase separation into a jam and a free-flow phase (from simulations of the VDR model [93]).

3.1.1 Stop-and-Go Waves, Phantom Jams, and Phase Separation

The term *stop-and-go waves* was introduced in the late 1970s [85] to describe vehicular traffic in a tunnel. Extensive research on stop-and-go waves in traffic flow has been conducted for decades [86–88], with comprehensive reviews available [29, 89, 90].

The phenomenon refers to a wave, moving in the opposite direction of the agents' motion, with a characteristic velocity. These waves consist of two regions, a stop-part in which the agents have a small velocity and a go-part in which they move with a larger velocity, cf. Fig. 3.1 (left) for an exemplary snapshot of pedestrian trajectories. The region featuring a small (or zero) velocity is, in vehicular traffic, typically called a *jam* or a *phantom jam*. The latter term emphasizes that the jam did not arise due to any kind of bottleneck, in which case the front of the jam would not move upstream but would remain fixed at the bottleneck. Such *phantom jams* have been observed in vehicular, bicycle, and pedestrian pedestrian traffic [87, 91, 92]. The related concept of *phase separation* emphasizes the coexistence of two qualitatively different states which are separated in space. The jam itself which consists of stopped vehicles and another region in which the vehicles are able to move, cf. Fig. 3.1 (right).

Stop-and-go waves are collective phenomenona that arise from self-organization: While at small density the pedestrians or vehicles self-organize into a homogeneous free-flow state, at larger densities inhomogeneities occur and the system self-organizes into stop-and-go traffic. Since all agents (usually) try to avoid jams, their occurrence is remarkable already and indicates complex, non-linear behavior. Apart from that the occurance of
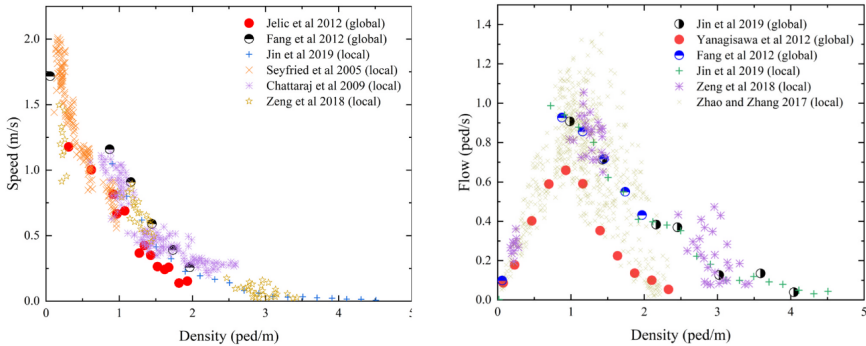
FIGURE 3.2: The fundamental diagram for a large collection of Single-File experiments in its two typical representations, $v(\rho)$ (left) and $J(\rho)$ (right). Fundamental diagrams using local or global density are here depicted in one diagram. Both figures are taken from [95].

traffic jams is, of course, of practical relevance since it has a negative impact on safety, economy and comfort in transportation networks.

For vehicular traffic, the situation is relatively well understood (see e.g. [29, 89] and references therein): stop-and-go traffic features a clear phase-separation into a region of standing vehicles and a region in which the cars hardly interact and move with speeds close to their desired speed. Remarkebly, a characteristic speed of the jam exists. This behaviour is related to metastable states at intermediate densities where free-flow states can be stable for a long time but eventually break down due to fluctuations. This leads to a significant reduction in the flow (capacity drop), and the free-flow state can only be reached again by reducing the density (hysteresis) [94].

Surprisingly this seems to be quite different for pedestrian dynamics [46]. In particular, metastable states have yet not been observed. The system also separates into two phases but the differences between these are much more weakly pronounced: it features regions with speeds close to zero as well as another region in which pedestrians have larger velocities. However, in contrast to vehicular traffic, even in the moving 'phase' the interactions are strong, the corresponding speeds are small, and depend on the density [46].

3.1.2 Fundamental Diagram

Apart from the occurrence of stop-and-go waves, the most important relation for single-file motion (and traffic in general) is the fundamental diagram, whether it be for practical purposes of engineering or for the validation of traffic models [42].

The fundamental diagram describes the relation between mean speed (or flow) and density. Both typical representations are shown in Fig. 3.2 for a collection of experiments on single-file motion from [95]. On the left, a typical $1/\rho$ shape is evident, whereas on the right a triangular shape can be seen. For small densities, the flow increases linearly with density, i.e., the 'free-flow' branch, which is followed by a peak denoting the maximum flow (the capacity) at a critical density. Until the maximum, interactions between pedestrians are scarce. For larger densities, the flow decreases with density as pedestrians slow down due to the interactions. The system is in a 'congested' state and, eventually, stop-and-go waves arise. This applies not only to pedestrian traffic, but also to bicycle and vehicle traffic [91]. Note that several factors influence the exact shape of the fundamental diagram. We have discussed some of these factors in chapter 2.

3.2   Force-Based Models

How are these empirical results reproduced in mathematical models of crowds? A natural starting point to try to answer this question is by studying force-based models. These are, with regard to models continuous in space and time, the most popular models for crowd motion (see e.g. the reviews [25, 26, 80] and references therein). The *social-force model (SFM)* [16] describes the movement of pedestrians by means of repulsive forces that decay exponentially with distance. These repulsive interactions are superimposed with other factors, most importantly, with a driving force that represents the desire to move. Note that, conceptually, the social-force model is predated by the model of Hirai and Tarui [14] which uses algebraic forces instead of exponentials.

The appeal of these models lies in their resemblance to classical mechanics. Pedestrians are treated as individual particles, subject to interactions characterized by diverse forces, encompassing both physical and 'social' elements. These different factors are summed over and result in an acceleration for each individual pedestrian. The social force, in particular, represents an individual's desire to maintain personal space and a preference for avoiding proximity to others. The flexibility in the design of force-based models, owing to these characteristics, has resulted in the formulation of various analytical expressions for these forces.

For a more detailed description, refer to [84] and the references therein.

3.2.1   Conceptual Problems

The force-based approach described above has some conceptual issues that remain incompletely addressed. Notably, concerns such as unrealistic motion, including oscillations,

violations of the exclusion principle (e.g., agents overlapping and 'tunneling' through others, resulting in a reordering of agents in single-file motion), and acceleration leading to velocities exceeding the desired velocity, were underscored in [96, 97]. Moreover, possibly correlated with these issues, it has been observed that achieving realistic motion often requires assigning physically unrealistic values to certain model parameters [98]. It should be emphasized that these effects do not arise from numerical challenges [99], such as in the discretization of the system of differential equations describing motion, but rather stem from fundamental conceptual issues.

Another issue arises from the observation that social forces typically do not adhere to Newton's Third Law, where action equals reaction. This poses fundamental questions, particularly concerning the distinction between force and mass, which relies on the Third Law in classical mechanics. Additionally, the principle of the *superposition of forces*, asserting that the action of different forces on a body is determined by the vector sum of contributions, proves invalid in numerous scenarios encountered in pedestrian dynamics [100]. This deviation often results in numerical challenges, manifesting as unrealistically high forces and total forces pointing in incorrect directions. For instance, in single-file motion, combining the driving force with an asymmetric repulsion can induce unrealistic backward motion.

Some challenges observed in force-based models can be ascribed to excessive inertia effects, leading the model to exhibit damped oscillations rather than the intended overdamped behavior [101–103]. In practical applications, the pedestrian's mass is commonly employed as the mass parameter, resulting in substantial inertia. To mitigate this, a smaller 'effective' mass could be introduced in simulations of second-order models, necessitating the determination of the mass as a parameter through calibration.

Disregarding inertia effects simplifies the dynamic equation for the damped harmonic oscillator, transforming it into a first-order differential equation. This insight has sparked interest in the exploration of first-order, or velocity-based, models for pedestrian motion. This approach is sensible considering that pedestrians can abruptly stop and turn, a behavior achievable only when inertia effects are minimal.

However, disregarding inertia also leads to the fact that the homogeneous configuration will remain stable across all densities and the model can not describe stop-and-go dynamics [27] which, however, is an important factor of model validation in single-file pedestrian models. Even though the original SFM features instabilities and consequently a breakdown of the homogeneous solution. These do not resemble the observed properties of stop-and-go dynamics in pedestrian crowds which are, for example, much better captured in models featuring coloured noise [102, 104, 105].

So far we have discussed some fundamental problems of the force based models related to the analogy to actual Newtonian forces in physics. Thereby, we have focused mainly on problems of local stability and oscillations as well as global stability in terms of stop-and-go dynamics. (How) does the social-force model reproduce the slowing down at increasing density, i.e. the fundamental diagram?

Let us start by noting that a purely distance-based repulsive interaction does not lead to a slowing down in general: imagine pedestrian i right in the middle of two other pedestrians. He or she will feel an equally strong repulsion of both in opposite direction. Due to the superposition of 'forces' these cancel out and allow a movement with the desired speed. Thus, to reproduce the fundamental diagram in such a model, an anisotropic interaction is needed [106]. For example, it is argued that due to the limited perception an interaction is only present to the agent in front. Consequently, the desire to keep a distance to the person in front mitigates the desire to move and the agents slow down. For the social-force model, however, the resulting fundamental diagram is unrealistic [30] and cf. Appendix A. Additionally, even though studies on proxemics indicate that the personal space shows some degree of asymmetry, i.e. a larger extension in front than in the rear, such a strong asymmetry is not supported empirically [107].

Another way to explain the fundamental diagram in such a model was introduced in [108], where closer attention was payed to the details of *volume exclusion*. Generically, pedestrians are represented by disks with constant radius. Observations have, however, shown that the space requirement of pedestrians is not constant, but depends on the walking speed since the step length increases with increasing speed. This introduces a velocity dependent size $\ell = \ell(v)$, which allows the pedestrians 'to make themselves smaller' by slowing down. This offers an alternative explanation of the fundamental diagram and matches experimental results reasonably well, cf. [108].

Let us recapitulate, the class of Social Force models seem to suffer from inherent (conceptual) problems and can neither describe stop-and-go waves nor the fundamental diagram reasonably well. In the following we will therefore study a different class of models that originates in vehicular traffic. Interestingly, even though inertia effects are much more relevant here than for pedestrian dynamics, several models that neglect inertia have been developed. Given the preceding arguments, it appears worthwhile to investigate in more detail their suitability for pedestrian dynamics, perhaps after some modifications.

3.3 Following Models based on the Time-Gap

The idea of 'car-following' models discussed in this section originates not in pedestrian dynamics but in vehicular traffic where the first analyses of single-file, or rather single-lane, traffic date back to the 1950s [109]. Since then numerous models have been proposed. For readers interested in a historical overview refer to [84]. We will start by organizing the existing zoo of models by defining three categories of car-following models. Subsequently, we will focus on one of these model classes, so called 'Optimal Velocity' models.

These can be derived from a simple first principle, based on the assumption that agents pay attention mainly to the time distance instead of Euclidean distances which gave rise to the force like interactions discussed in the previous section. Specifically, we will assume that people pay attention to the time-gap, which denotes the time one would need, given the current speed, to reach the rear of the vehicle in front. The time-gap accounts for the fact that the Euclidean safety distance depends on the speeds. Accordingly, a rule of thumb to estimate the safety distance on highways is based on the time-gap: the two second rule.[1] In particular, the driver should always make sure that the time-gap to the preceding vehicle is larger than two seconds. Starting from there, we will introduce other time scales such as reaction and anticipation time which will allow us to reveal some interesting interrelations between different models.

We will investigate how these affect the stability properties, related to the occurrence of stop-and-go waves. Furthermore, we will discuss the influence of noise which gives rise to an alternative mechanism to reproduce stop-and-go dynamics. Finally we will pay attention to the fundamental diagram of these models and the variables that characterize it.

3.3.1 Categorizing Following Models

As mentioned above many different types of following models exist. In the following we try to subdivide these models into different classes which then will help us to understand the relations between the models better. Without loss of generality we consider here only interactions with the nearest neighbor in front. The general case of interactions with more than one predecessor is discussed in [110].

Since we focus on single-file motion, we assume a one-dimensional space with N agents of size ℓ. We denote their positions, velocities and accelerations by x_i, $v_i = \dot{x}_i$ and $a_i = \ddot{x}_i$, respectively (Fig. 3.3). The distance between two agents i and j is $\Delta x_{ij} = x_j - x_i$, i.e. defined as the distance between the centers. The agents are sorted in ascending order

---

[1]See for example https://en.wikipedia.org/wiki/Two-second_rule.

in the direction of motion, i.e. agent $i + 1$ is the predecessor of agent i. Most of the time it is sufficient to consider the predecessor i only, therefore Δx_i denotes the distance between the centres of i and $i + 1$. In single-file motion this order will be preserved as overtaking is not possible. In the following, we will omit the time-dependencies of the dependent variables if no delays are present, i.e., if they are evaluated at the same time.
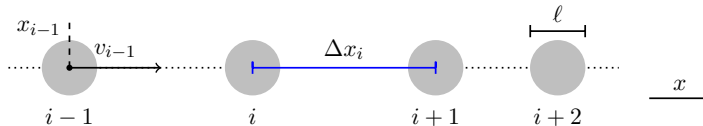
FIGURE 3.3: Illustration of an one-dimensional chain of self-driven particles.

Generically, all *following models* then have the form

$$\ddot{x}_i = A(\Delta x_i, \dot{x}_i, \dot{x}_{i+1}), \tag{3.1}$$

for 2nd order models [111] or

$$\dot{x}_i = V(\Delta x_i, \dot{x}_{i+1}), \tag{3.2}$$

for 1st order models. The functions A and V are model-dependent.

For all models, there exists at least one equilibrium solution where the agents are evenly distributed in the system (i.e. $\Delta x_i = x_{\text{eq}}$) and move with the same speed $v_i = v_{\text{eq}}$. Equilibrium speed v_{eq} and equilibrium spacing x_{eq} are determined by the conditions

$$A(x_{\text{eq}}, v_{\text{eq}}, v_{\text{eq}}) = 0, \tag{3.3}$$

and

$$V(x_{\text{eq}}, v_{\text{eq}}) = v_{\text{eq}}, \tag{3.4}$$

respectively. While for *Stimulus-Response Models* this equilibrium solution is not unique, *Optimal Velocity* (OV) models explicitly include a function F such that the equilibrium solution is $(x_{\text{eq}}, F(x_{\text{eq}}))$. In some cases, to which we refer as *Implicit Optimal Velocity models*, this function exists implicitly, but may be non-analytical. This categorization is sketched in Fig. 3.4.

In OV models, the existence of the described optimal velocity function $F(s)$ directly gives rise to the fundamental diagram (i.e. flow-density or speed-density relation) of the equilibrium solution. This will be discussed in section 3.3.5.

Stimulus Response	**Optimal Velocity**	**Implicit Optimal Velocity**
No unique eq. solution	Explicit Function F: $(x_{\mathrm{eq}}, F(x_{\mathrm{eq}}))$ eq. solution	F exists implicitly, e.g. non-analytical
Pipes [112], Chandler [113], Gazis [114]	Optimal Velocity Model [115], FVDM [116]	Gipps [117], Intelligent Driver Model [118]

FIGURE 3.4: The proposed categorization of car-following models (top row) with popular examples of each category (bottom row) and typical mathematical properties of the underlying dynamical equations (middle row).

3.3.2 Generalized Optimal Velocity Models

The classification of Optimal Velocity models in Section 3.3.1 is based on mathematical properties. It does not involve detailed behavioural assumptions about the agents and can include a broad variety of models. New models are often defined by adding *ad-hoc* terms to existing models. Frequently these additional terms only have a small quantitative effect without changing the overall behavior. The following considerations might lead to a deeper understanding of this observation.

In this section, we try to show how and under which assumptions a class of Optimal Velocity models can be derived from a behavioural first principle, namely that agents keep a certain time-gap to their neighbors [91]. By attributing human properties to the agents, i.e., adding *anticipation* and a finite *reaction* time, several well-known Optimal Velocity models are introduced and related to each other. We will see that different timescales will become relevant here. These timescales have been introduced previously to capture certain aspects of pedestrian motion, in particular the desired time-gap, reaction or relaxation time, and anticipation time.

In force-based models the *relaxation time* τ_R, or, more precisely, the speed-relaxation time, is usually implemented by a driving force $(\boldsymbol{v}_{\mathrm{des}} - \boldsymbol{v}_i)/\tau_R$ where $\boldsymbol{v}_{\mathrm{des}}$ is the desired velocity. Neglecting other forces, this leads to an exponential relaxation of the walking speed to the desired velocity. As pointed out in [119], in a 2d scenario the same relaxation time also controls the dynamics of evasive motion when encountering obstacles or other pedestrians. The fact that the timescales for these different types of motion are identical can lead to problems. In OV models, the inverse relaxation time $1/\tau_R$ is interpreted as a sensitivity to deviations of the actual velocity from the optimal velocity [115]. The difference between reaction, update and adaptation time has been analyzed in [120] for

vehicular traffic. For pedestrian motion the time-gap is used in the *Collision Free Speed model* [81], where the desired time-gap can be used to model the motivation in a crowd [121].

3.3.2.1   Time-Gap and Optimal Velocity Models

The typical *time-gap* (in one-dimension) between agents i and j is

$$T_{ij} = \begin{cases} \dfrac{\Delta x_{ij} - \ell}{v_i} & \text{for } v_i > 0 \\ \infty & \text{else,} \end{cases} \tag{3.5}$$

where we assume that i is behind j such that $x_i < x_j$. It denotes the time until agent i would collide with agent j, if j suddenly stops and i keeps moving at a constant speed. Therefore, it can also be viewed as a *time-to-collision*.

In order to define a minimal model, we assume a behavioral first-principle. In particular, the agents want to move as fast as possible while keeping a time-gap greater or equal than the *desired time-gap* T to all other agents. This can be written as:

> *Agents choose their velocity v_i such that $T_{ij} \geq T$ for all $j \neq i$ while at the same time maximizing v_i.*

Note that, the agents can always fulfill this constraint by stopping, i.e., choosing $v_i = 0$. More formally, the model can be written as

$$v_i = \max \left\{ v \in \mathbb{R} \,\middle|\, \frac{\Delta x_{ij} - \ell}{v} \geq T \text{for} \forall j \neq i \right\}, \tag{3.6}$$

where the domain of v might be restricted by a minimal or maximal speed. The model defined by Eq. (3.6) in principle includes interactions with all other agents. However, by definition, the ordering is preserved in single-file motion, i.e., $x_{i+1}(t) > x_i(t)$ which entails that the smallest time-gap in front is the one to the predecessor. Here we leave aside the frequent problem of tunneling, which leads to a destruction of this order and can give rise to numerical problems and artifacts. In the back, a finite time-gap is only obtained for negative speeds. Negative speeds can only occur if the distance between two agents falls below ℓ which can happen due to specific initial conditions or instabilities. In these cases an interaction with the person behind would arise from Eq. (3.6) which has been investigated in [122]. We will neglect these specific cases here.[2]

---

[2]Additionally speeds are often capped between 0 and v_{max} which prohibits these special cases. Apart from that, due to the limited human perception, the interaction between pedestrians is often restricted to those in front.

This means that Eq. (3.6) simplifies to an *Optimal Velocity* model which only includes an interaction with the nearest neighbor in front, i.e.

$$v_i = \frac{\Delta x_i - \ell}{T}. \qquad (\text{OV, } 1^{st})$$

This minimal model is the original first-order Optimal Velocity model introduced by Reuschel [109] and Pipes [112] with a linear OV function.

3.3.2.2   Reaction and Anticipation Time

An important constraint in human traffic is the *reaction time*, by which human reactions to a change in the environment are delayed. A finite reaction time can be included by adding τ_R as a delay to the corresponding quantities, i.e., evaluating them at a later time. The corresponding delayed first-order model of Eq. (OV, 1st) reads

$$v_i(t + \tau_R) = \frac{\Delta x_i(t) - \ell}{T}, \qquad (\text{OV, } del)$$

which is a delay differential equation. Second-order models can be obtained by employing a Taylor expansion for small τ_R as

$$v_i(t + \tau_R) \simeq v_i(t) + \tau_R \cdot a_i(t), \qquad (3.7)$$

where $a_i = \dot{v}_i$. Applying Eq. (3.7) to Eq. (OV, del), results in

$$a_i = \frac{1}{\tau_R} \left(\frac{\Delta x_i - \ell}{T} - v_i \right), \qquad (\text{OV, } 2^{nd})$$

the second-order OV model [115]. The Taylor expansion in Eq. (3.7) considerably simplifies the model Eq. (OV, del). This linearisation can have consequences on the stability properties of the models which will be discussed in Section 3.3.3.

In order to allow a higher and more comfortable flow, and to account for the reaction time, humans *anticipate* (possible) changes of the current situation. The time-gap Eq. (3.5) can be interpreted as anticipating a worst case scenario, i.e. that the preceding agent suddenly stops. Another typical anticipation strategy is to assume that the preceding agent keeps on moving with a constant velocity. At the level of a time distance this gives rise to the time-to-collision which will be discussed below. In our case, a forecast of future positions based on the relative velocity can be implemented as

$$\Delta x_i(t + \tau_A) \simeq \Delta x_i(t) + \tau_A \cdot \Delta v_i(t), \qquad (3.8)$$

where τ_A is the *anticipation time*. Adding $\Delta x_i(t+\tau_A)$ as a forecast, i.e., as true knowledge of the future positions, to Eq. (OV, *del*) changes its delay simply to $\tau_R - \tau_A$. This is an example where the introduction of an additional parameter does not lead to changes in the fundamental behavior of a model.

Even though Eq. (3.8) and Eq. (3.7) are very similar, their natural interpretation is different. In particular the former is an assumption about the behaviour of the agents, whereas the latter is an approximation to obtain a simpler model.

If anticipation is added as in Eq. (3.8) to the model Eq. (OV, 1st), one obtains

$$v_i = \frac{\Delta x_i - \ell}{T + \tau_A} + v_{i+1} \cdot \frac{\tau_A}{T + \tau_A}, \qquad \text{(ANT, } 1^{st})$$

which is a specific version of the time-to-collision model proposed in [83]. A reaction time τ_R can be included as

$$v_i(t + \tau_R) = \frac{\Delta x_i(t) - \ell}{T + \tau_A} + v_{i+1}(t) \cdot \frac{\tau_A}{T + \tau_A}. \qquad \text{(ANT, } del)$$

Employing Eq. (3.7) yields

$$a_i = \frac{1}{\tau_R} \left(\frac{\Delta x_i - \ell}{T + \tau_A} + v_{i+1} \cdot \frac{\tau_A}{T + \tau_A} - v_i \right). \qquad \text{(ANT, } 2^{nd})$$

Anticipation can also be included in Eq. (OV, *del*), i.e.

$$v_i(t + \tau_R) = \frac{\Delta x_i(t) - \ell}{T} + \Delta v_i(t) \cdot \frac{\tau_A}{T}. \qquad \text{(FVDM, } del)$$

Together with Eq. (3.7) this leads to

$$a_i = \frac{1}{\tau_R} \left(\frac{\Delta x_i - \ell}{T} + \Delta v_i \cdot \frac{\tau_A}{T} - v_i \right), \qquad \text{(FVDM, } 2^{nd})$$

the well-known *Full-Velocity-Difference model* [116]. In the models (ANT, *del*) and (ANT, 2nd) anticipation is added before a finite reaction time, while in (FVDM, *del*) and (FVDM, 2nd) we first added a finite reaction time and then anticipation. This boils down to the question if agents know their own velocity without a delay (as in the former) or with a delay (as in the latter).

3.3.2.3   Summary of Model Relations

The connections of the proposed models by the various time-scales is summarized in Fig. 3.5. The derivation of Optimal Velocity models from the *time-gap* leads to a loss of generality: In the typical formulation, the optimal velocity function $F(\cdot)$ is not specified but
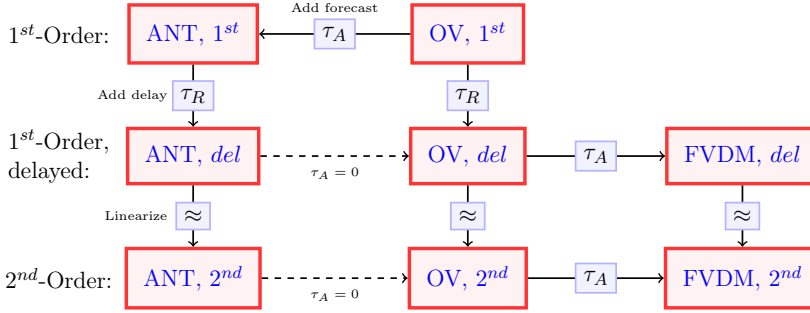
FIGURE 3.5: Chart of the generalized Optimal Velocity models.

only constrained by few assumptions [123]. From another perspective, however, it is more general: the Ansatz Eq. (3.6), is neither restricted to a specific time 'distance', an one-dimensional setting nor to circular shapes. If the time-gap in Eq. (3.5) is formulated in two dimensions, the collision-free speed model [81] follows directly from the same assumptions.

The time-scales introduced above, namely, the time-gap, the desired time-gap, the reaction time, and the anticipation time, have helped to uncover relations between various models. In order to further understand their meaning and effects, these models are investigated regarding their stability properties in Section 3.3.3 and the effect of noise in Section 3.3.4.

Before studying the models in greater detail, let us discuss a relation to another, quite different class of models which we can uncover through the way we defined the Optimal Velocity models above. In particular, they are equivalent to models based on *Velocity Obstacles*. These are usually defined in two dimensions and were introduced for motion planning of robots in complex environments [124] and used to model pedestrian motion as well [125, 126].

3.3.2.4   Relation to Velocity Obstacles

While we are mostly concerned with describing and understanding the empirical findings of crowd or vehicular motion with the help of mathematical models, our investigation touches on the development of automated vehicles. Here, the growth of perturbations, which eventually leads to a jam, is still present in current commercial automated vehicles [127]. Improved regulations, that take stability properties known from Car-Following models into account, can prevent the occurrence of stop-and-go waves, even if only a small fraction of vehicles is automated [128]. Automated autonomous vehicles can be

considered as a one-dimensional limit of the more general, at least two dimensional, problem of motion planning of autonomous robots in which the concept of Velocity Obstacles originates. Their main objective is to provide a collision-free path to reach the goal.

However, practical problems such as noise, delays or inertia are, apart from sensing errors [129], hardly studied yet. Even though, the concept has been applied to actual robots [130] problems of instabilities have been reported [131]. Analytical results for Velocity Obstacles are not known to the author, apart from [132], where only two agents are considered. The resemblance to Optimal Velocity models may deepen our understanding of Velocity Obstacles. Especially, the effect of various influences has been studied extensively in the field of car-following models as well as powerful methods such as stability analysis have been used in the field for a long time.

Typically Velocity Obstacles are not based on time-gaps but instead on the time-to-collision. This will be discussed in section 3.4 where we will see that this leads to inherent problems in the case of single-file motion. Let us now repeat the derivation of optimal velocity models performed in section 3.3.2 but this time as Velocity Obstacle models.

Optimal Velocity or Velocity Obstacle: Velocity Obstacles are based on a reasoning in velocity space. In particular, the velocity space of each agents is restricted by potential collisions with obstacles and other agents. The agents choose a velocity, which lies outside of these Velocity Obstacles, according to an optimization goal.

Consider the set of velocities that do *not* fulfill $T_{ij} \geq T$, i.e.

$$VO_{ij}^T = \{v | (\Delta x_{ij} - \ell)/v < T\}. \tag{3.9}$$

This is, apart from exchanging the time-to-collision with the time-gap, equivalent to the definition of Velocity Obstacles [124]. The parameter T is here usually referred to as the horizon time above which potential collisions are not taken into consideration. We will however continue calling it the desired time-gap.

The union of the velocity obstacles reads

$$VO_i^T = \bigcup_{j \neq i} VO_{ij}^T. \tag{3.10}$$

This set includes all velocities that do *not* fulfill $T_{ij} \geq T$ for $\forall j$. Let us now define a set of reachable velocities as

$$RV_i = \{v | v \in [v_{\min}, v_{\max}]\}. \tag{3.11}$$

where also more complex constraints might be implemented such as physical acceleration constraints.

We can now define the reachable avoidance velocities as the difference between the reachable velocities and the union of the Velocity Obstacles

$$RAV_i = RV_i \ominus VO_i^T. \tag{3.12}$$

Combined with an optimization goal, a model can now be defined as

$$v_i = \max_{v \in RAV_i}(v), \tag{3.13}$$

where we assumed continuous time. Alternatively one might define it with a finite update time δt. If we assume positive speeds and an ordered chain, as above, Eq. (3.13) is equivalent to the first-order Optimal Velocity model specified in (OV, 1st).

As earlier we might include a reaction time τ_R in Eq. (3.9) which yields

$$VO_{ij}^T(t + \tau_R) = \{v | (\Delta x_{ij}(t) - \ell) / v \geq T\} \tag{3.14}$$

This resembles the delayed first-order Optimal Velocity model (OV, *del*). Employing the approximation in Eq. (3.7), leaves the Velocity Obstacles Eq. (3.9) unchanged and a second-order model is obtained as

$$a_i = \frac{\max_{v \in RAV_i}(v) - v_i}{\tau_R}, \tag{3.15}$$

i.e. we recover (OV, 2nd).

In accordance with Eq. (3.8), anticipation might be added as

$$VO_{ij}^T = \{v | (\Delta x_{ij} + \tau_A(v_j - v) - \ell) / v \geq T\}, \tag{3.16}$$

which leads to the first-order anticipation model (ANT, 1st). Adding a delay yields (ANT, *del*), to which approximation Eq. (3.7) can be applied to obtain the corresponding second-order model (ANT, 2nd).

On the other hand, including anticipation in Eq. (3.14) yields

$$VO_{ij}^T(t + \tau_R) = \{v | (\Delta x_{ij} + \tau_A \Delta v_{ij} - \ell) / v \geq T\}, \tag{3.17}$$

i.e. the delayed Full-Velocity-Difference model (FVDM, *del*). If, again, Eq. (3.7) is employed, a Velocity Obstacle formulation of the Full-Velocity-Difference model (FVDM, 2nd) is obtained. We can fully recover the class of Generalized Optimal Velocity models by only referring to the Velocity Obstacle framework.

Note that, a large difference between the two model classes is the role of the update time δt. Optimal Velocity models are defined as mathematical models in continuous time, i.e., in terms of differential equations. The update time is only introduced in order to numerically solve the equations of motion. The results need to be independent of it. In our case, a simple first-order Euler-scheme with $\delta t = 0.01$s ($\delta t = 0.001$s for the delayed models) proved to ensure this independence.

Models based on Velocity Obstacles are, on the other hand, typically defined with an explicit time-step, i.e., $\delta t \sim 0.1$s. Thus, the dynamics are, in general, not independent of the discretization and the update time δt has to be treated as a model parameter.

3.3.3 Stability Analysis

Let us now investigate the stability properties of the proposed models. Here, two different types of stability are known in the literature of car-following models: *platoon stability* and *string stability* [123]. Platoon stability is also called local stability because it refers to the growth of a perturbation at a fixed car. String stability is also referred to as global stability which describes the perturbation as it moves upstream from car to car. On the level of an individual car, one can further derive conditions whether perturbations are *overdamped* [86].

These types of stability give rise to different 'regimes of stability' which are shown in Fig. 3.6, where the y-axis shows the velocity and the x-axis shows the time. A string of $N = 10$ agents is shown each with a different color, the orange car is the leader and the blue car is the last car. All of the cars initially move with the same velocity v_{eq} and the same spacing to the preceding vehicle Δx_{eq}. Now, due to some perturbation, the leader suddenly decelerates and then accelerates back to the equilibrium speed. This is the setting we will study in this chapter.

To begin with, for all cases in Fig. 3.6, the perturbation declines at a fixed car, i.e. the conditions for *platoon stability* are fulfilled. This is a very weak form of stability that should be fulfilled in every traffic model [123]. Conditions for *overdamping* are only fulfilled in **(a)**, where the agents decelerate due to the perturbation and then accelerate to reach the equilibrium speed. In contrast to this, in **(b)** and **(c)**, they overshoot this equilibrium speed which leads to oscillations at an individual car. Finally, in **(c)**, the

(a) Overdamped   **(b) Oscillating**   **(c) String Unstable**
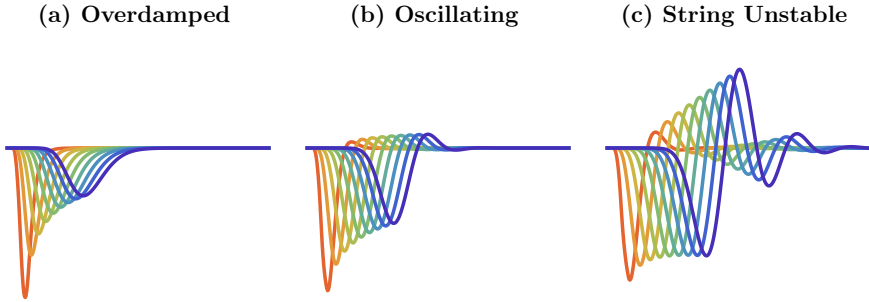
FIGURE 3.6: Numerical solutions of a string of 10 agents for the Full-Velocity-Difference model (FVDM, 2nd). All strings are platoon stable, i.e. perturbations decline at an individual agent. While in (a) and (b) The perturbation is declining upstream, the agents 'overshoot' only in (b). In (c) The perturbation grows when moving upstream. The system is not string stable.

system is string unstable as the perturbation grows as it propagates from car to car whereas in the other two cases it declines, accordingly the system is string stable in **(a)** and **(b)**.

We will start by looking at *platoon stability*, which can be analyzed by studying a single agent only. This will allow us to draw a close analogy with the harmonic oscillator and to gain insight in the physical meaning of the different parameters. For *overdamping*, we will discover some problems in its definition and finally, we will investigate *string stability* and the occurrence of stop-and-go dynamics.

Let us note that, all first-order models without any delay are platoon stable, overdamped, and string stable. This means any kind of oscillation or instability can only occur as soon as a finite reaction time is included. Therefore we will only study models that include τ_R either as a delay or as a relaxation time in the following.

3.3.3.1   Platoon Stability

To investigate platoon stability, it is sufficient to analyze the differential equation of a single agent. If the real part of the solutions of the corresponding characteristic equation are negative, the model is platoon stable.

The second-order models (OV, 2nd), (ANT, 2nd), and (FVDM, 2nd) then correspond to the harmonic oscillator, cf. Appendix B,

$$\ddot{x} = -\frac{k}{m}x - \frac{\gamma}{m}\dot{x}. \tag{3.18}$$

Let us match the time-scales, T, τ_A, and τ_R, introduced in our models with the physical parameters of the harmonic oscillator.

The reaction time τ_R corresponds to the mass m. A larger mass leads to an increased inertia which corresponds the resistance of a physical object against a change in its velocity. In (OV, 2nd) and (FVDM, 2nd), the desired time-gap T can be identified with the inverse of the stiffness k.[3] According to Hooke's law, k determines the force exerted by a spring if it is displaced from its equilibrium position. Thus, the desired time-gap T determines how fast gaps are closed between the agents. In crowds it has been used to model differences in motivation e.g. in [51, 121]. The dampening factor γ is constant and equals one in (OV, 2nd) and (ANT, 2nd). In (FVDM, 2nd), a second term is added, i.e. $\gamma = (1 + \tau_A/T)$. Damping leads to a dissipation of energy and, hence, to damped motion. Accordingly, all second-order models are platoon stable for all parameter values

The first-order delayed models can be written as

$$\dot{x}(t + \tau_R) = -kx(t) - \gamma \dot{x}(t), \tag{3.19}$$

with $k > 0$, $\gamma = 0$ for (OV, *del*) and (ANT, *del*), and $k, \gamma > 0$ for (FVDM, *del*). In the first case, Eq. (3.19) simplifies to a linear, first-order delayed differential equation. The stability conditions are well-known and read

$$T > \frac{2}{\pi}\tau_R - \tau_A, \tag{3.20}$$

for (ANT, *del*) and (OV, *del*) with $\tau_A = 0$.

In the second case, for (FVDM, *del*), Eq. (3.19) is a neutral delayed differential equation (NDDE) which is much more difficult to solve. Employing the results from [133] yields

$$\tau_R < \cos^{-1}\left(-\frac{\tau_A}{T}\right)\sqrt{T^2 - \tau_A^2} \text{ and } T > \tau_A, \tag{3.21}$$

which can not be solved for T explicitly. A sufficient condition can, however, be obtained as

$$T > \sqrt{\left(\frac{2\tau_R}{\pi}\right)^2 + \tau_A^2}. \tag{3.22}$$

All conditions for platoon stability are plotted in Fig. 3.7 on the left.

By employing the approximation Eq. (3.7) we have changed delayed first-order models to second-order models. This leads to a different meaning of the reaction time τ_R. Namely, a delay of the reaction to a change is transformed into a resistance against a change. Only in the former case it can lead to platoon instabilities.

---

[3]It has the slightly different form $(T + \tau_A)^{-1}$ in (ANT, 2nd).

3.3.3.2 Overdamping

Let us now study the overdamping of the local oscillations as it is shown in the difference between Fig. 3.6 **(a)** and Fig. 3.6 **(b)**. Note that damped oscillations around the equilibrium position are a frequent problem in models for crowds [27, 96].

Typically, overdamping means that all roots of the characteristic equation are real and negative. As we are still concerned with local stability, for the second-order models, we can again refer to the harmonic oscillator. Accordingly the conditions read as

$$\tau_R < \frac{T + \tau_A}{4}, \tag{3.23}$$

for (ANT, 2nd) and

$$\tau_R < \frac{(T + \tau_A)^2}{4T}, \tag{3.24}$$

for (FVDM, 2nd). The conditions for (OV, 2nd) can be obtained by setting $\tau_A = 0$.

The idea of overdamping has been applied to delayed models as well [86, 134] and the corresponding conditions for the (ANT, *del*) model reads

$$T \geq e \cdot \tau_R + \tau_A, \tag{3.25}$$

where again the condition for (OV, *del*) is obtained by setting $\tau_A = 0$.

However, the reasoning behind this is more intricate. Delayed differential equations have infinitely many (complex) eigenvalues. This means that there are imaginary solutions of the characteristic equation even if Eq. (3.25) is fulfilled. However, there is one real eigenvalue that is much larger than all realparts of the other, imaginary, eigenvalues. Consequently, even though the solution could show oscillations for some initial conditions, numerical solutions show a simple exponential decay which is conspicuous of overdamped behaviour. Note that the condition in Eq. (3.25) determines the parameter values at which the largest eigenvalue becomes purely real, which means qualitatively there is a sharp transition from oscillatory to overdamped behaviour.

The situation is different for the neutral delayed differential equation in Eq. (3.19) which corresponds to (FVDM, *del*). The equation always has a real root [135]. By solving the characteristic equation numerically, using [136], we can see that as T increases, the real eigenvalue gets larger and the real parts of the imaginary eigenvalues decline. Consequently, the system continuously changes from oscillatory to overdamped behaviour. However, we can not define a clear point as there is no sharp transition as in the other models.
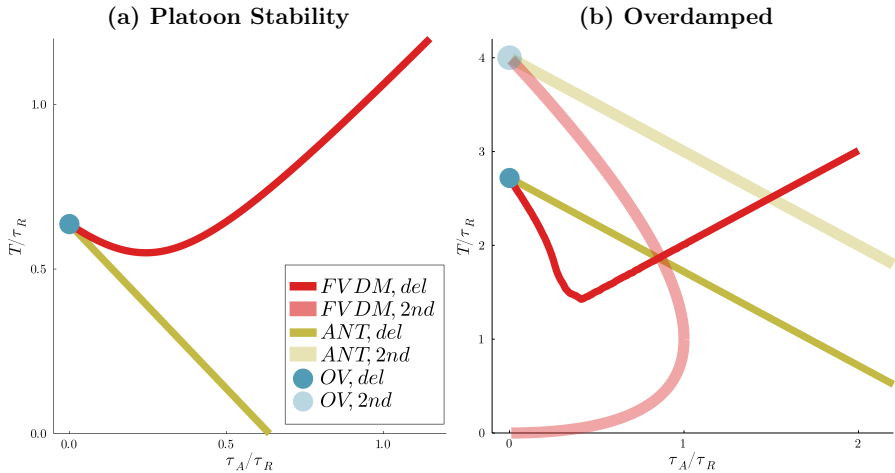
FIGURE 3.7: The platoon stability conditions for the delayed models **(a)** and the conditions for overdamping **(b)** of the Generalized Optimal Velocity models. For parameter values in the area below the corresponding curve the model becomes platoon unstable or non-overdamped respectively.

In practice we just define overdamping in (FVDM, *del*) as overshooting the equilibrium position and solve the equation numerically.[4] The results are shown, together with the conditions for the other models, in Fig. 3.7 **(b)**.

Apart from simple first-order models, all models show oscillatory behavior for some parameter values. The conditions for these are, of course, much more restrictive than for platoon stability as overdamping includes platoon stability. Even though we found that only the delayed models showed platoon instabilities, second-order models seem to be more prone to oscillations.

3.3.3.3   String Stability

To investigate string stability we will analyze a semi-infinite chain agents. In particular, we will use periodic boundary conditions in which the N agents are placed on a ring of length L where the predecessor of the last agent is the first agent. Due to the closed boundaries, a perturbation can not leave the system. Linear stability analysis is then used to determine under which conditions a perturbation grows or declines while it moves downstream. Specifically, whether the homogeneous configuration characterized by the equilibrium spacing and velocity is linearly stable. In the following, we will employ the very general results from [137] to obtain the stability conditions. These conditions, however, do not apply to (FVDM, *del*) for which we study the linear stability.

---

[4]The initial conditions are fixed as $x_L = 0$, $v_L = 0$ for the leader, and $x = 1$, $v = 0$ for the follower.

Let us start with the second-order model (OV, 2nd) and its delayed counterpart (OV, *del*). These have the same stability-condition, i.e.

$$T > 2\tau_R. \tag{3.26}$$

An instability is created by adding a reaction time. Whether it is added as a delay or a 'resistance', does not influence the stability.

The model (ANT, *del*) and its second-order companion (ANT, 2nd) yield

$$T > 2\tau_R - \frac{\tau_A}{1 + \tau_A/T}, \tag{3.27}$$

where the critical value of the desired time-gap monotonically decreases with a larger anticipation time and approaches the limit $T > \tau_R$ for $\tau_A \to \infty$. In particular, a larger anticipation time always increases stability but can not account for an reaction time larger than the desired time-gap. Similarly for (FVDM, 2nd), which is stable for

$$T > 2(\tau_R - \tau_A), \tag{3.28}$$

a larger anticipation time increases the critical value of τ_R for which instabilities would arise.

The stability condition of the corresponding delayed model (FVDM, *del*) could not be obtained in an analytical form. In contrast to the other models, multiple wavelength determine the string-stability. Therefore, there is little hope to find an analytic condition. However, the exact stability condition can be visualized and is shown, together with the conditions of the other models in Fig. 3.8. See the appendix C for details of the calculation.

All criteria for string stability are depicted in Fig. 3.8. The delayed models exhibit equivalent string stability conditions to their second-order counterparts, with the exception of (FVDM, *del*) and (FVDM, 2nd). Initially, these conditions align for small values of τ_A/τ_R. However, unlike the second-order model where critical parameter values change linearly, the delayed model displays a non-linear, potentially non-analytical behavior.

In all models excluding (FVDM, *del*), an increase in anticipation time τ_A enables compensation for larger reaction times τ_R without inducing instabilities. Within these models, the dominant unstable mode corresponds to the one with the longest wavelength, resulting in (spatially) large inhomogeneities resembling traffic jams, as illustrated in Fig. 3.9 (left). Contrastingly, for (FVDM, *del*), there exists an 'optimal' ratio τ_A/τ_R where critical parameter values reach a minimum. Interestingly, during this minimum,
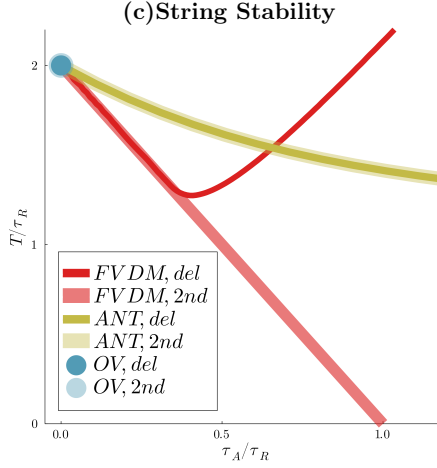
FIGURE 3.8: Conditions for string stability for the generalized Optimal Velocity models. For parameter values located in the area below the corresponding curve the model becomes string unstable.
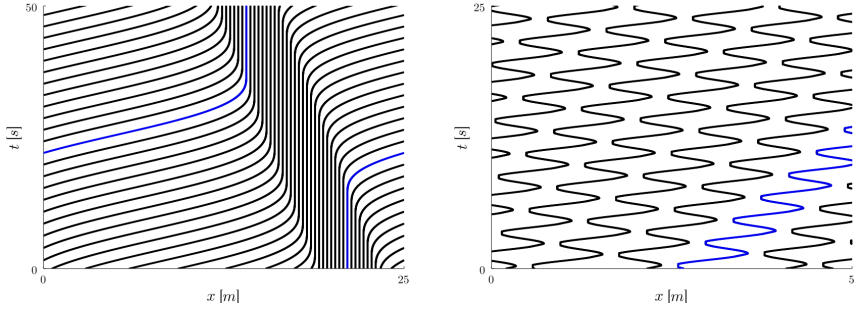
FIGURE 3.9: Trajectories of the numerical solution of (FVDM, *del*). On the *left*, τ_A/τ_R is small and the most unstable mode corresponds to the one having the largest wavelength. For large τ_A/τ_R, on the other hand, there are many very fast oscillations (*right*).

the dominant unstable mode shifts from the largest wavelength to much smaller wavelengths, giving rise to oscillations, as depicted in Fig. 3.9 (right).

Summary In Table 3.1 we have summarized all stability conditions for all models discussed in this section. There are some clear trends: reaction time destabilizes the traffic locally and globally, anticipation time, and a larger desired time-gap, on the other hand has a stabilizing effect. For the anticipation time, if the agents know their own velocity with a delay only, i.e. in the case of (FVDM, *del*), there exists an optimum and anticipation can give rise to inhomogeneities with a short wave-length. This is not

empirically observed but could be of interest in the case of practical issues, e.g. the development of automated vehicles.

Model	Platoon Stability	Overdamped	String Stability
OV, 1st	✓	✓	✓
ANT, 1st	✓	✓	✓
OV, *del*	$T > \frac{2}{\pi}\tau_R$	$T \geq e \cdot \tau_R$	$T > 2\tau_R$
ANT, *del*	$T > \frac{2}{\pi}\tau_R - \tau_A$	$T \geq e \cdot \tau_R - \tau_A$	$T > 2\tau_R - \frac{\tau_A}{1+\tau_A/T}$
FVDM, *del*	$T > \sqrt{(2/\pi\tau_R)^2 + \tau_A^2}$	cf. Fig. 3.7, (b)	cf. Fig. 3.8
OV, 2nd	✓	$T > 4\tau_R$	$T > 2\tau_R$
ANT, 2nd	✓	$T > 4\tau_R - \tau_A$	$T > 2\tau_R - \frac{\tau_A}{1+\tau_A/T}$
FVDM, 2nd	✓	$T \gtrless 2(\pm\sqrt{\tau_R^2 - \tau_R\tau_A} + \tau_R) - \tau_A$	$T > 2\left(\tau_R - \tau_A\right)$

TABLE 3.1: Summary of the stability conditions of the generalized Optimal Velocity models. The checkmark denotes that the corresponding stability is always fulfilled.

It has been argued that vehicular traffic is shaped by the ration T/τ_R, which gauges whether agents keep (time) distances large enough to compensate for their reaction time [138]. From our study it becomes apparent that the ratio between τ_A/τ_R has to be considered as well. Apart from this, the way different factors are incorporated into the models has a strong influence on the different stability conditions.

Finally, we observe that for most models overdamping includes string stability, which means that it is difficult to avoid local oscillations while reproducing stop-and-go dynamics. In some models, however, e.g. (FVDM, 2nd), a regime exists in which the model is overdamped and shows stop-and-go behaviour. These regimes are promising candidates to reproduce features of real traffic. Note that, in this regime, overshooting is still observed in the numerical simulations. Overshooting of the equilibrium position seems to be a necessary condition in these models to reproduce stop-and-go dynamics.

Generally, stop-and-go waves occur in these models through the same mechanism: the homogeneous solution is deterministically unstable. A small perturbation leads to the breakdown and eventually to stop-and-go waves. Lets us now investigate a different mechanism by including noise in our models.

3.3.4 Noise Induced Stop-and-Go Waves

Noise is a random disturbance capable of altering the dynamics of a system. Typically, it is used in models to describe numerous unaccounted and maybe unknown factors which nonetheless remain relevant. Usually, noise is added as white noise, characterized by a time-independent random component following a Gaussian distribution. While noise

is often viewed as an undesirable interference, it can yield beneficial effects, such as preventing the system from becoming frozen in a particular state (gridlock).

Noise has to be distinguished from intrinsic stochasticity, as seen in cellular automata models, where stochasticity is frequently integral to the dynamics, capturing uncertainties in decision-making processes. Consequently, deterministic limits of cellular automata models often exhibit unrealistic behaviors.

In the ensuing discussion, we will explore the impact of both white and colored noise when introduced into the simplest Optimal Velocity model (OV, 1st). Subsequently, we will examine how noise affects other models discussed in this section, revealing an alternative mechanism for replicating stop-and-go behavior, distinct from the concept of string stability discussed earlier.

White Noise Models

In continuous time, white noise is included in a model using independent Wiener processes, with the increment W_i. The (OV, 1st) model including an additive white noise in the speed reads

$$dx_i(t) = \frac{\Delta x_i - \ell}{T} dt + \sigma dW_i(t), \tag{3.29}$$

with σ the noise volatility. As the noise is centered, it does not impact the linear stability of the system [139, 140].

The white noise has little influence on the overall dynamics of the system as evidenced by the absence of stop-and-go waves, a fact corroborated, for instance, by the autocorrelation of the headway [101]. This observation remains consistent across other first-order models that do not inhibit a time-delay [102].

Colored Noise Models

White noise exhibits no correlation over time and possesses a constant frequency power spectrum. In contrast, colored noise is correlated over time with power spectra that can either increase (as seen in blue or violet noise) or decrease (for instance, in pink or Brownian noise). Empirical analyses of pedestrian speed time-series demonstrate a power spectrum that roughly follows a $1/f^2$ proportionality across a significant frequency range [141, 142].

The stochastic model introduced in [142] is equivalent to the (OV, 1st) model with a correlated truncated Brownian noise $\varepsilon_n(t)$ described by an Ornstein-Uhlenbeck process,
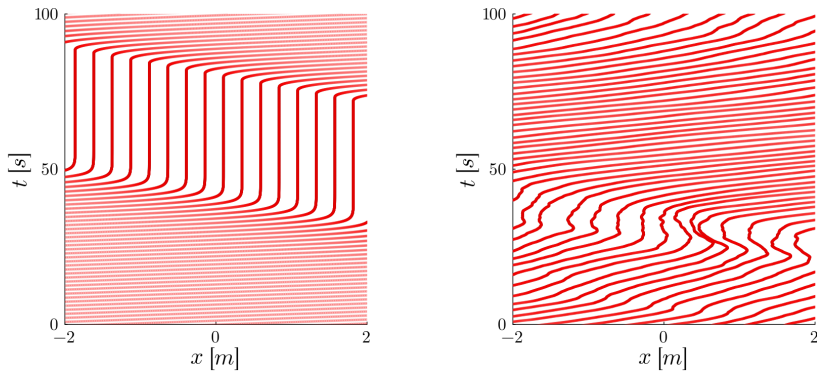
FIGURE 3.10: Numerical trajectories of $N = 50$ agents on a ring of length 25m. Left: deterministic instability, i.e. the (FVDM, 2nd) in the string-unstable regime where a minimal and a maximal velocity is included. Right: noise-induced stop-and-go waves for the (OV, 1st) model with a correlated truncated Brownian noise. Note that this is equivalent to the (FVDM, 2nd) with a white noise and $\tau_R = \tau_A$.

i.e., as

$$\dot{x}_i(t) = \frac{\Delta x_i - \ell}{T} + \varepsilon_i(t),$$
$$d\varepsilon_i(t) = -\frac{1}{\tau}\varepsilon_i(t)dt + \sigma dW_i(t)\,, \tag{3.30}$$

where the $W_i(t)$ are Wiener processes. The (positive) parameters σ and τ related to the noise can be interpreted as volatility and noise relaxation time, respectively.

In accordance with the condition specified in Table 3.1, the deterministic model is always stable. As the noise is additive, centred, and independent of the vehicle states it is also linearly stochastically stable [139]. Nonetheless it features stop-and-go behaviour as evidenced from the resulting trajectories in Fig. 3.10 (right) or the autocorrelation of the speeds [141].

The stop-and-go waves caused by noise contrast significantly with the stop-and-go waves resulting from the instabilities explored earlier. Illustrative snapshots of trajectories showcasing deterministic (on the left) and noise-induced (on the right) stop-and-go waves are depicted in Fig. 3.10. Specifically, the deterministic mechanism resembles vehicular traffic, featuring a clear phase separation, while the noise-induced mechanism bears closer resemblance to pedestrian dynamics, with a less pronounced phase separation.

The mechanism described here differs fundamentally from the traditional deterministic instability encountered in traffic models, where stop-and-go behaviour is caused by an instability of the homogeneous solution. This homogeneous solution breaks down due
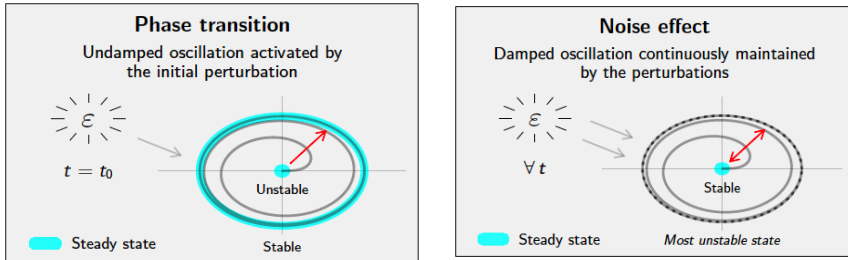
FIGURE 3.11: Illustrative scheme for the modelling of stop-and-go dynamics. Left: phase transition in the periodic solution. Right: noise-induced stop-and-go behaviour. Figure taken from [141].

to a small perturbation, as schematically illustrated in Fig. 3.11 (left). Here, on the other hand, the system is permanently perturbed by the noise which results in a steady state in which stop-and-go dynamics are present, cf. Fig. 3.11 (right). The stop-and-go dynamics are reflected in variance-covariance and autocorrelation characteristics of the system [140, 142].

This mechanism to reproduce stop-and-go behaviour is not unique for this specific model but seems to be quite generic [102]. Specifically, the noisy first-order model in Eq. (3.30) is equivalent to the (FVDM, 2nd) model with a white noise and $\tau = \tau_R = \tau_A$ [102]. Simulation show that a white noise can trigger stop-and-go waves in all delayed or second-order models discussed in Section 3.3.2.

3.3.5 The Fundamental Diagram: Scaling Analysis of the OV Model

Let us shift our focus from discussions on stability and stop-and-go dynamics to investigate the fundamental diagram, particularly of the (OV, 1st) model without any noise. Through a scaling analysis, we aim to illustrate that the models' parameters can be condensed into a single parameter, which determines its dynamics. Consequently, we identify a solitary parameter that shapes the fundamental diagram. This elucidates the scaling behavior observed empirically among the fundamental diagrams of vehicular, bicycle, and pedestrian traffic.

It is worth noting that the homogeneous solution of (OV, 1st) remains stable at all times. Consequently, there is no need for numerical analysis; instead, we can derive the analytical fundamental diagram directly from the equations of motion. Remarkably, *all* models described in sec. 3.3.2 share this same homogeneous solution. Hence, the analysis conducted here applies equally to the homogeneous solutions of these models. While instabilities may lead to variations in the fundamental diagram, simulations suggest that such deviations are not substantial.

Let us recall the definition of the (OV, 1st) model

$$v_i = \min\left(v_{\max}, \frac{\Delta x_i - \ell}{T}\right), \tag{3.31}$$

where we have included a maximal velocity $v_{\max}$.

Now, our objective is to transform this equation to dimensionless variables. This can be formally accomplished by expressing the dependent variables as $v_i = \overline{v}_i/v_c$ and $\Delta x_i = \Delta \overline{x}_i/x_c$, where the variables with the overline represent the non-dimensionalized dependent velocity and distance and the variables v_c and x_c represent the typical length and velocity scales. Upon inserting these non-dimensional coordinates into Eq. (3.31), we arrive at the non-dimensional Optimal Velocity model

$$\overline{v}_i = \min\left(\frac{v_{\max}}{v_c}, \frac{\Delta \overline{x}_i x_c - \ell}{T} \cdot \frac{1}{v_c}\right). \tag{3.32}$$

Let us now select suitable values for the scales v_c and x_c, which requires careful consideration [143]. Typically, these are chosen as the maximum value, ensuring the dependent variable lies within the range $[0, 1]$. Therefore, a natural choice is $v_c = v_{\max}$, as it confines the non-dimensional velocity to $\overline{v}_i \in [0, 1]$.

The decision for a suitable length scale is more ambiguous. Instead of constraining the non-dimensional distance, we opt to limit the non-dimensional density $\overline{\rho} \sim 1/\Delta \overline{x}$ by setting $x_c = \ell$. This choice restricts the rescaled density to one, given that the minimal center-to-center distance is $\Delta x = \ell$. Consequently, this establishes a typical time-scale of $v_{\max}/\ell$, representing the minimum time an agent needs to traverse its own length.[5]

If we insert this into Eq. (3.32) we obtain

$$\overline{v}_i = \min\left[1, (\Delta \overline{x}_i - 1)\pi_1\right], \tag{3.33}$$

where $\pi_1 = \ell/(Tv_{\max})$. Remarkably, we have successfully reduced the number of parameters from three - ℓ, T, and $v_{\max}$ - to a single parameter π_1. Exploring the parameter space numerically becomes more straightforward as it involves solving the system for values of π_1 rather than for a three-dimensional parameter space. Changing the parameters while fixing π_1 corresponds to a mere rescaling of time and space: the actual dependent variables can then be calculated by a simple multiplication, i.e. $(x_i, v_i) = (\overline{x}_i x_c, \overline{v}_i v_c)$.

In addition to considerations of numerical efficiency, it is noteworthy that a singular parameter governs the qualitative behavior in the model. To illustrate this point, let us

---

[5]We could have alternatively chosen a typical time scale, where the desired time-gap T is a natural choice. This leads to another meaningful length scale $x_c = t_c \cdot v_c = v_{\max} \cdot T$, representing the maximal interaction length.
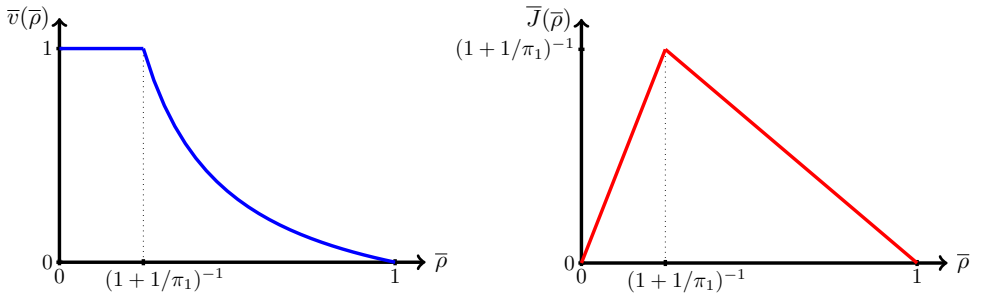
FIGURE 3.12: The non-dimensional fundamental diagram of the simple Optimal Velocity model in the typical representations.

examine the non-dimensional fundamental diagram. Since the homogeneous solution of Eq. (3.31) is always linearly stable, the fundamental diagram can easily be obtained as

$$\overline{v}\left(\overline{\rho}\right) = \min\left[1, \left(1/\overline{\rho} - 1\right)\pi_1\right] \text{ and } \overline{J}\left(\overline{\rho}\right) = \min\left[\overline{\rho}, \left(1 - \overline{\rho}\right)\pi_1\right], \tag{3.34}$$

where we inserted $\overline{\rho} = 1/\Delta\overline{x}_i$ wihch always holds for the homogeneous solution. Both representations are depicted in Fig. 3.12. The empirically observed shape of the fundamental diagram (sec. 3.1.2), i.e. a $1/\rho$ for the mean velocity and a triangular shape for the flow, is recovered.

It is worth noting that when $\pi_1 = 1$, the fundamental diagram $\overline{J}\left(\overline{\rho}\right)$ is symmetric and the capacity equals $1/2$. This corresponds to the solution of a quite different model, namely the Totally Asymmetric Simple Exclusion Process (TASEP) with a hopping probability $p = 1$ and a parallel updated scheme [29]. Accordingly the rules and parameters of the TASEP would translate to $v_{\max} = \ell = T = 1$. If on the other hand π_1 is increased the capacity grows and is reached at smaller densities. This is typically observed in vehicular, pedestrian, and bycicle traffic.

Beyond that, in [91], it is empirically shown that the fundamental diagram of vehicular, pedestrian, and bicycle traffic shows good agreement if density and velocity are scaled with the same parameters as above. Assuming a constant value of T across these various types of human traffic, the empirically derived values for ℓ and $v_{\max}$ in [91] result in the very same value of π_1. Specifically, we obtain $\pi_{1,\text{Bicycle}} = 0.31\text{s}/T$, $\pi_{1,\text{Pedestrian}} = 0.31\text{s}/T$, and $\pi_{1,\text{Vehicular}} = 0.32\text{s}/T$. Thus, the theoretical analysis performed here aligns well with the empirical scaling which has been reported in [91].

With help of the dimensional analysis we showed that the computational complexity of investigating the parameter space of the model can be reduced significantely. Furthermore, we have found that the shape of the fundamental diagram is determined by one

single parameter which gives a possible explanation of the empirically observed scaling between different types of human traffic. This is another argument in favour of the time-gap as one essential mechanism behind the fundamental diagram in uni-directional settings.

It could be fruitful to employ scaling analysis to more complex models of human traffic as well. For example, if we analyse the second-order OV model we obtain, in addition to π_1, a second parameter $\pi_2 = \tau_R/T$ which determines the stability of the homogeneous solution in this model.

3.3.6 Summary

In this section, we have extensively researched Optimal Velocity (OV) models, which stand out from other following models due to their possession of a unique homogeneous solution. Beginning with a straightforward behavioral heuristic rooted in the time-gap, we derived the simplest (OV, 1st) model. Incorporating finite reaction time and anticipation led to the development of the generalized OV model framework, shedding light on the relationships among various well-known Optimal Velocity models. This perspective also facilitated our comprehension of the parallels between Optimal Velocity models and Velocity Obstacles.

We delved into the local and global stability properties of these models, that can give rise to stop-and-go waves as well as undesirable local oscillations. These conditions were already known, with the exception of the (FVDM, *del*) model, characterized by a neutral delayed differential equation (NDDE). Here, we successfully visualized the exact condition for string stability, which is likely to be non-analytic. Unlike other models, it exhibited a different type of global instability, induced by large anticipation times giving rise to inhomogeneities characterized by a short wave length. In all other models, the string instability gives rise to inhomogeneities that resemble stop-and-go waves. Additionally, certain models exhibit parameter regimes in which local oscillations are overdamped yet stop-and-go behaviour persisted.

However, reproducing stop-and-go traffic is not limited to deterministic instabilities alone. Introducing white or correlated noise induces oscillatory behavior, capturing the weakly pronounced phase separation in pedestrian single-file motion much better than the deterministic instability does. Linear stability analysis provides robust conditions for deterministic models' ability to describe stop-and-go wave phenomena but is limited in the context of stochastic models where methods are needed that examine oscillations in variance-covariance and auto-correlation characteristics. Stochastic models present new avenues for modeling and nonlinear analysis paradigms for single-file agent dynamics.

Despite their differences, all models exhibit essentially the same fundamental diagram, with the time-gap being central to their formulation, resulting in the expected triangular shape of $J(\rho)$. Furthermore, scaling analysis indicates a scaling relation between pedestrian, bicycle, and vehicular traffic, aligning with empirical observations.

In contrast to force-based or spatial distance-based approaches discussed earlier, models based on the time-gap can reasonably capture the basic features of pedestrian single-file motion. The similarity between Velocity Obstacles and Optimal Velocity models found here suggests another category of models: time-to-collision-based following models, as Velocity Obstacles typically rely on this temporal distance rather than the time-gap. This avenue will be explored in the subsequent section.

3.4   Following Models based on the Time-to-Collision

The argument has been made that crowds are more effectively characterized by time-to-collision (TTC) than distances [82]. The TTC integrates spatial distances with (relative) velocities to measure the 'distance' to a collision, making it a promising parameter in pedestrian models [82, 144–146]. However, none of the previous models has been applied to single-file motion. Therefore, let us explore how the TTC can be utilized to define a following model for single-file motion.

To achieve this, we will start by defining the time-to-collision and highlighting some distinctions from the time-gap introduced in the previous section. Subsequently, employing the same heuristic as before - where agents adjust their velocity to maintain a safe time 'distance' from others - we will define TTC-based Optimal Velocity models. These models are an one-dimensional limit of Velocity Obstacle models.

Applying these models to the single-file scenario will reveal fundamental problems encountered in these models. This exploration will enable us to gain a deeper understanding of issues related to diverging times-to-collision and unrealistically high flows even at high density, as briefly mentioned in [51].

This section is based on results published in [83].

3.4.1   Definition of Time-to-Collision

Consider two pedestrians, denoted as i and j, represented by disks with a diameter ℓ as depicted in Fig. 3.13. A collision between them will occur if there exists a time $t_C \in [t, \infty)$
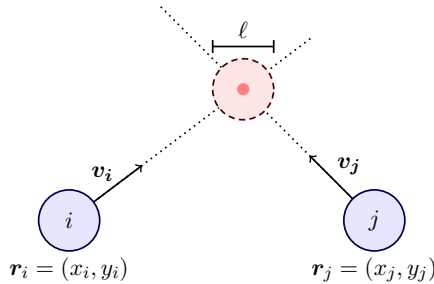
FIGURE 3.13: Schematic illustration of two colliding pedestrians. The position vectors $\boldsymbol{r}_i$ and $\boldsymbol{r}_j$ point to the centers of the disks.

such that $r_{ij}(t_C) = \ell$. The time-to-collision τ between i and j at time t is defined as:

$$\tau_{ij}(t) \equiv t_C - t. \tag{3.35}$$

If no such time t_C exists, the TTC τ_{ij} is considered infinite. In cases where multiple times t_C exist, the minimum among them determines the time-to-collision.

Since the future evolution is unknown, the TTC is calculated by assuming constant velocities for both pedestrians i and j. Conversely, for the time-gap, it is assumed that pedestrian i maintains a constant velocity while pedestrian j suddenly stops. Mathematically, these approximations correspond to different Taylor expansions and could be extended to higher orders. From a behavioral standpoint, these represent two distinct anticipation strategies. While the time-gap represents a 'worst-case' anticipation, the TTC extrapolates where the current situation will lead in the future. In the ensuing discussion, we will focus on the TTC, based on the assumption of constant velocities, and apply it to one-dimensional single-file motion.

Let us again consider a one-dimensional chain of N pedestrians on a ring of length L. Denote x_i as the pedestrian positions and v_i as their velocities, sorted in ascending order in the direction of motion, where pedestrian $i + 1$ is the predecessor of i. Under the assumption of constant velocities, the time-to-collision τ_{ij} is given by

$$\tau_{ij} = \begin{cases} \dfrac{\Delta x_{ij} - \ell}{v_i - v_j} & \text{for } (v_i - v_j) \cdot (\Delta x_{ij} - \ell) > 0, \\ \infty & \text{else.} \end{cases} \tag{3.36}$$

Here, $\Delta x_{ij} = x_j - x_i$ represents the spatial distance between the centers. While it may be helpful to think of the time-to-collision as a temporal distance, it should be noted that it does not adhere to the properties of a metric. The TTC is symmetric, but it neither satisfies the identity of indiscernibles nor the triangle inequality.

3.4.2 Definition of the Model and Inherent Problems

Now we can define a TTC-based Optimal Velocity model, applying the same behavioral assumption as in Section 3.3.2, i.e.

> *Agents choose their velocity v_i such that $\tau_{ij} \geq \tau_0$ for all $j \neq i$ while at the same time maximizing v_i.*

where we have introduced a desired TTC τ_0.

If we assume that the interaction is restricted to the agent in front[6], a first-order model is straightforwadly defined as

$$v_i = v_{i+1} + \frac{\Delta x_i - \ell}{\tau_0}. \tag{3.37}$$

When considering a homogeneous population of N agents on a ring of length L, the model is generically inconsistent as the velocities of all agents would diverge. The only solution with a finite velocity requires $N \cdot \ell = L$. In which case, only trivial solutions with

$$\Delta x_i = \ell \qquad \text{and} \qquad v_i = c \geq 0 \tag{3.38}$$

exist. This can be understood intuitively from the definition of the model: Since, according to Eq. (3.37), every agent wants to move faster or equally fast as his or her predecessor. Therefore, the only way to achieve a finite velocity in the solution is when all agents move at the same speed and maintain zero headway between them.

Of course, to circumvent this problem, a maximal velocity $v_{\max}$ can be added to Eq. (3.37) as

$$v_i = \min\left(v_{\max}, v_{i+1} + \frac{\Delta x_i - \ell}{\tau_0}\right). \tag{3.39}$$

In this model, a solution exists for all densities in which all agents move with $v_{\max}$, i.e.

$$\Delta x_i \geq \ell \qquad \text{and} \qquad v_i = v_{\max}. \tag{3.40}$$

A second-order model with a reaction time τ_R can be defined as

$$a_i = \frac{1}{\tau_R}\left(v_{i+1} + \frac{\Delta x_i - \ell}{\tau_0} - v_i\right), \tag{3.41}$$

---

[6]Note that this assumption does *not* naturally arises from the first-principle as it did for the time-gap. This is related to (a) the symmetry of the TTC, therefore one can not neglect the interaction to the person in the back without any further assumptions and (b) the next nearest neighbor in front (or back) might have a smaller TTC than the nearest neighbor. For the Time-Gap this is not the case.

which looks similar to the (FVDM, 2nd) model [116]. However, in that model the velocity relaxes to $(\Delta x_i - \ell)/T$ to which Δv is added. Contrastingly, in Eq. (3.41), the velocity relaxes to $v_{i+1} + (\Delta x_i - \ell)/\tau_0$. Accordingly, the only homogeneous solutions are the solutions of the first-order model (3.37) described above.

Summary We have used the TTC to define an Optimal Velocity model to which a reaction time can be added. The model is however generically inconsistent for periodic boundaries and a homogeneous crowd. The corresponding analytical solutions can easily be obtained but the solution space, i.e. Eq. (3.38) and Eq. (3.40), is very restricted. These inconsistencies can be solved by including a maximal velocity. However, the model then exhibits a mean velocity $v_{\max}$ at all densities. This is of course completely unrealistic and does not align with the fundamental diagram. Models based solely on the TTC can thus be dismissed for describing single-file motion.

This issue is closely tied to the fact that relative velocities between pedestrians in single-file motion are inherently small, often approaching zero, particularly within a model. Consequently, according to (3.36), the TTC between the pedestrians is mostly infinite. As a result, in the model, interactions between agents are scarce, allowing them to move freely at their desired velocities. This suggests that pedestrians do not (heavily) rely on the time-to-collision in the context of single-file motion.

3.5   Conclusion

In this chapter, we have explored three distinct model categories for pedestrian single-file motion: force-based models based on Euclidean spacings as well as following models based on either the time-gap or the TTC, respectively. Let us summarize the key findings for each category.

In force-based models, pedestrians interact via distance-dependent repulsive 'forces' superimposed with a driving term. These models vary between the type of decay in the interaction (exponential or algebraic) and whether inertia or relaxation time is accounted for (first or second-order). In addition to conceptual problems that arise from the analogy with Newtonian forces, force-based models often exhibit undesired oscillations, struggle to capture stop-and-go dynamics accurately, and fail to replicate the fundamental diagram without additional adjustments.

Subsequently, we introduced following models that originate in the description of vehicular traffic. Among these, we focused on Optimal Velocity models derived from a first principle based on the time-gap, a temporal 'distance' reflecting worst-case anticipation.

Incorporating factors like finite reaction time has spawned a range of models, as well as revealing connections between well-known models. These Optimal Velocity models provide a reasonable depiction of single-file motion, particularly regarding the fundamental diagram and stop-and-go dynamics, especially when noise is considered here.

Lastly, we explored the relationship between Optimal Velocity models and Velocity Obstacles to formulate time-to-collision based following models. However, despite the promise of using time-to-collision in other scenarios, its application to single-file motion leads to fundamental issues.

To summarize, our understanding of single-file motion is well-established both through experimental observation and theoretical analysis, for the latter largely facilitated by the concept of the time-gap. However, pedestrian dynamics encompass a broad spectrum of scenarios, including uni- and bidirectional flows [147], cross flows [52], and bottleneck evacuations [61]. These scenarios give rise to various collective behaviors such as clogging [148], lane or stripe formation [19], and vortex formation [20], studied through experiments and theoretically through (agent-based) models. Notably, unlike single-file motion, these scenarios typically require consideration of at least two spatial dimensions.

Although the Generalized Optimal Velocity models offer a straightforward formulation in two dimensions, primarily through a 2D definition of the time-gap [81], the worst-case anticipation is only represented realistically, assuming a clear predecessor. Another draw back is that these models do not distinguish between maximal and desired velocities. Thus they are not applicable in situations if the agents have no (strong) desire to move, e.g., during waiting. More importantly, in two dimensions, interactions between pedestrians encompass a wide range of behaviors, including personal space intrusions [107], anticipative avoidance [149], and mechanical interactions in dense crowds [38, 39]. Addressing these complexities raises questions about the fundamental differences between these interactions, as well as how to effectively integrate them with one another.

Before delving into a detailed theoretical analysis, it is prudent to organize the multitude of crowd scenarios. We will start by considering the microscopic determinants of pedestrian behavior, related to psychology and biomechanics, to define two dimensionless numbers. Employing these we categorize the diverse scenarios encountered in crowds leveraging extensive datasets, predominantly openly available. This categorization will shed light on different self-organized structures within crowds, serving as the basis for a more comprehensive theoretical framework in the subsequent chapter.

Chapter 4

Classification of Crowds with dimensionless Numbers

The idea of classifying pedestrian crowds traces back to Fruin [28], who introduced the notion of level of service in pedestrian dynamics. The level of service is used to assess the comfort of pedestrian facilities. The classification primarily hinges on density as a defining criterion, with each level associated with particular behaviors such as (un)avoidable contact, necessity to change gait or possibility to turn around. It has been contended that as density varies, crowd dynamics should be governed by distinct principles [30]. However, the boundaries between the classes appear to be rather arbitrary. Additionally, density alone is an insufficient classifier. This becomes apparent from a practical standpoint, for safety assessments, where crowds at similar densities show contrasted dynamics as well as risk profiles. For instance, consider the difference between a densely packed, but static audience in a concert hall and people vying for escape in an emergency evacuation [17].

Recognizing this limitation, alternative classifiers have been proposed. Recently, it has been suggested that a dimensionless number related to the vorticity of the velocity field better distinguishes between such scenarios [31]. Although this quantity is valuable for safety assessments, it is not based on microscopic determinants of pedestrian dynamics. This would, however, be highly desirable as it links the individual behaviour with flow regimes at the crowd's scale. This would allow to gain insights into the realm of applicability of the large zoo of models that have been proposed for pedestrian and crowd dynamics.

Our approach draws inspiration from hydrodynamics, where dimensionless numbers play a crucial role in characterizing fluid flows (e.g., the Reynolds number). In a similar spirit, we introduce two dimensionless numbers for crowd motion. Specifically, we argue that
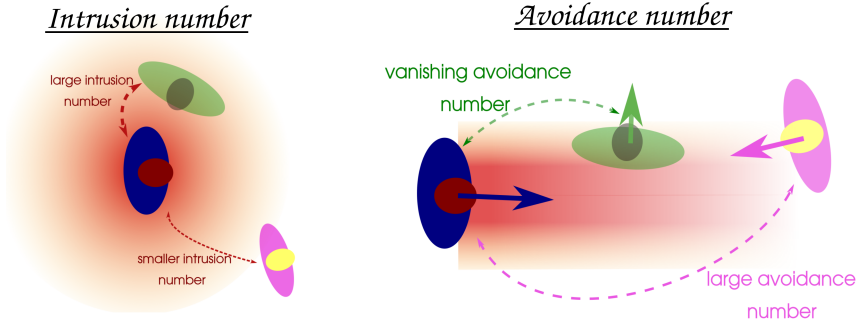
FIGURE 4.1: Schematic illustration of the meaning of the dimensionless Intrusion ($\mathcal{I}n_{ij}$) and Avoidance ($\mathcal{A}v_{ij}$) variables between agent i, dressed in blue, and agent j, in green or pink.

in common scenarios pedestrian dynamics are dominated by two variables, rendering the ideas of preservation of personal space (proxemics) and anticipation of collisions. Their averages over the crowd define two dimensionless numbers that delineate distinct regimes of crowd flow intuitively and empirically using an extensive dataset of pedestrian trajectories. The nature of the structural arrangement of the crowd is found to differ markedly between these regimes.

This chapter is an extended discussion of the ideas and results published in [150], its supplemental material, and [151].

4.1 Intrusion and Avoidance

Psychological studies on proxemics showed that people shun too close contacts with other (unrelated) people [152, 153]. The personal space is defined as "*the area individuals maintain around themselves into which others cannot intrude without arousing discomfort*" [152]. While the preferred interpersonal distances will vary between countries, cultures, and, of course, the relation to the other person [154], the will to preserve some interpersonal distance to others is virtually universal and, thus, naturally impacts the arrangement of crowds. To capture these effects in a quantitative fashion and to avoid ambiguities in the definition of a local density, we introduce a variable $\mathcal{I}n_{ij}$ for the intrusion between two pedestrians i and j, viz.,

$$\mathcal{I}n_{ij} = \left(\frac{r_{\text{soc}} - \ell_{\min}}{r_{ij} - \ell_{\min}} \right)^2, \tag{4.1}$$

where r_{ij} is the centre-to-centre distance of pedestrians i and j. It quantifies the areal encroachment of other agents j on the personal space of agent i. As illustrated in

Fig. 4.1 (*left*), $\mathcal{I}n_{ij}$ decays with the distance between two pedestrians; it vanishes for isolated pedestrians, but diverges when people come into physical contact. For simplicity, we assume that both agents and their personal space are circular (with diameter $\ell_{\min} = 0.2$m and radius $r_{\text{soc}} = 0.8$m, respectively), i.e. effects of anisotropy are neglected. As several agents j may surround agent i, the latter experiences an intrusion

$$\mathcal{I}n_i = \sum_{j \in \mathcal{N}_i} \mathcal{I}n_{ij}, \tag{4.2}$$

where the sum in Eq. (4.2) has been taken to run over the set $\mathcal{N}_i$ of all close neighbours j of i, here defined by $r_{ij} \leqslant 3\,r_{\text{soc}}$. That the intrusions of diverse neighbors should be additive makes sense for physical contacts (superposition of mechanical forces), but also for proxemic behavior [155, 156].

While this variable gives a sense of the level of crowding, it does not provide a comprehensive reflection of psychological experience (feeling of congestion) in the midst of the crowd [31, 157]. In addition, it does not fully control the individual dynamics: imagine two pedestrians running towards each other, even though $\mathcal{I}n_{ij} \to 0$, as they may still be separated by several meters, they will not behave as if they were isolated. Instead they will anticipate an impending collision and accordingly deviate from their path to avoid the other person. This behaviour is well captured by the anticipated time-to-collision (TTC) τ_{ij}, defined as the time until i and j would collide if they keep their current velocities. The TTC and some of its properties have already been introduced in section 3.4. Notably, humans can identify the most imminent collision between multiple objects and estimate TTCs [158] via purely optical quantities, specifically it is given by the optical angle divided by its derivative [159]. Experiments showed that humans use the TTC to decide 'when' to avoid an approaching pedestrian [149]. We quantify the risk of an imminent collision between two agents i and j with the avoidance variable

$$\mathcal{A}v_{ij} = \frac{\tau_0}{\tau_{ij}}, \tag{4.3}$$

where τ_{ij} is the anticipated time-to-collision (TTC) and $\tau_0 = 3\,$s denotes the timescale above which potential collisions are hardly dreaded. We set $\mathcal{A}v_{ij} = 0$ if no collision is expected. Importantly, as sketched in Fig. 4.1 (*right*), the avoidance variable between two pedestrians might be large even if the intrusion between them is strictly zero, and conversely it may be vanishing even if the personal space is strongly violated. In contrast to Eq. (4.2), we assume that each agent is mostly concerned with only the most imminent risk of collision, so that in the definition of the agent-centred variable

$$\mathcal{A}v_i = \sum_{j \in \mathcal{N}'_i} \mathcal{A}v_{ij}, \tag{4.4}$$
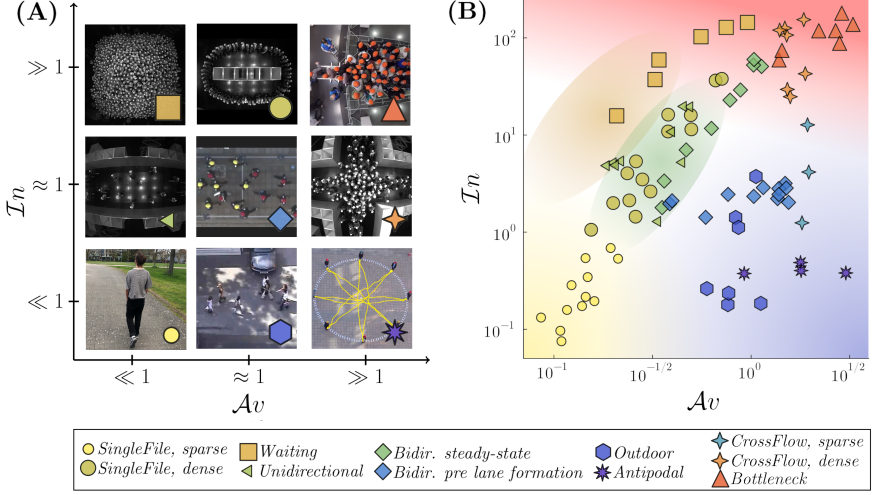
FIGURE 4.2: Classification of pedestrian crowds by the dimensionless numbers $\mathcal{I}n$ and $\mathcal{A}v$. **(A)** Schematic diagram drawn according to the intuition and illustrated with exemplary snapshots. **(B)** Empirical diagram obtained from the extensive pedestrian dataset. Each datapoint corresponds to one experimental run or observational sequence. The experimental data from *SingleFile* and *CrossFlow* were split into a *sparse* and a *dense* dataset.

we restrict the set $\mathcal{N}_i'$ to the agent j with the shortest τ_{ij}. Indeed, for collision avoidance, it has been ascertained that participants immersed in a virtual crowd tend to fixate a particular agent with a high risk of collision just before performing an avoidance maneuver around this person [160].

4.2 Delineation of Crowd Regimes

The intrusion and avoidance variables offer the potential for a finer delineation of pedestrian streams compared to conventional density-based levels of service. To achieve this, the foregoing agent-centered variables are averaged across the $N(t)$ agents observed in the crowd at time t, and subsequently over time. This average value defines two dimensionless numbers, the Avoidance number ($\mathcal{A}v$) and the Intrusion number ($\mathcal{I}n$). As $\mathcal{A}v$ should quantify the urgency of expected collisions we only consider data points with finite TTC in the average. Especially in sparse datasets, this allows to focus on the parts where interactions occur.

Figure 4.2 (A) showcases the regimes of crowd flow that one would intuitively expect to find in a diagram parameterized by $\mathcal{A}v$ and $\mathcal{I}n$, using exemplary cases. Close to the origin ($\mathcal{I}n, \mathcal{A}v \ll 1$), the agents can freely pursue their goals, indicating very sparse crowds with

minimal interactions. As one moves up the $\mathcal{I}n$-axis, the setting gets more crowded, and pedestrians strive to maintain a certain social distance to others, as in a *unidirectional* flow. When $\mathcal{I}n \gg 1$, personal space can no longer be preserved and physical contact may eventually be unavoidable, as in a tightly packed static crowd (*Waiting* scenario). Another departure from non-interacting scenarios involves individuals walking or running towards each other as approximated in the initial stages of an *Antipodal* experiment, where participants positioned along the circumference of a circle (with $\mathcal{I}n \ll 1$) are tasked to reach the antipodal position, introducing conflicting moves and collision risks in the circle's center ($\mathcal{A}v \gg 1$). Finally, competitive evacuations through a *bottleneck* illustrate the regime with large $\mathcal{I}n$ and $\mathcal{A}v$, featuring contacts, pushes, and conflicting moves.

Let us test these idealized expectations by calculating $\mathcal{A}v$ and $\mathcal{I}n$ from real pedestrian trajectories. Therefore, we have collected a large dataset including controlled experiments (single-file motion [46], bottleneck flows [61], corridor flows [18, 52, 147], antipodal scenarios [161]) and empirical observations in outdoor settings [162, 163]. Further details about the datasets as well as the influence of headsways and the filtering we have done to minimize these will be specified below. We have calculated the $\mathcal{A}v(t)$ and $\mathcal{I}n(t)$ every 0.5s in each scenario and realization and then averaged over the whole quasi-stationary state (unless otherwise stated).

Indeed, Figure 4.2 (B) affirms the idealized diagram we have worked out intuitively in Fig. 4.2 (A). Single-File experiments at low density are located at the bottom left corner at small $\mathcal{I}n$ and $\mathcal{A}v$. Conversely, the upper region of the diagram, marked by large $\mathcal{I}n$, corresponds to scenarios where physical contacts among pedestrians are nearly unavoidable, e.g. a densely packed static crowd (*Waiting*). While these could be delineated by the density (or the Level of Service) alone, many scenarios can only be distinguished by $\mathcal{A}v$. For example, unidirectional flows and cross-flows might share similar $\mathcal{I}n$ values, but their distinction lies in $\mathcal{A}v$, where cross-flows exhibit higher values, indicating a greater likelihood of conflicts. Similarly, antipodal maneuvers exhibit intrusion numbers comparable to certain typical outdoor scenarios, yet they feature larger Avoidance numbers.

Note that in many experiments, although the geometry (e.g., a corridor) remains the same, the experimental conditions, such as the inflow, are greatly altered, resulting in flows of different natures. Thus, the spread of points for a given type of scenario is both expected and sensible. On the flip side, scenarios labeled differently may exhibit overall similarities, leading to comparable dimensionless numbers. For instance, a bidirectional flow with thick lanes predominantly consists of unidirectional flows, with only occasional interactions between the lanes. Another example are crossing flows at high densities

which generate effective 'bottlenecks', so much so that the properties of crossing flows at higher densities are thought to be controlled by emergent bottlenecks; finding similar dimensionless numbers for crossing flows and actual bottlenecks is therefore not so surprising.

In the following, we will give more details on the datasets as well as the way we obtained the dimensionless numbers. After that we will discuss alternative definitions of the (somewhat arbitrary) precise ways we defined $\mathcal{I}n$ and $\mathcal{A}v$. Specifically, we will investigate the influence of the neighborhood and exponents chosen in the definitions of the agent-centred $\mathcal{I}n_i$, cf. Eq. (4.2), and $\mathcal{A}v_i$, cf. Eq. (4.4), on the diagram in Fig. 4.2. Furthermore, we will discuss the difference between density and Intrusion number in more detail.

A reader more interested in the main results might want to skip the following details and directly move to Sec. 4.4 where we investigate the qualitative differences of the regimes delineated here.

4.2.1 Description and curation of the datasets

Above, we have used a large collection of mostly openly available data on pedestrian dynamics. The collated data and the methods employed to pre-process and extract average dimensionless numbers $\mathcal{I}n$ and $\mathcal{A}v$ from them are detailed in this section.

4.2.1.1 Summary of the datasets

Name	Type	Scenario	Varied Param.	Details	Cit.	Data
Waiting	Exp.	Static	Density	Düsseldorf, Ger, 2013	-	Supp.
Single-File	Exp.	Single-File	Density	Jülich, Ger, 2006	[46]	[164]
Unidirectional I	Exp.	Uni-dir.	Density	Düsseldorf, Ger, 2013	[52]	[164]
Unidirectional II	Exp.	Uni-dir.	-	Tokyo, Jap, 2018	[147]	[147]
Bidirectional I	Exp.	Bi-dir.	Density	Düsseldorf, Ger, 2013	[52]	[164]
Bidirectional II	Exp.	Bi-dir.	-	Tokyo, Jap, 2020	[18]	[18]
Zara (Outdoor)	Obs.	Bi-dir.	-	Nicosia, Cy, 2007	[163]	[165]
EWAP (Outdoor)	Obs.	Bi-dir.	-	Zürich, Swi, 2007	[162]	[166]
Cross	Exp.	Multi-dir.	Density	Düsseldorf, Ger, 2013	[52]	[164]
Antipodal	Exp.	Multi-dir.	-	Beijing, PRC, 2019	[161]	-
Students (Outdoor)	Obs.	Multi-dir.	-	Tel Aviv, Isr, 2007	[163]	[165]
Bottleneck	Exp.	Bottleneck	Corr. Width	Wuppertal, Ger, 2018	[61]	[164]

TABLE 4.1: Summary of the different datasets used in our analysis. In *Bidirectional I* we analyzed the steady-state, whereas in *Bidirectional II* we focussed on the part prior to the formation of lanes.

Table 4.1 provides a concise overview of the utilized datasets, along with their respective references and, whenever available, download links. Additional information regarding the experimental setups can be found in the corresponding references.

Note that, for the *Waiting* scenario, we extracted the trajectories by ourselves from existing videos. These videos have been recorded within the *BaSiGo* project in 2013 in Germany.[1] In this experiment, 27 to 600 participants entered a square area through four entrances, enclosed by crowd control barriers, and were filmed from above. Following entry, participants waited for approximately one minute before people transversed the static crowd. Finally the crowd leaves through the entrances. We utilized the semi-automatic tracking mode of the "PeTrack" software [167] to extract parts of this waiting period. The corresponding trajectory data is provided as supplemental material.

4.2.1.2   Splitting and merging scenarios

Often, experimental scenarios encompass various stages and spatial regions. In some cases, specified below, our focus was directed solely towards parts of these stages and regions or we split the data into distinct scenarios.

In most experiments, there is a clear start and end, where the participants start to fill, or begin to leave the measurement area. We will start reporting those experiments where we analyzed the pseudo-stationary state by neglecting the beginning and end of each run. The *Single-File* trajectories were treated as purely one-dimensional by neglecting the transverse coordinate. The dataset was split into a *dense* and a *sparse* part, where the 6 runs with the lowest global density are considered as sparse and the rest as dense. In *Unidirectional I*, we have only used the runs where the width of the entrance and exit corresponds to the total width of the corridor; the other runs rather resemble a bottleneck. As for *Unidirectional II*, we have used the totally asymmetric runs where all people walk from one side to the other. As there is only a small crowd that passes the measurement area, no steady-state can be analyzed. For simplicity, we have merged the two unidirectional datasets into a *Unidirectional* scenario. In *Bidirectional steady-state*, we have used variant *B*, where the participants are instructed to use a fixed exit, i.e. either on the left or on the right at the end of the corridor. For the *Cross* scenario, we have limited our analysis to the area of the crossing itself. In particular, we have neglected the corridors leading to the crossing area. We have used the variant *A* of the 90° crossing, where people enter from all 4 sides, without an obstacle in the centre of the crossing. Note that, the runs 6 and 8, i.e., those with the highest Intrusion number, were cancelled after some time as the experimenters were afraid that participants could get

---

[1]For more information on the project see http://www.basigo.de/.

hurt due to the heavy congestion. We split the *Cross* dataset in a *sparse* part consisting of the 3 runs with the lowest global density and the *dense* part with the rest. In *Bottleneck*, only the runs with a number of participants $N > 40$ were used. Furthermore we have only used the runs with a high motivation. We restricted the analysis to the area right in front of the bottleneck.

In some experiments, we were interested in transient states, i.e. a specific temporal part of the experiment. In *Bidirectional pre lane formation*, we have used the runs without any distraction by cellphones, i.e. the baseline condition. We start the measurement after people have entered the measurement area and end it before the lanes have formed. For the *Antipodal* experiment, only the first ≈ 2s of each run are considered. In particular, the part before the pedestrians get close to each other. The runs with a radius of $r = 5$m and 8 participants were used.

4.2.1.3   The case of the *Outdoor* scenario (passive observations)

The *Outdoor* scenario gathers real-world observations from different datasets. We have used the complete sequences of each observation. As for the *Zara* and *Students* datasets, in the original publication the position of each pedestrian present was given in pixel instead of real-world position. Furthermore, the frame-rate is irregular, accordingly positions of neighbouring pedestrian might only be available at different frames. We have, therefore, used the amended data by [168], where real-world positions were estimated and it was linearly interpolated between the frames. Regarding the *EWAP* datasets, filmed from a *Hotel* and at the *ETH* campus, the velocities were given with the positions and frames in two-dimensional real-world units.

In contrast to the controlled experiments, many social groups are present in the *Outdoor* scenario. This has an effect on the structure of the crowd, as we will show in section 4.4.2.1. These groups (mostly pairs) must be excluded from the calculation of $\mathcal{A}v$ and more importantly $\mathcal{I}n$, as for example friends want to stay in each others personal space. To exclude social groups we detect these according to a simple rule: Two pedestrians are assumed to form a social group if their mean distance is smaller than 1m, their maximal distance smaller than 1.5m, and their mutual presence in the scene lasts at least 2s. We have checked that this indeed detects pairs that would be identified as pairs in the videos. Note that the corresponding scenes are very sparse and people move in very different directions which simplifies the classification significantly.
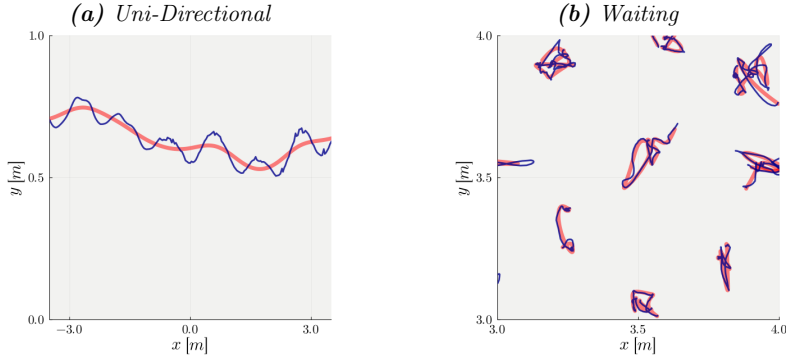
FIGURE 4.3: Exemplary original trajectories (blue) and the smoothed trajectories using a 4-th order Butterworth filter with critical frequency 0.5Hz (red).

4.2.1.4 Processing and smoothing of trajectories

Unless otherwise specified, in all datasets each pedestrian is assigned a unique ID, for which a two dimensional real-world trajectory is given at a certain frame-rate. In all videos the real-world positions are obtained by tracking the participants' heads. Due to the bipedal gait of humans the head performs an oscillatory swaying motion which depends on the speed of the pedestrian. Consequently, the trajectories do not directly show the actual movement direction of the pedestrian [169]. These head sways affect both the calculation of $\mathcal{I}n$ and above all $\mathcal{A}v$. To smooth out the head sways, a 4-th order Butterworth filter with critical frequency 0.5Hz was applied to the trajectories. From these positions and times we calculated the velocities as the distance covered in approximately 1s. The typical head sways in the original trajectory as well as the filtered data with reduced oscillations can be seen in Fig. 4.3 *(a)*.

In Fig. 4.3 *(b)*, we display trajectories of the waiting scenario. We can see oscillations which seem to originate in more irregular head motion of the waiting pedestrians. The Butterworth filter does not smooth these fluctuations which might be a reason that the *Waiting* scenario is not located at even smaller $\mathcal{A}v$ numbers in Fig. 4.2B.

Note that one must be careful with the application of the Butterworth filter because it alters the beginning and end of each trajectory strongly. Therefore, it can only be applied in cases where the beginning and end can be fully neglected. In hindsight another filtering method, e.g. one of the methods put forward in [169], might have been a better choice.

4.2.1.5 Computation of the $\mathcal{I}n$ and $\mathcal{A}v$ numbers

After the trajectories were filtered and the velocities were calculated, the time-to-collision (TTC) was computed by assuming that each pedestrian is a disk of diameter $\ell_{\min} = 0.2$m as it has also been chosen in the calculation of the $\mathcal{I}n$ value. This size was chosen in accordance with [82], in order to limit the number of measured overlaps between disks, which lead to ill-defined TTC. Nonetheless, especially in dense experiments, some overlaps are still observed; to mitigate this problem, we set an upper bound $\mathcal{I}n_{ij}^{\max} = 400$ and $\mathcal{A}v_{ij}^{\max} = 60$ on all computed $\mathcal{I}n$ and $\mathcal{A}v$ numbers.

Additionally, despite the segmentations detailed in section 4.2.1.2, certain scenarios, particularly the *Outdoor* one, feature a significant number of pedestrians walking in isolation. Another example is the sparse *Cross* scenario, where we want to focus on the first half before conflicts in the center of the crossing are resolved. To address this, we exclude pedestrians with $\mathcal{A}v_i = 0$ in the averaged $\mathcal{A}v$. Excluding these values narrows the datasets down to the parts where interactions really occur and thus yields a much finer and more robust delineation of the different regimes. It is worth noting that this is further related to the fact that only collisions between the hard-cores are taken into account so far. More specifically, we only consider anticipated collision between the disks of diameter $\ell_{\min}$. In reality, however, people also shun the 'soft' collisions with the private or intimate space, which are not captured with the discontinuous TTC.

4.2.2 Variations of the Phase Diagram

In the definition of $\mathcal{A}v$ and $\mathcal{I}n$ we have conceded that there is a certain freedom of choice in their definition, in especially regarding the neighbourhood and the exponents. Here, we investigate to what extent this choice impacts the delineation of different regimes. Moreover, we will investigate the similarity between $\mathcal{I}n$ and the commonly used density.

4.2.2.1 Variations in the definitions of $\mathcal{I}n$ and $\mathcal{A}v$

To begin with, let us alter the definition of the Intrusion number $\mathcal{I}n$. We defined it for an agent i as the sum of all intrusions over the set $\mathcal{N}_i$ of all close neighbors j of i, here delimited by $r_{ij} \leqslant 3\,r_{\mathrm{soc}}$. This additivity is similar to the superposition of forces in physics. However, of course, we are not dealing with Newtonian forces and, consequently, there is a priori no reason to assume this superposition. For example, it was found that the superposition of different factors can lead to unreasonable behaviour especially in more complex situations where humans much rather prioritize [100]. Therefore, one might
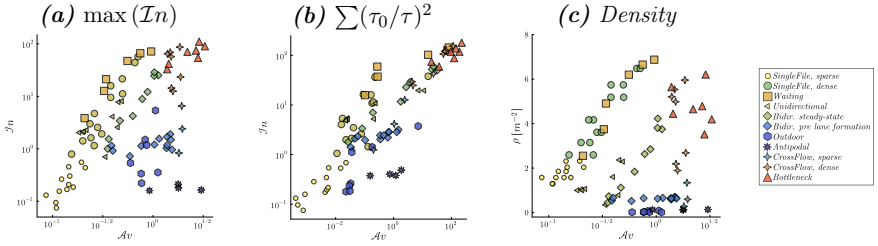
FIGURE 4.4: Empirical delineation of different regimes with alternative definitions of *(a)* the Intrusion number $\mathcal{I}n$ in Eq. (4.5), *(b)* the Avoidance number $\mathcal{A}v$ in Eq. (4.7), and *(c)* the global density.

choose an alternative neighborhood where the intrusion is dominated by its maximum value as

$$\tilde{\mathcal{I}}n_i = \max_{j \neq i} \mathcal{I}n_{ij}. \tag{4.5}$$

In Fig. 4.4 *(a)* an alternative 'phase' diagram is shown where we used the definition specified in Eq. (4.5). It is difficult to spot any substantial difference to the original diagram: the delineation is robust under this change.

Conversely, for the Avoidance number, we have defined the agent-centred variable to be dominated by the most imminent collision. Let us replace this with a sum over all possible collisions, viz.,

$$\tilde{\mathcal{A}}v_i = \sum_{j \neq i} \frac{\tau_0}{\tau_{ij}}. \tag{4.6}$$

In that case, the delineation of different regimes gets blurred to a large extent. On the other hand, if more weight is put on the large Avoidance numbers by defining it symmetrically to the Intrusion number, viz.,

$$\tilde{\tilde{\mathcal{A}}}v_i = \sum_{j \neq i} \left(\frac{\tau_0}{\tau_{ij}} \right)^2, \tag{4.7}$$

the delineation is at least partly recovered, see Fig. 4.4 *(b)*.

4.2.2.2 Use of the density instead of $\mathcal{I}n$

We opted to use distances as the basis for the Intrusion number instead of relying on local density, which is partly justified by the ambiguity in defining a local density. However, we acknowledge that the averaged Intrusion number ($\mathcal{I}n$) remains closely related to density, a quantity commonly used for classifying crowds.

Therefore, in Fig. 4.4 *(c)*, we replaced the Intrusion number with the global density (ρ), calculated as the number of pedestrians divided by the available space.[2] The delineation of different regimes is still evident.

Only the *Single-File* data strongly deviates from the original diagram. In this scenario, pedestrians lack lateral neighbors, potentially influencing their experienced intrusion. Alternatively, the deviation could be attributed to the presence of obstacles, such as walls, which are very close to all agents in the single-file scenario and were not considered in the calculation of $\mathcal{I}n$.

Furthermore, the *Cross* and the *Bottleneck* scenarios exhibit lower densities but higher $\mathcal{I}n$ values compared to the *Waiting* scenario. In the latter, people are distributed very homogeneously, whereas inhomogeneities are conspicuous in the former, including tightly packed regions. The Intrusion number puts more wheight on these.

The classification of crowd regimes can be accomplished by substituting the Intrusion number with the global density. This raises the question of whether the agent-centred intrusion variable $\mathcal{I}n_i$ still holds relevance or if a local density ρ_i should have been used instead. However, defining a local density in crowds presents challenges due to the similarity in the magnitude of the typical length scales (system size and distances between pedestrians), unlike in fluid dynamics where these differ markedly. Nonetheless, the use of Voronoi cells allows for the definition of a local density in crowds, with the inverse area of the cell providing an agent-centred local density. This density does not depend on the parameters r_{soc} and ℓ_{min} which are included in the definition of $\mathcal{I}n_i$. These parameters, however, hold significance by linking $\mathcal{I}n_i$ to both biomechanical properties, as represented by the incompressible size of humans ℓ_{min}, and psychological factors, as represented by r_{soc}.

For example, consider a large empty room with two individuals; even if one person significantly intrudes upon the other, the associated Voronoi density for each pedestrian would be minimal. Though such a scenario may seem artificial, it is typically investigated in the context of proxemics, where r_{soc} is measured in 'stop-distance' experiments. In these a subject approaches or is approached by an assistant until the subject begins to feel uncomfortable due to the proximity of the other person [107]. Such nuances are effectively captured by the agent-centred variable $\mathcal{I}n_i$.

Furthermore, while we have treated the crowd as homogeneous, with the same r_{soc} and ℓ_{min} for all pedestrians, these parameters can account for the heterogeneity present in crowds. This includes social relations (e.g., friends vs. strangers) or context (e.g., concert

---

[2]To enable us to plot the *Single-File* data along with the rest, the one-dimensional density, calculated as the number of people divided by the length of the track, was rescaled according to [170], where we assumed a width of 0.3m.

vs. work) in terms of r_{soc}, as well as diverse body shapes such as children and adults with respect to ℓ_{min}. Additionally, future considerations could involve more complex shapes, such as elliptical bodies, velocity dependent shapes, taking stepping into consideration, or asymmetrical social spheres. Though perception effects have been overlooked thus far, they can easily be incorporated in the neighborhood used to define $\mathcal{I}n_i$.

Moreover, the calculation of Voronoi diagrams, in comparison to $\mathcal{I}n_i$, is considerably more intricate, particularly in the presence of obstacles or walls where the precise methodology remains ambiguous. Thus, introducing a new yet related quantity is justified.

4.3   Correlations between $\mathcal{I}n$ and $\mathcal{A}v$

Looking at the diagram in Fig. 4.2 one might wonder whether $\mathcal{I}n$ and $\mathcal{A}v$ feature some correlations, i.e., that as one of them changes, the other one changes as well. More specifically, this owes to the impression of a systematic increase of $\mathcal{A}v$ with increasing $\mathcal{I}n$ in the *Waiting* scenario and, with a different slope, in the *unidirectional* or *Single-File* scenarios. This trend is apparent even after applying the Butterworth filter, which already considerably reduced the blurring effect of the participants' headways on the delineation. Especially for the *waiting* scenario, however, the trajectories still feature irregular motion due to head movement, cf. sec. 4.2.1.4. Consequently, the trend might still be related to the swaying of heads.

Nonetheless, we have seen that $\mathcal{I}n$ and $\mathcal{A}v$ are sufficiently independent to allow for a proper distinction between the typical scenarios encountered in pedestrian streams and even some degree of interdependence would mostly result in a skewed diagram (given that the $\mathcal{I}n$ and $\mathcal{A}v$ axes have been plotted orthogonally although they should not) with no impact on its topology. Ultimately, while for the overall correlation is difficult to make out the details, we can, of course, calculate the correlation between the agent-centred $\mathcal{I}n_i(t)$ and $\mathcal{A}v_i(t)$ in different regimes.

4.3.1   Crosscorrelation between $\mathcal{I}n$ and $\mathcal{A}v$

More specifically, let us study the crosscorrelation between $\mathcal{I}n$ and $\mathcal{A}v$ which tells us how much an anticipated collision at time t, quantified by $\mathcal{A}v_i(t)$, is correlated with an intrusion at a later time $t + \Delta t$, i.e. $\mathcal{I}n_i(t + \Delta t)$. We use the normalized crosscorrelation and assume a stationary process. In that case the crosscorrelation is defined as follows

$$K\left(\mathcal{A}v_i(t), \mathcal{I}n_i(t + \Delta t)\right) = \frac{E\left[\left(\mathcal{A}v_i(t) - E\left[\mathcal{A}v_i\right]\right)\left(\mathcal{I}n_i(t + \Delta t) - E\left[\mathcal{I}n_i\right]\right)\right]}{\sigma_{\mathcal{A}v_i} \sigma_{\mathcal{I}n_i}}, \qquad (4.8)$$
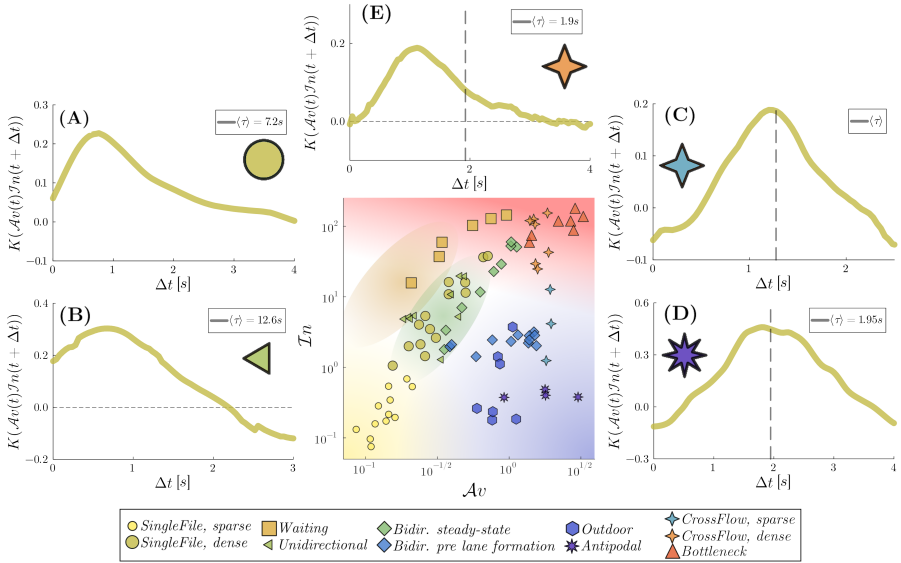
FIGURE 4.5: Crosscorrelation $K\left(\mathcal{A}v_i(t), \mathcal{I}n_i(t+\Delta t)\right)$ in different regimes of crowd flow, specifically for the dense *single-file* **(A)**, the *unidirectional* flow **(B)**, the sparse *cross* flow **(C)**, the *antipodal* scenario **(D)**, and the dense *cross* flow **(E)**. The vertical dashed grey line denotes the mean value of the TTC in the dataset.

where σ denotes the standard deviation and $E\left(\cdot\right)$ the expectation value. The range of this normalized crosscorrelation lies between $[-1, 1]$ where 1 corresponds to perfect correlation and -1 to perfect anticorrelation. We can empirically estimate this by calculating the corresponding quantities from the timeseries of each pedestrian present in the scene, and then average over all pedestrians.

The results for different scenarios are shown in Fig. 4.5 where we depict the crosscorrelation for different scenarios together with their location in the 'phase' diagram. Let us start by analyzing a regime of low $\mathcal{I}n$ and high $\mathcal{A}v$ number, represented here by the sparse *cross* flow and the *antipodal* scenario in Fig. 4.5C and D. We find that for Δt close to zero, $\mathcal{I}n_i$ and $\mathcal{A}v_i$ are slightly anticorrelated. The correlation increases with Δt and reaches a maximum value. Remarkably, this maximum is located exactly at the mean value of the TTC τ in the corresponding dataset. This can be understood as follows, two pedestrians approach each other but are still well separated, which results in a (slight) anticorrelation. They realize the impending risk of collision and slightly adjust their path which dissolves the anticipated risk of collision. As the scenario is considerably sparse both continue to move with a similar velocity as before towards their goal. Accordingly, the two pedestrians continue to approach each other and get proxemically closer to each

other. They are closest to each otehr around the time at which they initially antici-pated a collision to happen. As they continue to move along their path they grow apart spatially and accordingly the crosscorrelation decreases.

Let us now study the opposite regime with $\mathcal{I}n \sim 1$ and small $\mathcal{A}v$ number as shown in Fig. 4.5A and B for the *single-file* and the *unidirectional* scenario. As before, if a pedestrian faces an anticipated collision, the intrusion will typically increase in the future. In contrast to the regime of high $\mathcal{A}v$ and low $\mathcal{I}n$ numbers, however, for small Δt the correlation is still positive and quickly reaches a maximum located at $\Delta t \approx 0.8$s, i.e. at times much smaller than the mean value of the TTC. Both scenarios show the peak at almost the same time, which is associated with the step-frequency of pedestrians. This indicates, as already discussed above, that some effect of oscillations is still present even after applying the Butterworth filter.

Ultimately, for the dense *cross* in Fig. 4.5E, in a regime of high $\mathcal{I}n$ and high $\mathcal{A}v$ numbers, the crosscorrelation is zero for small times and approaches a maximum which is, as above, located at $\Delta t \sim 0.8$s. The mean value of the TTC is however located quite close to the maximum. In such non-asymptotic regimes, multiple effects might be superimposed onto each other.

4.4 Self-Organized Structure in Crowds

We have introduced two agent-centred variables $\mathcal{I}n_i$, based on the preservation of per-sonal space, and $\mathcal{A}v_i$, based on the anticipation of collisions. By averaging these over the whole crowd we defined two dimensionless numbers which allowed us to visually delineate regimes of crowd flow, as shown in Fig. 4.2. This indeed appears sensible. Nonetheless, its physical significance becomes apparent only if the delineated regimes exhibit consti-tutive differences. More specifically, we want to link the associated regimes with the typical self-organisation of the pedestrians. This would make the delineation especially useful for theoretical endeavours, i.e., for the modelling of pedestrian crowds.

Remarkably, a substantial difference is found here not in the static symmetry of the structure (as in distinguishing a liquid from a crystal), but rather in the nature of this self-organized 'structure' - more practically, in the variables that characterize it. Inspired by condensed matter physics and following the approach in [82], we utilize the pair-distribution function (pdf) $g(x) = P(x)/P_{\mathrm{NI}}(x)$ between pedestrians as a structural probe. This function quantifies the probability that two interacting pedestrians are found a given distance x apart, normalized by the probability P_{NI} of measuring this distance for pedestrians that do not interact. This will lead us to the observation that
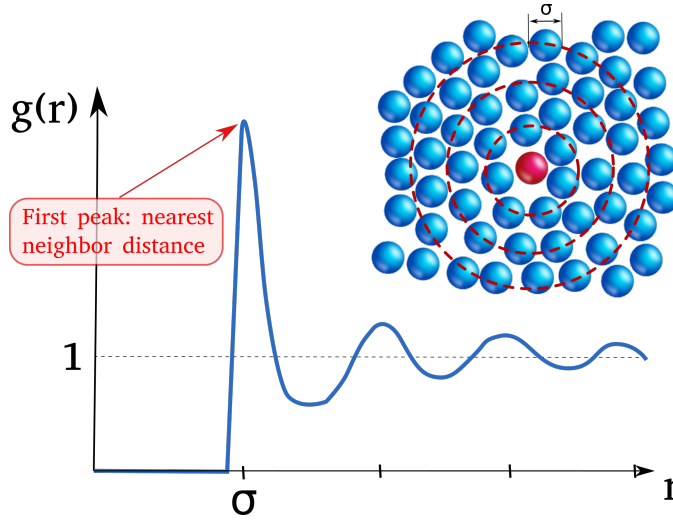
FIGURE 4.6: Exemplary figure of the pair-distribution function.

Euclidean distances are relevant for describing the crowd's structure at low Avoidance numbers, whereas Time-to-Collisions (TTCs) are relevant at low Intrusion numbers. In the former case, the interactions governing the dynamics can be considered as 'spatially controlled', while in the latter case, they are 'temporally controlled'. This distinction provides insight into the different nature of crowd dynamics and how it manifests in the structural characteristics of the crowd.

Before discussing these qualitative differences between the regimes in greater detail we will give some insights of how to approximate the aforementioned probabilities by randomizing the time or space information. Besides, we will need to show first that indeed the pair-distribution-function inhibits crucial information about the crowds' self-organized structure in various scenarios.

4.4.1 Definition of the Pair-Distribution Function

The pair-distribution function (pdf) is a common tool in materials science used to infer the atomic or molecular structure of materials. In general a value of $g(x) > 1$ indicates that the distance x is observed frequently between two atoms (or alternatively pedestrians), a value $g(x) < 1$, on the other hand, means that distance x is suppressed by the organization of the material (or the by the self-organized structure of the crowd). Figure 4.6 provides an illustration of the relation of the pdf to the structure of a material. Imagine starting from the red atom in the centre and moving radially away from it. For small values of r, we will not find another atom due to volume exclusion and accordingly

$g(r) \ll 1$. This is followed by a strong peak at the nearest neighbour distance. The peaks and minima decay at some length scale beyond which fluctuations wash away the structural features. An experimental example of a pdf, measured for solid and liquid Argon, can be found in [171].

In our case, we calculate the pdf of crowds according to the approach in [82]. For a variable x, the pdf is given by the probability that two pedestrians are separated by x normalized by the probability $P_{NI}(x)$ that two non-interacting pedestrians are separated by x, specifically $g(x) = P(x)/P_{NI}(x)$. This normalization is crucial in the definition of $g(x)$ as it corrects, for example the finite system size that leads to the fact that large distances are rarely observed irrespective of the structure itself.

While $P(x)$ can be straightforwardly estimated by the relative frequencies in the dataset, $P_{NI}(x)$ is, in principle, unknown. However, it can be estimated by randomizing either the spatial or the temporal information. To estimate the distribution, we employed strict binning with bins of size 0.1m or 0.1s.

4.4.1.1   Calculation in various Scenarios

The process of estimating $P_{NI}(x)$ is most comprehensible in the context of single-file motion. In this scenario, the observation area is confined to the x-coordinate, spanning from 0 to L. Since all pedestrians enter on the left and exit on the right, all positions are equally probable. However, due to the limited size of the area, finite-size effects strongly suppress large distances. Therefore, $P_{NI}(x)$ can be estimated by computing the distribution of distances between points randomly placed within the interval $[0, L]$. Another approach to estimate $P_{NI}(x)$ is by randomizing the time-information, creating a 'time-scrambled' version of the dataset as suggested by [82]. This ensures that distances calculated in the scrambled dataset correspond to non-interacting pedestrians, as they were not originally present in the same frame. Both methods yield the same result in the case of single-file motion.

For the static crowd (*Waiting* scenario), temporal information cannot be scrambled, as pedestrians exhibit minimal movement. Therefore, we assume that all positions within the rectangular measurement area are equally likely. This assumption is justified as we neglect the edges of the observation area, where people lean on the crowd-control barrier. On the other hand, in the *Outdoor* dataset, in addition to finite-size effects, considerations must be made for various forbidden areas (such as trees or cars) in the middle of scenes and different areas where people enter or leave the scene. This is achieved by randomizing the time-information.
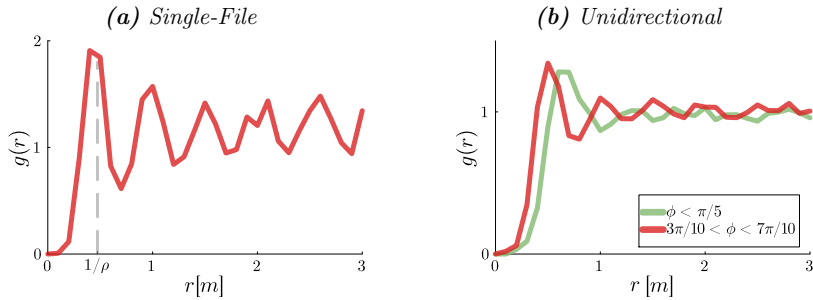
FIGURE 4.7: Evaluation of the pdf $g(r)$ in different scenarios. In *(a)* for one run of the *SingleFile, dense* dataset. In *(b)* the *Unidirectional I* dataset, the run with $\rho = 2.1/m^2$ the position of the peaks depends on the angle ϕ. In particular, the longitudal distances (to the front) are larger than the transversal distances (to the sides).

4.4.2 Insights into the crowd's structure in different scenarios

Let us return to our 'phase' diagram in Fig. 4.2. If we start from the origin $(\mathcal{I}n, \mathcal{A}v = 0)$ and move up along the $\mathcal{I}n$-axis while keeping $\mathcal{A}v \ll 1$, the scenery gets more and more crowded. Therby, the crowd structures itself in real space which is evidenced by its radial pdf $g(r)$, where r is the Euclidean spacing between people. This is best exemplified by one-dimensional configurations. More specifically, it is most clearly demonstrated in the experiments conducted by [46]: high density, periodic, single-file experiments with soldiers as the participants. The corresponding pdf is shown in Fig. 4.7 *(a)* for a single run at $\rho = 2.1/m$, where long-ranged correlations in the pdf can be seen, owing to the strong homogeneity, combined with the spatially confined setting. The pdf displays peaks that are well separated and located at the integral multiples of the mean spacing, i.e. correspond to the k-th neighbor. This resembles the pdf of a liquid or a dense suspension of active colloids [172].

But structural features are also visible in two-dimensional settings, notably in the unidirectional flow through a corridor with open boundaries at a density of $\rho = 2.1/m^2$. The corresponding pdf is shown in Fig. 4.7 *(b)*. Its pdf displays a strong dip at short distances, below $0.3 \sim 0.4\,m$, reflecting strong short-range repulsion, due to hard-core impenetrability and the reluctance for intrusion into the intimate space; the dip is followed by a peak at the nearest-neighbor distance. This is followed by multiple peaks which decay much faster than in the one-dimensional setting.

Furthermore, the curves are binned according to the angle ϕ between the velocity $\boldsymbol{v}_i$ and the vector connecting the centers of two pedestrians $\boldsymbol{r}_{ij}$. The two curves exhibit a difference between longitudinal (*green*) and transversal (*red*) distances, reflecting the existence of anisotropy. In particular, pedestrians keep smaller distances to their sides
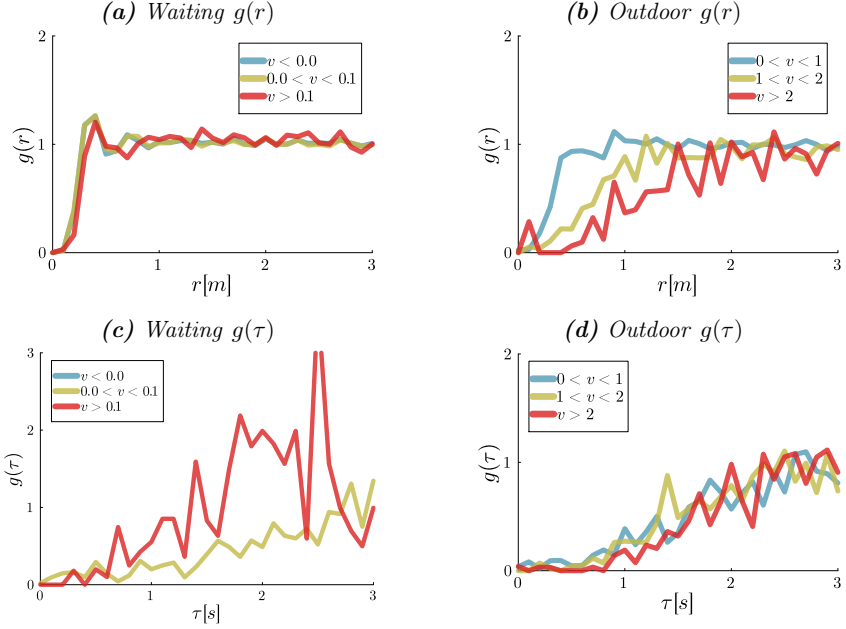
FIGURE 4.8: *(a)* and *(c)* pdf for the *Waiting* dataset and *(b)* and *(d)* for the *Outdoor* dataset. The curves are binned according to the rate of approach $v = -dr/dt$ (given in m/s). As for the *Waiting* the pdf is well parameterised by r and poorly by τ and for the *Outdoor* vice versa.

than to the front. The angular dependence may have practical implications as to whether the capacity of a corridor increases linearly or step-wise with its width.

Similarly, for the dense static waiting crowd in Fig. 4.8 *(a)*, we can see that small distances are strongly suppressed. This is followed by a peak representing the nearest-neighbor. This time, we have binned the pdf not in dependence on the angle ϕ, but on the rate of approach v (i.e., the rate at which the distance between two pedestrians declines). The described features are insensitive to changes in this dynamic variable: the radial pdf exhibit the very same trend Fig. 4.8 *(a)*, quite independently of v.

The situation is widely different if one departs from the non-interacting regime by increasing $\mathcal{A}v$, i.e., examining scenarios with very sparse crowds ($\mathcal{I}n \ll 1$) characterized by conflicting moves. Examples include the *antipodal* scenario or situations involving sparse outdoor crowds, as extensively analyzed in [82]. Strikingly, in this regime, the radial pdfs no longer collapse onto a single curve. When binned according to the rate of approach v as depicted in Fig. 4.8 *(b)*, the pdfs exhibit distinct shapes. Notably, as pedestrians approach each other at higher speeds, the Euclidean spacing at which their interactions commence becomes larger.
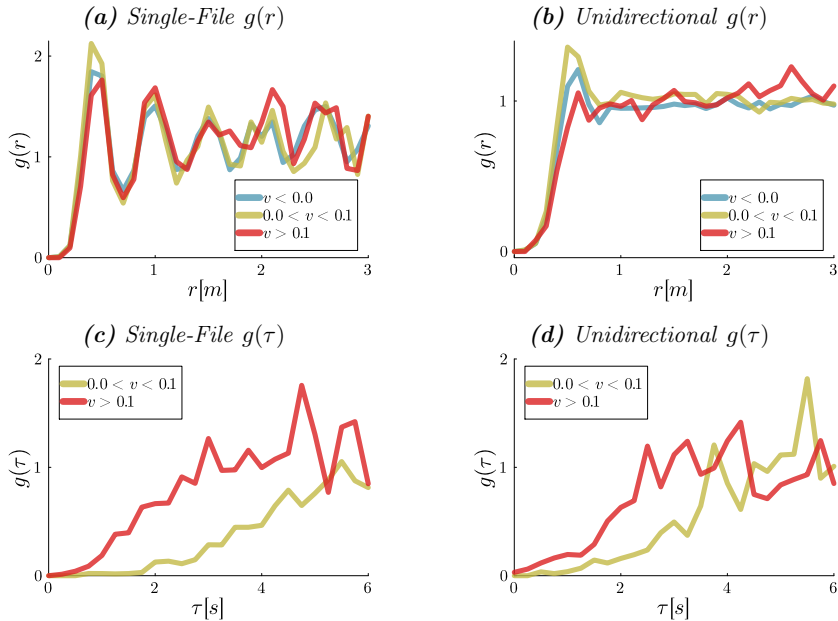
FIGURE 4.9: In *(a)* and *(c)* pdf for the *Single-File* dataset and in *(b)* and *(d)* for the *Unidirectional I* dataset. The curves are binned according to the rate of approach $v = -dr/dt$ (given in m/s). In both cases the pdf is reasonably well parameterised by r and poorly by τ.

Instead, if the TTC denoted as τ is used in place of r as the input for the pdf, a master curve emerges, as depicted in Fig. 4.8 *(d)* for the *Outdoor* dataset. Specifically, the pdf gets more and more strongly depleted as τ becomes shorter, signalling the risk of an imminent collision. In this regime, the structure of crowds is not readily apparent in real space but becomes evident in TTC space only. This major finding of [82] is here contextualized by ascribing it to a particular regime of crowd flow: it does not hold for the waiting room (finite $\mathcal{I}n$, small $\mathcal{A}v$) Fig. 4.8 *(c)*. It is important to note that, for negative rates of approach (thus, infinite TTC), no curve can be plotted in Fig. 4.8*(c)*, even though the structure remains independent of it in real space, as seen in Fig. 4.8 *(a)*.

The failure of $g(\tau)$ to describe the dynamics in the high $\mathcal{I}n$ and low $\mathcal{A}v$ regime can be further exemplified by considering starting waves, see e.g. [72, 173, 174]. Here, in an initially static and typically dense crowd the first person (or first row) starts to move. This allows the people behind them to move as well which triggers a backwards travelling starting wave. If we look at this phenomenon in 'TTC-space' we can not distinguish whether the pedestrians ahead of a reference agent stand still ($v \approx 0$) or move ahead ($v < 0$), their TTC is infinite in both cases.
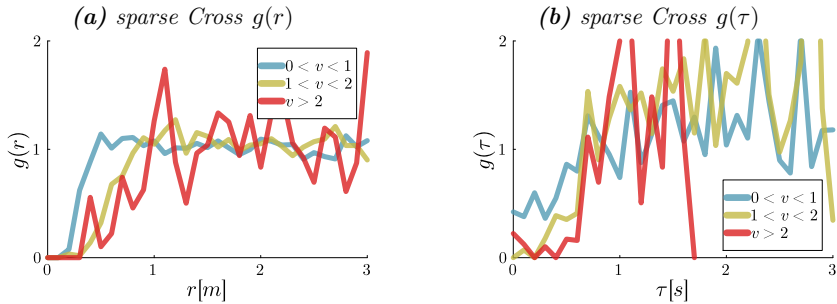
FIGURE 4.10: The pdf for the sparse *Cross* dataset. The curves are binned according to the rate of approach $v = -dr/dt$ (given in m/s). It seems that the pdf can neither be fully parameterized by r nor by τ.

Let us test these observations in different data sets. Therefore, we calculate the accordingly binned pdfs $g(r)$ for the *Single-File* experiment already discussed above, cf. Fig. 4.9 *(a)*, as well as for the *unidirectional* dataset, cf. Fig. 4.9 *(b)*, which are located at low but nonetheless higher $\mathcal{A}v$-numbers if compared to the *Waiting* dataset. The structure of nearest-neighbor or next-nearest-neighbor are still clearly visible for each binned curve. Moreover, the locations of the peaks seem to be independent of the rate-of-approach. On the other hand, in both cases, the nearest-neighbor has a reduced probability to have a large rate of approach. For the pdfs $g(\tau)$, it is clearly visible that the TTC alone can not at all describe the crowd in this regime.

These results are related to the modelling of Single-File motion in the first chapter 3. More specifically we found that a TTC based model completely fails in describing the main features of single-file motion. A simple model, in which the agents chose their velocity according to their headway leads to a homogeneous solution which is very closely resembled by $g(r)$ in Fig. 4.7 *(a)*. If we look at more subtle effects, however, one needs to take the relative velocity into consideration which seems to be reflected in the (slight) dependence of $g(r)$ on the rate of approach.

Along the $\mathcal{A}v$-axis, finding another dataset at low $\mathcal{I}n$-number with enough data-points is difficult. As these scenes are sparse by definition long observational sequences are needed. Moreover, the experiments located here (like *Antipodal*) only feature very specific distances and velocities such that estimating the pdf becomes even more challenging. Nonetheless, in Fig. 4.10 we show the pdfs for the sparse *cross-flow*. As for $g(r)$, the picture seems fairly similar to the *Outdoor* data: the faster two pedestrians approach each other, the larger will be the typical Euclidean spacing at which they begin to interact. The collapse on $g(\tau)$, on the other hand, can not be fully recovered. Even though the pdfs are quite noisy, probably due to the missing data (especially for $v > 2$) we can attest that for small values of τ the collapse is not recovered. But this might not be the
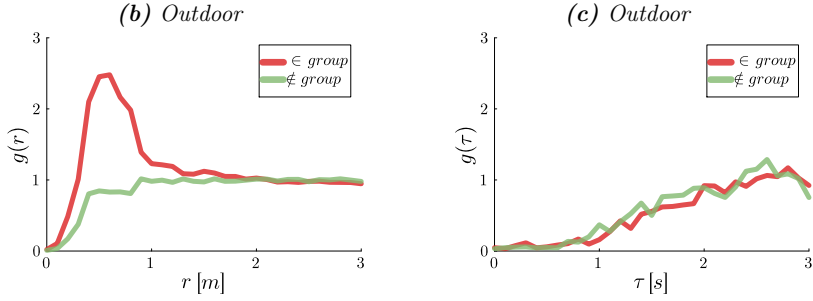
(b) *Outdoor*   **(c)** *Outdoor*

FIGURE 4.11: Evaluation of the pdf $g(r)$ in the *Outdoor* scenarios. In **(a)**, the marked peak at small distances to the sides arises from many pairs which are present in the observation. This cannot be observed in the TTC-based pdf $g(\tau)$, cf. **(b)**.

expectation anyway - the sparse *Cross-flow* is not in the close vicinity of the $\mathcal{A}v$-axis, especially the run with the highest number of participants which, consequently, consists of the most trajectories and can therefore be assumed to dominate in the calculation of the pdf.

4.4.2.1   Effect of pairs and social groups on the pdf

Finally, let us investigate the effect of social groups on the pdf. Therefore, once again we calculate the pdf for the *Outdoor* dataset but this time we bin the curves according to whether pedestrian i is part of a social group ($\in group$) or not ($\notin group$). To this end, we employ the classification described in section 4.2.1.3. Notably, distinct curves are evident in Fig. 4.11 **(a)** contingent upon whether we move away radially from a member of a social group ($\in group$) or a pedestrian which is not part of a social group. Specifically, for pedestrians within a social group, the pdf displays a pronounced peak at small (transversal) distances that originates in the presence of anohter member of the social group. These are characterized by a desire to maintain close proximity which allows for instance to talk or to walk hand in hand. Apart from this, and a robust short-ranged repulsion, no spatial structure is discernible. The pdf bears resemblance to a mixed gas consisting of single atoms and molecules. When the pdf is computed for the time-to-collision, as illustrated in Fig. 4.11 **(b)**, the two curves converge. This is because spatial proximity does not imply an imminent collision risk; pair members aim to remain close but without colliding.

Above, we have underlined that the finding of [82] (namely, that the TTC is a more suitable descriptor than the spatial distances) is valid in a certain regime only (i.e. low $\mathcal{I}n$, moderate $\mathcal{A}v$). Here, by turning the original argument upside down, we contend that further constraints are necessary when it comes to social groups. More specifically,

two types of interactions are present here, an attractive distance-based ('proxemic') interaction within each group and a TTC-based (avoidance) interaction with other people. These are both mirrored in their respective pdfs: the notable peak at short distances in $g(r)$ (but not in $g(\tau)$) and the depletion of $g(\tau)$ for imminent risks of collisions. Thus, the collapse of the two curves for $g(\tau)$ in Fig. 4.11 *(b)*, actually fails to reflect a fundamental difference in the interactions between members and non-members of social groups. Incidentally, this also explains the large variations in the pdf $g(r)$ in [82], binned by rates of approach: in [82], pairs were not excluded and the rate of approach of their members is very small, and thus falls in one specific bin.

4.5   Summary and Outlook

In summary, we have introduced two dimensionless parameters that quantify the desire to preserve one's personal space, the Intrusion number $\mathcal{I}n$, and the anticipation of collisions, the Avoidance number $\mathcal{A}v$. While on an individual level they are based on directly perceivable quantities capturing psychological properties of pedestrians, on the level of the crowd their averages define two dimensionless numbers that delineate different regimes of crowd flow.

In particular, we have collated an extensive data set of pedestrian trajectories in diverse scenarios and calculated $\mathcal{A}v$ and $\mathcal{I}n$ empirically. This allowed a visual delineation of different crowd regimes that aligns with our intuition. We showed that these regimes are marked by specific 'structural' arrangements: while at low $\mathcal{A}v$-numbers the crowd self-organizes in a way best described in terms of Euclidean spacings, at low $\mathcal{I}n$-numbers the self-organized structure is much better captured in terms of temporal spacings, i.e., times-to-collisions. Furthermore, we found that the cross-correlation differs markedly between these asymptotic regimes which gave complementary insight.

At present, the definition of $\mathcal{A}v$ only accounts for collisions between the hard-cores of pedestrians. A more sophisticated definition of $\mathcal{A}v$ should not be binary but also capture 'softer' collisions, i.e., anticipated intrusions into the private or intimate space. Such a definition would mitigate the number of pedestrians with $\mathcal{A}v_i = 0$ which have been neglected in the averaged value of $\mathcal{A}v$.

So far, our main focus has been on asymptotic regimes, which are in the vicinity of either one of the two axis. When moving to regimes with non-zero $\mathcal{A}v$ and $\mathcal{I}n$ number, empirical results are difficult to interpret. The effect of headways on the calculation of $\mathcal{A}v$ in regimes of large $\mathcal{I}n$ number, even after applying the Butterworth-Filter, complicates this matter. A different filtering method could allow a less obstructed view here. Another

track in improving our understanding of non-asymptotic regimes will be the theoretical description put forward in the concurring chapter.

There we will try to rationalize the findings presented here for a theoretical description by proposing perturbative models based on $\mathcal{A}v$ and $\mathcal{I}n$. Similarly to Fluid Mechanics, where dimensionless numbers guide the choice between different approximations, the dynamics of crowds can be approached in each regime by perturbative expansions, which yield pedestrian models applicable in the corresponding regime (and only there).

Finally, while the focus throughout this chapter has been on the delineation of crowd regimes with the help of $\mathcal{A}v$ and $\mathcal{I}n$, they can also be employed as measures with regard to all sorts of more nuanced behaviour observed in crowds. Therefore, before proceeding, let us try to utilize the Avoidance and Intrusion numbers to investigate motivation and pushing behavior of crowds at bottlenecks. To this end, we will also study the distributions of $\mathcal{A}v$ and $\mathcal{I}n$.

4.5.1   Outlook: Motivation at Bottlenecks

Let us start by explaining the different runs in the *Bottleneck* experiment in more detail. The experiments have been conducted to investigate the effect of the corridor width on the behaviour on the crowd. Accordingly, as noted in Table 4.1, the width of the corridor leading to the bottleneck was varied between the runs [61]. For each width two runs were performed, once with high motivation, on which we have been focused so far, and once with a lower motivation. To trigger these two levels of motivation, the instructions given to the participants were changed. In particular, for the high motivation runs the participants were told to (translated from German) *"imagine [that] you are on your way to a concert by your favourite artist. You know that at the back you can hardly see anything at all or only the video screen. You absolutely want to be standing next to the stage and therefore want to access the concert as fast as possible. After a signal, we will open the entrance"* [61], For the lower motivation, on the other hand, the participants were told to *"imagine again that you are on your way to a concert by your favourite artist. This time you know that everyone will have good view. Still, you would like to access the concert quickly"* [61]. We can distinguish these different levels of motivation on the level of the whole crowd by the averaged $\mathcal{A}v$ and $\mathcal{I}n$ number, where the latter is located at higher $\mathcal{I}n$ and higher $\mathcal{A}v$ numbers, cf. Fig. 4.12.

Thereby, we have assumed that motivation is static and homogeneous across the crowd which is known to be inaccurate. Motivation is a widely discussed topic in social sciences, in our case, however, it can simply be defined as the desire to reach the goal, i.e. to reach the bottleneck quickly [175]. This behaviour strongly varies between individuals and does
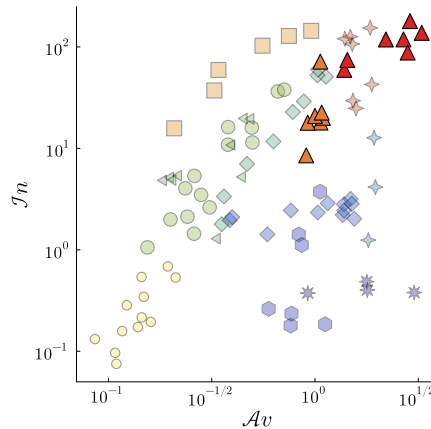
FIGURE 4.12: Location of the runs with low (orange triangles) and high motivation (red triangles) bottleneck runs in the 'phase' diagram.

not stay constant over time: some people are eager to reach the exit as fast as possible and for example push others to reach their goal. Other pedestrians, on the contrary, do not engage like that but instead get overtaken by others [175]. Exactly this time-dependent and individual information has been obtained by qualitatively rating each pedestrian in every frame as falling behind, just walking, mild pushing or strong pushing [176] which we can now employ to measure motivation in a heterogeneous and dynamic way.[3]

In Fig. 4.13 we depict the mean value of $\mathcal{A}v$ and $\mathcal{I}n$ averaged for each level of pushing. We can clearly see two things, first we see again that the global level of motivation leads to higher values of both $\mathcal{A}v$ and $\mathcal{I}n$, as it has already be verified in Fig. 4.12. Moreover, both $\mathcal{A}v$ and $\mathcal{I}n$ increases monotonically with the level of pushing in almost all runs. Note that this is also the case for the other runs which are not shown here. This means indeed that increased $\mathcal{A}v$ and $\mathcal{I}n$ numbers, in comparison to the rest of the crowd, are an indicator for higher motivation.

However, we have (again) only looked at the mean values of the accordingly binned data points. Let us now, instead, look at the distributions which are a blind spot in the overall investigation of the avoidance and intrusion variable so far. In Fig. 4.14 we show the distributions $P(\mathcal{A}v)$ which have been obtained by employing strict bins of size 0.1. While the 'global' trend of the mean value has been, the larger the level of pushing the larger the value of $\mathcal{A}v$, this seems not to be the case for the individual values: they can

---

[3]Note that high motivation might not always be associated with pushing, a counter-example would be a 'cornered' individual that pushes for protection in a very dense crowd.
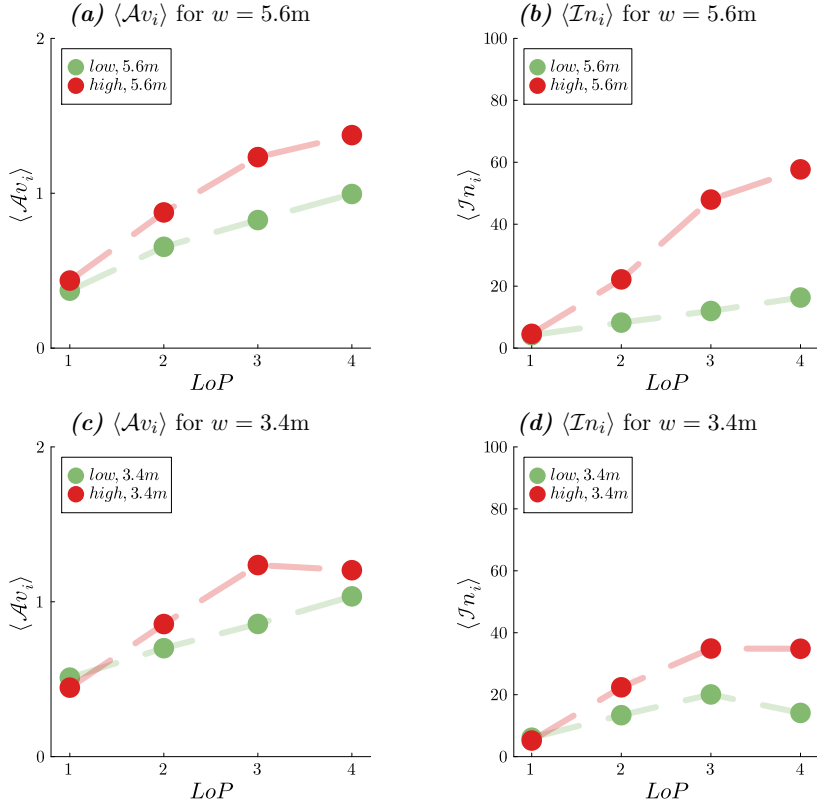
FIGURE 4.13: Mean value of $\mathcal{A}v$ and $\mathcal{I}n$ in dependence of the associated level of pushing: falling behind (1), just walking (2), mild pushing (3) or strong pushing (4). The color of the symbols refers to the 'global' level of motivation, i.e. green as *low* and red as *high*.

not be distinguished as the distributions themselves are fairly similar and display a quite large variance.

The result presented here unveil a change of the meaning of the Avoidance number at high densities, which is not correctly captured by its naming. Specifically, an increase of avoidance with a higher pushing intensity is counterintuitive because pushing refers to situations in which pedestrians do *not* avoid contact. Nonetheless the TTC, on which the Avoidance number is based, quantifies the conflicts that arise from the fact that two or more pedestrians face an anticipated collisions or heavy intrusion in their personal or intimate space. While at low densities pedestrians typically are able to avoid an anticipated collision by slightly changing their velocity, thus, by *avoidance*, this is often not possible in dense scenarios.
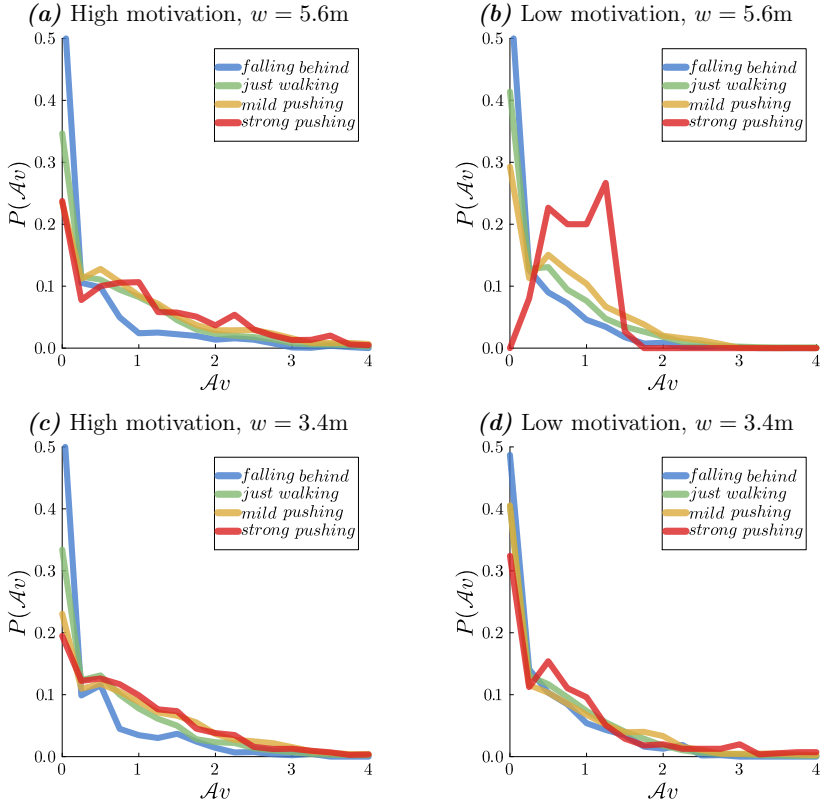
FIGURE 4.14: Distributions of the avoidance variable $\mathcal{A}v$ in different experimental runs for the different levels of pushing.

Nonetheless, the two variables $\mathcal{A}v$ and $\mathcal{I}n$ can indicate different levels of motivation which might prove useful in future endeavours to model motivation in a heterogeneous and dynamic way [177] because they provide means to measure the individual level of motivation which in the simulation can not be done by a complex qualitative rating of the actual experimental videos. Besides, in this section we have studied the distribution of the avoidance variable. To get further inside in the structure of the crowds' state in different regimes we will need to study these more closely - this might also allow a more detailed understanding on their dependence on individual and dynamic level of motivation. Apart from this, the analysis put forward here alludes to the usage of $\mathcal{A}v$ and $\mathcal{I}n$ beyond the classification of crowds as measures for diverse phenomena encountered in crowds.

Chapter 5

Perturbative Models

In the previous chapter we have drawn inspiration from the methodology of fluid dynamics and introduced dimensionless numbers to analyze and characterize pedestrian streams. Similarly as the Reynolds number in fluid dynamics, the Intrusion number $\mathcal{In}$ and the Avoidance number $\mathcal{Av}$ provide means to intuitively and quantitatively distinguish different regimes. In particular, we have used these to rationally organize a large collection of empirical data sets and showed that different regimes thus delineated are characterized by different types of arrangements, best understood in terms of either Euclidean distance or 'times to collision'. Thereby, we have connected the psychological underpinning with a classification of crowds, notably relevant for safety analysis. We will now try to rationalize the empirical classification of crowd flows theoretically, for the modelling of pedestrian crowds. Notably, in fluid dynamics, gauging the validity of approximations is the main utilization of dimensionless numbers like the Reynolds number.

In particular, the distinct types of arrangements evidenced above, depending on the regime, contribute to making the delineation of regimes useful. Based on this, we will argue that the dynamics of a pedestrian is in many cases governed only by the agent centred intrusion $\mathcal{In}_i$ and $\mathcal{Av}_i$ avoidance variable. Starting from a very general but only formal model, this will allow us to perform a first-order expansion around the non-interacting situation and to obtain asymptotic models for pedestrian crowds. We will show that the performance of each model is tightly connected to a specific the regime of crowd flow. More specifically, by testing these models in different regimes, we show that they are generically only applicable in the regime they were derived for.

5.1 Perturbative Analysis

Let us consider a crowd of N pedestrians at time t. Formally, the dynamics of a pedestrian i is a function of all positions and possibly body orientations observed so far. We denote the set of positions at time t by $\mathcal{R}(t) = (\boldsymbol{r}_1(t), \ldots, \boldsymbol{r}_N(t))$ and the shapes of the agents by the set $\mathcal{S}$, which might also be defined to include the infrastructure, e.g., walls. Apart from interactions with the other pedestrians or the infrastructure, pedestrians have certain goals they try to reach, typically represented by a desired velocity $\boldsymbol{v}_{\text{des},i}$ which might depend on time and space. Furthermore, there might be some unobserved internal parameter ξ_i that, for example, varies between different runs of the same experiment. It is possible to recast this functional dependence as a minimization, by *designing* a suitable mathematical (cost-)function $\mathcal{C}_i$ [106, 178, 179]. We are therefore led to phrase this functional dependence for each agent as,

$$\boldsymbol{v}_i^{\star} = \underset{\boldsymbol{v} \in \mathbb{R}^2}{\arg\min}\, \mathcal{C}_i \Big[\boldsymbol{v}, \{\mathcal{R}(t'), t' \leqslant t\}, \mathcal{S}, \xi_i \Big], \tag{5.1}$$

where $\boldsymbol{v}_i^{\star}$ denotes the decision of agent i which serves as an input to a mechanical layer which yields the actual velocity $\boldsymbol{v}_i(t)$. Unfortunately, neither the cost function $\mathcal{C}_i$ nor the hidden variables ξ_i are known.

Nevertheless generic perturbative expansions can provide a basis for the study of systems near their critical states, for example by utilizing symmetries. In this context, we can not rely on symmetry considerations, but the empirical classification of crowd regimes presented in the previous chapter has proved the significance of the Intrusion and Avoidance numbers. This justifies the assumption that the interactions between pedestrians are predominantly influenced by $\mathcal{I}n_i$ and $\mathcal{A}v_i$, simplifying the second part of Eq. (5.1) to

$$\boldsymbol{v}_i^{\star} = \underset{\boldsymbol{v} \in \mathbb{R}^2}{\arg\min}\, \mathcal{C}_i \left[\boldsymbol{v}, \mathcal{I}n_i \left(\boldsymbol{r}_i(t) + \delta t \boldsymbol{v} \right), \mathcal{A}v_i(\boldsymbol{v}) \right], \tag{5.2}$$

where $\mathcal{A}v_i$ is evaluated with the test velocity $\boldsymbol{v}$ and $\mathcal{I}n_i$ at the associated position $\boldsymbol{r}_i(t) + \delta t \boldsymbol{v}$ where δt is a time step. We have approximated the shapes $\mathcal{S}$ with discs.

The critical state is here represented by the non-interacting scenario ($\mathcal{I}n_i, \mathcal{A}v_i = 0$) in which the agent freely pursues her goal. This goal is represented by the desired velocity $\boldsymbol{v}_{\text{des},i}$, where without loss of generality we neglect temporal or spatial dependencies. Hence, to leading order, Eq. (5.2) simplifies to

$$\mathcal{C}_i(\boldsymbol{v}) \approx (\boldsymbol{v}_{\text{des},i} - \boldsymbol{v})^2. \tag{5.3}$$

Expanding Eq. (5.2) around this reference situation, as detailed in the following section, yields the $\mathcal{A}v \star \mathcal{I}n$-model,

$$\mathcal{C}_i \left[\boldsymbol{v}, \mathcal{I}n_i \left(\boldsymbol{r}_i(t) + \boldsymbol{v}\delta t \right), \mathcal{A}v_i(\boldsymbol{v}) \right] \approx \left[\boldsymbol{v}_{\text{des},i} - \boldsymbol{v} + \beta \nabla \mathcal{I}n_i \left(\boldsymbol{r}_i(t) \right) \right]^2 + \alpha \, \mathcal{A}v_i(\boldsymbol{v}), \qquad (5.4)$$

with $\alpha, \beta \geq 0$. We will refer to the case $\alpha = 0$ as the $\mathcal{I}n$-model and $\beta = 0$ as the $\mathcal{A}v$-model. Here, we have neglected all mechanical interactions between the agents and the actual velocity relaxes towards the optimum $\boldsymbol{v}_i^\star$ over a relaxation time-scale τ_R. Accordingly, the acceleration of agent i is given by $\boldsymbol{a}_i = \left(\boldsymbol{v}_i^\star - \boldsymbol{v}_i \right) / \tau_R$.

It should be emphasized here that the purpose of these models is *not* to describe pedestrians crowds in every conceivable situation. Rather the models should give some additional insights into the relevance of the characteristic numbers introduced, especially through their limitations. These limitations become conspicuous if we study the models in the asymptotic regimes.

Furthermore, these models are closely related to models that have previously been introduced to describe pedestrian crowds. In particular, the $\mathcal{I}n$-model resembles a simple algebraic-force model and the $\mathcal{A}v$-model is closely related to Velocity Obstacle models. If we chose a different exponent in the definition of $\mathcal{I}n_i$ or another neighborhood in $\mathcal{A}v_i$, the perturbative expansion would have resulted in other well-known models. This will be investigated in the subsequent chapter where we will gauge the range of applicability of numerous models for pedestrian crowds.

In the following, we detail the perturbative expansion that gives rise to the proposed $\mathcal{I}n$, $\mathcal{A}v$ and $\mathcal{A}v \star \mathcal{I}n$-models. Furthermore, we will give some details regarding the implementation. A reader more interested in the modelling results than in the details of the perturbative expansion might move directly to section 5.2.

5.1.1 Generic cost function

We have argued that, the interactions of agent i are mainly controlled by $\mathcal{A}v_i$ and $\mathcal{I}n_i$. Accordingly we have approximated the way in which pedestrians choose their velocity as

$$\boldsymbol{v}_i^\star = \underset{\boldsymbol{v} \in \mathbb{R}^2}{\arg \min} \, \mathcal{C}_i \left[\boldsymbol{v}, \mathcal{I}n_i(\boldsymbol{r}), \mathcal{A}v_i \left(\boldsymbol{v} \right) \right], \qquad (5.5)$$

where we shortened the dependencies $\mathcal{A}v_i \left(\boldsymbol{v} \right) = \mathcal{A}v_i \left(\boldsymbol{v}, \mathcal{R}(t), \mathcal{V}(t) \right)$ and $\mathcal{I}n_i(\boldsymbol{r}) = \mathcal{I}n_i \left(\boldsymbol{r}_i(t) + \boldsymbol{v}\delta t, \mathcal{R}(t) \right)$ this means that the TTC τ_{ij} entering $\mathcal{A}v_i$ are evaluated using the current positions and velocities of all agents, except that agent i's velocity is substituted by $\boldsymbol{v}$. Recall that $\boldsymbol{v}$ denotes the test-velocity and $\boldsymbol{r} = \boldsymbol{r}_i(t) + \boldsymbol{v}\delta t$ the associated test position.

Expanding the cost-function of Eq. (5.5) to lowest order in $\mathcal{I}n_i$ and $\mathcal{A}v_i$, notably, around the non-interacting situation, yields

$$C_i \left[\boldsymbol{v}, \mathcal{I}n_i \left(\boldsymbol{r} \right), \mathcal{A}v_i \left(\boldsymbol{v} \right) \right] \approx C_i^{(0)} \left(\boldsymbol{v} \right) + a_i \, \mathcal{A}v_i \left(\boldsymbol{v} \right) + b_i \, \mathcal{I}n_i \left(\boldsymbol{r} \right), \tag{5.6}$$

where we have shortened the dependencies as above.

Taking advantage of the simple form of Eq. (5.5) and without any other major assumption on the microscopic dynamics, we will show that expanding this equation naturally gives rise to the asymptotic models.

5.1.2 Reference situation: The isolated agent

The reference situation is that of an isolated pedestrian, walking at her desired velocity $\boldsymbol{v}_{\text{des},i}$ where the positional or temporal dependence of the desired velocity is not explicitly written. Specifically, in the absence of any interaction, $\mathcal{I}n_i = 0$ and $\mathcal{A}v_i = 0$, Eq. (5.5) reduces to

$$\boldsymbol{v}_i^\star = \underset{\boldsymbol{v} \in \mathbb{R}^2}{\arg \min} \, C_i \left(\boldsymbol{v}, 0, 0 \right), \tag{5.7}$$

and its minimum should be reached for $\boldsymbol{v}_i^\star = \boldsymbol{v}_{\text{des},i}$. It follows that

$$\boldsymbol{0} = \nabla_v \, \mathcal{C}_i^{(0)} \left(\boldsymbol{v} \right) \Big|_{\boldsymbol{v} = \boldsymbol{v}_{\text{des},i}}, \tag{5.8}$$

where $\nabla_v = (\partial / \partial v_{x_i}, \partial / \partial v_{y_i})$, and the Hessian matrix $\underline{M} = \partial^2 C_i^{(0)} \left(\boldsymbol{v} \right) / \partial \boldsymbol{v}^2 |_{\boldsymbol{v} = \boldsymbol{v}_{\text{des},i}}$ is positive definite. We assume that deviations around the desired velocity are penalized isotropically, in which case $\underline{M}$ is an identity matrix multiplied by a positive scalar γ_i. Since the cost function can be arbitrarily rescaled, we set γ_i to unity without loss of generality. Then, up to second order, the cost-function for an isolated pedestrian is

$$\mathcal{C}_i^{(0)} \left(\boldsymbol{v} \right) = \left(\boldsymbol{v}_{\text{des},i} - \boldsymbol{v} \right)^2. \tag{5.9}$$

The cost increases as the squared Euclidean distance between the test velocity and the desired velocity. In particular, deviations in the magnitude and the direction of the desired velocity are equally penalized. While this is a common assumption in the literature, this need not be exact in reality.

5.1.3   The $\mathcal{A}v$-model

Now, let us introduce a perturbation to the non-interacting system by allowing $\mathcal{A}v_i \neq 0$, while keeping $\mathcal{I}n_i = 0$. For instance, let us consider two joggers who are still well separated but face an anticipated collision. In this case, the cost function can be expanded into

$$\mathcal{C}_i \left[\boldsymbol{v}, 0, \mathcal{A}v_i \left(\boldsymbol{v} \right) \right] \approx \left(\boldsymbol{v}_{\mathrm{des},i} - \boldsymbol{v} \right)^2 + \alpha_i \mathcal{A}v_i \left(\boldsymbol{v} \right). \tag{5.10}$$

Here, we introduced $\alpha_i := \left(\partial \mathcal{C}_i / \partial \mathcal{A}v_i \right)_{\mathcal{A}v_i = 0}$, which is non-negative because pedestrians avoid collisions. Complemented with a relaxation process we recover the proposed $\mathcal{A}v$-model.

It is worth underlining, that this expansion is an expansion in $\mathcal{A}v_i$ and thus irrespective on the precise dependence of $\mathcal{A}v_i$ on the TTC. For instance, there is no obvious reason why the exponent in the definition of $\mathcal{A}v_i$ should be unity in which case the $\mathcal{A}v$-model shares the same dependence on the TTC as the RVO model [125]. However, setting it to two aligns more closely with the empirical analysis presented in [82]. Qualitatively, $\mathcal{A}v$-models derived with different exponents will exhibit similar behavior, but the extent to which agents anticipate collisions and deviate from their straight paths will differ.

5.1.4   The $\mathcal{I}n$-model

Now, we assume $\mathcal{I}n_i \neq 0$ while $\mathcal{A}v_i = 0$, for example in a moderately dense, static crowd as in the *Waiting* scenario. In this case, Eq. (5.6) simplifies to,

$$\mathcal{C}_i \left[\boldsymbol{v}, \mathcal{I}n_i \left(\boldsymbol{r} \right) \right] \approx \left(\boldsymbol{v}_{\mathrm{des},i} - \boldsymbol{v} \right)^2 + \tilde{\beta}_i \mathcal{I}n_i \left(\boldsymbol{r} \right), \tag{5.11}$$

where $\tilde{\beta}_i := \left(\partial \mathcal{C}_i / \partial \mathcal{I}n_i \right)_{\mathcal{I}n_i = 0}$. This function is extremal for $\boldsymbol{v} = \boldsymbol{v}_i^\star$, which implies that

$$\boldsymbol{0} = \nabla_{\boldsymbol{v}} \left(\boldsymbol{v}_{\mathrm{des},i} - \boldsymbol{v} \right)^2 \big|_{\boldsymbol{v} = \boldsymbol{v}_i^\star} + \tilde{\beta}_i \, \nabla_{\boldsymbol{v}} \mathcal{I}n_i \left(\boldsymbol{r} \right) \big|_{\boldsymbol{r} = \boldsymbol{r}_i(t) + \boldsymbol{v}_i^\star \delta t}. \tag{5.12}$$

Therefore, by substitution,

$$\boldsymbol{0} = -2 \left(\boldsymbol{v}_{\mathrm{des},i} - \boldsymbol{v}_i^\star \right) + \beta_i \delta t \, \nabla_{\boldsymbol{r}} \mathcal{I}n_i \left(\boldsymbol{r} \right) \big|_{\boldsymbol{r} = \boldsymbol{r}_i(t) + \boldsymbol{v}_i^\star \delta t}, \tag{5.13}$$

where $\nabla_r = \left(\partial / \partial x, \partial / \partial y \right)$, if $\boldsymbol{r} = (x, y)$. For sufficiently small δt, one can assume $\boldsymbol{r} \approx \boldsymbol{r}_i(t)$ and subsequently obtain

$$\boldsymbol{v}_i^\star = \boldsymbol{v}_{\mathrm{des},i} - \beta_i \, \nabla_r \mathcal{I}n_i \left(\boldsymbol{r}_i(t) \right), \tag{5.14}$$

where $\beta_i := \tilde{\beta}_i \delta t / 2$. Combined with a relaxation time-scale, Eq. (5.14) is the proposed $\mathcal{I}n$-model.

To improve our understanding of the $\mathcal{I}n$-model, let us rewrite Eq. (5.14) by inserting the definition of $\mathcal{I}n_i$ and the relaxation time-scale explicitly

$$\boldsymbol{a}_i = \frac{\boldsymbol{v}_{\text{des},i} - \boldsymbol{v}_i}{\tau_R} - A_i \sum_{j \in \mathcal{N}_i} \left(\frac{1}{r_{ij} - \ell}\right)^3 \boldsymbol{e}_{ij}, \tag{5.15}$$

where $A_i = \beta_i (r_{\text{soc}} - \ell)^2 / 2\tau_R$ and $\boldsymbol{e}_{ij}$ the vector pointing from i to j. Now it is easy to see that Eq. (5.15) resembles a simple algebraic force model. As discussed above, for the $\mathcal{A}v$-model, a different choice for the exact definition of $\mathcal{I}n_i$ would lead to a slightly different distance based model. For example in the case of an exponential in the definition of the $\mathcal{I}n$-number the simplest Social-Force model would be recovered. Besides, Eq. (5.11) could also be used directly and, on the other hand, one might also obtain a gradient-based $\mathcal{A}v$-model by a similar procedure as specified here.

5.1.5 The $\mathcal{A}v \star \mathcal{I}n$-model

Let us now turn to the general case $\mathcal{A}v_i \neq 0$ and $\mathcal{I}n_i \neq 0$. Combining the expansions of Eqs. (5.10) and (5.11), and expressing the extremal condition for $\boldsymbol{v}_i^\star$ in Eq. (5.5), we arrive at

$$\mathcal{C}_i\left[\boldsymbol{v}, \mathcal{I}n_i\left(\boldsymbol{r}\right), \mathcal{A}v_i\left(\boldsymbol{v}\right)\right] = \underbrace{(\boldsymbol{v}_{\text{des},i} - \boldsymbol{v})^2 + \tilde{\beta}_i\,\mathcal{I}n_i\left(\boldsymbol{r}\right)}_{\mathcal{C}_i^{(\mathcal{I}n)}} + \alpha_i\,\mathcal{A}v_i\left(\boldsymbol{v}\right). \tag{5.16}$$

Given that $\mathcal{A}v_i \neq 0$, the solution $\boldsymbol{v}_i^{(\mathcal{I}n)} := \boldsymbol{v}_{\text{des},i} - \beta_i\,\nabla_{\boldsymbol{r}}\mathcal{I}n_i\left(\boldsymbol{r}_i(t)\right)$ minimizes $\mathcal{C}_i^{(\mathcal{I}n)}$ (or, in other words, the $\mathcal{I}n$-model), to leading order, $\mathcal{C}_i^{(\mathcal{I}n)}$ is well approximated by the parabola

$$\mathcal{C}_i^{(\mathcal{I}n)} \approx \left[\boldsymbol{v}_{\text{des},i} - \beta_i\,\nabla_{\boldsymbol{r}}\mathcal{I}n_i\left(\boldsymbol{r}_i(t)\right) - \boldsymbol{v}\right]^2. \tag{5.17}$$

It follows that

$$C_i\left[\boldsymbol{v}, \mathcal{I}n_i\left(\boldsymbol{r}\right), \mathcal{A}v_i\left(\boldsymbol{v}\right)\right] \approx \left[\boldsymbol{v}_{\text{des},i} - \beta_i\,\nabla_{\boldsymbol{r}}\mathcal{I}n_i\left(\boldsymbol{r}_i(t)\right) - \boldsymbol{v}\right]^2 + \alpha_i\,\mathcal{A}v_i\left(\boldsymbol{v}\right), \tag{5.18}$$

which is the cost function of the $\mathcal{A}v \star \mathcal{I}n$-model.

This corresponds to applying the $\mathcal{I}n$-model first and then inserting the result as the optimization goal into the $\mathcal{A}v$-model in each time-step.

5.1.6 Implementation

The $\mathcal{A}v$, $\mathcal{I}n$, and $\mathcal{A}v \star \mathcal{I}n$-models have been implemented in *Julia*[1]. The corresponding code is available at [180].

A simple first-order Euler scheme with an explicit time-step ($\delta t = 0.01$s) was used to solve the differential equations. The optimization problem was solved by a random sampling algorithm, taking 3000 samples each time-step. If not specified differently, we used uniform and constant model parameters: $\alpha = 1.5\,\mathrm{m^2/s^2}$, $\beta = 0.02\,\mathrm{m^2/s}$, $v_\mathrm{des} = 1.4\,\mathrm{m/s}$, and $\tau_R = 0.1\,$s. Speeds were capped at $v_\mathrm{max} = 1.7\,\mathrm{m/s}$. Agents are modeled as hard disks of diameter $\ell_\mathrm{min} = 0.2\,$m. Nevertheless, to account for the fact that people shun collisions not only between their hard cores, but also between their private spaces, the diameter was increased to $\ell_\mathrm{soc} = 0.4\,$m for the computation of $\mathcal{A}v_i$. Also note that a small scalar $\varepsilon > 0$ is subtracted from $\mathcal{I}n_{ij}$ in Eq. (4.2) to make $\mathcal{I}n_i$ continuous across the cut-off distance.

In some scenarios, walls and obstacles exist. These have been implemented as numerous small ($\ell = 0.1$m) circular, nonmotile 'agents' where it is not distinguished between a social-size and an incompressible size. Furthermore, the value of β is reduced ($\beta_\mathrm{Geometry} = 0.002$m^2/s), which is related to the fact that numerous small obstacles, combined with superposition of intrusive interactions, can lead to excessive repulsion of the geometry. Apart from that obstacles are treated equivalently as actual agents. This has the advantage that no additional interactions need to be introduced.

Let us now test this perturbative expansion in the different regimes which have been delineated in the previous chapter. The dynamics of all scenarios are shown in the supplemental video, which has also been uploaded at https://youtu.be/E8NvgRLPvLg.

5.2 Waiting Scenario

Let us start testing our models. Probably the simplest regime (apart from the non-interacting case) is a regime of low $\mathcal{A}v$ and moderate $\mathcal{I}n$-number. To find a suitable scenario, let us recall the 'phase' diagram introduced in the previous chapter: in Fig. 5.1 we see that the waiting scenario is conspicuous of this regime. It will therefore serve as an exemplary case in the following. According to the perturbative expansion, we expect the $\mathcal{I}n$-model as well as the $\mathcal{A}v \star \mathcal{I}n$-model to describe the scenario reasonably well. The $\mathcal{A}v$-model, on the other hand, should not be applicable to the regime under study.
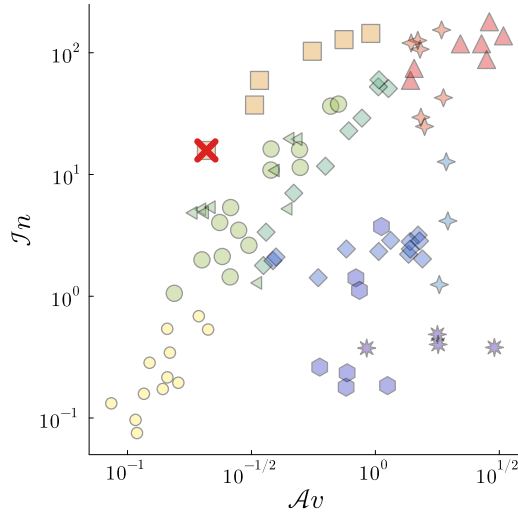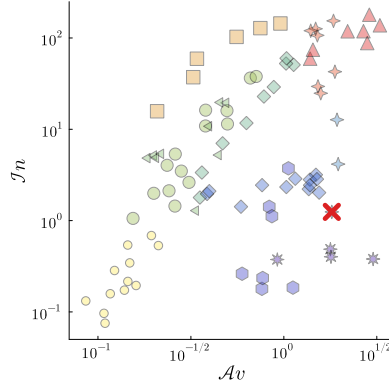
---

[1] https://julialang.org/

FIGURE 5.1: Location of the Waiting scenario in the 'phase' diagram. The experimental run analyzed in this section is highlighted by a red cross.

The experiment begins as soon as the crowd enters the rectangular measurement area through four door-ways. After some time, the crowd seems to reach a steady-state in which the available space is more or less evenly occupied, as depicted in the exemplary snapshot in Fig. 5.2 *(a)*. We will focus on this static part of the experiment. In the simulations, in order to avoid the complex inflow process, we initially assign random positions to the agents within the rectangle, set $\boldsymbol{v}_{\text{des},i} = \boldsymbol{0}$, and let the system equilibrate.

In the $\mathcal{I}n$-model, the agents make use of the available space to keep social distances to each other. Similarly to the experiments, the crowd self-organizes into a spatially homogeneous state, cf. Fig. 5.2 *(b)*. This is reflected in comparable averaged $\mathcal{I}n$ numbers: $\mathcal{I}n = 16$ for the experiments vs. 14 with the $\mathcal{I}n$-model. The $\mathcal{I}n$-model can reproduce the basic features of the scenario. Consequently, in Fig. 5.1 the waiting scenario simulated by the $\mathcal{I}n$-model would be located at almost the same position as the actual experiment. The central role of $\mathcal{I}n$ is also readily understood in the case of a waiting line, where people halt to preserve each other's personal space.

By contrast, the $\mathcal{A}v$-model fails to capture these features: the system remains frozen in its initial state as no collision is expected. An example is shown in Fig. 5.2 *(c)* where the agents are very densely packed in one part of the system, whereas the rest of the space is left completely empty. In this model there is no mechanism which makes the agents avoid each others personal or private space. Accordingly, the averaged $\mathcal{I}n$ number would

(a) Experiment   **(b)** $\mathcal{I}n$-model   **(c)** $\mathcal{A}v$-model   **(d)** $\mathcal{A}v \star \mathcal{I}n$-model
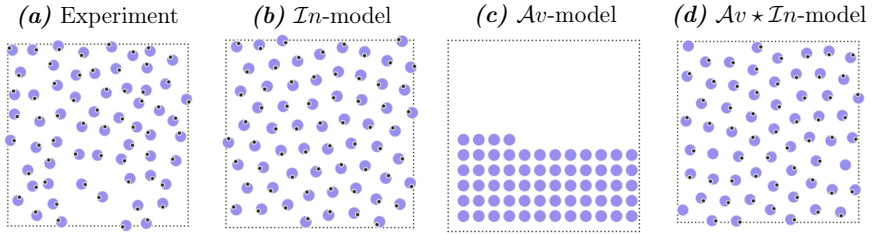
FIGURE 5.2: Snapshots of the waiting scenario.

be way higher than the one observed in the experiments and the position of the waiting scenario in the $(\mathcal{A}v, \mathcal{I}n)$-plane would be strongly altered.

In Fig. 5.2 *(d)*, a snapshot of the waiting scenario simulated by $\mathcal{A}v \star \mathcal{I}n$-model is shown. As expected there is no substantial difference between the results of the $\mathcal{I}n$-model and the $\mathcal{A}v \star \mathcal{I}n$-model.

Of course, in the experiment the spatial homogenization is less perfect than in the $\mathcal{I}n$-model (or the $\mathcal{A}v \star \mathcal{I}n$-model) which is reflected in the larger $\mathcal{I}n$-number found for the former. This could be related to multiple, more complex ('second-order') effects. People not only shun intrusions into the personal space but also extrusions out of the personal space can arouse discomfort [107]. Specifically people that want to talk to each other prefer to stay close to each other, as it can be spotted in the videos. Furthermore, it has been observed that minor violations of the personal space do not trigger a compensation in terms of adjusting the position [107] - such a mechanism is lacking in our model where it would translate into something similar as a slow-to-start rule which is often included into models for vehicular traffic [29]. Note that we have neglected the boundary of the experiment as pedestrians prefer to stay there because they can lean onto the crowd-control barrier. Similar preferential areas are known to lead to strongly pronounced inhomogeneities in the distribution of the crowd over the available space [181].

In summary, we have shown that the $\mathcal{I}n$-model can describe the basic features of the waiting scenario whereas the $\mathcal{A}v$-model fails to do so. These observations align with the perturbative expansion by means of which we derived the models. Let us now turn to the 'opposite' regime by departing from the origin along the $\mathcal{A}v$-axis instead of the $\mathcal{I}n$-axis.

5.3 Cross Flow

So let us return to the 'phase' diagram in Fig. 5.3. The sparse *CrossFlow* seems to be suited best to test our models in the regime of low $\mathcal{I}n$-number and non-zero $\mathcal{A}v$-number because in contrast to the *Outdoor* scenario the boundary conditions are much

FIGURE 5.3: Location of the Cross scenario in the 'phase' diagram. The experimental run analyzed in this section is highlighted by a red cross.

less complicated and in contrast to the *Antipodal* scenario we can analyze a 'steady-state' instead of only the beginning of an experiment, cf. Section 4.2.1.2.

This time, the basic features of the sparse *CrossFlow*, notably successful collision avoidance, are well replicated by the $\mathcal{A}v$-model. The agents approach the centre of the crossing from all four entrances and often face a collision conflict in the centre. Due to the anticipative nature the agents in the $\mathcal{A}v$-model successfully avoid each other and continue to walk towards their goal. This is testified by similar values of the dimensionless numbers if compared to the experiments, i.e. $\mathcal{A}v = 1.8$ and $\mathcal{I}n = 1.2$ for the experiment and $\mathcal{A}v = 1.1$ and $\mathcal{I}n = 2.9$ in the $\mathcal{A}v$-model.

In contrast to this, in the $\mathcal{I}n$-model the agents bump into each other. They are unable to maintain reasonable spacings (in TTC or in real space) to each other. This is reflected in the values of the dimensionless numbers which do not match the experimental results, i.e. $\mathcal{A}v = 1.8$ and $\mathcal{I}n = 1.2$ for the experiment and $\mathcal{A}v = 1.1$ and $\mathcal{I}n = 5.3$ in the $\mathcal{I}n$-model.

As expected, the results of the $\mathcal{A}v \star \mathcal{I}n$-model are similar to those of the $\mathcal{A}v$-model in this case, i.e. $\mathcal{A}v = 1.0$ and $\mathcal{I}n = 2.2$. From the viewpoint of the perturbative analysis it is reasonable that the $\mathcal{A}v \star \mathcal{I}n$-model slightly outperforms the model solely based on the $\mathcal{A}v$-number as the $\mathcal{I}n$-number of this scenario is low but not strictly zero.

As we will discuss below in more detail the mismatch between the model and the experiment can partly be traced back to the fact that only hard-core collisions are included in our model - to which an alternative has been proposed in [182]. Apart from that there seems to be a tendency to underestimate the Avoidance number in simulations which
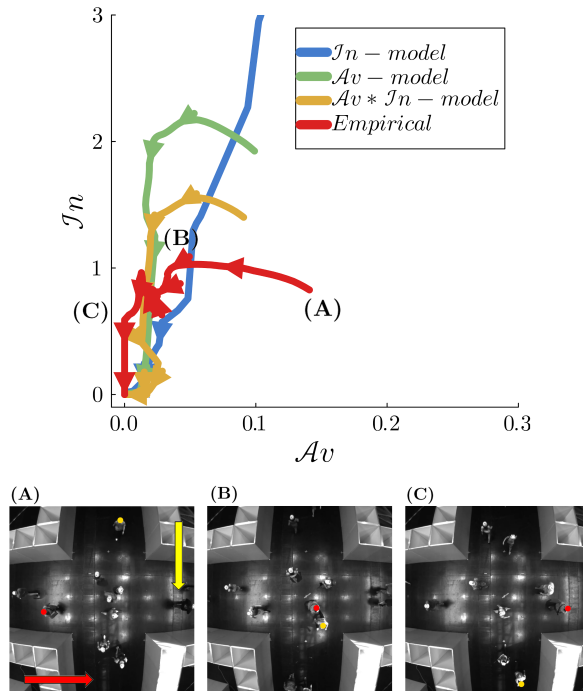
FIGURE 5.4: Phase space trajectory for the sparse CrossFlow. The arrows in the $\mathcal{I}n - \mathcal{A}v$ plot are spaced by 1s. In the simulation the temporal values of $\mathcal{A}v$ and $\mathcal{I}n$ are averaged over multiple realizations with random initial conditions. Exemplary snapshots of the sparse CrossFlow scenario are shown below.

could be related to the strong influence of the swaying of the participants' heads on the empirical Avoidance number as discussed already in section 4.2.1.4.

Finally, we can also look a bit closer at the sparse CrossFlow, namely the temporal evolution of the experiment as it is experienced by each agent. Agent i enters the scene at $t_{0,i}$, we denote the individual time-series of the avoidance and intrusion variable by $\mathcal{A}v_i(t)$ and $\mathcal{I}n_i(t)$. Subsequently, to obtain an averaged 'individual' time-series as

$$\langle \mathcal{A}v_i \rangle(t) = \frac{1}{N(t)} \sum_{i=1}^{N} \mathcal{A}v_i(t - t_{0,i}), \tag{5.19}$$

and analogously for $\langle \mathcal{I}n_i \rangle(t)$ and vary t from 0 to the mean time an agent spends in the scene. The corresponding time-evolution of $\mathcal{A}v$ and $\mathcal{I}n$ is shown in Fig. 5.4.

The pedestrian enters the scene in **A**, where she is well separated from others and accordingly the value of $\mathcal{I}n$ is relatively low. As other pedestrians are also approaching the centre of the crossing the value of $\mathcal{A}v$ on the other hand is maximal. In **B**, the two
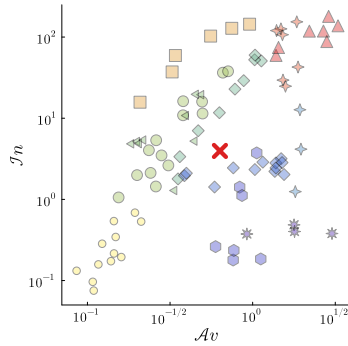
FIGURE 5.5: Location of the Bidirectional scenario in the 'phase' diagram. The red cross denotes the averaged value of the similar experimental runs analyzed in this section. The deviation from between the cross and the blue roms stems from the fact that the former is averaged over the whole run wheras the latter over the part before lanes have formed.

pedestrians have solved the anticipated collision already which results in a low $\mathcal{A}v$ number. Now, however, they are proxemically close to each other and accordingly $\mathcal{I}n$ reaches its maximum. Finally in **C**, the two agents have passed each other and both $\mathcal{I}n$ and $\mathcal{A}v$ are low, the pedestrians can freely approach their goal. The picture discussed above for the averaged value of $\mathcal{A}v$ and $\mathcal{I}n$ is confirmed here: the $\mathcal{I}n$-model fails to capture the observed behaviour. The $\mathcal{A}v$-model and the $\mathcal{A}v \star \mathcal{I}n$-model qualitatively reproduce the empirical curve where the latter is slightly closer to the observed trajectory in the $(\mathcal{A}v, \mathcal{I}n)$-plane.

Let us wrap up: the perturbative expansion works as expected in the asymptotic regimes, in both along the $\mathcal{I}n$-axis as well as along the $\mathcal{A}v$ axis. In these asymptotic regimes the $\mathcal{A}v \star \mathcal{I}n$-model has not been 'needed'. However, the deficiency of models premised solely on $\mathcal{I}n$ or $\mathcal{A}v$ becomes manifest in scenarios which are not confined to the vicinity of the axes of the $(\mathcal{A}v, \mathcal{I}n)$ plane. An example of which will be discussed next.

5.4 Bidirectional Flow

Let us therefore pay attention to the temporal evolution of a bidirectional flow for which the average value of $\mathcal{A}v$ and $\mathcal{I}n$ is located right in the centre of our 'phase' diagram in Fig. 5.5.
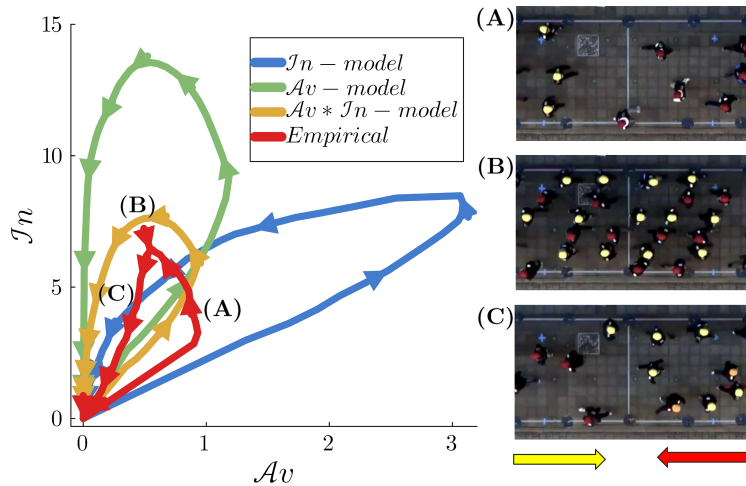
FIGURE 5.6: Phase space trajectory during and after the formation of lanes using empirical results [18] and simulations of the proposed models. The arrows in the $\mathcal{I}n-\mathcal{A}v$ plot are spaced by 2.5 s. The temporal values of $\mathcal{A}v$ and $\mathcal{I}n$ are averaged over multiple realizations of the experiment as well as the simulations, with random initial conditions.

We will focus on the temporal evolution of the $\mathcal{A}v$ and $\mathcal{I}n$ number to calculate a phase space trajectory. In contrast to the procedure specified above, we average over pedestrians ($\mathcal{A}v(t) = 1/N(t)\sum_i \mathcal{A}v_i(t)$, and analogously for $\mathcal{I}n$) and over multiple similar realizations. For input we will use the experimental data of [18].

The process of lane formation and then disappearance of the lanes after the two groups have passed each other entails a loop in the phase space, as represented in Fig. 5.6. Shortly after pedestrians enter the measurement area, in **A**, the limited space for each crowd leads to moderate values of $\mathcal{I}n$, but $\mathcal{A}v$ gets relatively high as the groups are walking towards each other. In **B**, they have formed lanes which reduces $\mathcal{A}v$. The intrusion $\mathcal{I}n$, on the other hand, is large because the limited space is now occupied by both groups. Finally, in **C**, the crowds have passed each other (low $\mathcal{A}v$) and the pedestrians make use of the available space by dissolving the lanes (moderate $\mathcal{I}n$), marking a return to the origin.

Even though all models reproduce the formation of lanes, only the $\mathcal{A}v \star \mathcal{I}n$-model produces a loop comparable to the empirical one. In the $\mathcal{I}n$-model the agents can not anticipate the impending collisions and start interacting just before bumping into each other which leads to high $\mathcal{A}v$ numbers or stated differently small distances in TTC-space. This anticipative behaviour is well captured by the $\mathcal{A}v$-model which, accordingly, reproduces the $\mathcal{A}v$-number much closer. It, however, fails to ensure sufficient space between
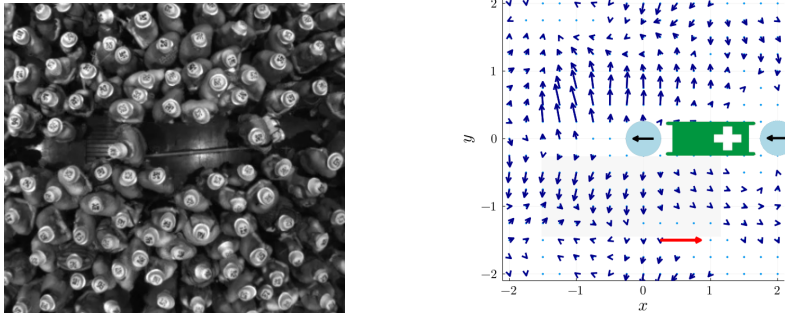
FIGURE 5.7: On the left, a snapshots from the Jülich experiment where two assistants dressed up as paramedics cross a static crowd. On the right, the displacement field of the surrounding pedestrians for a run at lower density.

people when lanes have formed, leading to very high $\mathcal{I}n$ values. Moreover, the lanes do not dissolve even after the two groups have passed each other!

Let us now turn towards another scenario that is located even further away from the origin of the 'phase' diagram, namely the intruder scenario. We will study it in greater detail as it will allow both a further understanding of the fundamental differences between the $\mathcal{A}v$ and the $\mathcal{I}n$-model and it will point to limitations of the approach put forward here.

5.5 The Intruder Scenario

The intruder experiment originates in the study of granular materials, where an object (the intruder), is injected into a granular medium to study its response to this perturbation [183]. It has been introduced to the study of pedestrians too, where it refers to a static crowd, like in the *Waiting* scenario, which is additionally transversed by an intruder [79]. The intruder might be another pedestrian, paramedics as in the snapshot in Fig. 5.7, an ambulance [184], or as in the laboratory setting studied here, a circular obstacle that is moved through the crowd [79].

While the static crowd all alone is located in a regime of low $\mathcal{A}v$-number, the traversing intruder leads to anticipated collisions and consequently a strongly increased $\mathcal{A}v$ number. The data obtained in [79], in the dense condition, are therefore located almost in the top-right corner of the 'phase' diagram in Fig. 5.8.

Let us start by quickly summarizing the main results obtained by [79] which elucidated differences and similarities between crowds and granular matter. Then we will apply the perturbative models to this scenario. We will see that the $\mathcal{I}n$-based interaction
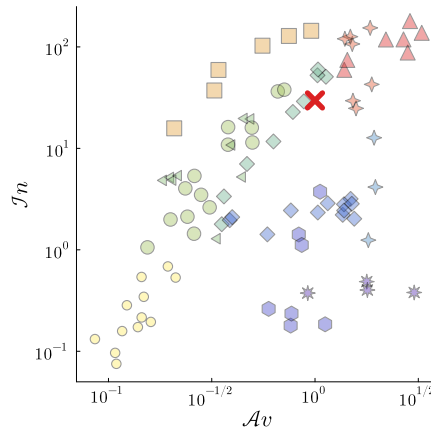
FIGURE 5.8: Relative position of the Intruder scenario in the 'phase' diagram.

resembles a passive granular behaviour wheras $\mathcal{A}v$-based interaction - at least in some conditions - is able to explain the anticipative nature of human interactions which were experimentally found here. Besides, the intruder scenario confirms the importance of anticipation in regimes far away from the origin of our 'phase' diagram. But it also points to more complex types of anticipation encountered in crowds than those captured by the $\mathcal{A}v$-number so far.

5.5.1 Empirical Results

The main results from the intruder scenario are shown in Fig. 5.9. In the top row we see the density profiles and in the bottom row we see the corresponding displacement fields for different experimental conditions. The fields were averaged over time and over multiple experimental runs. We are operating in the intruder's frame of reference regarding the positions, i.e. the intruder is always placed at the origin represented by a blue disc. The densities are calculated with Voronoi diagrams [40]. The velocities are calculated in the laboratory frame of reference as the distance travelled over time. Subsequently the displacement field has been obtained by smoothing over truncated Gaussian kernels. For a more detailed description of the methods refer to [79].

In the leftmost column, Fig. 5.9 *(a)* and **(d)**, all participants face the intruder. In the density-field, we see a depleted area in front and in the back of the intruder. At each side of the intruder, 'wings' of increased density emerge. This matches with the transversal arrows in front of the intruder in the displacement field. The participants are aware of the approaching intruder, anticipate an impending collision, and, accordingly, step to the side to avoid the collision. In the back of the intruder the arrows point towards
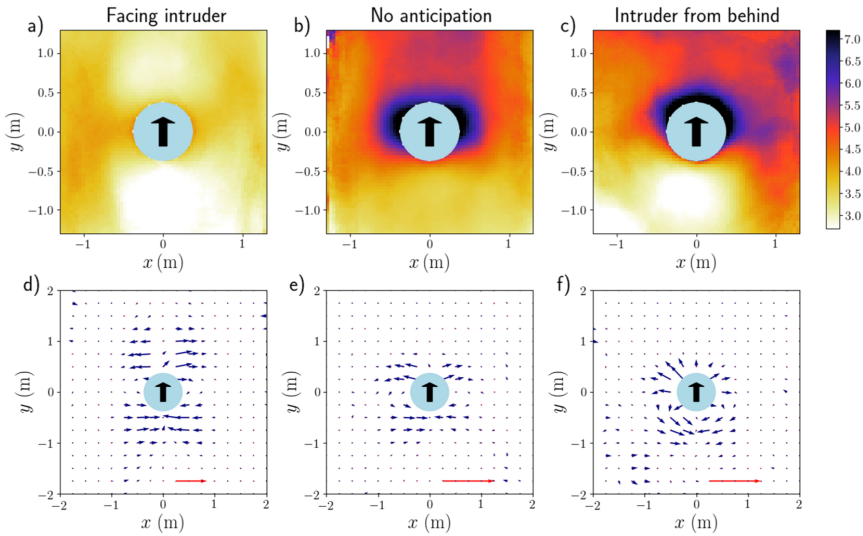
FIGURE 5.9: Empirical results for the intruder experiment for the dense condition where $\rho \approx 3/\text{m}^2$. In the top row the density profiles are shown and in the bottom row the displacement fields. Each column corresponds to a different experimental condition. The figure was taken from [79].

the depleted area as people step into the free space the intruder leaves behind. This behaviour is observed for different densities and experimental conditions [79]. It can also be seen in Fig. 5.7, which originates in different experiments and has been observed in the footage of an ambulance crossing a demonstration [184].

In comparison to granular matter, we can observe similarities and differences. Granular matter and crowds are both dissipative, which leads to a quick decay of the intruders' influence: even though the crowd is quite dense the perturbation of the intruder decays quickly. This stands in contrast to a liquid, where perturbations are typically long-ranged. On the other hand, in contrast to granular matter, humans are able to self-propel and to anticipate. They react in advance to the approaching intruder. They can anticipate that the impending conflict is simply solved by stepping to the side. In granular matter, the intruder pushes the medium through mechanical interaction forces which leads to a radial displacement field in front of the intruder Fig. 5.10 [183].

By changing the initial conditions of the experiment, namely the orientation of the participants or the instructions given to them, the authors of [79] were trying to suppress anticipation in the crowd. Instructing the participants 'not to anticipate' led to an increased density in front the intruder. The transversal, anticipative motion is, however, still present in the displacement field, cf. middle column of Fig. 5.9. A more extreme initial
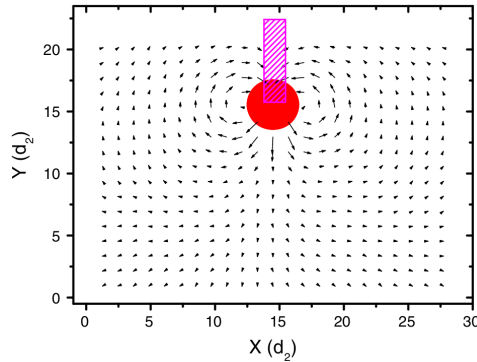
FIGURE 5.10: Empirical displacement field of granular matter around a circular intruder. The figure was taken from [183].

condition in which all participants turn their back to the intruder successfully suppressed the anticipative behaviour: the density in front of the intruder is strongly increased and the displacement field resembles the radial interaction conspicuous of granular matter.

Let us now try to replicate these features in our models. To this end we initially distribute the agents randomly in the system and let the crowd equilibrate for some time. Then an intruder ($\ell_{\min} = 0.6$m, $\ell_{\mathrm{soc}} = 0.8$m) transverses the crowd at velocity 0.4m/s. For the pedestrians, we use the same parameters as reported above (apart from the social radius which we reduce to a more suitable value for larger densities, $r_{\mathrm{soc}} = 0.5$m). We set $\boldsymbol{v}_{\mathrm{des},i} = \boldsymbol{0}$ as in the waiting scenario. While the experiments were specifically focused on high density conditions we will look at sparse systems as well. Because we want to see how the perturbative models break down the further away we move from the origin of our phase diagram. The dynamics of all models for the different conditions of the intruder scenario are shown in the additional supplemental video which has also been uploaded at https://youtu.be/14bzj2gZKlY.

5.5.2   Results of the $\mathcal{I}n$-model

In Fig. 5.11 the results of the $\mathcal{I}n$-model are shown for three different densities. All density profiles show an increased density directly in front of the intruder whereas the area in the back is depleted. The displacement fields show a radial repulsion at all densities in front of the intruder. Furthermore, apart from the lowest density, the agents move into the depleted area in the vicinity of the intruder. As for the lowest density the overall density seems to be so small that the agents do not feel the need to increase their distances to the rest of the crowd and are thus hardly repelled into the (only slightly) depleted area.
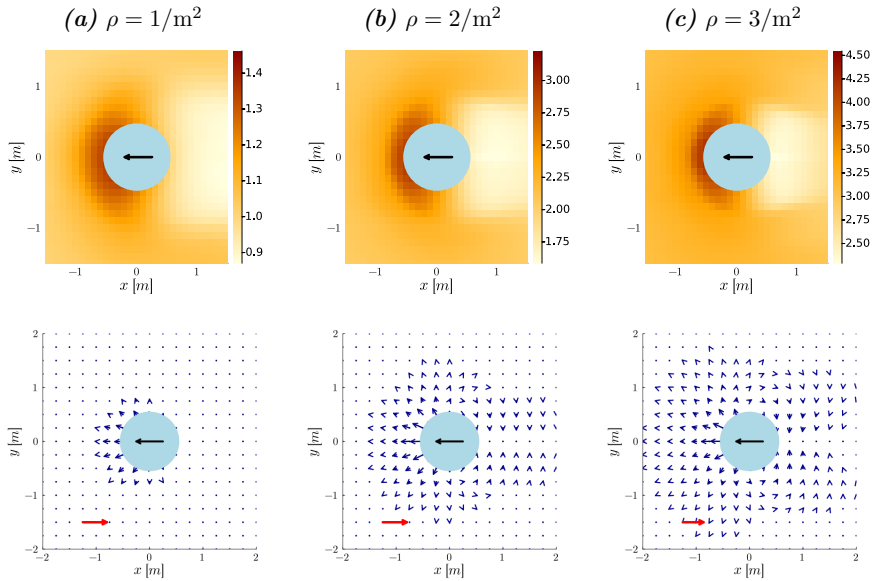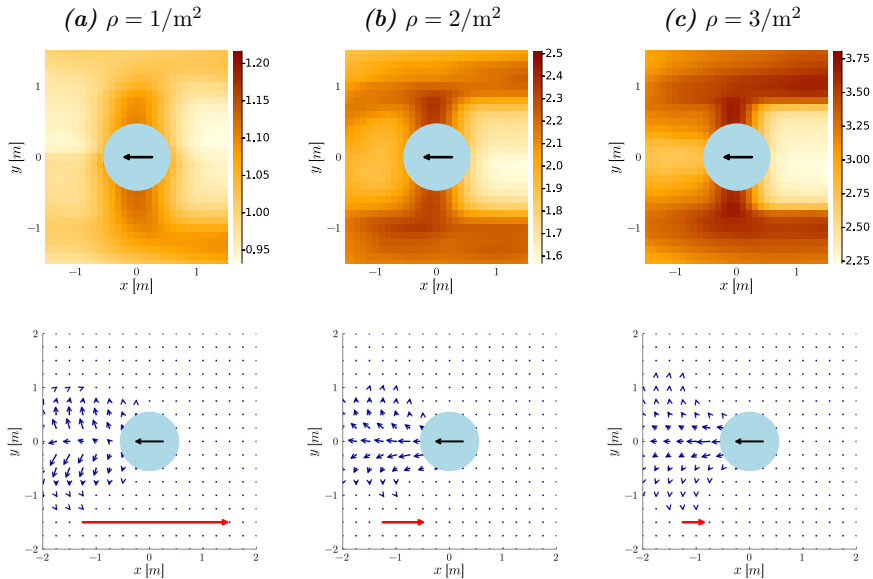
FIGURE 5.11: The density profiles and displacement fields for the $\mathcal{I}n$-model for three different densities. The profiles are obtained by averaging over multiple realizations of the same experiments with randomized initial conditions.

The $\mathcal{I}n$-model quite closely resembles the experimental condition where the participants turn their back to the intruder which was found to be conspicuous of passive granular behaviour. The anticipative nature of human behaviour is however not captured in this model - let us therefore move towards the $\mathcal{A}v$-model.

5.5.3 Results of the $\mathcal{A}v$-model

As we have seen in the simulation of the waiting scenario, the $\mathcal{A}v$ model will not alter the initial distribution. It will not equilibrate into a more or less spatially homogeneous state but remains frozen in the initial condition. To nonetheless allow a study of the intruder scenario, we chose a semi-homogeneous initial condition where agents are randomly placed into the system but if the distance to any other agent is below $1/\sqrt{\rho} - \varepsilon$ a new position is drawn until this condition is met. For $\varepsilon = 0$, this would result in a perfectly homogeneous initial condition. We chose $\varepsilon = 0.2$m for this semi-homogeneous initial condition.

The density profiles and displacement fields for the $\mathcal{A}v$-model are shown in Fig. 5.12. In the density profiles, the area in front and in the back of the intruder is depleted. Characteristic wings emerge on both sides of the intruder. Regarding the density field the experimental findings are matched, at least qualitatively. As for the displacement
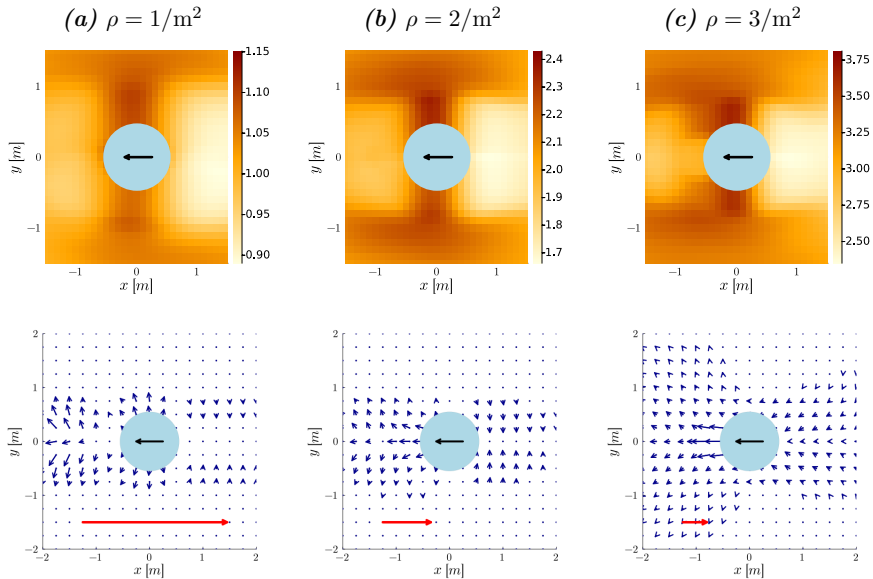
FIGURE 5.12: The density profiles and displacement fields for the $\mathcal{A}v$-model for three different densities. The profiles are obtained by averaging over multiple realizations of the same experiments with randomized initial conditions.

fields, if we look at the lowest density we clearly observe transverse motion, i.e., the agents move to the side to avoid the approaching intruder. Thereby the anticipated collision is dissolved and the agents can come to a halt quickly. At higher densities, however, the behaviour seems to change: the arrows point in the radial direction similar as in the $\mathcal{I}n$-model. The resemblance of the density profiles in the intruder scenario by a TTC (and thus $\mathcal{A}v$-based model) was already reported by [185] where it was found that the model did not capture the transverse motion. The authors, however, did not study the scenario for sparse crowds.

This break down of the anticipative behaviour in terms of the displacement fields can be understood as follows: in principle, the agents want to step to the sides. However, as the scene gets more and more crowded it becomes more difficult for the agents to find a gap they can move into, specifically towards the sides where 'wings' of increased density emerge. In the depleted area in front of the intruder the agents can avoid a collision with the intruder - however only at cost of a constant motion. The agents get 'trapped' and continue to move in the same direction as the intruder. This can be very well seen in the supplemented videos. In reality this is not the case, the pedestrians make room for each other and find gaps to squeeze into.

Let us look at the back of the intruder. Here, no motion is triggered at all and the

FIGURE 5.13: The density profiles and displacement fields for the $\mathcal{A}v \star \mathcal{I}n$-model for three different densities. The profiles are obtained by averaging over multiple realizations of the same experiments with randomized initial conditions.

intruder leaves a totally depleted area behind. Even though the formation of gaps after the transversal of a pedestrian has been reported [186], it is unrealistic at densities between $2/\text{m}^2$ and $3/\text{m}^2$. This is related to the incapability of the $\mathcal{A}v$-model to replicate the waiting scenario, cf. section 5.2: the agents see no reason to move into this depleted area because no collisions are impending. As we have seen above, the behaviour in the back of the intruder is well replicated by the $\mathcal{I}n$-model. Thus, we can follow that it needs both $\mathcal{A}v$ and $\mathcal{I}n$ to replicate the basic features of the intruder scenario, which is of course indicated already by its positioning in the 'phase' diagram. Accordingly, we will study the $\mathcal{A}v \star \mathcal{I}n$-model next.

5.5.4   Results of the $\mathcal{A}v \star \mathcal{I}n$-model

The results of the $\mathcal{A}v \star \mathcal{I}n$-model are shown in Fig. 5.13. Similarly as in the $\mathcal{A}v$-model the density profiles resemble the experimental results well. As for the displacement fields depicted in the row below, we can partially see the expected transversal motion in front and in the back of the intruder. If the density is increased, the transversal behaviour is maintained a little longer than in the $\mathcal{A}v$-model, specifically if we compare the results for $\rho = 2/\text{m}^2$. This behaviour is completely lost for the density $\rho = 3/\text{m}^2$, notably the density for which the described features are strongly pronounced in the experiments.

5.5.5 Conclusions

The distance based $\mathcal{I}n$-related interaction leads to a radial repulsion which is conspicuous of passive granular matter - or pedestrians whose ability to anticipate is strongly hindered. However, this is only relevant for the behaviour in front of the intruder. In the back of the intruder, the empirical behaviour is can be explained by a distance-based intrusive interaction.

The $\mathcal{A}v$-model shows the ability to capture the transversal motion in front of the intruder. This, however, breaks down as soon as the density is becoming larger. While the $\mathcal{A}v\star\mathcal{I}n$-model combines these two essential mechanisms it only pushes the density at which the observed behaviour is lost a bit further to larger densities. At large densities ($\rho = 3/\mathrm{m}^2$) which have been the main focus of the experiments the models can not replicate the findings.

This points to at least two problems in our models. We have approximated the shapes $\mathcal{S}$ with discs which of course is not true for pedestrians. The circular shape makes it much more difficult for the agents to find a suitable gap to squeeze into. More importantly, the TTC and thus the $\mathcal{A}v$ number has been derived under the assumption of constant velocities. It seems that more complex anticipation strategies are needed here. Specifically, the agents in front of the intruder can not anticipate that they will stop after moving to the side - instead they assume constant motion in this direction. This leads to a lot of anticipated collisions which humans rightfully do not take into consideration. Moreover, an actual pedestrian in front of the intruder can anticipate that the others will make room for her as soon as she tries to move to either one of the sides. This is not included in our models. Both of these limitations are related to the assumption of constant velocities.

These more complex types of anticipation have been incorporated into crowds models by game theorazical considerations. This has lead to a successful replication of the intruder scenario [185]. The corresponding model is, however, quite different than most agent-based models, very difficult to solve, and has not yet been applied to less specific scenarios. Another approach originates in the navigation of robots where accelerations can be included in the anticipation [187]. In a similar approach we will try to bridge the gap between operational and tactical level by including a more complex planning in a pedestrian model in Appendix D. These complex anticipation strategies, are crucuial in other scenarios as well, for instance corner flows which are inherently 'non-linear'. Related to the assumption of constant velocities, in all approaches specified above the future costs are taken into consideration in much greater detail as in any of the agent based models typically encountered in pedestrian dynamics. It remains to be seen if

there is another way of including such complex anticipation strategies in the TTC which would allow to keep the corresponding model much simpler.

Nonetheless, we have further identified fundamental differences between the interaction types that arise from the $\mathcal{A}v$ and the $\mathcal{I}n$-number which have both proven to be essential in different regimes of pedestrian motion. Let us therefore now introduce the concept of field-lines to pedestrian dynamics. This will allow us to directly visualize interactions in models in a similar way as one would visualize the field-lines of a magnet. This will prove especially useful in the next chapter where we will study the implications of our results for numerous existing pedestrian models.

5.5.6 Pedestrian Field-Lines

In physics, the repulsion or attraction that, for example, a specifically shaped magnet would have on a test sample, is usually visualized by field-lines. In Fig. 5.14 three exemplary representations of field-lines are shown for an axially magnetized ring-magnet.

The magnetic field can be visualized experimentally for example using iron filings that arrange themselves according to the magnetic field, cf. the left of Fig. 5.14. Note that, even though this is the typical experiment to visualize magnetic fields, the obtained picture is not equivalent to the field-lines because the iron filings themselves have a non-negligible effect on the magnetic field.

Strictly spoken field-lines are, thus, rather mathematical objects. They are derived by integrating a vector field along its direction starting from some set of initial positions. More specifically, after choosing some initial position $\boldsymbol{x}_0$ the next positions are calculated recursively as

$$\boldsymbol{x}_{i+1} = \boldsymbol{x}_i + \frac{\boldsymbol{F}(\boldsymbol{x}_i)}{|\boldsymbol{F}(\boldsymbol{x}_i)|} ds, \tag{5.20}$$

where $\boldsymbol{F}(\boldsymbol{x})$ denotes some vector-field and ds an increment along which we integrate. In the middle of Fig. 5.14, a set of starting positions on the surface of the ring-magnet are chosen which are then integrated until the opposite pole of the magnet is reached.

An alternative representation is shown on right of Fig. 5.14, where a fixed grid of initial positions is chosen and each of these is just integrated once. Figuratively this can be imagined as placing a compass-needle at each initial position. The direction of the needle represents the field-line. The concept of field-lines is not limited to magnets. For example in Fluid Dynamics, stream-lines, i.e. the velocity-field, display the direction and velocity of the flow.
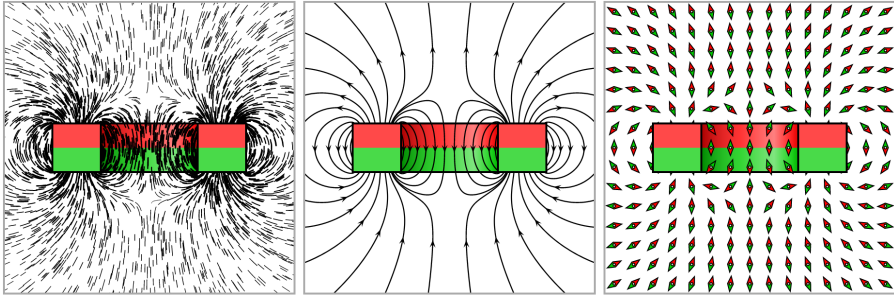
FIGURE 5.14: Three different representations of the field of an axially magnetized ringmagnet (shown in profile). On the left a schematic illustration of an experimentally visualized for example using iron filing on paper. In the middle typical field-lines with initial positions located on the surface of the magnet. On the right a regular grid of initial positions is chosen at which the direction of the field is shown by a compass needle. The picture is taken from Wikipedia Commons.

Let us employ the concept of field-lines to models for pedestrian dynamics. To this end, recall the definition of our model. More specifically, we have defined $\boldsymbol{v}_i^\star$ as the decision of agent i. As we have disregarded any mechanical interactions all interactions are inhibited in this vector field. In the presence of another agent j, $\boldsymbol{v}_i^\star$ depends on the relative position $\Delta\boldsymbol{x}_{ij}$ and on the relative velocity $\Delta\boldsymbol{v}_{ij}$.

In the following, we want to vary the position of agent i relative to agent j. Therefore we will again operate in the reference frame of agent j which corresponds to placing agent j at the origin. Furthermore, we fix the relative velocity as $\Delta\boldsymbol{v}_{ij} = (-1,0)$m/s. The remaining parameters are chosen as in the rest of the chapter. We can now, starting from an initial position $\boldsymbol{x}_0$, calculate the field-lines according to

$$\boldsymbol{x}_{i+1} = \boldsymbol{x}_i + \boldsymbol{v}^\star\left(\boldsymbol{x}_i, \Delta\boldsymbol{v}_{ij}\right)\delta t, \tag{5.21}$$

where we have introduced a small time-step δt.

We choose a regular grid of initial positions and integrate only once at each position. Furthermore, as in the intruder experiment, we choose $\boldsymbol{v}_{\text{des},i} = \boldsymbol{0}$. The results for the three perturbative models are shown in Fig. 5.15.

As one can see for the $\mathcal{I}n$-model in Fig. 5.15 *(a)*, the interaction is a simple isotropic radial interaction force, similar to radial repulsion in many systems in classical physics. The interaction strength in independent of the relative velocity. This indicates why the $\mathcal{I}n$-model leads to a spatial homogenization in the waiting scenario, a reasonable distancing in the bidirectional flow within each lane, and a realistic behaviour in the vicinity of the intruder. On the other hand, if we recall the example of the two joggers approaching each other, it is apparent that this short-ranged interaction is not capable
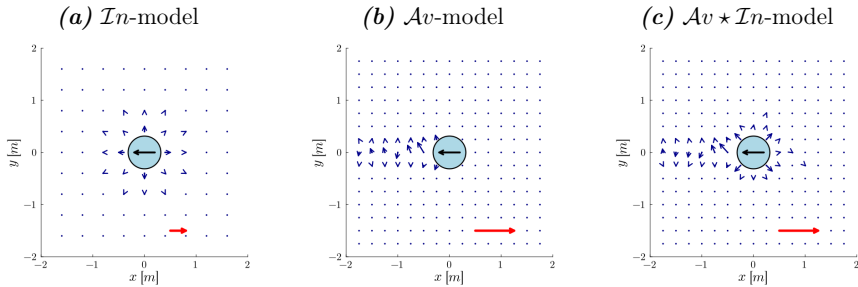
FIGURE 5.15: Field-lines of the perturbative Models with a regular grid of test-positions and $\boldsymbol{v}_{\mathrm{des},i} = \boldsymbol{0}$. The blue arrows correspond to the chosen velocity $\boldsymbol{v}^\star$ and red arrow is a legend representing a velocity of 1.5m/s. In *(b)* and *(c)* a slightly finer grid was chosen.

to describe the long-ranged interaction that would be present in such a case. Besides, if we compare the results to the displacement field obtained above we can already see that the $\mathcal{I}n$-model can not reproduce the transversal movement observed in that case.[2]

In the middle, Fig. 5.15 *(b)*, the field-lines of the $\mathcal{A}v$-model are shown. An interaction is only present if a collision is impending, accordingly most positions have no arrow assigned to them. If we chose $\Delta\boldsymbol{v}_{ij} = \boldsymbol{0}$ the interaction would have been zero everywhere. Similarly no matter how close we chose the test-position to agent j to the sides or the back no interaction is present. This reflects the fact that the $\mathcal{A}v$-model is incapable to maintain realistic Euclidean spacings between agents, e.g., it can not explain the behaviour observed in the back of the intruder. In front of agent j, however, a long-ranged and transversal motion is present. Consequently, the model is able to solve collision conflicts and shows the transversal motion observed in the intruder scenario, at least for sparse settings.

At last, in Fig. 5.15, the field-lines of the $\mathcal{A}v \star \mathcal{I}n$-model are shown. They resemble a superposition of the $\mathcal{I}n$ and the $\mathcal{A}v$-model as it has been defined.

Of course, as for the magnet, we could have chosen another representation of the field-lines. In Fig. 5.16 we have chosen initial positions along the line parallel to the y-axis at $x = -2$m, set $\boldsymbol{v}_{\mathrm{des},i} = (1,0)$m/s and integrated many steps. Here we can see the difficulties of the $\mathcal{I}n$-model to solve the collision conflict. Apart from this we see that in the $\mathcal{A}v$-model only the hard-core repulsion is present which leads to a very close avoidance in which the agents i and j almost touch. On the right, the superposition seems to lead to unrealistic behaviour in terms of another repulsion after the two have already passed.

---

[2]The main difference between the displacement-field and the field-lines is that in the latter no information is included whether an agent would actually end-up at a certain position as we have chosen this grid of initial positions. Furthermore inertia-effects are disregarded in the field-lines.
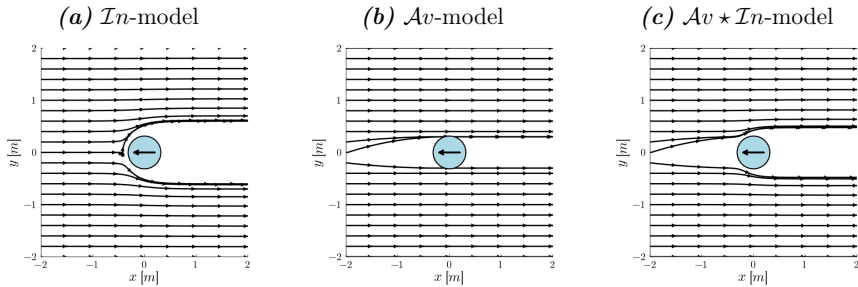
FIGURE 5.16: Alternative representation of the field-lines of the perturbative Models with $\boldsymbol{v}_{\text{des},i} = (1,0)$m/s. The initial positions resemble a line parallel to the y-axis located at $x = -2$m.

In the following chapter we will, however, stick to the former representation as it focuses only on the interaction instead of the desire to move. This allows us to draw some conclusions regarding the applicability of the models in different regimes. Moreover the representation in Fig. 5.16 is slightly misleading as these paths are not actual paths agents would take in the model. Specifically, the interaction would strongly be changed as soon as agent i changes its velocity in the next time-step whereas here we assumed that $\Delta \boldsymbol{v}_{ij}$ remains constant during the procedure specified by Eq. (5.21).

5.6 Summary

In this chapter, we have rationalized the empirical classification of crowds by performing a perturbative analysis. This way we have obtained three models, the $\mathcal{I}n$-model closely related to an algebraic force model, the $\mathcal{A}v$-model related to a velocity obstacle model, and the $\mathcal{A}v \star \mathcal{I}n$-model a combination of both. We have verified that, as expected from the perturbative expansion, the $\mathcal{A}v$-model is applicable in regimes of low $\mathcal{I}n$-number, and the $\mathcal{I}n$-model is applicable in regimes of low $\mathcal{A}v$-number. If we leave the close vicinity of either one of the axis both $\mathcal{A}v$ and $\mathcal{I}n$ are needed to reproduce the basic features. Consequently, only the $\mathcal{A}v \star \mathcal{I}n$-model is applicable here.

To compare the results of our models with the empirical findings we extended the analysis of the previous chapter by studying the temporal evolution of $\mathcal{I}n$ and $\mathcal{A}v$. Similarly to the crosscorrelation between $\mathcal{I}n$ and $\mathcal{A}v$, these phase-space trajectories seem to show a typical shape, where large $\mathcal{A}v$ numbers lead to an increased $\mathcal{I}n$ number at a later time. Investigating these typical trajectories in the $(\mathcal{I}n, \mathcal{A}v)$-plane in more detail or identifying further 'shapes' could deepen our understanding of the different regimes.
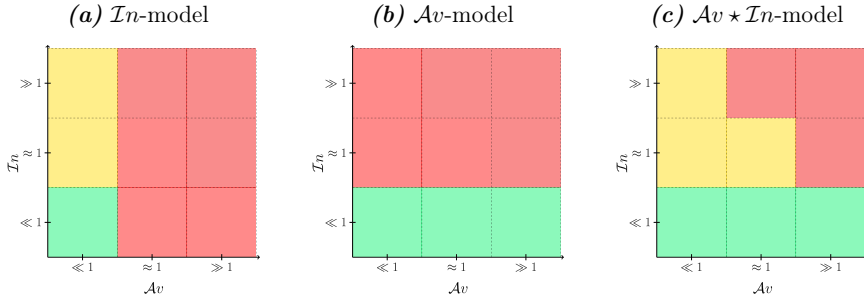
FIGURE 5.17: Range of applicability of the Perturbative models. The three colors indicate whether a the corresponding model can be applied in the regime. Specifically, green means that the model can be applied, yellow means caution is needed if the model is applied, and red means that the model can not be applied in the corresponding regime.

Finally we have studied the intruder scenario at high density which can not be fully replicated by our perturbative models. This appears sensible, given that it is located almost at the top right corner, far away from the origin, of our 'phase' diagram. But it also points to more specific limitations of the $\mathcal{A}v$-number, namely the assumption of constant velocities in the definition of the TTC.

However, at lower densities, the $\mathcal{A}v \star \mathcal{I}n$-model can replicate both essential behaviours observed here: transversal motion in front of the intruder and closing the gap behind the intruder. These behaviours can be identified with two distinct types of interaction, transversal avoidance which originates in the $\mathcal{A}v$-part of the model and an intrusive radial interaction related to the $\mathcal{I}n$-part of the model. In order to visualize these types of interactions, we have introduced field-lines. The field-lines seem to be a good indicator of range of applicability of the models studied here. We can qualitatively guess (or rule out) in which regimes a model is applicable by studying the field-lines instead of implementing and simulating the model in various scenarios, as it was done for the perturbative models in this chapter. This simplicity will prove be very useful when approaching the zoo of pedestrian models in the next chapter.

Finally, to visualize the range of applicability, let us introduce a 'traffic-light' system. For our perturbative models, it is depicted in Fig. 5.17. The three colors indicate whether the corresponding model can be applied in the regime. Specifically, green means that the model can be applied, yellow means caution is needed if the model is applied, and red means that the model can not be applied in the corresponding regime. We have set these colors according to the simulations performed in this chapter. Note that, we have colored the $\mathcal{I}n$-model as yellow in regimes with low $\mathcal{A}v$-number. This is justified by observations from the first chapter, where we found that a force-based model, such as the $\mathcal{I}n$-model, can not replicate the fundamental diagram without any further assumptions.

This incapability to reproduce the fundamental diagram points towards limitation of our work, which will be discussed in the last chapter.

Chapter 6

Classification and Validation of Models

While in the previous chapter the focus was put on the asymptotic $\mathcal{I}n$ and $\mathcal{A}v$-models, the discussion has bearing on the broader category of agent-based models: their equations of motion often hinge on variants of either the $\mathcal{I}n_i$ variable or the $\mathcal{A}v_i$ variable, thereby limiting their range of applicability to the associated regime.

Therefore, in this chapter, we want to extend this discussion to the large zoo of models for pedestrian crowds. Since the first agent-based models for pedestrian crowds have been proposed in the 70s [14], its number has been growing steadily [24–27]. Often modelers realize that an existing model can not be applied to a certain scenario and, thus, propose an new model or a slightly altered extension. This leads to numerous models and extensions or different versions of these. To help sort out this mess, several classifications of pedestrian models exist. These mainly focus on the mathematical properties, for example, continuous vs. discrete models or first vs. second order models [29]. While this is an important step to get some idea of the variety of models and to emphasize their structural differences, it usually contains little information about the ability of the corresponding models to reproduce certain aspects of pedestrian dynamics.

On the other hand, different approaches exist to validate models of pedestrian crowds. These try to gauge whether certain models are better than others, for example, by designing numerous test-cases which generally have to be met [23, 76] or by assigning a general score to each model [77, 78]. While this approach might be helpful for the practical use of pedestrian models in the planning of real scenarios, it fails to capture the context dependency of different models. For example, a certain model that can only describe one specific regime but fails in describing another, might still be a very good model - as long as the modeller is aware of its limited range of applicability. This

is actually almost a platitude which is, however, often forgotten: a complete model definition includes an associated range of applicability.

We propose a scheme which is much more similar to the situation typically encountered in physics. For example in fluid dynamics, certain approximations only exist to describe specific flow regimes. An approximation for laminar flow provides a precise description of (and only of) laminar flow. It is tautological to point out that it fails to capture the behaviour of turbulent flows correctly. The task of a modeller is then to resort to the correct approximation in the different situations. The choice of an approximation is usually guided by dimensionless numbers, such as the Reynolds number. For pedestrian dynamics, such a classification of different flow regimes has been largely missing so far. However, as we showed in the previous chapters, the dimensionless Intrusion number $\mathcal{I}n$ and Avoidance number $\mathcal{A}v$ delineate different flow regimes in pedestrian dynamics. Thus, we can now propose a flow regime based validity of models for pedestrian crowds.

From a practical point of view this allows to pose the question of modeling quite differently. Without such a scheme, one would easily be left with various very specific models, applicable to a certain situation only, or in desperate search of the complete pedestrian model. It might turn out to be much easier to have different models for different regimes to which the modeller can resort to, instead of having the need to combine all different factors correctly.

We will start by reformulating various pedestrian models such that their dependency on the agent-centered intrusion $\mathcal{I}n_i$ or avoidance $\mathcal{A}v_i$ variables is highlighted. For each model, we visualize the interactions by plotting the field-lines, as it was proposed in the previous chapter. This allows to get a more intuitive understanding of the proposed interactions while avoiding to simulate all models in numerous scenarios. Based on this, we estimate the range of applicability using the traffic-light system introduced in the previous chapter. Finally, we will test this intuition by investigating the collective behaviour of the crowd in some models by simulations of test-cases that are representative for different flow regimes.

We will see that, indeed, the intrusion and avoidance variables appear in many pedestrian models. In particular, in some models, like the simple Social-Force model or Velocity Obstacle models, either $\mathcal{I}n_i$ or $\mathcal{A}v_i$ appears directly. We will see that, similarly to the perturbative models proposed in the previous chapter, this clearly limits the range of applicability to certain regimes.

Other models do not include $\mathcal{I}n_i$ or $\mathcal{A}v_i$ in their 'pure' form. These models are often extensions of simpler models and can be understood as endeavours to extend the range of applicability of the original model to another flow regime. As a result, while the extended

model may acquire the capability to describe a different regime, it often does so at the expense of losing its applicability in a regime that is well-captured by the original model. This points to the problem of the correct combinations of the different behaviours. For instance, rather than relying on two independent interactions, one might try to construct a single repulsion that includes various behaviours. This approach, however, swiftly yields complicated 'non-minimal' interactions. This can lead to artifacts when the model is applied to situations slightly different from those the model was tested in.

An extensive testing of all different models in the different regimes would be an unfeasible task. Therefore, we estimate the range of applicability for each model based on the equations of motion and by analyzing the field-lines. Even though we test this for some models by actually simulating the model in different regimes, the range of applicability has to be taken with some caution. Besides, this is not the only aim of this chapter. We also want to follow the evolution of different models and see how the implicit knowledge of different regimes encountered in pedestrian crowds has shaped the development of new models and extensions of these.

6.1   General Form of the Considered Models

Before delving into the broad realms of pedestrian models we have to restrict ourselves to a certain 'structural' class. In particular, we will study models continuous in space, defined either by differential equations or by an iterative map with an explicit time-step. We further neglect all mechanical interactions. The class of models studied here can then be formulated as

$$\boldsymbol{v}_i = \boldsymbol{v}^\star \left(\dots \right), \tag{6.1}$$

for first-order models and

$$\boldsymbol{a}_i = \frac{\boldsymbol{v}^\star \left(\dots \right) - \boldsymbol{v}_i}{\tau_R}, \tag{6.2}$$

for second-order models. In both cases $\boldsymbol{v}^\star$ is a function of various parameters. In particular, $\boldsymbol{v}^\star$ is the result of the decisional layer that includes the goal and the interactions between the agents.[1] These of course vary strongly between the models, it might for example be defined as the result of a minimization process or related to the gradient of a potential.

Mathematically, $\boldsymbol{v}^\star$ is a vector field that assigns to each set of variables a unique vector. While in some models, the form of $\boldsymbol{v}^\star$ is quite intuitive, its interpretation can be very

---

[1]For simplicity we have left aside the complex dependencies of $v^\star$ which without loss of generality would read as $v^\star = v^\star \left(\boldsymbol{x}_1, \dots \boldsymbol{x}_N, \boldsymbol{v}_1, \dots, \boldsymbol{v}_N \right)$.

difficult in others. Therefore, we want to visualize the decisions of agents in different models by plotting $\boldsymbol{v}^\star$.

In particular, we plot the field-lines in the same setting as discussed in Section 5.5.6 where an agent j is placed at the origin.[2] Another agent i is positioned at a fixed grid of test-positions where, in absence of agent j, she would prefer to remain without moving $(\boldsymbol{v}_{\text{des},i} = \boldsymbol{0})$. We assign a relative velocity $\Delta\boldsymbol{v}_{ij} = \boldsymbol{v}_j - \boldsymbol{v}_i$ to the agents which is plotted as a black arrow in the center. Then, we plot the result of the decisional layer $\boldsymbol{v}^\star$ at each test-position. We apply a maximal velocity of $v_{\max} = 2\text{m/s}$ in all models. In the visualization, the size of agent i is 'absorbed' into agent j which basically makes i a point-particle and doubles the size of agent j. If not stated differently, for each model we have used the parameters that are given by the authors of the corresponding citation.

6.2   Social-Force Models

Let us start with the original Social-Force model, in particular, its simplest form, as it was proposed in [60]. The dynamics of agent i can be written as

$$\boldsymbol{a}_i = \frac{\boldsymbol{v}_{\text{des},i} - \boldsymbol{v}_i}{\tau_R} - \alpha \cdot \nabla_r \left[\sum_{j \neq i} f\left(\mathcal{I}n_{ij}\right) \right], \qquad (6.3)$$

where we neglected terms that should account for mechanical interactions as well as an anisotropy which is often used to model effects of limited perception.

Apart from the driving term, Eq. (6.3) only depends on the agent-centered intrusion variable $\mathcal{I}n_{ij}$. The intrusions of various neighbours are added up, analogous to the superposition of Newtonian forces, and weighted by the function $f(x) = \exp\left(-1/\sqrt{x}\right)$. Direction and strength of the interaction are given by the gradient of this potential. Consequently, the repulsion between two pedestrians i and j always acts radial, i.e. along the vector $\boldsymbol{e}_{ij}$ connecting the centers of the two. This can also be seen in Fig. 6.1 *(a)*, where we plotted the field-lines of the Social-Force model. Many models of pedestrian crowds include interactions based only on Euclidean distances. This corresponds to a qualitatively analogous radial interaction.

As we have seen in the last chapter, this radial interaction is conspicuous of passive granular matter and fails to capture anticipative effects, such as moving sideways to avoid an approaching pedestrian. Moreover, the parameter values reported in [60], i.e., $r_{\text{soc}} = 8\text{cm}$, result in a very short-ranged repulsion. To elucidate the limitations of the Social-Force model in regimes with moderate or large $\mathcal{A}v$ number, let us recall the

---

[2]We add a small off-set $\boldsymbol{\varepsilon} = (0.0001, 0.0001)\text{m}$ to avoid perfectly symmetrical situations.
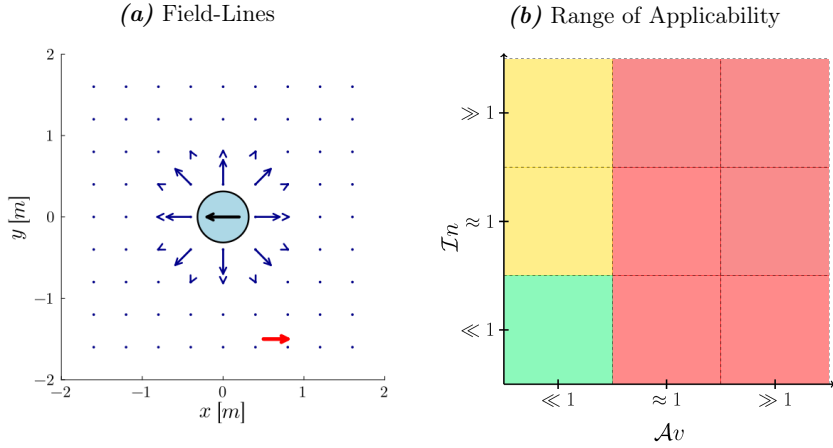
FIGURE 6.1: In *(a)*, the field-lines of the Social-Force model are plotted. Qualitatively the same picture is obtained for the $\mathcal{I}n$-model, the Collision-Free Speed model and the simplest Algebraic-Force models. The red arrow depicts the scale of the velocities and corresponds to 2m/s. In *(b)* the estimated range of applicability of the Social-Force model is plotted.

example of two joggers who approach each other on a collision course. In the Social-Force model, they would start interacting at the length scale r_{soc}, i.e., just before they bump into each other.

Accordingly, the range of applicability of the Social-Force model is limited to flow regimes with negligible $\mathcal{A}v$ numbers, cf. Fig. 6.1 *(b)*. Note that the low $\mathcal{A}v$ regimes are colored yellow as well, which is justified by the difficulties of the Social-Force model in reproducing the uni-directional fundamental diagram [30] and the lack of proper mechanical forces in Eq. (6.3).

These limitations are of course anything but new and numerous extensions or alternative specifications have been proposed. As we will see in the following, these can often be understood as endeavours to extend the range of applicability to regimes of larger Avoidance numbers.

6.2.1 Elliptical Specifications

The original Social-Force model, i.e. Eq. (6.3), is based on a radial repulsion, consequently equipotential lines take on the form of circles. In contrast to this, a specification with elliptical equipotential lines is proposed in [16]. Here, the repulsive interaction does
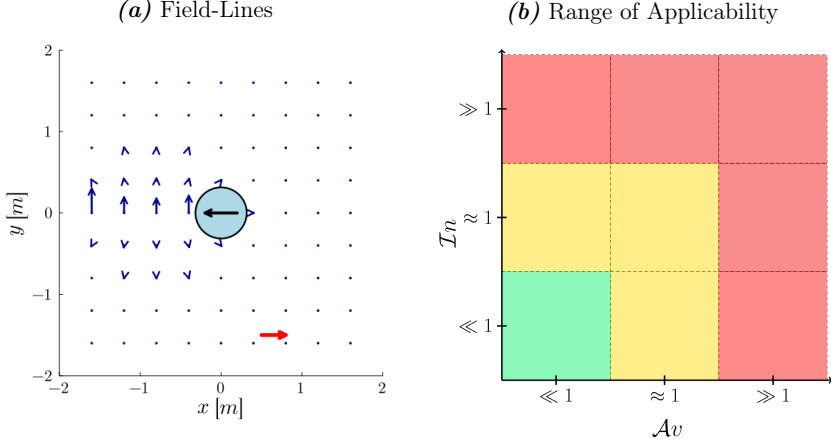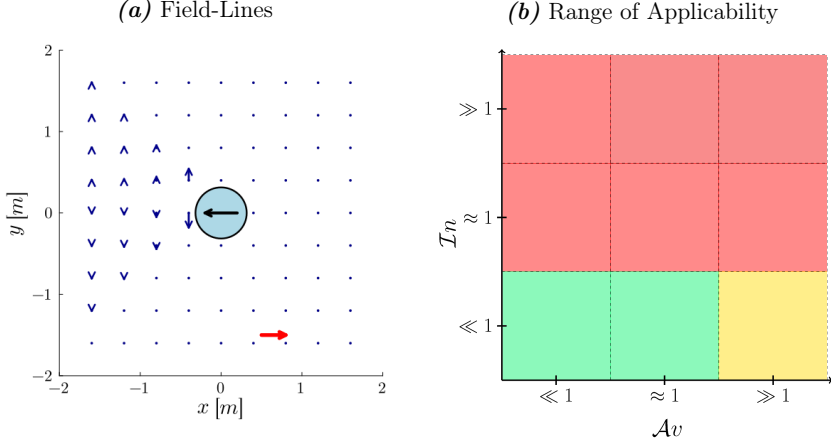
FIGURE 6.2: In **(a)** we show the repulsion in the Social-Force model with the elliptical specification. The red arrow depicts the scale of the velocities and corresponds to 2m/s. In **(b)** the estimated range of applicability of the Social-Force model with elliptical interactions is plotted.

not depend on the Euclidean distance but on an 'effective distance' given by

$$r_{\text{eff},ij} = \frac{1}{2}\sqrt{\left(r_{ij} + |\boldsymbol{r}_{ij} - \boldsymbol{v}_j\tau_A|\right)^2 - \left(\boldsymbol{v}_j\tau_A\right)^2}, \tag{6.4}$$

which is based on the idea that agent i takes into consideration where she is going to step, τ_A representing the duration of one step. Another elliptical specification is introduced in [188]. Here, the effective distance is given by

$$r_{\text{eff},ij} = \frac{1}{2}\sqrt{\left(r_{ij} + |\boldsymbol{r}_{ij} - \Delta\boldsymbol{v}_{ij}\tau_A|\right)^2 - \left(\Delta\boldsymbol{v}_{ij}\tau_A\right)^2}, \tag{6.5}$$

where, in contrast to Eq. (6.4), the relative velocity between i and j is taken into account. Aiming at a translation into the $\mathcal{I}n$ and $\mathcal{A}v$ framework, we are led to define an effective intrusion variable as

$$\mathcal{I}n_{\text{eff},ij} = \left(\frac{r_{\text{soc}}}{r_{\text{eff},ij}}\right)^2. \tag{6.6}$$

The elliptical Social-Force models can then be defined by replacing $\mathcal{I}n_{ij}$ in Eq. (6.3) with this effective intrusion.

In both models, for $\tau_A = 0$ the interaction is radial and the original Social-Force model is recovered. The only difference that remains is that the size of the agents is not taken into account here, i.e. $\ell = 0$. In the following, we will only consider the second variant, i.e. Eq. (6.5), as both are equivalent if we assume that j does not move and therefore $\Delta\boldsymbol{v}_{ij} = \boldsymbol{v}_i$.
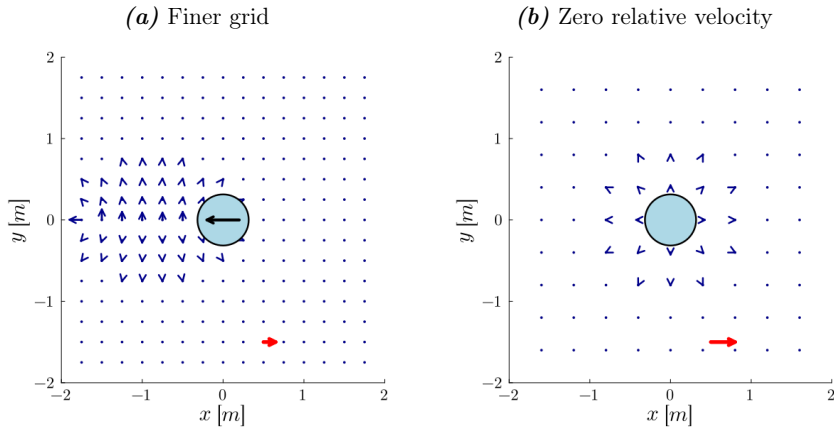
FIGURE 6.3: Repulsion in the elliptical variant of the Social-Force Model for a finer grid of test-positions in *(a)* and for a zero relative velocity in *(b)*. The red arrow depicts the scale of the velocities and corresponds to 2m/s.

In Fig. 6.2 *(a)*, the field-lines of the elliptical Social-Force model are plotted. The typical sideways motion to avoid an approaching pedestrian seems to be captured correctly as well as a more long-ranged interaction. If we look a bit closer, i.e. the finer grid in Fig. 6.3 *(a)*, we see that these specifications still yield a repulsion in the radial direction close to $x = -2$m. Furthermore, the strength of the repulsion, in some cases, seems to increase with the distance which seems unreasonable. In Fig. 6.3 *(b)* a scenario is plotted in which $\Delta \boldsymbol{v}_{ij} = \boldsymbol{0}$ for the same set of parameters. As expected for a situation without any relative velocity ($\mathcal{A}v \ll 1$), the repulsion is radial. In this case, however, even if the agents are almost at contact, the repulsion is very weak which most likely leads to overlaps and related problems.

In the elliptical specifications, attempts are made to address issues present in the original Social-Force model by incorporating anticipation into the repulsive interaction. Accordingly the models might be applicable in regimes of moderate $\mathcal{A}v$ number. In the low-$\mathcal{A}v$ regime, however, the original Social-Force model should outperform the elliptical extension because the corresponding interactions are very weak. This is also related to the fact that the physical size of the agents is neglected. We have chosen the range of applicability accordingly, cf. Fig. 6.2 *(b)*.

Of course, the parameters can be adjusted to yield a reasonable repulsion in regimes of low Avoidance number as well - but only at the cost of loosing the ability to describe regimes of non-zero $\mathcal{A}v$ number. Especially the parameter τ_A is critical for adjusting the level of anticipation in this model. This observation has led to the proposal of the extension discussed next.

FIGURE 6.4: In *(a)* we show the repulsion in the Social-Force model with explicit collision prediction. The red arrow depicts the scale of the velocities and corresponds to 2m/s. In *(b)* the corresponding estimated range of applicability is depicted.

6.2.2 Explicit Collision Prediction

In [189] a variant of the Social-Force model is proposed which includes an explicit collision prediction. Instead of using a fixed anticipation time τ_A as above, the model relies on the time-to-closest-approach (tca) which 'self-gauges' the anticipation time in dependence on the situation. The time-to-closest-approach is the time until the distance between two pedestrians is minimal, under the assumption of constant velocities.

Let us define tca_i as the smallest time-to-closest-approach for agent i over the set of all other agents j. This set is further restricted to agents for which the angle between the relative velocity $\Delta \boldsymbol{v}_{ij}$ and their binding vector $\boldsymbol{e}_{ij}$ is smaller than $\pi/4$. Already note that the interaction detailed below is set to zero if this set is empty. Apart from that, if no agent in this set approaches agent i the interaction is set to zero as well.

The proposed model can now be written as

$$\boldsymbol{a}_i = \frac{\boldsymbol{v}_{\text{des},i} - \boldsymbol{v}_i}{\tau_R} - \alpha \cdot \frac{v_i}{tca_i} \sum_{j \neq i} f\left(\mathcal{I}n_{ij}\right) \cdot \frac{\Delta \boldsymbol{x}_{ij} + tca_i \cdot \Delta \boldsymbol{v}_{ij}}{|\Delta \boldsymbol{x}_{ij} + tca_i \cdot \Delta \boldsymbol{v}_{ij}|}, \tag{6.7}$$

where instead of a radial repulsion along the vector $\boldsymbol{e}_{ij} = \Delta \boldsymbol{x}_{ij}/|\Delta \boldsymbol{x}_{ij}|$ the interaction is based on the anticipated binding vector between i and j at the later time $t + tca_i$ under the assumption of constant velocities. Again, and notably, the size of the pedestrians is chosen as $\ell = 0$.
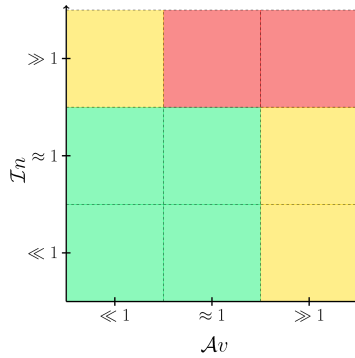
FIGURE 6.5: Possible range of applicability of the Social-Force model with explicit collision prediction and further extensions from [190].

The authors show that the proposed model outperforms the other Social-Force models discussed so far, notably, in a low-density situation, where people go in different directions. This is presumably a regime with $\mathcal{I}n \ll 1$ and $\mathcal{A}v \sim 1$. Concurrently, the repulsion shown in Fig. 6.4 *(a)* seems to describe avoidance processes well. This is not surprising as the time-to-closest approach is linked to the TTC on which the Avoidance number is based. In 'spatially' controlled regimes of non-zero $\mathcal{I}n$ numbers, however, the interaction will be zero most of the times. The model can, therefore, not be applied in these regimes. We have estimated the range of applicability accordingly, cf. Fig. 6.4 *(b)*.

These limitations have been realized by the authors as well. In particular, in [190], the model is applied to moderately dense cross-flows, i.e. a regime with $\mathcal{A}v \gg 1$ and $\mathcal{I}n \sim 1$. Here, the authors show that the model captures the experimental results reasonably well - but only after it has been extended to include, among other things, a short-ranged distance-based interaction. In Fig. 6.5, we have plotted a possible range of applicability. Note that this range of applicability has to be taken with even more caution than those showed so far because the model ends up being quite complicated and contains many parameters. Thus, it is much more difficult to test and might lead to artifacts or new problems in other regimes.

6.2.3   Rotated Forces

In [191] another variant of the Social-Force model is proposed, explicitly for collision avoidance problems. In particular, a tendency of the agents to avoid each other on the left side or on the right side is included by rotating the 'force'.
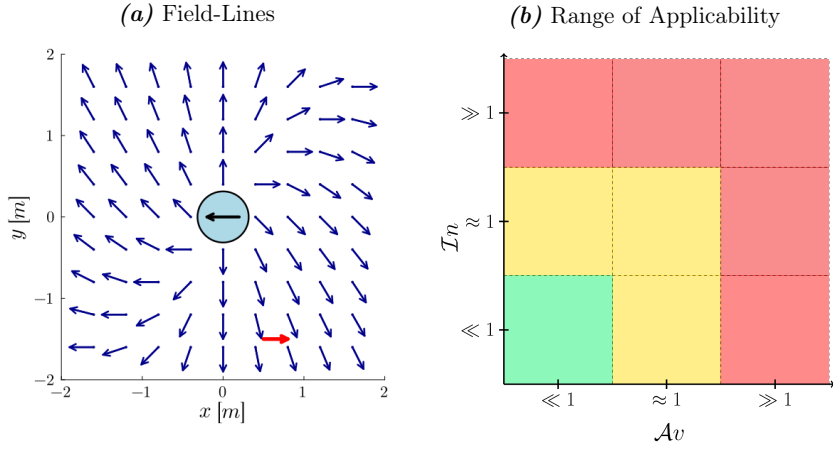
FIGURE 6.6: In *(a)* the field-lines for the Social Force model with a rotated interaction are shown. The red arrow depicts the scale of the velocities and corresponds to 2m/s. In *(b)* the corresponding estimated range of applicability is depicted.

The model can be written as

$$\boldsymbol{a}_i = \frac{\boldsymbol{v}_{\mathrm{des},i} - \boldsymbol{v}_i}{\tau_R} - \alpha \cdot R(\lambda\phi) \cdot \nabla_r \left[\sum_{j \neq i} f\left(\mathcal{I}n_{ij}\right) \right], \tag{6.8}$$

where $R(\cdot)$ is the $2d$ rotation matrix, ϕ is the angle between $\boldsymbol{v}_i$ and $\boldsymbol{v}_j$, and λ is a dimensionless constant. The angle is set to zero if either $\boldsymbol{v}_i$ or $\boldsymbol{v}_j = 0$, in which case the original Social-Force model is recovered. We note that, as above, the size of the pedestrians is set to zero.

As it can be seen in the field-lines in Fig. 6.6 *(a)*, the rotation triggers movement to the sides in front of agent j, which is conspicuous of avoidance behaviour. Accordingly, in [191], it is shown that this model clearly outperforms the original Social-Force model with regard to simple avoidance scenarios, like a heads-on collision or sparse cross-flows. However, multiple unrealistic parts can also be seen in the field-lines. In particular, at certain initial positions the pedestrian i is drawn towards a collision-course. Moreover, if pedestrian i is located in the back of agent j the repulsion is asymmetric as well which seems unreasonable. The estimated range of applicability is shown in Fig. 6.6 *(b)*.

6.2.4 Moussaid

A quite different extension of the Social-Force model has be proposed in [144]. Instead of changing the details of the repulsion in Eq. (6.3), another layer is added to the model. In particular, the desired velocity $\boldsymbol{v}_{\mathrm{des},i}$ is not treated as a constant but determined

dynamically by 'simple rules'. This introduces a long-ranged interaction to the inherently short-ranged Social-Force model, thereby making the desired velocity frequently more predominant.

It is assumed that agent i wants to go towards the goal, in direction $\boldsymbol{e}_0$, with speed v_0. This velocity is used to calculate the desired velocity which is then passed to the original Social-Force model. The desired velocity is decomposed into its absolute value, the speed $v_{\text{des},i}$, and the orientation $\boldsymbol{e}_{\text{des},i}$ which are calculated one after another.

The desired orientation $\boldsymbol{e}_{\text{des},i}$ is determined by an optimization process based on the distance to the closest collision, denoted by *dcc*. This quantity is closely related to the TTC, in especially, the closest collision of agent i is given by $dcc_i = v_i \cdot \tau_i$ where τ_i is the minimal TTC of agent i. The minimization reads as

$$\boldsymbol{e}_{\text{des},i} = \underset{\boldsymbol{e} \in \mathcal{D}_\phi}{\arg\min} \left(d_{\max}^2 + dcc_i^2 - 2d_{\max}dcc_i \cdot \boldsymbol{e} \cdot \boldsymbol{e}_0 \right), \qquad (6.9)$$

where the set of possible 'test directions' is given by all 2d, unit-vectors that are within the current field of vision.[3] The distance to the closest collision is calculated using the current velocity of agent j and the test velocity of agent i, i.e. $v_0 \cdot \boldsymbol{e}$. The constant $d_{\max}$ denotes the 'horizon distance'. This distance is also implemented as an upper bound for the distance to the closest collision.

Subsequently, the desired speed is caluclated as

$$v_{\text{des},i} = \min \left[v_0, \frac{\Delta x_i(\boldsymbol{e}_{\text{des},i})}{T} \right], \qquad (6.10)$$

where $\Delta x_i(\boldsymbol{e}_{\text{des},i})$ denotes the minimal center-to-center distance in the desired direction and T the desired time-gap. Note that this corresponds to the heuristic that the agents chose their speed such that the time-gaps T_{ij} to all other agents j are larger than the desired time-gap T. This idea has been at the heart of the models we discussed in Section 3.3.2 with the only difference that the size of the agents has been neglected here.

In principle, the model includes all different factors which we have found to be important to describe pedestrians in different situations: a distance-based interaction, an interaction related to avoidance behaviour, as well as the time-gap. Unfortunately, it is not possible to estimate the range of applicability analogously to the other models because this model inherently strongly depends on the desire to reach a goal. Thus, we can not plot the field-lines easily.

---

[3]i.e. unit-vectors that incline an angle with the current direction of motion of less than ϕ, more formally $\mathcal{D}_\phi = \{\boldsymbol{e} \in \mathbb{R}^2 \text{ with } |\boldsymbol{e}| = 1 \text{ and } |\boldsymbol{e} \cdot \boldsymbol{e}_i(t)| \leq \phi\}$.

However, we will see later, when simulating the collective behaviour of the crowd, that this model struggles to replicate the test cases which are representative of the different regimes. This exemplifies problems often encountered in complex models: the combination of different mechanisms is one of the most difficult tasks. If more and more behaviours are taken into account this might yield an 'over-controlled' and inflexible model.

6.3 Algebraic-Distance Models

Even before the Social-Force model was proposed, Hirai and Tarui [14] introduced a model with several distance-based interactions. Among those, they propose a repulsive interaction which decays algebraically with the distance, in contrast to the exponential decay in the Social-Force model.

To begin, it is worth noting that such a simple algebraic-distance model, qualitatively, yields the same radial repulsion as the original Social-Force model, for instance regarding the field-lines in Fig. 6.1 *(a)*. The range of applicability can therefore be expected to be similar as well, cf. Fig. 6.1 *(b)*. Of course, there exist more subtle differences between the two, i.e. regarding stability properties which have been investigated in the chapter about single-file motion.

In the following section, we will focus on two models based on the idea of an algebraic interaction 'force' that take the relative velocities between pedestrians into account - in a quite different way than the models discussed so far.

6.3.1 Centrifugal-Force Model

The Centrifugal-Force model, introduced in [192], reads as

$$a_i = \frac{v_{\text{des},i} - v_i}{\tau_R} - \alpha \left[\sum_{j \neq i} v_{ij}^2 \cdot \nabla_r h \left(\mathcal{I} n_{ij} \right) \right], \qquad (6.11)$$

where $h(x) = \ln \left(1/\sqrt{x} \right)$ and v_{ij} the rate of approach between i and j. The size of the pedestrians is neglected ($\ell = 0$). The gradient in Eq. (6.11) only acts on the part of the interaction based on the intrusion variable. It therefore points in the radial direction, i.e. $\nabla_r h \left(\mathcal{I} n_{ij} \right) \propto e_{ij}/r_{ij}$. Note that this repulsion decays much slower with distance than, for example, an exponential interaction. The multiplication with the rate of approach entails, that the faster two pedestrians approach each other the larger is the amplitude
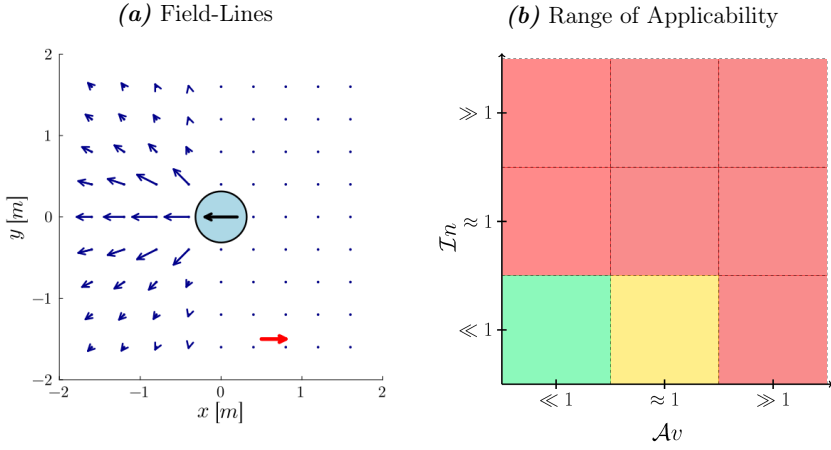
FIGURE 6.7: **(a)** We visualized the repulsion of the Centrifugal Force Model. The red arrow depicts the scale of the velocities and corresponds to 2m/s. In **(b)** we show its estimated range of applicability.

of the repulsion between the two. If the rate of approach is negative, i.e. if they grow apart or keep a constant distance, their mutual interaction is set to zero.

Consequently, pedestrians that heavily intrude each others personal space do not interact at many instances which is also shown in the field-lines in Fig. 6.7 **(a)**. This leads to problems that have been observed by the authors as well: the definition of the model in [192] further includes a collision detection algorithm to avoid overlapping. The model defined by Eq. (6.11) alone, however, is not applicable to regimes of non-zero $\mathcal{I}n$ numbers.

In front of pedestrian j, where the rate of approach is positive, the model correctly captures the long-ranged interaction conspicuous of the moderate $\mathcal{A}v$ and low $\mathcal{I}n$ regime. In an analogy with the centrifugal force in physics, the authors chose the amplitude of the repulsion as $\propto v_{ij}^2/r_{ij}$. This is similar to the TTC ($1/\tau \propto v_{ij}/r_{ij}$) on which the Avoidance number is based. But, as mentioned above, the repulsion still acts in radial direction which has proven unrealistic in many collision conflicts. Furthermore, the square more heavily weights the 'approaching-part' which can lead to a vanishing interaction strength in situations where two people approach each other slowly but nonetheless face an imminent risk of collision.

Besides, an essential part of the definition of the TTC are the conditions that indicate whether a collision occurs at all. In the Centrifugal-Force model, instead of this, only one simple condition indicates whether two pedestrians are approaching each other or not. Thus, the model leads to a strong interaction when pedestrians approach each other even though a collision is not impending. This can be seen in the field-lines in Fig. 6.7 **(a)**, e.g., in the top left corner. In the last chapter, in contrast to this, we have seen in
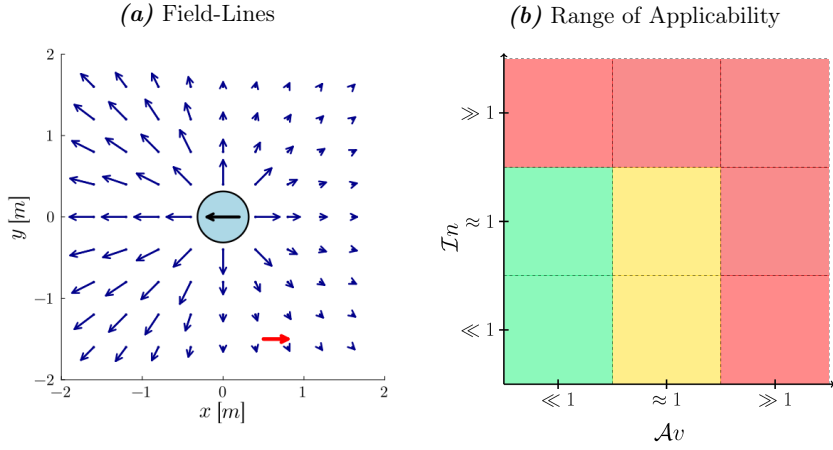
FIGURE 6.8: In *(a)* the repulsion in the Generalized Centrifugal-Force Model is shown. The red arrow depicts the scale of the velocities and corresponds to 2m/s. In *(b)* the range of applicability is visualized.

the cross-correlation of the sparse cross flow that pedestrians continue to approach each other after solving the collision conflict, without any sign of further interactions.

According to this discussion, we have chosen the range of applicability, cf. Fig. 6.7 *(b)*.

6.3.2 Generalized Centrifugal-Force Model

In the Generalized Centrifugal-Force model [193], some of these problems have been addressed. The model is defined as

$$\boldsymbol{a}_i = \frac{\boldsymbol{v}_{\mathrm{des},i} - \boldsymbol{v}_i}{\tau_R} - \alpha \left[\sum_{j \neq i} (v_{ij} + \beta)^2 \cdot \nabla_r h\left(\mathcal{I}n_{ij}\right) \right], \qquad (6.12)$$

where as above v_{ij} is set to zero if the rate of approach is negative. We have neglected perception which was originally included by an anisotropy that weights pedestrians in the direction of motion more strongly and disregards those that are outside a visual cone. Furthermore, Chraibi et al [193] introduced elliptic shapes to the model which we have disregarded here as well.

One can easily see that by introducing the parameter β a solely distance-dependent interaction is present - which should allow for a realistic simulation of regimes with a moderate $\mathcal{I}n$ number, e.g., the *Waiting* scenario. In the field-lines, in Fig. 6.8 *(a)*, this is reflected in a radial repulsion between i and j even if the distance between them is increasing. Besides, here, a non-zero size of the pedestrians is included which strongly increases the

repulsion between pedestrians that are close to each other. Consequently, the authors show that the collision detection algorithm which was employed in the Centrifugal-Force model to avoid overlapping is not needed anymore [193]. The very slow decay of the repulsion might, however, still lead to problems in regimes of high $\mathcal{I}n$ numbers.

Regarding collision-avoidance and interactions conspicuous of non-zero $\mathcal{A}v$ numbers, the same discussion as for the Centrifugal-Force model applies because this part of the model remains largely unchanged. This can also be seen in the field-lines. The estimated range of applicability is shown in Fig. 6.8 *(b)*.

From the viewpoint of the perturbative analysis performed in the last chapter, the model is non-minimal. In particular, the perturbative analysis resulted in two independent interactions, one based on $\mathcal{I}n_i$ and the other one on $\mathcal{A}v_i$. In Eq. (6.12), on the other hand, the squared term $(v_{ij} + \beta)^2$ yields mixed terms of the type $\sim \mathcal{A}v \cdot \mathcal{I}n$ which correspond to a Taylor expansion of higher order. This might be beneficial in more complex regimes but could also be more difficult to control.

6.4   Collision-Free Speed Model

Let us now consider the Collision-Free Speed model introduced in [81]. In contrast to the models discussed so far, speed $v_i = |\boldsymbol{v}_i|$ and orientation $\boldsymbol{e}_i$ are calculated independently. The model can be seen as a two-dimensional version of the simplest Optimal Velocity model which has been discussed in chapter 3.

As for the orientation, however, the model is similar to the 'force'-based models discussed so far. In particular, we can write the sub-model as

$$\boldsymbol{e}_i = \frac{1}{Z} \left\{ \boldsymbol{e}_{\text{des},i} - \alpha \cdot \nabla_r \left[\sum_{j \neq i} f\left(\mathcal{I}n_{ij}\right) \right] \right\}, \tag{6.13}$$

where the same exponential function $f(x)$ as in Eq. (6.3) is used, and Z such that $|\boldsymbol{e}_i| = 1$.

For the speed, the definition in [81] is based on the heuristic that the agents choose a maximal speed while ensuring that the time-gaps T_{ij} to all other agents j are larger than the desired time-gap T. This can be written as an optimization process

$$v_i = \operatorname*{arg\,min}_{v \in [0, v_{\text{des},i}]} \left[\frac{1}{\varepsilon} \cdot \Theta\left(\frac{T}{T_i(v \cdot \boldsymbol{e}_i)} - 1 \right) + (v - v_{\text{des},i})^2 \right], \tag{6.14}$$

with $\varepsilon \to 0$, the Heaviside step function Θ, and T_i the minimal time-gap in direction $\boldsymbol{e}_i$ calculated with the test-speed v.
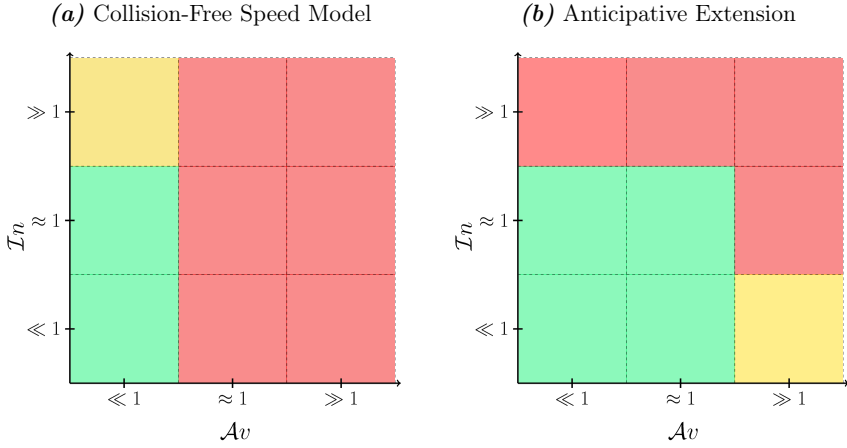
FIGURE 6.9: In *(a)* the range of applicability of the Collision-Free Speed model is shown and in *(b)* of the anticipative Collision-Free Speed model.

The first part of the model is a radial repulsion based on $\mathcal{I}n$ and thus should allow an applicability in the low $\mathcal{A}v$ regime. Note that the model does not distinguish between v_{des} and v_{max}, therefore one could only plot the field-lines of the dimensionless vector $\boldsymbol{u}^\star$ defined by $\boldsymbol{e}_i = (\boldsymbol{e}_{\text{des},i} + \boldsymbol{u}^\star)/Z$ in Eq. (6.13). This yields qualitatively the same picture as the Social-Force model, cf. Fig. 6.1 *(a)*.

The second part of the model, given by Eq. (6.13), is based on the Time-Gap which allows a robust replication of the (uni-directional) fundamental diagram. Moreover, the model is inherently collision-free which allows a safer application in the high $\mathcal{I}n$-regime. However, neither the time-gap nor the $\mathcal{I}n$ based repulsion allows a convincing solution of collision avoidance conflicts [49].

We have set the range of applicability according to these considerations, cf. Fig. 6.9 *(a)*.

6.4.1 Anticipation in the Collision-Free-Speed Model

The lack of collision avoidance and the observation of frequent grid-locks at sparse bidirectional flows has led to the amendment proposed in [49]. In this model, the repulsion is changed to be non-radial and includes anticipative effects.

In particular, the strength of the repulsion does not depend on the current positions. Instead it depends on the anticipated distance at time $t + \tau_A$ under the assumption of constant velocities.[4] Furthermore, the amplitude of the repulsion that agent i feels is chosen to be stronger if agent j is positioned in the direction that i desires to move to.

---

[4]More precisely, on its projection on the binding vector between i and j.
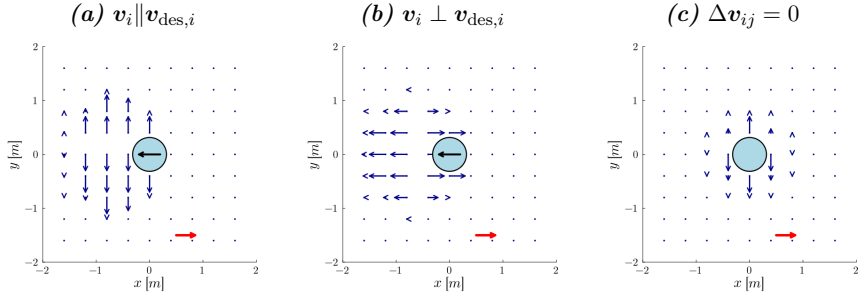
FIGURE 6.10: Repulsion in the Collision-free speed model with anticipation for different scenarios. Instead of plotting the velocity $\boldsymbol{v}^\star$, we plot the dimensionless vector $\boldsymbol{u}^\star$ that inhibits the interactions regarding the orientation. In this case the red arrow corresponds to a length of 2.

More importantly, instead of a radial repulsion, the direction of the repulsion is set to be always perpendicular to the desired direction.

These changes allow to reproduce movement to the sides in collision avoidance conflicts, as it is shown in Fig. 6.10 *(a)*. Concurrently, in [49], the authors show that the model outperforms the Collision-Free Speed model in simple avoidance scenarios and bidirectional flows. In the latter, it is shown to replicate experimental results well.

The amendments put forward here can, however, also result in unexpected behaviour. For instance, if there is a significant misalignment between the current velocity and the desired velocity, as illustrated in Fig. 6.10 *(b)*, the agents can feel some attraction towards each other. Such a strong deviation from the desired path would however only occur in regimes of high $\mathcal{A}v$ number and/or high $\mathcal{I}n$ number. Furthermore, in contrast to the simple Collision-Free Speed model, the anticipative extension can not capture the simple radial interaction conspicuous of the low $\mathcal{A}v$ regimes as shown in Fig. 6.10 *(c)*.

The estimated range of applicability is shown in Fig. 6.9 *(b)*. Note that this has to be taken with additional caution as the interactions introduced here seem to be difficult to control, i.e., lead to unexpected behaviour if tested in different situations.

6.5 Time-to-Collision Based Models

So far, we have discussed multiple models and their extensions. We have seen that these models were grounded in the idea of a distance based interaction, and thus related to the intrusion variable. This naturally limits their range of applicability to regimes of low Avoidance number. This observation has prompted multiple extensions in which it was
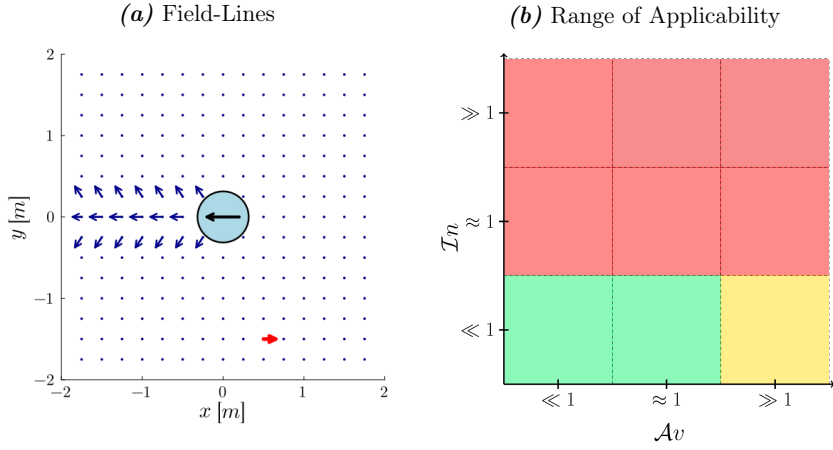
FIGURE 6.11: In *(a)*, the repulsion in the the gradient based Power-Law model is shown. We show the field-lines in a finer grid as otherwise only the row with $y = 0$ would show an interaction. The red arrow depicts the scale of the velocities and corresponds to 2m/s. In *(b)* the corresponding range of applicability.

tried to include anticipation to extend the range of applicability to regimes of non-zero $\mathcal{A}v$ number.

Now, let us shift our focus to models that have been introduced more recently, ones that are inherently grounded in anticipation. Specifically, we will explore various models that rely on the concept of time-to-collision and, consequently, are closely connected to the Avoidance number.

6.5.1 Power-Law Model

In [82], the Power-Law model has been proposed. To highlight its dependence on $\mathcal{A}v$, we write it as

$$\boldsymbol{a}_i = \frac{\boldsymbol{v}_{\text{des},i} - \boldsymbol{v}_i}{\tau_R} - \alpha \cdot \nabla_r \left[\sum_{j \neq i} g\left(\mathcal{A}v_{ij}\right) \right], \tag{6.15}$$

where the function $g(x) = x^2 \exp\left(-1/x\right)$ was chosen by fitting an empirically obtained interaction potential.[5]

Even though Eq. (6.15) looks very similar to the Social-Force model in Eq. (6.3), the interaction potential is widely different. This can be seen in the field-lines plotted in Fig. 6.11 *(a)*. The two agents do not interact as long as no collision is expected even if they are almost at physical contact. Accordingly, the model can not be applied in regimes of non-zero $\mathcal{I}n$ number.

---

[5]Under the debatable assumption of a Boltzmann like distribution function.

Conversely, when a collision is anticipated a strong and long ranged interaction comes into play. This interaction which acts along the gradient of $\mathcal{A}v_i$ partially leads to the expected movement to the side. The expected avoidance behaviour, however, can not be completely reproduced. This observation aligns with [185], where this model yields a similiar displacement field as depicted in Fig. 6.11 *(a)* for an intruder crossing a densely packed crowd. This displacement field, as well as the field-lines shown here, fails to accurately capture the empirically observed lateral movement right in front of the intruder.

We have chosen the range of applicability according to this in Fig. 6.11 *(b)*.

6.5.2 Velocity Obstacle Model

Let us now look at a class of models based on reasoning in velocity space, in particular, Velocity Obstacle models. The concept of Velocity Obstacles originates in motion planning of robots around moving obstacles and was introduced in [124]. More recently, it has also been applied to pedestrian dynamics.

In these models, each agent has a set of admissible velocities which is further restricted by the presence of other agents or (moving) obstacles. In particular, velocities that lead to an anticipated collision within the next τ_0 seconds (equivalently: velocities that have $\mathcal{A}v_i < 1$) are forbidden. Geometrically, this translates into non-admissible cone-shaped areas in the velocity space of agent i.

To highlight the dependency on $\mathcal{A}v_i$ we write the Velocity Obstacle model as

$$\boldsymbol{v}_i^\star = \underset{\boldsymbol{v} \in \mathbb{R}^2}{\arg\min} \left[\frac{1}{\varepsilon} \cdot \Theta\Big(\mathcal{A}v_i\left(\boldsymbol{v}\right) - 1\Big) + \left(\boldsymbol{v}_{\text{des},i} - \boldsymbol{v}\right)^2 \right], \tag{6.16}$$

with $\varepsilon \to 0$ and Heaviside step function Θ. Velocities inside such a collision-cone, are assigned an infinite cost whereas all other velocities have a cost corresponding to the distance to the optimisation goal $\boldsymbol{v}_{\text{des},i}$.

Note that if Eq. (6.16) is defined as a first-order differential equation (continuous in time), it becomes an implicit equation, which is more difficult to solve. Typically, it is, however, defined with an explicit time-step. One can also define it as a second-order model continuous in time with a relaxation time τ_R.

The field-lines are illustrated in Fig. 6.12 *(a)* and are essentially identical to those in the $\mathcal{A}v$-model discussed in the preceding chapter. The characteristic lateral movement is evident, indicating that avoidance conflicts are likely to be resolved accurately. In

(a) Field-Lines ⁣⁣⁣⁣⁣⁣⁣⁣⁣⁣ ***(b)*** Range of Applicability
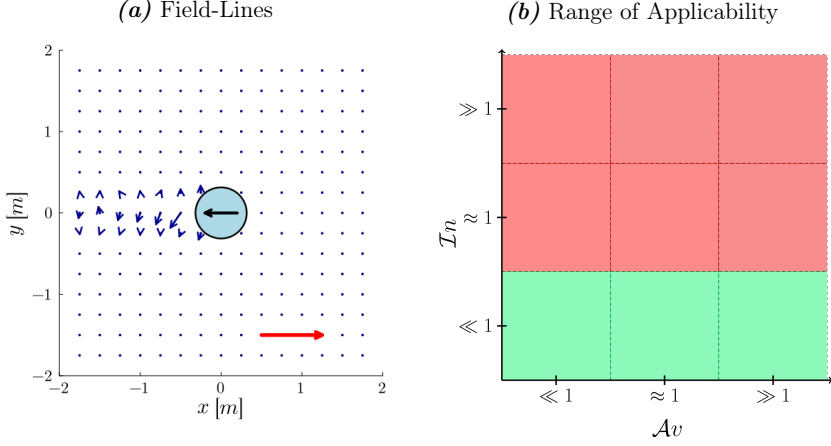
FIGURE 6.12: In ***(a)***, the field-lines of the Velocity Obstacle model are shown. The red arrow depicts the scale of the velocities and corresponds to 2m/s. We show the field-lines in a finer grid as otherwise only the row with $y = 0$ would show an interaction. In ***(b)*** the estimated range of applicability of the Velocity Obstacle model, the RVO model, and the ORCA model is shown.

comparison to the Power-Law model, the anticipative behavior appears to be more so-phisticated, as sideways motion is evident in the middle row ($y = 0$) as well. This suggests an advantage of the optimization-based approach over a gradient-based model.

As no $\mathcal{I}n$-related variable is present in Eq. (6.16), the agents have no tendency to spread homogeneously in the system, i.e. to make use of the available space. Accordingly, no radial interaction can be spotted in Fig. 6.12 ***(a)***. Furthermore, it was shown that this yields a very unrealistic Fundamental Diagram [83]. Consequently, we have set the range of applicability in Fig. 6.12 ***(b)***.

6.5.3 Reciprocal Velocity Obstacles

Van den Berg and colleagues, found that if Eq. (6.16) is implemented as a first-order time-discrete model, it leads to unrealistic oscillations between mutually interacting agents. Therefore, the Reciprocal Velocity Obstacle model [125] is introduced where agents take shared responsibility to avoid each other.

The model is defined as

$$\boldsymbol{v}_{i,t+\delta t} = \underset{\boldsymbol{v} \in \mathbb{R}^2}{\arg \min} \left[\mathcal{A}v_i \left(2 \cdot \boldsymbol{v} - \boldsymbol{v}_{i,t} \right) + \frac{1}{\alpha} \cdot \left| \boldsymbol{v}_{\text{des},i} - \boldsymbol{v} \right| \right], \tag{6.17}$$

with an explicit time-step δt and $\mathcal{A}v_i$ is calculated with the velocity $(2 \cdot \boldsymbol{v} - \boldsymbol{v}_{i,t})$ which models the shared responsibility.

The definition was changed to a discrete time as the average of old and new velocity does not have a reasonable limit as $\delta t \to 0$. In contrast to Eq. (6.16), the authors changed the cost-function to allow a (reasonable) application even if all velocities are assigned an infinite cost.

Despite of these changes we expect the field-lines and the range of applicability to be very similar to Fig. 6.12. Consequently, the model was shown to solve all different kinds of avoidance conflicts convincingly [125].

6.5.4 ORCA Model

Optimization-based models appear to incorporate more advanced anticipation compared to gradient-based models. The optimization problem, however, has to be solved. This is usually done by sampling the velocity space which comes at a high computational cost. In the ORCA model [126], the Velocity Obstacles are reformulated to enable a computationally efficient, collision-free, and exact solution of the optimization. Specifically, the collision-cones are transformed into more strict conditions resembling lines, allowing the application of linear programming. We denote the new Avoidance number based on the transformed Velocity Obstacles as $\tilde{\mathcal{A}}v$.

We then obtain the ORCA model by inserting $\tilde{\mathcal{A}}v$ into Eq. (6.16), i.e.

$$\boldsymbol{v}_i = \underset{\boldsymbol{v} \in \mathbb{R}^2}{\arg\min} \left[\frac{1}{\varepsilon} \cdot \Theta\Big(\tilde{\mathcal{A}}v_i\left(\boldsymbol{v}\right) - 1\Big) + \left(\boldsymbol{v}_{\text{des},i} - \boldsymbol{v}\right)^2 \right], \qquad (6.18)$$

where $\varepsilon \to 0$ and Heaviside step function Θ. In the case that all velocities have $\tilde{\mathcal{A}}v_i < 1$, another cost-function is employed.

As expected from Eq. (6.18), and the discussion of the other Velocity Obstacle models, it was found that the ORCA model does not show a reasonable fundamental diagram, neither in uni-directional flow, nor in bi-directional flow [30].

On the other hand, the ORCA has been shown to solve avoidance conflicts convincingly. It has, however, also been found that the reformulation of the Velocity Obstacles can lead to non-intuitive behaviour discussed in [194]. Nonetheless, we expect the range of applicability to be the same as in Fig. 6.12 *(b)*.

A typical application of the ORCA models is computer graphics, where smooth and optically realistic trajectories with small computational effort are desired. In this application a realistic speed-density relation is much less important than a smooth collision avoidance.

6.5.5   ORCA and Density Dependent Behaviour

The observation that certain models struggle to describe regimes at larger density (or regimes at larger $\mathcal{I}n$-number) accurately has prompted the formulation of the model presented in [30]. This model aims to integrate 'density-dependent behavior' into models for pedestrian crowds. To this end, similarly to [144], an additional layer is proposed which determines the dynamics of $\boldsymbol{v}_{\mathrm{des},i}$. In theory, this layer can be applied to any other model. Nonetheless, our emphasis will be on using it as an extension to the ORCA model, a choice also made by the authors in [30].

In this model, the desired velocity is decomposed into the desired direction and the desired speed. The desired direction is given by the orientation that minimizes the distance to the goal in a given time-period τ_A, i.e. by

$$\boldsymbol{e}_{\mathrm{des},i} = \underset{\boldsymbol{e} \in \mathcal{D}}{\arg\min} |\boldsymbol{x}_{\mathrm{goal},i} - [\boldsymbol{x}_i + v_{\mathrm{FD}}\left(\boldsymbol{e}\right) \cdot \boldsymbol{e}]\, \tau_A|, \tag{6.19}$$

where $\boldsymbol{x}_{\mathrm{goal},i}$ the position of the goal and $\mathcal{D}$ the set of 2d unit vectors. The function $v_{\mathrm{FD}}\left(\boldsymbol{e}\right)$ gives the 'fundamental diagram adherent' speed in direction $\boldsymbol{e}$ which is based on the idea of preservation of personal space.

Contrary to the Intrusion number $\mathcal{I}n$, the size of the personal space is assumed to increase with the speed. In particular, the socially acceptable distance is given by the typical step length at a certain speed, $L(v) = \tilde{\alpha}\sqrt{v}$, scaled by a constant factor. For the social radius, this yields $r_{\mathrm{soc}}(v) = \beta L(v) = \alpha\sqrt{v}$. The 'fundamental diagram adherent' speed in direction $\boldsymbol{e}$ is then given by

$$v_{\mathrm{FD}}\left(\boldsymbol{e}\right) = \min\left[v_{\max}, \frac{\Delta x_i(\boldsymbol{e})^2}{\alpha^2}\right]. \tag{6.20}$$

This is equivalent to the heuristic that pedestrians always chose the largest speed with $v \leq v_{\max}$ that yields an intrusion, here defined as $r_{\mathrm{soc}}(v)/\Delta x_i$, that is smaller than one.

Note that instead of using the headway or distance in direction $\boldsymbol{e}$ directly, in this model, the pedestrians estimate the distance via the local density at the position $\boldsymbol{x}_i + \boldsymbol{e}$ which is calculated using Gaussian kernels. Finally, the desired velocity is given by $\boldsymbol{v}_{\mathrm{des},i} = \boldsymbol{e}_{\mathrm{des},i} \cdot v_{\mathrm{FD}}\left(\boldsymbol{e}_{\mathrm{des},i}\right)$.

In this model, the absence of personal space for individuals with zero velocity (note that $r_{\mathrm{soc}}(v = 0) = 0$) stands in contrast to the typical scenarios studied in psychology [152], which may be considered a drawback when compared to the personal space conceptualization proposed by the $\mathcal{I}n$-number. However, unlike the $\mathcal{I}n$-model, this interpretation of personal space, based on the variable size of pedestrians, enables the reproduction of
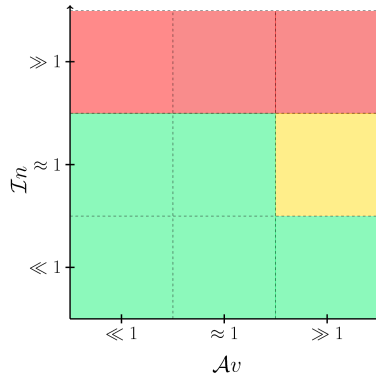
FIGURE 6.13: The estimated range of applicability of the ORCA model combined with the DenseSense model.
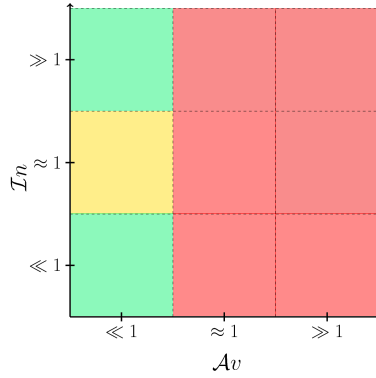
FIGURE 6.14: Estimated range of applicability of a granular model.

the fundamental diagram. As demonstrated in [30], when combined with ORCA, it can successfully reproduce the fundamental diagram in both uni- and bidirectional flow.

Consequently, it is expected to expand the range of applicability of the ORCA model to regimes of moderate $\mathcal{I}n$-values. The estimated range of applicability is illustrated in Fig. 6.13.

6.6 Granular Model

A granular model, as defined in [27] that includes a goal reaching mechanism but only short-ranged mechanical interactions might have a range of applicability as depicted in Fig. 6.14.

6.7   Multi-Agent Simulations

In this section, we want to investigate whether the models discussed in the last section are actually applicable in the associated regimes (only). Therefore, we have chosen four scenarios, namely, the *Uni-directional* corridor, the *Waiting* scenario, and the *sparse* and the *dense Cross* flow. We simulated the ORCA, RVO, Social-Force, its extension 'Moussaid', and the Power-Law models using the UMANS software [178]. We have changed the definition of the Social-Force model from [16] to [60], as it is shown in Eq. (6.3). Furthermore, we have implemented the Collision-Free Speed model as well as the proposed $\mathcal{A}v$-model, $\mathcal{I}n$-model, and $\mathcal{A}v \star \mathcal{I}n$-model. We calculate $\mathcal{A}v$ and $\mathcal{I}n$, as well as the mean speed $\langle v \rangle$, from the simulated trajectories and compare them to empirical values. The results are summarised in Fig. 6.15.

Let us first consider the *Waiting* scenario depicted in Fig. 6.15 *(a)*. Models that do not inhibit $\mathcal{I}n$ can not reproduce the basic features of the crowd, namely a more or less even distribution of the agents over the available space. They do not (or hardly) alter the initial condition at all and, thus, strongly overestimate $\mathcal{I}n$. All models that inhibit $\mathcal{I}n$, on the other hand, are able to approximately reproduce the experimental $\mathcal{I}n$-value. An exception is the Collision-Free Speed model and the Moussaid model: A static crowd lies beyond the scope of these models as it is not distinguished between a desired and a maximal speed.

As for the *Unidirectional* scenario Fig. 6.15 *(b)* the picture is similar regarding the intrusion variable, however, now the pedestrians have a desire to walk, thus, leading to a non-zero mean speed. The $\mathcal{A}v$-based models can neither reproduce $\mathcal{I}n$ nor the speed which aligns with [30, 83] where TTC based models were shown to yield completely unreasonable fundamental diagrams. However, also purely $\mathcal{I}n$ based models do not reproduce the mean speed, which aligns with [30]. The mean speed is reproduced in the Collision-Free Speed model only. This indicates that there might be a third 'essential' mechanism based on the dimensionless variable $\mathcal{T}$. The Moussaid model, however, includes this variable and is unable to reproduce the slowing down related to the uni-directional fundamental diagram. Furthermore, the agents do not spread evenly in the system which is reflected in an increased Intrusion number if compared to the experiments - even though an $\mathcal{I}n$ related interaction is present. This points to the problem of the correct combination of different factors in complex models.

Let us now turn to the *sparse Cross* scenario in Fig. 6.15 *(c)*. All $\mathcal{A}v$ based models lead to a successful collision avoidance. They are able to reproduce the mean speed, the $\mathcal{A}v$-value, and the $\mathcal{I}n$-value relatively well. The overestimation of $\mathcal{I}n$ is probably related to the fact that in $\mathcal{A}v$ only collisions between the hard-cores are taken into consideration
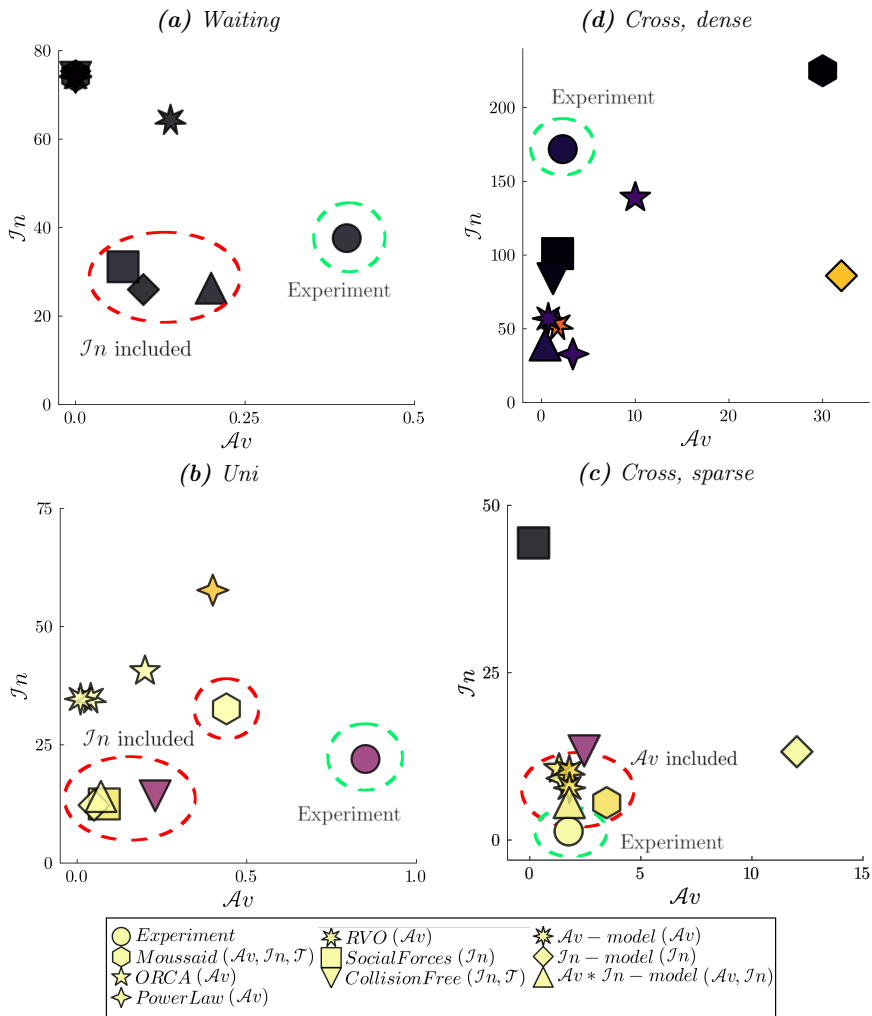
FIGURE 6.15: The dimensionless numbers for different models in four different scenarios. The color of the symbols corresponds to the mean speed, i.e. the darker the slower.

whereas 'softer' anticipated intrusions are left aside. The models that do not include $\mathcal{A}v$, however, fail in different ways to reproduce the experiment. The Social-Force model ends up in a complete grid-lock, which is reflected in the high $\mathcal{I}n$-value and the zero speed. In the Collision-Free Speed model, the system is heavily congested (small mean speed) which is in stark contrast to the experiment which is still in the free-flow branch of the fundamental diagram. In the $\mathcal{I}n$-model, on the other hand, the agents do not slow down at all, however, without solving the avoidance conflicts convincingly: the agents bump into each other which leads to very high Intrusion and Avoidance numbers.

The *dense Cross* scenario in Fig. 6.15 *(d)* can not be reproduced by any of the models. Here, more realistic shapes as well as mechanical interactions need to be taken into account. None of the models inhibits these features. Apart from this tunneling through the walls can be observed in some models.[6]

6.8   Summary

In this chapter, we observed that numerous models rely directly on either the intrusion or avoidance variable. Through the utilization of field-lines, we explored how their appearance shapes the interactions between agents. An interaction based on intrusion ($\mathcal{I}n$) tends to be radial, short-ranged, and reactive, while an avoidance ($\mathcal{A}v$) based interaction acts in lateral direction, is long-ranged, and anticipative in nature. The appearance of $\mathcal{A}v$ or $\mathcal{I}n$ in the equations of motion limits the applicability of the corresponding model to the associated regimes. This has been verified by simulations of the whole pedestrian crowd in different scenarios.

The described factors are two different behaviours, in particular we have intrusion and anticipated (heavy) intrusions. Consequently, endeavours to reformulate an $\mathcal{I}n$-based interaction such that it also captures $\mathcal{A}v$-related behaviour fails. We have seen that anticipation can be incorporated into a distance based interaction, this adaptation comes at the expense of forfeiting the original short-range, radial, and reactive interaction. Alternatively, one might end up 'somewhere in the middle' of both interaction types which leads to models that are difficult to control and to understand.

Apart from that, we have encountered another factor in several models, namely, the time-gap. The time-gap has been at the heart of the models put forward in Section 3.3 for single-file motion. But it also appeared in this chapter, namely in the 'Moussaid' model (Section 6.2.4) as well as in the Collision Free Speed model (Section 6.4). Thus,

---

[6]Note that this might be related to the fact that in many models the authors do not specify how interaction with walls or other obstacles should be handled.

we are tempted to introduce a third dimensionless variable that quantifies the risk while following as

$$\mathcal{T}_i = \sum_{j \in \mathcal{N}_i} \frac{T}{T_{ij}} \tag{6.21}$$

where T_{ij} denotes the time-gap between i and j, and T the desired time-gap. The neighborhood $\mathcal{N}_i$ may be chosen such that only the maximum value of T/T_{ij} is taken into account. The heuristic of all time-gap based models we have come across so far, would translate to the statement that the agents chose their speed such that $\mathcal{T}_i < 1$. The 'Risk-while-Following' number would correspond to different regimes as

- $\mathcal{T} < 1$: the situation is safe, the follower could even increase her speed

- $\mathcal{T} = 1$: the situation is safe, no need to adjust speed or spacing

- $\mathcal{T} > 1$: the situation is not safe, in case of an abrupt stopping of the predecessor a collision may be unavoidable. The follower should slow down.

However, before claiming the Risk-while-Following number, on a similar basis as $\mathcal{A}v$ and $\mathcal{I}n$, it would need to prove its empirical relevance in crowds. Interestingly, while for vehicular traffic there are multiple studies investigating the time-gap, for instance its distribution on highways [29], no such studies exist for pedestrian dynamics.

Coming back to modeling, we are now confronted with at least two or three fundamental aspects of pedestrian motion at the micro level, captured by $\mathcal{I}n_i$, $\mathcal{A}v_i$, and potentially $\mathcal{T}_i$. Furthermore, the desire to move, is at the heart of any active system such as crowds. This poses the problem of how to combine these factors in a model.

We have argued that the delineation of flow regimes allows the modeler to resort to different models in different regimes. This partly allows to circumvent the problem of modeling how humans choose between different heuristics. It is worth noting, however, that our focus has primarily been on extensively studied asymptotic regimes. This considerably simplifies the question because only one interaction comes into play anyway.

In any 'mixed' regime where neither $\mathcal{A}v$ nor $\mathcal{I}n$ is low, we will likely have to combine different interactions. For a regime with $\mathcal{I}n, \mathcal{A}v \sim 1$, as demonstrated in the last chapter, the $\mathcal{A}v \star \mathcal{I}n$ model produces realistic results through a straightforward superposition. By summing up the $\mathcal{I}n$ and $\mathcal{A}v$ interactions and assigning relative weights between them, we successfully replicated empirical findings of a bi-directional flow. This has also been shown in other works discussed in this chapter. If this is possible in other regimes, further away from the origin of the 'phase diagram', such as those with either $\mathcal{I}n$ or $\mathcal{A}v \gg 1$, remains uncertain.

The superposition principle is indeed a prevalent way for combining different factors in models, but there are several other approaches to achieve this in spatially continuous models. Let us briefly explore some of these ideas encountered in this chapter:

- *Superposition:* Borrowed from the superposition principle of Newtonian forces, different factors can be combined by summing over them. It allows a straightforward incorporation of different factors. This approach is utilized to some extent in all models discussed here. The Social-Force model and its numerous variants serve as a prominent example. However, especially for more complex scenarios, it may fall short in capturing the ability of humans to prioritize [100]. For instance, consider someone wanting to use the restroom and also stay with their friends; they are unlikely to navigate somewhere in the middle (as a superposition of both factors yields) but would instead address each need sequentially.

- *Restriction:* Here, agents choose from a specific set of decisions, such as the space of admissible velocities which is further restricted by certain conditions that have to be met. Subsequently, some quantity is maximized or minimized within the remaining set of possible decisions. This approach is evident in granular models [27] to ensure volume exclusion or in Velocity Obstacle models to avoid anticipated collisions [124]. While this demonstrates some ability to prioritize, challenges arise if no admissible velocity is available. In such cases, an alternative procedure must be specified, as exemplified in [126].

- *Multi-Layer:* In this approach multiple effects are combined not by superimposing but by passing the result of one layer as an input to the next layer. The final layer yields, for instance, the velocity that is actually realized in the system. For example, the model put forward in [182], consists of a decisional layer whose result is passed on to a mechanical layer which yields the actual velocity. This is also exemplified by [144] where the result of a more complex cognitive model is passed as the desired velocity to the social-force model according to which the actual velocity is determined. Different layers could also distinguish between short and long term planning.

- *Decomposition:* Through the decomposition of velocity into direction of motion and speed, different factors can be combined. Typically, the direction of motion is calculated first, followed by the determination of the corresponding speed. This process is exemplified in works such as [30, 81, 144]. This decomposition is however limited as it can only combine two different factors (speed and direction). It might prove unreasonable in some situations to chose one after the other.

Often, models depend on multiple concepts of combinations. For instance, the Collision-Free Speed Model is built on a decomposition, where the direction of motion is determined through superposition, and the speed is derived from a restriction on admissible speeds.

Finally, let us consider another approach, particularly applicable in more complex scenarios, such as evacuating a stadium, where various regimes are at play but are spatially separated. Leveraging the microscopic determinants of $\mathcal{A}v$ and $\mathcal{I}n$, one could measure these quantities to assess the regime and dynamically adjust the model. In other words, the dimensional numbers could serve as indicators to switch between different heuristics locally. This strategy may find parallels in more complex Fluid Dynamics simulations, where challenges might arise in simulating a large interconnected system of different flow regimes. Maybe algorithms already exist in which the approximation of the underlying equations is adjusted based on dimensionless numbers like the Reynolds number associated with the nearby region.

Throughout the text the Reynolds number was used as an illustration for our study. Before concluding and discussing the limitations of the work presented in this thesis, let us discuss a major difference between the Reynolds number and the numbers we have put forward here.

6.8.1 Relation to Scaling Analysis

Drawing inspiration from the methodology of fluid mechanics, we have been able to define two dimensionless numbers for crowd dynamics that serve similar purposes as dimensionless numbers in Fluid Dynamics, namely,

- to delineate different flow regimes,

- to gauge the validity of some approximations in the model.

Of course, we do not claim that there is a strict analogy between the Reynolds number and numbers introduced here. Let us therefore turn towards a fundamental difference between the Reynolds number and the dimensionless numbers introduced here. In particular the Reynolds number can be derived by a scaling analysis of the Navier-Stokes equation, see e.g. [195]. Scaling analysis is a powerful tool to study various problems in physics. An introduction into the topic as well as numerous other (pedagogical) examples can be found in [143]. Another example can be found in the first chapter of this work - let us therefore recall the discussion of the non-dimensional Optimal Velocity model in Section 3.3.5.

By introducing suitable length and velocity scales we have non-dimensionalized the dependent parameters and, thus, the complete differential equation. Thereby, the number of parameters was reduced and we obtained a single non-dimensional parameter that encapsulates the essential physical properties of the underlying system.

Similarly, the $\mathcal{I}n_i$ and $\mathcal{A}v_i$ numbers introduced here are non-dimensional variants of the dependent parameters. They depend on the positions $\boldsymbol{r}_j$ and the velocities $\boldsymbol{v}_j$ for potentially all other agents j, more specifically on the Euclidean spacings r_{ij} and the 'time-distances' τ_{ij}. In order to non-dimensionalize these we have introduced a length-scale r_{soc} and a time-scale τ_0. However, the models discussed here still depend on the actual positions and velocities as well. It seems that we can not express the dynamics of the system in terms of the set of $\mathcal{I}n_i(t)$ and $\mathcal{A}v_i(t)$ for $i \in [1, N]$ alone. For example by a set of coupled partial differential equation that connects the intrusion and avoidance variables with its time derivatives.

On the contrary, we always have to include the definitions of our dimensionless variables and can not reduce the number of parameters with the analysis performed here. This problem can be illustrated by the non-bijectivity of the $\mathcal{A}v_i$ variable - there is no one-to-one correspondence between configurations of the systems because many different configurations lead to a zero avoidance variable. This could be related to the fact that we study a microscopic model. Possibly a macroscopic model could actually consist of dynamics purely described by space and time dependent $\mathcal{A}v$ and $\mathcal{I}n$ variables.

Chapter 7

Conclusions

In summary, we have introduced two variables that quantify the desire to preserve one's personal space from intrusions and the anticipation of collisions. With these two variables at hand we delineated different regimes in crowd flows. This allowed a much finer classification than the traditional density-based level of service. More importantly, we also showed that the way in which the crowd self-organizes is best described by 'distances' in time (TTCs) in the low-$\mathcal{I}n$ regime and by distances in space in the low-$\mathcal{A}v$ regime.

These structural differences between the regimes have led to a perturbative expansion around the non-interacting situation. Thereby, three different models have been put forward, based on $\mathcal{A}v$, $\mathcal{I}n$, or on both. These models are applicable in the corresponding regime (and only there). Furthermore, we have shown that this discussion has a much wider bearing on the plethora of agent-based pedestrian models: many of these are either based on $\mathcal{A}v$ or $\mathcal{I}n$, which limits their range of applicability to specific crowd regimes. These limitations have been observed by modelers beforehand, who, accordingly, put forward new or slightly different interactions in order to extend the models' range of applicability. This has sometimes led to non-minimal or 'mixed' interactions which can blur our understanding of the microscopic determinants of pedestrian motion. We have now clearly separated two essential mechanisms, as quantified by the intrusion number $\mathcal{I}n$ and the avoidance number $\mathcal{A}v$ which link the psychological and biomechanical underpinning with different flow regimes on the level of the whole crowd.

At present, however, only collisions between the hard-cores have been taken into account. This leads to many instances at which $\mathcal{A}v_i = 0$ who have been left aside in the averaged $\mathcal{A}v$. In reality, the 'softer' collisions, i.e. the anticipated intrusions into the private or intimate space, are also avoided. A more sophisticated, non-binary definition of $\mathcal{A}v$ should be able to capture these. This would also lead to a more sophisticated $\mathcal{A}v$-model,

where currently these effects can only be incorporated by choosing a larger size when calculating the anticipated collisions.

In our empirical analysis, the main focus has been put on asymptotic regimes. When moving further away from the origin of our 'phase' diagram the corresponding regimes get more and more complex. Thereby, results are difficult to interpret which is related to the stronger influence of headways even after applying the Butterworth filter but also owes to the fact that neither $\mathcal{A}v$ nor $\mathcal{I}n$ can be neglected. This is reflected in the theoretical description as well: away from the vicinity of the $\mathcal{A}v$ and $\mathcal{I}n$ axis, only the $\mathcal{A}v \star \mathcal{I}n$-model was able to replicate the essential features of crowd flow, as evidenced by the bidirectional flow as well as the intruder scenario at low-density. If the density is increased in the latter, the perturbative expansion breaks down and can not replicate the empirical findings.

While this breakdown is sensible for a linear expansion, it also points towards a specific limitation in the way anticipation is captured by the TTC and thus the $\mathcal{A}v$ number. In particular, the assumption of constant velocities is violated and more sophisticated anticipation strategies come into play that take into account future accelerations. Such problems are not only relevant for the intruder scenario, but also for corner-flows which are inherently 'non-linear' and, thus, difficult to replicate in any pedestrian model. Interestingly, in both cases, the intruder scenario and corner flows, 'successful' modelling approaches take long term planning into consideration, for instance by factoring in future costs or through a floor-field. In Appendix D another modelling approach is introduced which includes more complex anticipation strategies by bridging the gap between tactical and operational level. Here, each agent plans its trajectory multiple time steps ahead. The trajectory can here be pictured as a string connecting start and goal through space-time which the agents can deform or stretch according to their needs. In the presence of multiple agents, such complex anticipation strategies naturally pose questions related to game theory, which are much more difficult to solve than traditional modelling approaches. Developing models based on such elaborate anticipation strategies presents an important next step in modeling intelligent behaviour. It remains to be seen, if relatively simple and generic models can nonetheless be obtained that way.

Interestingly, we have encountered a 'non-linear' and yet simple anticipation strategy in the first chapter of this dissertation, namely, the time-gap which is grounded in the worst-case anticipation that the neighbors may suddenly come to a halt. This quantity is closely related to the fundamental diagram. To elaborate on this let us quickly summarize the main results of the first chapter.

Here, instead of trying to understand pedestrian dynamics by looking at the large picture we have considerably simplified the system by studying single-file motion. This simplicity

allowed us to closely investigate the meaning of different parameters as well as to unveil connections between different models. More importantly, we have found that models based on the TTC (and thus $\mathcal{A}v$) or models grounded in a distance-based repulsion (i.e., based on $\mathcal{I}n$) are not well suited to describe single-file motion. Models that originate in vehicular traffic based on the time-gap, on the other hand, capture the essential properties of single-file motion. This stands in contrast to the line of argumentation followed above, where we have stated that in most scenarios the dynamics of the agents are mostly controlled by $\mathcal{I}n$ and $\mathcal{A}v$. However, we have also found that neither $\mathcal{I}n$ nor $\mathcal{A}v$ on its own include a mechanism to replicate the fundamental diagram. The fundamental diagram is however well described by the time-gap which, for instance, shows the expected scaling behavior between vehicular, bicycle, and pedestrian traffic. Consequently, we have discussed whether a third dimensionless variable, the Risk-of-Following number $\mathcal{T}$ based on time-gaps could be a third axis of our 'phase' diagram. However, it would still need to prove its empirical relevance in crowds.

The observed similarity between the fundamental diagram of vehicular and pedestrian traffic, however, seems not to apply for high densities [91] where other effects such as motivation or biomechanical constraints come into play. Such effects have been emphasized in [196] where a forbidden region of the fundamental diagram has been identified by analyzing pedestrians at different levels of motivation, i.e., from waiting to fleeing at a bulls' race. Based on these findings, the same authors proposed a classification of crowds based on motivation and congestion where each regime is tied to a different fundamental diagram [197]. These findings strongly indicate that not a single effect or mechanism governs the emergence of the fundamental diagram but different constraints and heuristics come into play depending on the regime. This is reflected in the strong disagreement that exists regarding the maximum flow and the density at which this maximum is reached. More notably, the density at which the flow is expected to approach zero ranges over a large interval [42]. Paying close attention to the multidirectionality of the flow helped to clarify some of these controversies [147]. Tieing the different shapes of the fundamental diagram to their psychological and biomechanical underpinning and thereby to the different regimes of crowd flows would be a crucial next step in developing a more comprehensive theory of crowd flows.

With regard to regimes at very high $\mathcal{I}n$ number, a more realistic shape of pedestrians and mechanical interactions would be needed. In such regimes the naming of the 'Avoidance number' $\mathcal{A}v$ becomes ambiguous, because not every anticipated collision can or is tried to be avoided as we come to realize when studying pushing behaviour at bottlenecks. The occurrence of physical contact also states a 'breakdown' of the analogy between vehicular and pedestrian traffic which we have drawn in the first chapter. While in the former collisions are dangerous in any case, they are non-critical or even fun at many

instances in the latter. This is exemplified by mosh pits at rock-concerts [198] but also becomes apparent when conducting experiments: many participants are eager to perform high motivation runs or pushing experiments. Of course, this can switch completely in cases when the situation becomes potentially hazardous and people can not leave the crowd at any time. Understanding these regimes is crucial to get insight into hazardous situations. New experimental methods in crowds like tracking shoulder movement [37] or even complete body posture [39] as well as measuring contact forces through pressure sensors [38] have given complementary insights into these regimes. These need to be facilitated by models for pedestrian streams as well.

Beyond that, other dimensionless numbers can, and certainly should, be introduced to describe specific features of crowd dynamics such as an analogue of the Mach number to quantify the propagation of waves or information in crowds. A variant of the Péclet number (diffusion over advection), which is frequently used to characterize active systems, e.g., [199], could be defined to account for the variability in the outcome of nominally similar experiments caused by some unknown parameters. In models this would be reflected by introducing noise or stochasticity which we only considered in the case of single-file motion.

Interestingly, such a series of dimensionless numbers would allow to successively depart from very simple systems to more complex ones: while along the $\mathcal{I}n$-axis agents do not differ from particles subjected to distance-based interactions, $\mathcal{A}v$ introduces a velocity based component in the interaction violating the reciprocity of forces. Paying attention to effects of limited perception would introduce another violation of that principle, which has important implications for active systems [200]. This sets the stage for a general theoretical study of the statistical physics of pedestrian assemblies. In particular, it should be tried to derive a macroscopic flow theory by starting from regimes at which $\mathcal{A}v = 0$, and thus interactions are local. Relaxing that constraint one would face challenges raised by the non-locality inherent to the Avoidance number. Such a macroscopic flow theory would be an important step in understanding the fundamental differences between the diverse active systems.

In terms of practical purposes, the classification of crowds put forward here should be used as a basis to develop an extended Level of Service concept. It would be better suited to capture the comfortability but also risk-profiles of real pedestrian facilities. Apart from that it should be tested as a tool for real-time risk assessment of pedestrian assemblies: a map showing $\mathcal{A}v$ and $\mathcal{I}n$ as spatially resolved values could help crowd managers to identify potentially hazardous situations timely.

Afterword

I would like to end with some more general considerations. In many fields of science, mathematical descriptions have become increasingly important. This is true for crowds, but also for biology, as exemplified by the growing number of physicists that engage in its investigation. But also in the social sciences, for example in economics, where the introduction of game theory was an important step in its transformation into a mathematical discipline. A quantitative description brings order and objectivity to what might otherwise be considered a somewhat 'vague' social science. This is particularly valuable in the study of emergent behavior, where relatively simple assumptions lead to unexpected and complex behavior - this is where the tools of statistical physics and agent-based modeling seem invaluable.

On the other hand, the use of sophisticated mathematics can just create a sense of precision and objectivity. Especially for those who are not 'fluent' in math or programming, models are black boxes, that seem to allow, like a magic trick, to predict the outcome of hypothetical situations. This can be encouraged by the way models are presented: as scientists are incented to emphasize the 'usefulness' of their work and negative results are generally hard to publish, results can be oversold. More worryingly, in commercial software, the assumptions are typically proprietary and fancy visualizations may indicate a false level of detail. For example, commercial crowd modeling software typically visualizes pedestrians as 3d humans including detailed stepping processes even though the underlying model presumably treats pedestrians as disks navigating in the 2d plane.

Ever since I started thinking about physics outside of its traditional branches, I have been two-minded about it. With regard to pedestrian dynamics, by writing this thesis, I am now convinced that employing tools from statistical physics truely facilitates a deeper understanding of crowds. This conviction could only be established because of the high quality empirical data that exists for crowds. With respect to other fields, especially those with fewer experimental opportunities and much more complex initial and boundary conditions, I remain sceptikally interested in what physics has to offer to improve our understanding of the world.

Appendix A

The Fundamental Diagram of the Social-Force Model

In the main text we have stated that the social-force model, in its simplest form struggles to replicate the fundamental diagram. In this appendix we will investigate this in more detail. In particular, we will non-dimensionalize the equations of motion to identify the essential parameters which determine the fundamental diagram of the homogeneous solution (cf. the definition in section 3.3.1) in single-file motion.

For simplicity, let us consider the overdamped social-force model given by

$$v_i = v_{\text{des}} - \alpha \sum_{j \neq i} k_{ij} e^{-\frac{\Delta x_{ij} - \ell}{r_{\text{soc}}}}, \tag{A.1}$$

where the factor k_{ij} models an anisotropy in the interaction. The following discussion applies equally to the second-order social-force model, as long as its homogeneous solution is stable.

Let us start by noting that, if $k_{ij} = 1$ the homogeneous solution would simply be given by $v_i = v_{\text{des}}$ for all agents i as each agent is equally repelled from the agent in the front as from the agent in the back.

In single-file motion it is, however, usually assumed that the interaction is restricted to the agent in front which simplifies the model to

$$v_i = v_{\text{des}} - \alpha e^{-\frac{\Delta x_i - \ell}{r_{\text{soc}}}}. \tag{A.2}$$

Let us identify the essential parameters by non-dimensionalizing Eq. (A.2). As we argue in more detail in section 3.3.5, a suitable length scale is the agents' size ℓ and a suitable
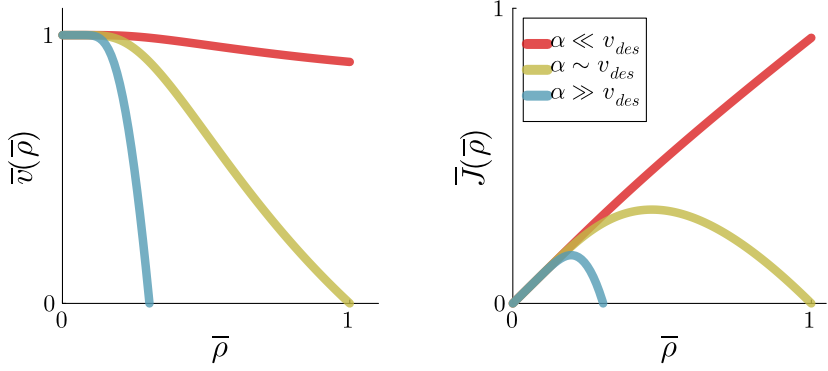
FIGURE A.1: The non-dimensional fundamental diagram of the simple social-force model in the typical representations with $\pi_1 = \alpha/v_{\text{des}}$ varied and $\pi_2 = 1$, i.e. the size of the pedestrians is as large as the length-scale at which the interaction decays. The legend applies for both diagrams.

second scale is the velocity v_{des}. Inserting these into Eq. (A.2) we arrive at

$$\overline{v}_i = 1 - \pi_1 e^{-\pi_2(\Delta \overline{x}_i - 1)}, \tag{A.3}$$

where we have been able to reduce the number of parameters from four parameters - v_{des}, α, ℓ, and r_{soc} - to two parameters $\pi_1 = \alpha/v_{\text{des}}$ and $\pi_2 = \ell/r_{\text{soc}}$. To obtain the fundamental diagram of the homogeneous solution we simply exchange $\overline{\rho} = 1/\Delta \overline{x}_i$ and obtain

$$\overline{v}(\overline{\rho}) = 1 - \pi_1 e^{-\pi_2(1/\overline{\rho}-1)} \text{ and } \overline{J}(\overline{\rho}) = \overline{\rho}\left(1 - \pi_1 e^{-\pi_2(1/\overline{\rho}-1)}\right). \tag{A.4}$$

Let us start by investigating the influence of $\pi_1 = \alpha/v_{\text{des}}$ which determines the relative strength between driving force and repulsion. Therefore we will fix $\pi_2 = 1$, i.e., assume that the size of the agents equals the length scale of the interactions. The corresponding fundamental diagrams are depicted in Fig. A.1. It can be seen that, in order to reproduce the fundamental diagram, one has to chose $\pi_1 \sim 1$ as it leads to a vanishing flow at $\overline{\rho} = 1$. Otherwise if any of the two, driving force or repulsion, is predominant either a high flow is maintained at high densities (dominant driving) or the flow becomes zero for small densities already (dominant repulsion).

Let us now fix $\pi_1 = 1$ and vary π_2. As it can be seen in Fig. A.2 the capacity in- or decreases and is reached at larger or smaller densities $\overline{\rho}$. If the size of the agents is much larger than the length of the interaction, the maximum is reached at larger densities $\overline{\rho}$ and reaches higher flows and vice-versa if the interaction length is much larger than the
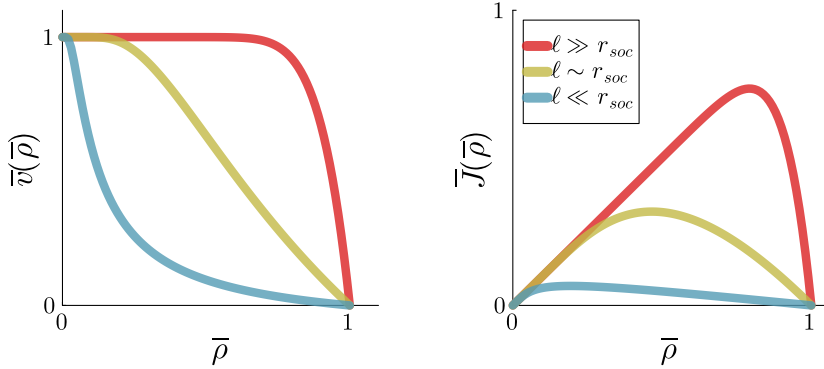
FIGURE A.2: The non-dimensional fundamental diagram of the simple social-force model in the typical representations with $\pi_2 = \ell/r_{\text{soc}}$ varied and $\pi_1 = 1$, i.e. the strength of the driving term is equally strong as the distance based-repulsion. The legend applies for both diagrams.

size of the agents. If both $\pi_1 \sim 1$ and $\pi_2 \sim 1$ the resulting fundamental diagram shows a realistic shape.

Thus, parameters can be chosen to replicate the fundamental diagram of single-file motion. However, typically the parameter values are chosen quite differently, e.g., $\pi_1 = 33$ and $\pi_2 = 7.5$ in [60] or $\pi_1 = 33$ or $\pi_2 = 0.5$ in [189]. Accordingly, the fundamental diagram using the parameters specified in [60] was shown to be unrealistic [30].

Besides, it is highly questionable if one set of parameters can replicate the fundamental diagram of both single-file motion and a wider uni-directional corridor: due to the superposition of the repulsion, the number of nearest neighbors in front has a strong influence on the fundamental diagram in the model. Empirically, however, it has been shown that there is no significant difference between the fundamental diagram of these two scenarios [170]. Such effects could be mitigated by taking into account the dependency of space requirement on the speed, as for instance proposed in [108].

Appendix B

The Harmonic Oscillator

The role of inertia can be understood most easily using the damped harmonic oscillator. A body or particle is subject to different forces: 1) an elastic or restoring force that is proportional to the displacement x from the equilibrium position of the body and 2) a frictional damping force that is proportional to its velocity $v = \dot{x}$. The equation of motion is then given by

$$m\frac{d^2x}{dt^2} + \gamma\frac{dx}{dt} + kx = 0, \tag{B.1}$$

where m is the inertial mass of the body and γ and k are proportionality constants for the frictional and elastic force, respectively. For convenience, one introduces the relaxation time $\tau = \frac{m}{\gamma}$ and the free oscillation frequency $\omega_0^2 = \frac{k}{m}$.

Three different types of solutions of Eq. (B.1) exist, depending on the relative values of the proportionality constants m, γ and k. The different cases are depicted in Fig. B.1.

1. Underdamped: for $k < \frac{\gamma^2}{4m}$ the body performs an oscillating motion with decreasing amplitude; the solution has the form $x(t) = x_0 e^{-t/2\tau} \sin(\omega t + \varphi)$ where x_0 and φ are determined by initial conditions. The frequency ω is smaller than the free frequency ω_0 which is reached in the limit of vanishing damping ($\gamma \to 0$).

2. Overdamped: for $k > \frac{\gamma^2}{4m}$ no oscillations occur and the body returns exponentially fast to the equilibrium position; the solution then has the form $x(t) = e^{-t/2\tau}\left(Ae^{\alpha t} + Be^{-\alpha t}\right)$ where α depends on k, m, γ and A, B on the initial conditions.

3. Critically damped: for $k = \frac{\gamma^2}{4m}$ the body returns quickly to the equilibrium position; the solution has the form $x(t) = e^{-t/2\tau}\left(A + Bt\right)$ with A, B on determined by the initial conditions.
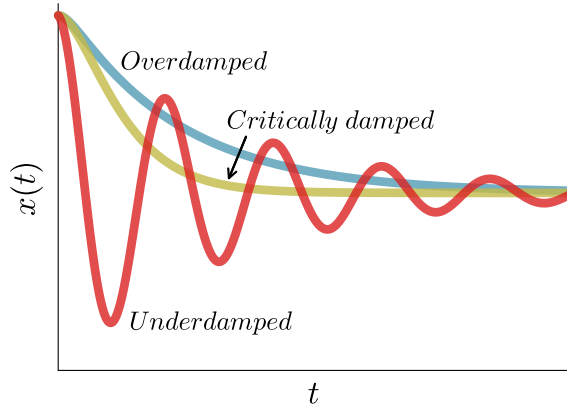
FIGURE B.1: Schematic representation of the behavior in the three regimes of a damped harmonic oscillator. Red: underdamped, blue: overdamped, yellow: critically damped.

The behavior in the overdamped regime is similar to that without inertia, i.e. for $m = 0$. Therefore, the dynamics in this regime is well described by a 1st order equation.

Appendix C

Linear Stability Analysis

In this part of the Appendix we analyze the linear string stability of the model defined by (FVDM, del). Its equations of motion for N agents on a ring of length L reads

$$x_1(t + \tau_R) = \alpha \left(x_2(t) - x_1(t) - \ell \right) + \beta \left(\dot{x}_2(t) - \dot{x}_1(t) \right),$$

$$...$$

$$x_{N-1}(t + \tau_R) = \alpha \left(x_N(t) - x_{N-1}(t) - \ell \right) + \beta \left(\dot{x}_N(t) - \dot{x}_{N-1}(t) \right),$$

$$x_N(t + \tau_R) = \alpha \left(x_1(t) - x_N(t) + L - \ell \right) + \beta \left(\dot{x}_1(t) - \dot{x}_N(t) \right),$$

(C.1)

with $\alpha = 1/T$ and $\beta = \tau_A/T$. The equilibrium values $\Delta x^{eq} = 1/\rho$ and $v^{eq} = \alpha(\Delta x^{eq} - \ell)$ define the equilibrium solution

$$x_i^{eq}(t) = x_i^{eq}(0) + t v^{eq} \text{ for } \forall i \in [1, N]. \tag{C.2}$$

The differences between Eq. (C.1) and Eq. (C.2) are

$$\bar{x}_1(t + \tau_R) = \alpha \left(x_2(t) - x_1(t) \right) + \beta \left(\dot{x}_2(t) - \dot{x}_1(t) \right),$$

$$...$$

$$\bar{x}_{N-1}(t + \tau_R) = \alpha \left(x_N(t) - x_{N-1}(t) \right) + \beta \left(\dot{x}_N(t) - \dot{x}_{N-1}(t) \right),$$

$$\bar{x}_N(t + \tau_R) = \alpha \left(x_1(t) - x_N(t) \right) + \beta \left(\dot{x}_1(t) - \dot{x}_N(t) \right),$$

(C.3)

which can be rewritten as a single vector equation

$$\vec{y}(t + \tau_R) + \alpha \vec{y}(t) + \beta \dot{\vec{y}}(t) = \alpha \Lambda \vec{y}(t) + \beta \Lambda \dot{\vec{y}}(t), \tag{C.4}$$

with $\vec{y}(t) = (\bar{x}_1(t), ..., \bar{x}_{N-1}(t), \bar{x}_N(t))^T$ and Λ the shifting operator, i.e. $\Lambda \vec{y}(t) = (\bar{x}_2(t), ..., \bar{x}_{N-1}(t), \bar{x}_N(t), \bar{x}_1(t))^T$.

A linear delayed differential system is solved by a linear combination of exponential terms. Let us, therefore, assume that

$$y_i(t) = \gamma_i e^{\lambda t} \text{ for } i \in [1, N].$$ (C.5)

Then the characteristic polynomial is obtained as

$$\lambda e^{\lambda \tau_R} + \alpha + \beta \gamma - (\alpha + \beta \lambda) \, \epsilon_k = 0,$$ (C.6)

with $\epsilon_k = \exp\left(i2\pi(k-1)/N\right)$. Note that, for $k = 1$ Eq. (C.6) is solved by $\lambda = 0$. For $k \in [2, N]$, however, the equation can not be solved. Therefore, the critical points with $Re(\lambda) = 0$ are analyzed. Let us write $\lambda = i\omega$ and $\epsilon_k = c_k + is_k = \cos\left(2\pi(k-1)/N\right) + i\sin\left(2\pi(k-1)/N\right)$. The characteristic equation Eq. (C.6) can be divided into the real and imaginary parts as

$$\begin{aligned} -\omega \sin(\omega\tau) + \alpha \left(1 - c_k\right) + \beta s_k &= 0, \\ \omega \cos(\omega\tau) + \beta\omega \left(1 - c_k\right) - \alpha s_k &= 0. \end{aligned}$$ (C.7)

These equations give rise to the critical parameter values

$$\begin{aligned} \alpha_{CR} &= \frac{\omega}{2} \left(\sin(\omega\tau) + \cos(\omega\tau) \frac{s_k}{1 - c_k} \right), \\ \beta_{CR} &= \frac{1}{2} \left(\sin(\omega\tau) \frac{s_k}{1 - c_k} - \cos(\omega\tau) \right). \end{aligned}$$ (C.8)

The curves are plotted in Fig. C.1. In contrast to the other models in section 3.3.2, no curve $(\alpha, \beta)_k$ confines the other curves. The lines intersect and no single line delimits a region for which stability conditions then might be obtained. The stability depends on many values of k, i.e., which wavelength is the most unstable depends on the model parameters. Therefore, a it can not be hoped to obtain a 'simple' stability condition. With the result Eq. (C.8), however, the stability condition can easily be visualized and numerically be obtained by finding the maximum T for a single τ_A for all k and large N as in Fig. 3.8.
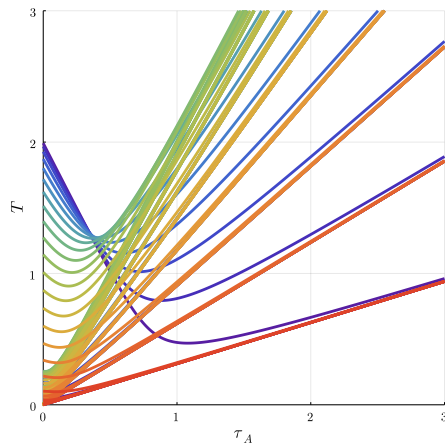
FIGURE C.1: The critical curves of (τ_A, T) with $\tau_A = \beta/\alpha$ and $T = 1/\alpha$ for $\tau_R = 1$ and $N = 20$.

Appendix D

Spin Off: Merging Operational and Tactical Level

As we have argued in the main text, originally most modelling approaches were based on a distance dependent interaction. Limitations of such models have led to the proposal of numerous models which include anticipation in different ways. In that regard, we have shown, following [82], that the time-to-collision accurately captures anticipation in a way that is essential in many regimes of crowd flow. However, we have mainly focussed on the asymptotic regimes, at low $\mathcal{I}n$ numbers. By studying the intruder scenario we found that more complex anticipation strategies are needed, in particular the assumption of constant velocities is violated and, consequently, the observed behaviour can no longer be modelled based on the TTC.

Another, even simpler, example are corner flows, as investigated, e.g., in [201]. Such 'non-linear' scenarios are often inadequately described by models, in which corners effectively act as a strong bottleneck, leading to heavy congestions [187]. This is related to (at least) two factors: the desired velocity is no longer constant but strongly depends on the position of the agent. This is typically achieved by including a floor-field. Thus, the models can no longer be purely restricted to the operational level but the tactical level gains some influence as well. Secondly, and related to that, the assumption of constant velocities is heavily violated. Consequently, most anticipation strategies fail: agents struggle to solve conflicts at corners which can lead to an unrealistic reduction of flow in models.

In this part of the appendix we will discuss some premiliary ideas and results of a quite different modeling approach. Here we envision the trajectory of each agent as a flexible string connecting the start and the goal through space-time. Each agent individually
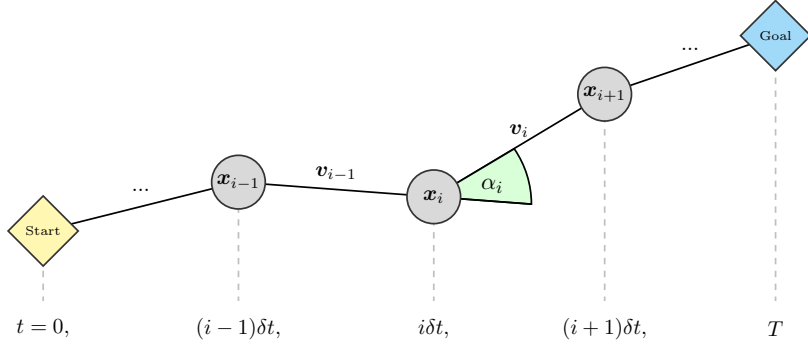
FIGURE D.1: Illustration of a typical trajectory $x \in \mathcal{X}$. Note that the velocities and angles are completely fixed by chosing the travel time T and the spatial coordinates $\boldsymbol{x}_i$.

adjusts its future trajectory according to some cost-function. Compared to traditional modelling approaches this means that the agents will plan many time steps ahead.

Let us assume a single agent who wants to navigate in a complex environment through space-time. She starts from $(\boldsymbol{x}_{\text{Start}}, t_0)$ and plans to arrive at the goal $(\boldsymbol{x}_{\text{Goal}}, t_0 + T)$, where T denotes the total travel-time. Let $\mathcal{X}$ denote the set of all possible trajectories x and total travel-times T connecting start and goal, discretised in time. In particular,

$$\begin{aligned} \mathcal{X} = \{ x = ([\boldsymbol{x}_1, \boldsymbol{x}_2, ..., \boldsymbol{x}_i, ..., \boldsymbol{x}_N], T) \, | \\ \boldsymbol{x}_i \in \mathbb{R}^2, \, \boldsymbol{x}_1 = \boldsymbol{x}_{\text{Start}}, \, \boldsymbol{x}_N = \boldsymbol{x}_{\text{Goal}} \text{ and } T \in \mathbb{R}^+ \}, \end{aligned} \tag{D.1}$$

where the subscript i indicates the time, i.e. $t = t_0 + i \cdot \delta t$ and $\delta t = T/N$. As mentioned above trajectories may be pictured as a flexible strings connecting start and goal through space-time. In order to achieve their goal, to avoid obstacles or areas of discomfort, the agent can change its route by deforming or stretching the string. In other words, change her route and velocity. A schematic trajectory is shown in Fig. D.1.

The agents deform or stretch their trajectory by minizing an energy functional. This functional assigns a scalar-valued energy to each trajectory $x \in \mathcal{X}$ as

$$E : \mathcal{X} \to \mathbb{R}, \, x \rightarrowtail E[x]. \tag{D.2}$$

In our model, the agent will follow the optimal trajectory x^{Final} which is given by the minimum of the energy-functional, i.e.

$$x^{\text{Final}} = \min_{x \in \mathcal{X}} E[x]. \tag{D.3}$$

Numerically the optimal trajectory is approximated by applying a gradient descent optimisation scheme to an initial guess. In particular, every element of the trajectory is moved down the energy gradient ∇E with the step-size α until some convergence criterium is met. This corresponds to the iterative scheme

$$x^j = x^{j-1} - \gamma \nabla E[x^{j-1}], \tag{D.4}$$

where the superscript j indicates the step. If not stated differently, the initial-guess is a straight line from $\boldsymbol{x}_{\text{Start}}$ to $\boldsymbol{x}_{\text{Goal}}$ with $T = v_{\text{des}}/d$ where v_{des} is the desired velocity and d the euclidian distance between start and goal.

The Energy Functional

This energy functional is given by superposition of different costs. In our case we chose the following factors

$$E[x] = E_{\text{Biomechanics}}[x] + E_{\text{Goal}}[x] + E_{\text{Comfort}}[x]. \tag{D.5}$$

The first term corresponds to the biomechanical energy needed to move, the second represents the desire to reach the goal, and the third quantifies the comfort along the trajectory. Each of these will be described in more detail below.

The biomechanical energy corresponds to the cost of propulsion. In [202] the energy consumption of people walking on a treadmill has been measured. The following function represents as reasonable fit to the obtained data, cf. [182],

$$f(v) = \begin{cases} 7.6v - 35.4v^2 & \text{for } v < 0.1\text{m/s}, \\ 0.4 + 0.6v^2 & \text{else.} \end{cases} \tag{D.6}$$

Accordingly, we define the biomechanical energy of a trajectory x as

$$E_{\text{Biomechanics}}[\boldsymbol{x}_1, \boldsymbol{x}_2, ..., \boldsymbol{x}_N] = \delta t \sum_{i=1}^{N} f(|\boldsymbol{v}_i|), \tag{D.7}$$

where the velocity is given by $\boldsymbol{v}_i = (\boldsymbol{x}_{i+1} - \boldsymbol{x}_i)/\delta t$.

The goal energy incorporates the desire of the agent to reach its goal. It is constructed from the assumption that, in the absence of any other agents or obstacles the agent should walk with $\boldsymbol{v}_{\text{des}}$ towards its goal. In particular, if $E_{\text{Comfort}} = 0$, the trajectory with

$|\boldsymbol{v}_i| = v_{\text{des}}$ is the global minimum of the energy E. This results in

$$E_{\text{Goal}}[\boldsymbol{x}_1, \boldsymbol{x}_2, ..., \boldsymbol{x}_N] = \alpha \delta t \sum_{i=1}^{N} \left(v_{\text{des}} f'(v_{\text{des}}) - f(v_{\text{des}}) \right). \tag{D.8}$$

The comfort energy is determined by two factors, the avoidance of uncomfortable regions, and the desire for a smooth trajectory without abrupt changes. The energy is given by

$$E_{\text{Comfort}}[\boldsymbol{x}_1, \boldsymbol{x}_2, ..., \boldsymbol{x}_N] = \sum_{i=1}^{N} \left(\eta(\boldsymbol{x}_i) \cdot |\boldsymbol{v}_i| + \beta \alpha_i^2 \right), \tag{D.9}$$

where the angle α_i is the angle between the lines from $\boldsymbol{x}_{i-1}$ to $\boldsymbol{x}_i$ and from $\boldsymbol{x}_i$ to $\boldsymbol{x}_{i+1}$. The field $\eta(\boldsymbol{x})$ assigns for each point in space a value between 0 (comfortable) and 1 (uncomfortable). It is multplied by the velocity to account for the fact that agents will be more cautious in regions of low comfort. Depending on the reason for discomfort this could be vice-versa. In our case, the field corresponds to the collision probability at position $\boldsymbol{x}_i$ at time $t_0 + i \cdot \delta t$.

To estimate this probability, assume a disk shaped obstacle of radius r_O and a disk shaped agent with radius r. Let us further assume that the initial position $\boldsymbol{x}_O$ is not perfectly known but subject to some uncertainty. We will model this uncertainty to be Gaussian with a standard deviation σ. The collision probability between the obstacle and the agent at position $\boldsymbol{x}_i$ is then given by

$$P_C(\boldsymbol{x}_i) = \iint_{|\boldsymbol{x} - (\boldsymbol{x}_i - \boldsymbol{x}_O)| \leq (r + r_O)} \frac{1}{2\pi\sigma^2} \exp\left[-\frac{|\boldsymbol{x} - (\boldsymbol{x}_i - \boldsymbol{x}_O)|^2}{2\sigma^2} \right] d\boldsymbol{x}, \tag{D.10}$$

where the velocities, or a time-dependent uncertainty could be introduced as well. The integral in Eq. (D.10) is often studied to estimate the collision probabilities of satellites. According to [203] it can be approximated by

$$P_C(\boldsymbol{x}_i) \approx \exp\left(-\frac{|\boldsymbol{x}_i - \boldsymbol{x}_O|^2}{2\sigma^2} \right) \cdot \left[1 - \exp\left(-\frac{(r + r_O)^2}{2\sigma^2} \right) \right]. \tag{D.11}$$

Let us now define the field $\eta(\boldsymbol{x}_i)$ by combining the collision probabilities of all (moving) obstacles. In especially

$$\eta(\boldsymbol{x}_i) = \sum_k P_C^k(\boldsymbol{x}_i) - \sum_{k, l > k} \left(P_C^k(\boldsymbol{x}_i) \cdot P_C^l(\boldsymbol{x}_i) \right). \tag{D.12}$$

Thereby we have defined all factors that determine our energy functional in Eq. (D.5). Let us now test the model.

Results

Let us test our model in a simple scenario, i.e. a static obstacle placed in the centre of a narrow corridor, as it was empirically conducted in [204]. In Fig. D.2 the field $\eta(\boldsymbol{x})$ is visualized with the optimal trajectory in *(a)* and the convergence of the numerical scheme is shown in *(b)*. Finally we have chosen the parameters such that the resulting trajectory matches the experimental results reasonably well, cf. *(c)*.[1]

Let us now take a second minimal example, namely a single agent that moves around a corner. As an input we will be using the experimental data from [164] and keep the parameters the same as above. The results are depicted in Fig. D.3 - our model reasonably well aligns with the empirical trajectory.

Even though the development of this model is still in a very early stage, the results are quite promising. Arguably, the model is unfinished and multiple interacting agents are not included yet. While it is straightforward to incorporate agents into the energy functional defined above, close attention will have to be paid to the update procedure. So far, we have dealt with a single agent only, therefore it does not make a difference whether the trajectory is planned once, from the beginning to the end, or if the agents will make corrections during walking. In the presence of unexpected changes, e.g. reactions from other agents due to the trajectories that has been chosen such questions will arise. Essentially, so far we faced an optimal control problem, whereas in the presence of other agents the model will become a differential game. This will raise questions of Nash Equilibria or solutions with imperfect knowlegde. Such considerations might be needed if complex anticipation strategies in crowds ought to be modelled in future.

---

[1]The following parameter have been used $v_{\mathrm{des}} = 1.29$m/s, $\delta t = 0.2$s, $\alpha = 1$, $\beta = 0.125$, $\sigma = 0.3$, $r = 0.15$m and $\gamma = 0.0001$.

(a) The Field $\eta(\boldsymbol{x})$ and x^{Final}

(b) The convergence of the numerical procedure

(c) Experimental data and x^{Final}
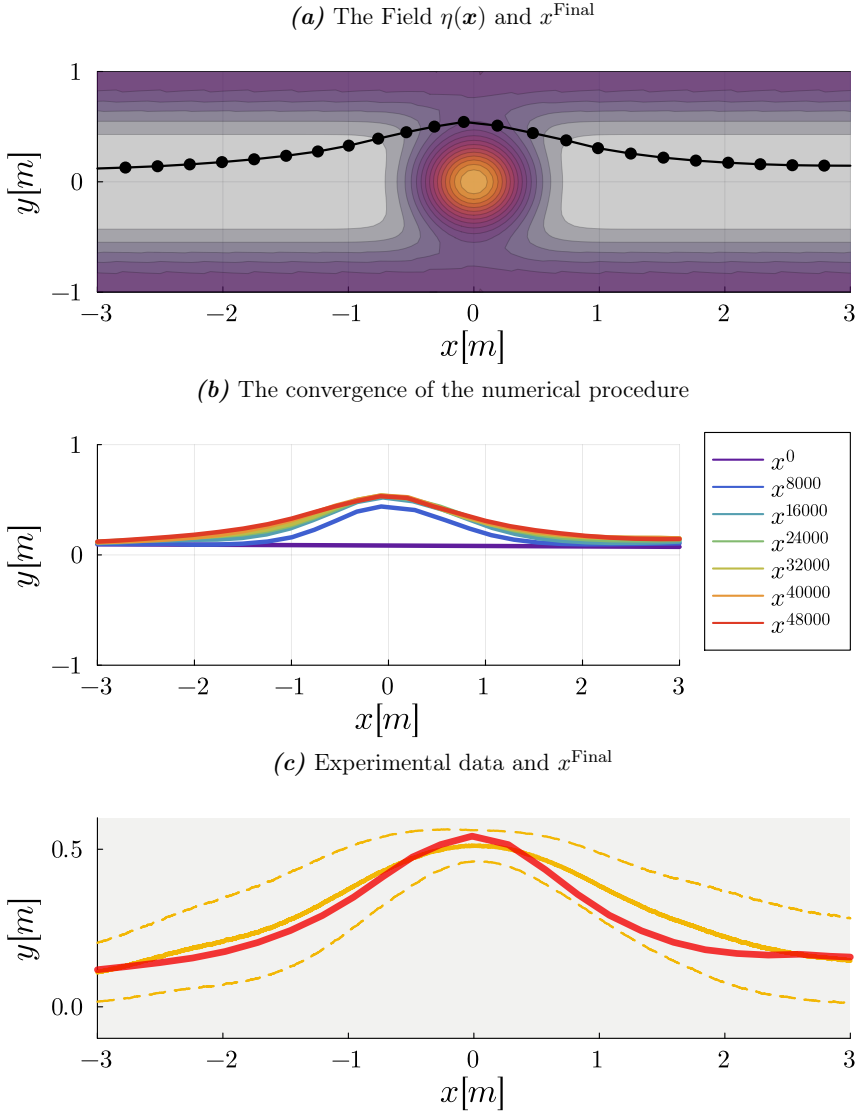
FIGURE D.2: The proposed model applied to a corridor with a static obstacle in the centre, as empirically investigated by [204]. In **(a)** We display the field $\eta(\boldsymbol{x})$, where grey corresponds to $\eta(\boldsymbol{x}) = 0$ (comfortable) and yellow to $\eta(\boldsymbol{x}) = 1$ (uncomfortable). The black line represents the optimal trajectory which discretization is indicated by the black circles. In **(b)** the convergence of the numerical procedure is verified. In **(c)** the result (red) is compared to the empirical data, i.e., the mean trajectory (yellow) with its standard deviation indicated by the dashed line.
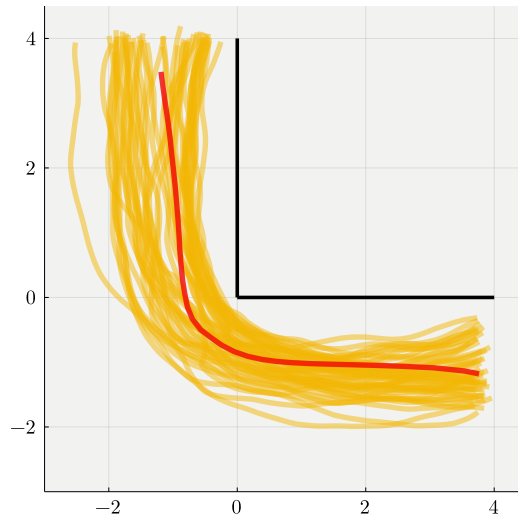
FIGURE D.3: Single agents walk around a corner. The yellow lines correspond to different single agents going around the corner. Note that each pedestrian *individually* walked around the corner. The red line depicts the result of the proposed model.

Bibliography

[1] *Physics of Life*. National Academies Press, Washington, D.C., December 2022. ISBN 978-0-309-27400-5. doi:10.17226/26403.

[2] Franklin, R.E. and Gosling, R.G. Molecular Configuration in Sodium Thymonucleate. *Nature*, 171(4356):740–741, April 1953. ISSN 1476-4687. doi:10.1038/171740a0.

[3] Balzarotti, F., Eilers, Y., Gwosch, K.C., Gynnå, A.H., Westphal, V., Stefani, F.D., Elf, J., and Hell, S.W. Nanometer resolution imaging and tracking of fluorescent molecules with minimal photon fluxes. *Science (New York, N.Y.)*, 355(6325):606–612, February 2017. doi:10.1126/science.aak9913.

[4] Nicholson, D.J. Is the cell really a machine? *Journal of Theoretical Biology*, 477: 108–126, September 2019. ISSN 0022-5193. doi:10.1016/j.jtbi.2019.06.002.

[5] Shaebani, M.R., Wysocki, A., Winkler, R.G., Gompper, G., and Rieger, H. Computational models for active matter. *Nature Reviews Physics*, 2(4):181–199, April 2020. ISSN 2522-5820. doi:10.1038/s42254-020-0152-1.

[6] Levine, H. and I. Goldman, D. Physics of smart active matter: Integrating active matter and control to gain insights into living systems. *Soft Matter*, 19(23):4204–4207, 2023. doi:10.1039/D3SM00171G.

[7] Weber, W.E. and Weber, E.F. *Mechanik der menschlichen Gehwerkzeuge: eine anatomisch-physiologische Untersuchung*. Dieterich, 1836.

[8] Roberts, M., Mongeon, D., and Prince, F. Biomechanical parameters for gait analysis: A systematic review of healthy human gait. *Physical Therapy and Rehabilitation*, 4(1):6, 2017. ISSN 2055-2386. doi:10.7243/2055-2386-4-6.

[9] Le Bon, G. *The Crowd*. The British Library, 1895.

[10] Drury, J., Cocking, C., and Reicher, S. Everyone for themselves? A comparative study of crowd solidarity among emergency survivors. *British Journal of Social Psychology*, 48(3):487–506, 2009. ISSN 2044-8309. doi:10.1348/014466608X357893.

[11] Lügering, H., Tepeli, D., and Sieben, A. It's (not) just a matter of terminology: Everyday understanding of "Mass panic" and alternative terms. *Safety Science*, 163:106123, July 2023. ISSN 0925-7535. doi:10.1016/j.ssci.2023.106123.

[12] Giavina, E. *Der Hoftheaterbrand in Karlsruhe Am 28. Februar 1847: Dessen Entstehung, Verlauf Und Folgen; Beschrieben Aus Mitteilungen Geretteter Augenzeugen Und Andern Zuverlässigen Materialien.* Macklot, 1847.

[13] Predtechenskii, V.M. and Milinskii, A.I. *Planning for Foot Traffic Flow in Buildings.* Amerind Publishing, New Delhi, 1979.

[14] Hirai, K. and Tarui, K. A simulation of the behavior of a crowd in panic. In *Proc. of the 1975 International Conference on Cybernetics and Society*, pages 409–411, 1975.

[15] Burstedde, C., Klauck, K., Schadschneider, A., and Zittartz, J. Simulation of pedestrian dynamics using a two-dimensional cellular automaton. *Physica A: Statistical Mechanics and its Applications*, 295:507–525, 2001. doi:10.1016/S0378-4371(01)00141-8.

[16] Helbing, D. and Molnár, P. Social force model for pedestrian dynamics. *Physical Review E: Statistical Physics, Plasmas, Fluids, and Related Interdisciplinary Topics*, 51:4282–4286, 1995. doi:10.1103/PhysRevE.51.4282.

[17] Feliciani, C., Shimura, K., and Nishinari, K. *Introduction to Crowd Management.* Springer, Cham, Switzerland, 2021.

[18] Murakami, H., Feliciani, C., Nishiyama, Y., and Nishinari, K. Mutual anticipation can contribute to self-organization in human crowds. *Science Advances*, 7:eabe7758, March 2021. doi:10.1126/sciadv.abe7758.

[19] Bacik, K.A., Bacik, B.S., and Rogers, T. Lane nucleation in complex active flows. *Science (New York, N.Y.)*, 379(6635):923–928, March 2023. doi:10.1126/science.add8091.

[20] Echeverría-Huarte, I., Nicolas, A., Hidalgo, R.C., Garcimartín, A., and Zuriguel, I. Spontaneous emergence of counterclockwise vortex motion in assemblies of pedestrians roaming within an enclosure. *Scientific Reports*, 12(1):2647, December 2022. ISSN 2045-2322. doi:10.1038/s41598-022-06493-0.

[21] Garcimartín, Angel., Zuriguel, Iker., Pastor, J.M., Martín-Gómez, C., and Parisi, D.R. Experimental evidence of the "Faster Is Slower" Effect. *Transportation Research Procedia*, 2(0):760–767, 2014. ISSN 2352-1465. doi:http://dx.doi.org/10.1016/j.trpro.2014.09.085.

[22] Schadschneider, A. and Seyfried, A. Validation of CA Models of Pedestrian Dynamics with Fundamental Diagrams. *Cybernetics and Systems*, 40(5):367–389, July 2009. doi:10.1080/01969720902922400.

[23] 20414:2020, I.S.. Fire safety engineering — Verification and validation protocol for building fire evacuation models. Standard 20414, ISO, November 2020.

[24] Martinez-Gil, F., Lozano, M., Garcia-Fernandez, I., and Fernandez, F. Modeling, evaluation, and scale on artificial pedestrians: A literature review. *ACM Computing Surveys (CSUR)*, 50:72, 2017. doi:10.1145/3117808.

[25] Schadschneider, A., Chraibi, M., Seyfried, A., Tordeux, A., and Zhang, J. Pedestrian Dynamics: From Empirical Results to Modeling. In Gibelli, L., editor, *Crowd Dynamics, Volume 1*, Modeling and Simulation in Science, Engineering and Technology, pages 63–102. Springer International Publishing, 2018. ISBN 978-3-030-05128-0 (print).

[26] Chraibi, M., Tordeux, A., Schadschneider, A., and Seyfried, A. Modelling of Pedestrian and Evacuation Dynamics. In Meyers, R.A., editor, *Encyclopedia of Complexity and Systems Science*, pages 1–22. Springer, Berlin, Heidelberg, 2018. ISBN 978-3-642-27737-5. doi:10.1007/978-3-642-27737-5_705-1.

[27] Maury, B. and Faure, S. *Crowds in Equations: An Introduction to the Microscopic Modeling of Crowds*. World Scientific Publishing, Hackensack, NJ, September 2018. ISBN 978-1-78634-551-6. doi:10.1142/q0163.

[28] Fruin, J.J. *Pedestrian Planning and Design*. Elevator World, New York, 1971.

[29] Schadschneider, A., Chowdhury, D., and Nishinari, K. *Stochastic Transport in Complex Systems: From Molecules to Vehicles*. Elsevier, Amsterdam Boston Heidelberg, 2011. ISBN 978-0-444-52853-7.

[30] Best, A., Narang, S., Curtis, S., and Manocha, D. DenseSense: Interactive crowd simulation using density-dependent filters. In *Proceedings of the ACM SIGGRAPH/Eurographics Symposium on Computer Animation*, SCA '14, pages 97–102, Goslar, DEU, July 2015. Eurographics Association.

[31] Zanlungo, F., Feliciani, C., Yücel, Z., Jia, X., Nishinari, K., and Kanda, T. A pure number to assess "Congestion" in pedestrian crowds. *Transportation Research Part C: Emerging Technologies*, 148:104041, March 2023. ISSN 0968-090X. doi:10.1016/j.trc.2023.104041.

[32] Adrian, J., Bode, N., Amos, M., Baratchi, M., Beermann, M., Boltes, M., Corbetta, A., Dezecache, G., Drury, J., Fu, Z., Geraerts, R., Gwynne, S., Hofinger, G., Hunt, A., Kanters, T., Kneidl, A., Konya, K., Köster, G., Küpper, M.,

Michalareas, G., Neville, F., Ntontis, E., Reicher, S., Ronchi, E., Schadschneider, A., Seyfried, A., Shipman, A., Sieben, A., Spearpoint, M., Sullivan, G.B., Templeton, A., Toschi, F., Yücel, Z., Zanlungo, F., Zuriguel, I., der Wal, N.V., van Schadewijk, F., von Krüchten, C., and Wijermans, N. A glossary for research on human crowd dynamics. *Collective Dynamics*, 4:1–13, March 2019. ISSN 2366-8539. doi:10.17815/cd.2019.19.

[33] Lee, D., Lishman, J., and Thomson, J. Regulation of gait in long jumping. *Journal of Experimental Psychology: Human Perception and Performance*, 8:448–459, June 1982. doi:10.1037/0096-1523.8.3.448.

[34] Chatagnon, T. *Standing Balance Recovery Strategies Following External Perturbations : A Multiscale Approach with Applications to Dense Crowds.* PhD thesis, Université de Rennes, December 2023.

[35] Tailleur, J., Gompper, G., Marchetti, M.C., Yeomans, J.M., and Salomon, C. *Active Matter and Nonequilibrium Statistical Physics: Lecture Notes of the Les Houches Summer School: Volume 112, September 2018.* Oxford University Press, October 2022. ISBN 978-0-19-267409-8.

[36] Gompper, G., Winkler, R.G., Speck, T., Solon, A., Nardini, C., Peruani, F., Löwen, H., Golestanian, R., Kaupp, U.B., Alvarez, L., Kiørboe, T., Lauga, E., Poon, W.C.K., DeSimone, A., Muiños-Landin, S., Fischer, A., Söker, N.A., Cichos, F., Kapral, R., Gaspard, P., Ripoll, M., Sagues, F., Doostmohammadi, A., Yeomans, J.M., Aranson, I.S., Bechinger, C., Stark, H., Hemelrijk, C.K., Nedelec, F.J., Sarkar, T., Aryaksama, T., Lacroix, M., Duclos, G., Yashunsky, V., Silberzan, P., Arroyo, M., and Kale, S. The 2020 motile active matter roadmap. *Journal of Physics: Condensed Matter*, 32(19):193001, February 2020. ISSN 0953-8984. doi:10.1088/1361-648X/ab6348.

[37] Boomers, A.K., Boltes, M., and Kersting, U.G. How Approaching Angle, Bottleneck Width and Walking Speed Affect the Use of a Bottleneck by Individuals. *Sensors*, 24(6):1720, January 2024. ISSN 1424-8220. doi:10.3390/s24061720.

[38] Feldmann, S. and Adrian, J. Forward propagation of a push through a row of people. *Safety Science*, 164:106173, August 2023. ISSN 0925-7535. doi:10.1016/j.ssci.2023.106173.

[39] Chatagnon, T., Olivier, A.H., Hoyet, L., Pettré, J., and Pontonnier, C. Stepping strategies of young adults undergoing sudden external perturbation from different directions. *Journal of Biomechanics*, 157:111703, August 2023. ISSN 0021-9290. doi:10.1016/j.jbiomech.2023.111703.

[40] Steffen, B. and Seyfried, A. Methods for measuring pedestrian density, flow, speed and direction with minimal scatter. *Physica A: Statistical Mechanics and its Applications*, 389(9):1902–1910, May 2010. ISSN 03784371. doi:10.1016/j.physa.2009.12.015.

[41] Schrödter, T., Hirt, C., Chraibi, M., and Kratz, K. PedestrianDynamics/PedPy: V1.0.2. Zenodo, October 2023.

[42] Schadschneider, A., Klingsch, W., Klüpfel, H., Kretz, T., Rogsch, C., and Seyfried, A. Evacuation Dynamics: Empirical Results, Modeling and Applications. In Meyers, R.A., editor, *Encyclopedia of Complexity and Systems Science*, pages 3142–3176. Springer, New York, NY, 2009. ISBN 978-0-387-30440-3. doi:10.1007/978-0-387-30440-3_187.

[43] Chattaraj, U., Seyfried, A., and Chakroborty, P. Comparison of pedestrian fundamental diagram across cultures. *Advances in Complex Systems*, 12(3):393–405, 2009. doi:10.1142/S0219525909002209.

[44] Jelić, A., Appert-Rolland, C., Lemercier, S., and Pettré, J. Properties of pedestrians walking in line: Fundamental diagrams. *Physical Review E*, E 85(85):9, March 2012. doi:10.1103/PhysRevE.85.036111.

[45] Liu, X., Song, W., and Zhang, J. Extraction and quantitative analysis of microscopic evacuation characteristics based on digital image processing. *Physica A: Statistical Mechanics and its Applications*, 388(13):2717–2726, July 2009. doi:10.1016/j.physa.2009.03.017.

[46] Seyfried, A., Portz, A., and Schadschneider, A. Phase Coexistence in Congested States of Pedestrian Dynamics. In Bandini, S., Manzoni, S., Umeo, H., and Vizzari, G., editors, *Cellular Automata*, volume 6350, pages 496–505. Springer, Berlin, Heidelberg, 2010. ISBN 978-3-642-15978-7 978-3-642-15979-4. doi:10.1007/978-3-642-15979-4_53.

[47] Navin, F.P. and Wheeler, R.J. Pedestrian flow characteristics. *Traffic Engineering, Inst Traffic Engr*, 39, July 1969.

[48] Feliciani, C. and Nishinari, K. Empirical analysis of the lane formation process in bidirectional pedestrian flow. *Physical Review E*, 94(3):032304, September 2016. doi:10.1103/PhysRevE.94.032304.

[49] Xu, Q., Chraibi, M., and Seyfried, A. Anticipation in a velocity-based model for pedestrian dynamics. *Transportation Research Part C: Emerging Technologies*, 133:103464, December 2021. ISSN 0968-090X. doi:10.1016/j.trc.2021.103464.

[50] Vissers, T., van Blaaderen, A., and Imhof, A. Band Formation in Mixtures of Oppositely Charged Colloids Driven by an ac Electric Field. *Physical Review Letters*, 106(22):228303, June 2011. doi:10.1103/PhysRevLett.106.228303.

[51] von Krüchten, C. *Development of a Cognitive and Decision-Based Model for Pedestrian Dynamics*. PhD thesis, Universität zu Köln, Köln, 2019.

[52] Cao, S., Seyfried, A., Zhang, J., Holl, S., and Song, W. Fundamental diagrams for multidirectional pedestrian flows. *Journal of Statistical Mechanics: Theory and Experiment*, 2017(3):033404, March 2017. ISSN 1742-5468. doi:10.1088/1742-5468/aa620d.

[53] Daamen, W. and Hoogendoorn, S.P. Flow-Density Relations for Pedestrian Traffic. In Schadschneider, A., Pöschel, T., Kühne, R., Schreckenberg, M., and Wolf, D.E., editors, *Traffic and Granular Flow'05*, pages 315–322. Springer, Berlin, Heidelberg, 2007. ISBN 978-3-540-47640-5. doi:10.1007/978-3-540-47641-2_27.

[54] Garcimartín, A., Parisi, D.R., Pastor, J.M., MartӃn-GӃ³mez, C., and Zuriguel, I. Flow of pedestrians through narrow doors with different competitiveness. *Journal of Statistical Mechanics: Theory and Experiment*, 2016(4):043402, 2016.

[55] Muir, H.C., Bottomley, D.M., and Marrison, C. Effects of motivation and cabin configuration on emergency aircraft evacuation behavior and rates of egress. *The International Journal of Aviation Psychology*, 6:57–77, 1996. doi:10.1207/s15327108ijap0601_4.

[56] Garcimartín, A., Pastor, J.M., Ferrer, L.M., Ramos, J.J., Martín-Gómez, C., and Zuriguel, I. Flow and clogging of a sheep herd passing through a bottleneck. *Physical Review E*, 91:022808, 2015.

[57] Wolf, D.E. and Grassberger, P. *Friction, Arching, Contact Dynamics*. World Scientific, Singapore, September 1997. ISBN 978-981-02-3142-2. doi:10.1142/9789814529747.

[58] Caitano, R., Guerrero, B.V., González, R.E.R., Zuriguel, I., and Garcimartín, A. Characterization of the Clogging Transition in Vibrated Granular Media. *Physical Review Letters*, 127(14):148002, September 2021. doi:10.1103/PhysRevLett.127.148002.

[59] Rzezonka, J. *Analysis of the Microscopic Structure of Pedestrian Bottleneck Flow Based on Experiments and Simulations*. PhD thesis, Universität zu Köln, Köln, May 2023.

[60] Helbing, D., Farkas, I., and Vicsek, T. Simulating dynamical features of escape panic. *Nature*, 407(6803):487–490, September 2000. ISSN 1476-4687. doi:10.1038/35035023.

[61] Adrian, J., Seyfried, A., and Sieben, A. Crowds in front of bottlenecks at entrances from the perspective of physics and social psychology. *Journal of The Royal Society Interface*, 17(165):20190871, April 2020. ISSN 1742-5689, 1742-5662. doi:10.1098/rsif.2019.0871.

[62] Helbing, D., Johansson, A., and Al-Abideen, H.Z. Dynamics of crowd disasters: An empirical study. *Physical Review E*, 75(4):046109, April 2007. doi:10.1103/PhysRevE.75.046109.

[63] Solon, A.P., Chaté, H., and Tailleur, J. From Phase to Microphase Separation in Flocking Models: The Essential Role of Nonequilibrium Fluctuations. *Physical Review Letters*, 114(6):068101, February 2015. doi:10.1103/PhysRevLett.114.068101.

[64] Sieben, A. and Seyfried, A. Inside a life-threatening crowd: Analysis of the Love Parade disaster from the perspective of eyewitnesses. *Safety Science*, 166:106229, October 2023. ISSN 0925-7535. doi:10.1016/j.ssci.2023.106229.

[65] Wioland, H., Woodhouse, F.G., Dunkel, J., Kessler, J.O., and Goldstein, R.E. Confinement Stabilizes a Bacterial Suspension into a Spiral Vortex. *Physical Review Letters*, 110(26):268102, June 2013. doi:10.1103/PhysRevLett.110.268102.

[66] Gautrais, J., Jost, C., and Theraulaz, G. Key Behavioural Factors in a Self-Organised Fish School Model. *Annales Zoologici Fennici*, 45(5):415–428, October 2008. ISSN 0003-455X, 1797-2450. doi:10.5735/086.045.0505.

[67] Echeverría-Huarte, I. The unwavering counter-clockwise movement in humans - a three-act study -. *presentation at PED 2023, Eindhoven, Netherlands*, 2023.

[68] Jo, A., Sano, T., Ikehata, Y., and Ohmiya, Y. Analysis of Crowd Flow Capacity through a Door Connected to a Crowded Corridor. *Transportation Research Procedia*, 2:10–18, 2014. ISSN 23521465. doi:10.1016/j.trpro.2014.09.003.

[69] Daamen, W. *Modelling Passenger Flows in Public Transport Facilities*. PhD thesis, DUP Science, Delft, 2004.

[70] Hoogendoorn, SP., Bovy, PHL., and Daamen, W. Microscopic pedestrian wayfinding and dynamics modelling. *Pedestrian and evacuation dynamics*, pages 123–154, 2001. ISSN 3-540-42690-6.

[71] Hughes, R.L. A continuum theory for the flow of pedestrians. *Transportation Research Part B: Methodological*, 36(6):507–535, July 2002. ISSN 01912615. doi:10.1016/S0191-2615(01)00015-7.

[72] Bain, N. and Bartolo, D. Dynamic response and hydrodynamics of polarized crowds. *Science (New York, N.Y.)*, 363(6422):46–49, January 2019. doi:10.1126/science.aat9891.

[73] Seitz, M.J. and Köster, G. Natural discretization of pedestrian movement in continuous space. *Physical Review E*, 86(4):046108, October 2012. ISSN 1539-3755, 1550-2376. doi:10.1103/PhysRevE.86.046108.

[74] Korbmacher, R., Nicolas, A., Tordeux, A., and Totzeck, C. Time-Continuous Microscopic Pedestrian Models: An Overview. In Bellomo, N. and Gibelli, L., editors, *Crowd Dynamics, Volume 4: Analytics and Human Factors in Crowd Modeling*, pages 55–80. Springer International Publishing, Cham, 2023. ISBN 978-3-031-46359-4. doi:10.1007/978-3-031-46359-4_3.

[75] Weisberg, M. *Simulation and Similarity: Using Models to Understand the World*. Oxford University Press, January 2013. ISBN 978-0-19-933300-4. doi:10.1093/acprof:oso/9780199933662.001.0001.

[76] RiMEA. Guideline for Microscopic Evacuation Analysis. Technical Report 3.0, 2009.

[77] Kurtc, V., Chraibi, M., and Tordeux, A. Automated Quality Assessment of Space-Continuous Models for Pedestrian Dynamics. In Hamdar, S.H., editor, *Traffic and Granular Flow '17*, pages 317–325, Cham, 2019. Springer International Publishing. ISBN 978-3-030-11440-4. doi:10.1007/978-3-030-11440-4_35.

[78] Xiao, Y., Xu, J., Chraibi, M., Zhang, J., and Gou, C. A generalized trajectories-based evaluation approach for pedestrian evacuation models. *Safety Science*, 147: 105574, March 2022. ISSN 0925-7535. doi:10.1016/j.ssci.2021.105574.

[79] Nicolas, A., Kuperman, M., Ibañez, S., Bouzat, S., and Appert-Rolland, C. Mechanical response of dense pedestrian crowds to the crossing of intruders. *Scientific Reports*, 9(1):105, January 2019. ISSN 2045-2322. doi:10.1038/s41598-018-36711-7.

[80] Chraibi, M., Kemloh, U., Schadschneider, A., and Seyfried, A. Force-based models of pedestrian dynamics. *Networks and Heterogeneous Media*, 6:425, 2011. doi:doi:10.3934/nhm.2011.6.425.

[81] Tordeux, A., Chraibi, M., and Seyfried, A. Collision-Free Speed Model for Pedestrian Dynamics. In Knoop, V.L. and Daamen, W., editors, *Traffic and Granular*

Flow '15, pages 225–232, Cham, 2016. Springer International Publishing. ISBN 978-3-319-33482-0. doi:10.1007/978-3-319-33482-0_29.

[82] Karamouzas, I., Skinner, B., and Guy, S.J. A universal power law governing pedestrian interactions. *Physical Review Letters*, 113(5):238701, December 2014. doi:10.1103/PhysRevLett.113.238701.

[83] Cordes, J., Chraibi, M., Tordeux, A., and Schadschneider, A. Time-To-Collision Models for Single-File Pedestrian Motion. *Collective Dynamics*, 6(0):1–10, January 2022. ISSN 2366-8539. doi:10.17815/CD.2021.133.

[84] Cordes, J., Chraibi, M., Tordeux, A., and Schadschneider, A. Single-File Pedestrian Dynamics: A Review of Agent-Following Models. In Bellomo, N. and Gibelli, L., editors, *Crowd Dynamics, Volume 4: Analytics and Human Factors in Crowd Modeling*, Modeling and Simulation in Science, Engineering and Technology, pages 143–178. Springer International Publishing, Cham, 2023. ISBN 978-3-031-46359-4. doi:10.1007/978-3-031-46359-4_6.

[85] Duckstein, L. Control of traffic in tunnels to maximize flow. *Highway Research Record*, (154), 1967.

[86] Herman, R., Montroll, E.W., Potts, R.B., and Rothery, R.W. Traffic Dynamics: Analysis of Stability in Car Following. *Operations Research*, 7(1):86–106, 1959. ISSN 0030-364X.

[87] Kerner, B. and Rehborn, H. Experimental properties of phase transitions in traffic flow. *Physical Review Letters*, 79:4030, 1997. doi:10.1103/PhysRevLett.79.4030.

[88] Orosz, G., Wilson, R., Szalai, R., and Stepan, G. Exciting traffic jams: Nonlinear phenomena behind traffic jam formation on highways. *Physical Review E*, 80: 046205, 2009. doi:10.1103/PhysRevE.80.046205.

[89] Chowdhury, D., Santen, L., and Schadschneider, A. Statistical physics of vehicular traffic and some related systems. *Physics Reports*, 329:199–329, 2000.

[90] Kerner, B.S. *The Physics of Traffic*. Springer, 2004.

[91] Zhang, J., Mehner, W., Holl, S., Boltes, M., Andresen, E., Schadschneider, A., and Seyfried, A. Universal flow-density relation of single-file bicycle, pedestrian and car motion. *Physics Letters A*, 378(44):3274–3277, September 2014. ISSN 03759601. doi:10.1016/j.physleta.2014.09.039.

[92] Sugiyama, Y., Fukui, M., Kikuchi, M., Hasebe, K., Nakayama, A., Nishinari, K., Tadaki, S.i., and Yukawa, S. Traffic jams without Bottlenecks—Experimental evidence for the physical mechanism of the formation of a jam. *New New Journal of Physics.*, 10(3):033001, 2008.

[93] Barlovic, R., Santen, L., Schadschneider, A., and Schreckenberg, M. Metastable states in cellular automata for traffic flow. *The European Physical Journal B*, 5(3): 793–800, October 1998. ISSN 1434-6028. doi:10.1007/s100510050504.

[94] Hall, F., Allen, B., and Gunter, M. Empirical analysis of freeway flow-density relationships. *Transportation Research Part A: Policy and Practice 20*, 20:197, 1986.

[95] Xue, S. and Shiwakoti, N. A meta-synthesis of experimental studies of pedestrian movement in single-file flow. *Physica A: Statistical Mechanics and its Applications*, 630:129255, November 2023. ISSN 0378-4371. doi:10.1016/j.physa.2023.129255.

[96] Chraibi, M. Oscillating behavior within the social force model. *arXiv:1412.1133 [physics]*, December 2014. doi:10.48550/arxiv.1412.1133.

[97] Kretz, T. On oscillations in the social force model. *Physica A: Statistical Mechanics and its Applications*, 438:272, 2015. doi:http://dx.doi.org/10.1016/j.physa.2015.07.002.

[98] Lakoba, T.I., Kaup, D.J., and Finkelstein, N.M. Modifications of the Helbing-Molnár-Farkas-Vicsek social force model for pedestrian evolution. *Simulation*, 81: 339–352, 2005.

[99] Köster, G., Treml, F., and Gödel, M. Avoiding numerical pitfalls in social force models. *Physical Review E*, 87:063305, 2013. doi:DOI:10.1103/PhysRevE.87.063305.

[100] Seyfried, A. Intentions and superposition of forces in pedestrian models. *presentation at PED 2018, Lund, Sweden*, 2018.

[101] Schadschneider, A. and Tordeux, A. Noise-Induced Stop-and-Go Dynamics in Pedestrian Single-file Motion. *Collective Dynamics*, 5:356–363, March 2020. ISSN 2366-8539. doi:10.17815/CD.2020.70.

[102] Cordes, J., Schadschneider, A., and Tordeux, A. The Trouble with 2nd Order Models or How to Generate Stop-and-Go Traffic in a 1st Order Model. In Zuriguel, I., Garcimartin, A., and Cruz, R., editors, *Traffic and Granular Flow 2019*, Springer Proceedings in Physics, pages 45–51, Cham, 2020. Springer International Publishing. ISBN 978-3-030-55973-1. doi:10.1007/978-3-030-55973-1_6.

[103] Sticco, I., Frank, G., Cornes, F., and Dorso, C. A re-examination of the role of friction in the original Social Force Model. *Safety Science*, 121:42, 2020. doi:10.1016/j.ssci.2019.08.041.

[104] Cordes, J. Modeling of Stop-and-Go Waves in Pedestrian Dynamics. Master's thesis, Universität zu Köln, Köln, 2020.

[105] Chraibi, M., Ezaki, T., Tordeux, A., Nishinari, K., Schadschneider, A., and Seyfried, A. Jamming transitions in force-based models for pedestrian dynamics. *Physical Review E: Statistical Physics, Plasmas, Fluids, and Related Interdisciplinary Topics*, 92(4):042809, October 2015. doi:10.1103/PhysRevE.92.042809.

[106] Hoogendoorn, S. and H.L. Bovy, P. Simulation of pedestrian flows by optimal control and differential games. *Optimal Control Applications and Methods*, 24(3): 153–172, 2003. ISSN 1099-1514. doi:10.1002/oca.727.

[107] Hayduk, L.A. Personal space: Where we now stand. *Psychological Bulletin*, 94: 293–335, 1983. ISSN 1939-1455. doi:10.1037/0033-2909.94.2.293.

[108] Seyfried, A., Steffen, B., and Lippert, T. Basics of modelling the pedestrian flow. *Physica A: Statistical Mechanics and its Applications*, 368(1):232–238, 2006-08, 2006. ISSN 03784371. doi:10.1016/j.physa.2005.11.052.

[109] Reuschel, A. Fahrzeugbewegungen in der Kolonne. *Österreichisches Ingenieur Archiv*, 4:193–215, 1950.

[110] Tordeux, A., Chraibi, M., Schadschneider, A., and Seyfried, A. Influence of the number of predecessors in interaction within acceleration-based flow models. *Journal of Physics A: Mathematical and Theoretical*, 50(34):345102, 2017.

[111] Orosz, G., Wilson, R.E., and Stépán, G. Traffic jams: Dynamics and control. *Philosophical Transactions of the Royal Society A: Mathematical, Physical and Engineering Sciences*, 368(1928):4455–4479, October 2010. doi:10.1098/rsta.2010.0205.

[112] Pipes, L.A. An operational analysis of traffic dynamics. *Journal of Applied Physics*, 24(3):274–281, March 1953. doi:10.1063/1.1721265.

[113] Chandler, R.E., Herman, R., and Montroll, E.W. Traffic dynamics: Studies in car following. *Operations Research*, 6(2):165–184, 1958.

[114] Gazis, D.C., Herman, R., and Rothery, R.W. Nonlinear follow-the-leader models of traffic flow. *Operations Research*, 9(4):545–567, 1961.

[115] Bando, M., Hasebe, K., Nakayama, A., Shibata, A., and Sugiyama, Y. Dynamical model of traffic congestion and numerical simulation. *Physical Review E: Statistical*

Physics, Plasmas, Fluids, and Related Interdisciplinary Topics, 51(2):1035–1042, February 1995. doi:10.1103/PhysRevE.51.1035.

[116] Jiang, R., Wu, Q., and Zhu, Z. Full velocity difference model for a car-following theory. *Physical Review E*, 64(1):017101, June 2001. ISSN 1063-651X, 1095-3787. doi:10.1103/PhysRevE.64.017101.

[117] Gipps, P. A behavioural car-following model for computer simulation. *Transportation Research Part B: Methodological*, 15(2):105–111, April 1981. ISSN 01912615. doi:10.1016/0191-2615(81)90037-0.

[118] Treiber, M., Hennecke, A., and Helbing, D. Congested traffic states in empirical observations and microscopic simulations. *Physical Review E*, 62(2):1805–1824, August 2000. doi:10.1103/PhysRevE.62.1805.

[119] Johansson, F., Duives, D., Daamen, W., and Hoogendoorn, S. The Many Roles of the Relaxation time Parameter in Force based Models of Pedestrian Dynamics. *Transportation Research Procedia*, 2:300–308, January 2014. ISSN 2352-1465. doi:10.1016/j.trpro.2014.09.057.

[120] Kesting, A. and Treiber, M. How Reaction Time, Update Time, and Adaptation Time Influence the Stability of Traffic Flow. *Computer-Aided Civil and Infrastructure Engineering*, 23(2):125–137, 2008. ISSN 1467-8667. doi:10.1111/j.1467-8667.2007.00529.x.

[121] Rzezonka, J., Chraibi, M., Seyfried, A., Hein, B., and Schadschneider, A. An attempt to distinguish physical and socio-psychological influences on pedestrian bottleneck. *Royal Society Open Science*, 9(6):211822, 2022. doi:10/gqbv9j.

[122] Subaih, R. and Tordeux, A. Modeling pedestrian single-file movement: Extending the interaction to the follower. *Physica A: Statistical Mechanics and its Applications*, 633:129394, January 2024. ISSN 0378-4371. doi:10.1016/j.physa.2023.129394.

[123] Wilson, R. and Ward, J. Car-following models: Fifty years of linear stability analysis – a mathematical perspective. *Transportation Planning and Technology*, 34(1):3–18, February 2011. ISSN 0308-1060. doi:10.1080/03081060.2011.530826.

[124] Fiorini, P. and Shiller, Z. Motion planning in dynamic environments using velocity obstacles. *The International Journal of Robotics Research*, 17(7):760–772, 1998. doi:10.1177/027836499801700706.

[125] van den Berg, J., Ming Lin, and Manocha, D. Reciprocal Velocity Obstacles for real-time multi-agent navigation. In *2008 IEEE International Conference on*

Robotics and Automation, pages 1928–1935, Pasadena, CA, USA, May 2008. IEEE. ISBN 978-1-4244-1646-2. doi:10.1109/ROBOT.2008.4543489.

[126] van den Berg, J., Guy, S., Lin, M., and Manocha, D. Reciprocal N-Body Collision Avoidance. In *Springer Tracts in Advanced Robotics*, volume 70, pages 3–19. April 2011. ISBN 978-3-642-19456-6.

[127] Ciuffo, B., Mattas, K., Makridis, M., Albano, G., Anesiadou, A., He, Y., Josvai, S., Komnos, D., Pataki, M., Vass, S., and Szalay, Z. Requiem on the positive effects of commercial adaptive cruise control on motorway traffic and recommendations for future automated driving systems. *Transportation Research Part C: Emerging Technologies*, 130:103305, September 2021. ISSN 0968-090X. doi:10.1016/j.trc.2021.103305.

[128] Stern, R.E., Cui, S., Delle Monache, M.L., Bhadani, R., Bunting, M., Churchill, M., Hamilton, N., Haulcy, R., Pohlmann, H., Wu, F., Piccoli, B., Seibold, B., Sprinkle, J., and Work, D.B. Dissipation of stop-and-go waves via control of autonomous vehicles: Field experiments. *Transportation Research Part C: Emerging Technologies*, 89:205–221, April 2018. ISSN 0968-090X. doi:10.1016/j.trc.2018.02.005.

[129] Gopalakrishnan, B., Singh, A.K., Kaushik, M., Krishna, K.M., and Manocha, D. PRVO: Probabilistic Reciprocal Velocity Obstacle for multi robot navigation under uncertainty. In *2017 IEEE/RSJ International Conference on Intelligent Robots and Systems (IROS)*, pages 1089–1096, September 2017. doi:10.1109/IROS.2017.8202279.

[130] Snape, J., van den Berg, J., Guy, S.J., and Manocha, D. Independent navigation of multiple mobile robots with hybrid reciprocal velocity obstacles. In *2009 IEEE/RSJ International Conference on Intelligent Robots and Systems*, pages 5917–5922, October 2009. doi:10.1109/IROS.2009.5354821.

[131] Levy, A., Keitel, C., Engel, S., and McLurkin, J. The Extended Velocity Obstacle and applying ORCA in the real world. In *2015 IEEE International Conference on Robotics and Automation (ICRA)*, pages 16–22, May 2015. doi:10.1109/ICRA.2015.7138974.

[132] Qu, Z., Wang, J., and Plaisted, C. A new analytical solution to mobile robot trajectory generation in the presence of moving obstacles. *IEEE Transactions on Robotics*, 20(6):978–993, December 2004. ISSN 1941-0468. doi:10.1109/TRO.2004.829461.

[133] Weedermann, M. Hopf bifurcation calculations for scalar neutral delay differential equations. *Nonlinearity*, 19(9):2091, August 2006. ISSN 0951-7715. doi:10.1088/0951-7715/19/9/005.

[134] Zhang, X. and Jarrett, D.F. Stability analysis of the classical car-following model. *Transportation Research Part B: Methodological*, 31(6):441–462, November 1997. ISSN 0191-2615. doi:10.1016/S0191-2615(97)00006-4.

[135] Sficas, Y.G. and Stavroulakis, I.P. Necessary and sufficient conditions for oscillations of neutral differential equations. *Journal of Mathematical Analysis and Applications*, 123(2):494–507, May 1987. ISSN 0022-247X. doi:10.1016/0022-247X(87)90326-X.

[136] Bachrathy, D. and Stépán, G. Bisection method in higher dimensions and the efficiency number. *Periodica Polytechnica Mechanical Engineering*, 56(2):81–86, September 2012. ISSN 1587-379X. doi:10.3311/pp.me.2012-2.01.

[137] Lassarre, S., Roussignol, M., and Tordeux, A. Linear stability analysis of first-order delayed car-following models on a ring. *Physical Review E*, 86:036207, September 2012. ISSN 1063-651X. doi:10.1103/PhysRevE.86.036207.

[138] Bîrlea, N.M. Shaping traffic flow with a ratio of time constants. *Central European Journal of Engineering*, 4(2):155–161, June 2014. ISSN 2081-9927. doi:10.2478/s13531-013-0156-z.

[139] Treiber, M. and Kesting, A. The intelligent driver model with stochasticity-new insights into traffic flow oscillations. *Transportation research procedia*, 23:174–187, 2017.

[140] Friesen, M., Gottschalk, H., Rüdiger, B., and Tordeux, A. Spontaneous wave formation in stochastic self-driven particle systems. *SIAM Journal on Applied Mathematics*, 81(3):853–870, 2021.

[141] Tordeux, A., Schadschneider, A., and Lassarre, S. Noise-Induced Stop-and-Go Dynamics. In Hamdar, S.H., editor, *Traffic and Granular Flow '17*, pages 337–345, Cham, 2019. Springer International Publishing. ISBN 978-3-030-11440-4. doi:10.1007/978-3-030-11440-4_37.

[142] Tordeux, A. and Schadschneider, A. White and relaxed noises in optimal velocity models for pedestrian flow with stop-and-go waves. *Journal of Physics A: Mathematical and Theoretical*, 18:185101, 2016.

[143] Langtangen, H.P. and Pedersen, G.K. *Scaling of Differential Equations*. Springer International Publishing, Cham, 2016. ISBN 978-3-319-32725-9 978-3-319-32726-6. doi:10.1007/978-3-319-32726-6.

[144] Moussaïd, M., Helbing, D., and Theraulaz, G. How simple rules determine pedestrian behavior and crowd disasters. *Proceedings of the National Academy of Sciences of the United States of America*, 108(17):6884–6888, 2011. doi:10.1073/pnas.1016507108.

[145] Xiao, Y., Gao, Z., Qu, Y., and Li, X. A pedestrian flow model considering the impact of local density: Voronoi diagram based heuristics approach. *Transportation Research Part C: Emerging Technologies*, 68:566–580, July 2016. ISSN 0968-090X. doi:10.1016/j.trc.2016.05.012.

[146] Asano, M., Iryo, T., and Kuwahara, M. Microscopic pedestrian simulation model combined with a tactical model for route choice behaviour. *Transportation Research Part C: Emerging Technologies*, 18(6):842–855, December 2010. ISSN 0968-090X. doi:10.1016/j.trc.2010.01.005.

[147] Feliciani, C., Murakami, H., and Nishinari, K. A universal function for capacity of bidirectional pedestrian streams: Filling the gaps in the literature. *PLOS ONE*, 13(12):e0208496, December 2018. ISSN 1932-6203. doi:10.1371/journal.pone.0208496.

[148] Zuriguel, I., Parisi, D.R., Hidalgo, R.C., Lozano, C., Janda, A., Gago, P.A., Peralta, J.P., Ferrer, L.M., Pugnaloni, L.A., Clément, E., Maza, D., Pagonabarraga, I., and Garcimartín, A. Clogging transition of many-particle systems flowing through bottlenecks. *Scientific Reports*, 4:7324, 2014.

[149] Pfaff, L.M. and Cinelli, M.E. Avoidance behaviours of young adults during a head-on collision course with an approaching person. *Experimental Brain Research*, 236 (12):3169–3179, December 2018. ISSN 1432-1106. doi:10.1007/s00221-018-5371-7.

[150] Cordes, J., Schadschneider, A., and Nicolas, A. Dimensionless numbers reveal distinct regimes in the structure and dynamics of pedestrian crowds. *PNAS Nexus*, page pgae120, March 2024. ISSN 2752-6542. doi:10.1093/pnasnexus/pgae120.

[151] Cordes, J., Schadschneider, A., and Nicolas, A. Classification of Pedestrian Crowds by Dimensionless Numbers. *Collective Dynamics*, under Review, 2024.

[152] Hayduk, L.A. Personal space: An evaluative and orienting overview. *Psychological Bulletin*, 85:117–134, 1978. ISSN 1939-1455. doi:10.1037/0033-2909.85.1.117.

[153] Beermann, M. and Sieben, A. Waiting Behavior and Arousal in Different Levels of Crowd Density: A Psychological Experiment with a "Tiny Box". *Journal of Advanced Transportation*, 2022:7245301, May 2022. ISSN 0197-6729. doi:10/gp55hm.

[154] Sorokowska, A., Sorokowski, P., Hilpert, P., Cantarero, K., Frackowiak, T., Ahmadi, K., Alghraibeh, A.M., Aryeetey, R., Bertoni, A., Bettache, K., et al. Preferred interpersonal distances: A global comparison. *Journal of Cross-Cultural Psychology*, 48(4):577–592, 2017.

[155] Lian, L., Song, W., Yuen, K.K.R., and Telesca, L. Analysis of repulsion states among pedestrians inflowing into a room. *Physics Letters A*, 382(35):2424–2430, 2018.

[156] Knowles, E.S., Kreuser, B., Haas, S., Hyde, M., and Schuchart, G.E. Group size and the extension of social space boundaries. *Journal of Personality and Social Psychology*, 33:647–654, 1976. ISSN 1939-1315. doi:10.1037/0022-3514.33.5.647.

[157] Jia, X., Feliciani, C., Murakami, H., Nagahama, A., Yanagisawa, D., and Nishinari, K. Revisiting the level-of-service framework for pedestrian comfortability: Velocity depicts more accurate perceived congestion than local density. *Transportation Research Part F: Traffic Psychology and Behaviour*, 87:403–425, 2022.

[158] Delucia, P.R. and Novak, J.B. Judgments of relative time-to-contact of more than two approaching objects: Toward a method. *Perception & Psychophysics*, 59(6):913–928, January 1997. ISSN 1532-5962. doi:10.3758/BF03205508.

[159] Lee, D.N. A Theory of Visual Control of Braking Based on Information about Time-to-Collision. *Perception*, 5(4):437–459, December 1976. ISSN 0301-0066. doi:10.1068/p050437.

[160] Meerhoff, L.A., Bruneau, J., Vu, A., Olivier, A.H., and Pettré, J. Guided by gaze: Prioritization strategy when navigating through a virtual crowd can be assessed through gaze activity. *Acta psychologica*, 190:248–257, 2018.

[161] Xiao, Y., Gao, Z., Jiang, R., Li, X., Qu, Y., and Huang, Q. Investigation of pedestrian dynamics in circle antipode experiments: Analysis and model evaluation with macroscopic indexes. *Transportation Research Part C: Emerging Technologies*, 103:174–193, June 2019. ISSN 0968090X. doi:10.1016/j.trc.2019.04.007.

[162] Pellegrini, S., Ess, A., Schindler, K., and van Gool, L. You'll never walk alone: Modeling social behavior for multi-target tracking. In *2009 IEEE 12th International Conference on Computer Vision*, pages 261–268, September 2009. doi:10.1109/ICCV.2009.5459260.

[163] Lerner, A., Chrysanthou, Y., and Lischinski, D. Crowds by Example. *Computer Graphics Forum*, 26(3):655–664, 2007. ISSN 1467-8659. doi:10.1111/j.1467-8659.2007.01089.x.

[164] Database Pedestrian Trajectories Forschungszentrum Jülich. https://doi.org/10.34735/ped.da.

[165] Observations: Zara and Students datasets. graphics.cs.ucy.ac.cy/research/downloads/crowd-data, Last access at 02.04.2024.

[166] Observations: ETH datasets. https://www.vision.ee.ethz.ch/datasets/, Last access at 02.04.2024.

[167] Boltes, M., Seyfried, A., Steffen, B., and Schadschneider, A. Automatic extraction of pedestrian trajectories from video recordings. In Klingsch, W.W.F., Rogsch, C., Schadschneider, A., and Schreckenberg, M., editors, *Pedestrian and Evacuation Dynamics 2008*, pages 43–54, Berlin Heidelberg, 2010. Springer. doi:10.1007/978-3-642-04504-2-3.

[168] Alahi, A., Goel, K., Ramanathan, V., Robicquet, A., Fei-Fei, L., and Savarese, S. Social LSTM: Human Trajectory Prediction in Crowded Spaces. In *2016 IEEE Conference on Computer Vision and Pattern Recognition (CVPR)*, pages 961–971, June 2016. doi:10.1109/CVPR.2016.110.

[169] Boltes, M., Pick, J., and Klein, J. Smoothing Trajectories of People's Heads. In Zuriguel, I., Garcimartin, A., and Cruz, R., editors, *Traffic and Granular Flow 2019*, Springer Proceedings in Physics, pages 21–29, Cham, 2020. Springer International Publishing. ISBN 978-3-030-55973-1. doi:10.1007/978-3-030-55973-1_3.

[170] Seyfried, A., Steffen, B., Klingsch, W., and Boltes, M. The fundamental diagram of pedestrian movement revisited. *Journal of Statistical Mechanics: Theory and Experiment*, P10002, 2005. doi:10.1088/1742-5468/2005/10/P10002.

[171] Franchetti, S. Radial distribution functions in solid and liquid argon. *Il Nuovo Cimento B (1971-1996)*, 26(2):507–521, April 1975. ISSN 1826-9877. doi:10.1007/BF02738574.

[172] Klongvessa, N. *Study of Dense Assemblies of Active Colloids: Collective Behavior and Rheological Properties.* PhD thesis, Université de Lyon, 2020.

[173] Tomoeda, A., Yanagisawa, D., Imamura, T., and Nishinari, K. Propagation speed of a starting wave in a queue of pedestrians. *Physical Review E*, 86(3):036113, September 2012. doi:10.1103/PhysRevE.86.036113.

[174] Rogsch, C. Start Waves and Pedestrian Movement— An Experimental Study. In Klingsch, W.W.F., Rogsch, C., Schadschneider, A., and Schreckenberg, M., editors, *Pedestrian and Evacuation Dynamics 2008*, pages 247–248. Springer Berlin

Heidelberg, Berlin, Heidelberg, 2010. ISBN 978-3-642-04503-5 978-3-642-04504-2. doi:10.1007/978-3-642-04504-2_19.

[175] Uesten, E., Schumann, J., and Sieben, A. Exploring the Dynamic Relationship between Pushing Behavior and Crowd Dynamics. *Collective Dynamics*, 8:1–29, September 2023. ISSN 2366-8539. doi:10.17815/CD.2023.143.

[176] Üsten, E., Lügering, H., and Sieben, A. Pushing and Non-pushing Forward Motion in Crowds: A Systematic Psychological Observation Method for Rating Individual Behavior in Pedestrian Dynamics. *Collective Dynamics*, 7:1–16, August 2022. ISSN 2366-8539. doi:10.17815/CD.2022.138.

[177] Üsten, E. *Dynamic Motivation in Crowds: Insights from Experiments and Pedestrian Models for Goal-Directed Motion.* PhD thesis, Bergische Universität Wuppertal, Wuppertal, Germany, 2023.

[178] van Toll, W., Grzeskowiak, F., Gandía, A.L., Amirian, J., Berton, F., Bruneau, J., Daniel, B.C., Jovane, A., and Pettré, J. Generalized Microscropic Crowd Simulation using Costs in Velocity Space. In *Symposium on Interactive 3D Graphics and Games*, pages 1–9, San Francisco CA USA, May 2020. ACM. ISBN 978-1-4503-7589-4. doi:10.1145/3384382.3384532.

[179] Guy, S.J., Curtis, S., Lin, M.C., and Manocha, D. Least-effort trajectories lead to emergent crowd behaviors. *Physical Review E*, 85(1):016110, January 2012. doi:10.1103/PhysRevE.85.016110.

[180] Modelling Framework. https://github.com/Jakob-KKU/Pedestrian_Models.

[181] Küpper, M. and Seyfried, A. Waiting in crowded places: Influence of number of pedestrians, waiting time and obstacles. *Journal of The Royal Society Interface*, 20(206):20230193, September 2023. doi:10.1098/rsif.2023.0193.

[182] Echeverría-Huarte, I. and Nicolas, A. Body and mind: Decoding the dynamics of pedestrians and the effect of smartphone distraction by coupling mechanical and decisional processes. *Transportation Research Part C: Emerging Technologies*, 157: 104365, December 2023. ISSN 0968-090X. doi:10.1016/j.trc.2023.104365.

[183] Kolb, E., Cixous, P., and Charmet, J.C. Flow fields around an intruder immersed in a 2D dense granular layer. *Granular Matter*, 16(2):223–233, April 2014. ISSN 1434-7636. doi:10.1007/s10035-014-0483-7.

[184] Ambulance Intruder Observation. https://twitter.com/i/status/1140374111258140673, Last access at 02.04.2024.

[185] Bonnemain, T., Butano, M., Bonnet, T., Echeverría-Huarte, I., Seguin, A., Nicolas, A., Appert-Rolland, C., and Ullmo, D. Pedestrians in static crowds are not grains, but game players. *Physical Review E*, 107(2):024612, February 2023. ISSN 2470-0045, 2470-0053. doi:10.1103/PhysRevE.107.024612.

[186] Wang, J., Lv, W., Jiang, H., Fang, Z., and Ma, J. Exploring crowd persistent dynamism from pedestrian crossing perspective: An empirical study. *Transportation Research Part C: Emerging Technologies*, 157:104400, December 2023. ISSN 0968090X. doi:10.1016/j.trc.2023.104400.

[187] Wolinski, D. and Lin, M. Generalized WarpDriver: Unified Collision Avoidance for Multi-Robot Systems in Arbitrarily Complex Environments. In *Robotics: Science and Systems XIV*. Robotics: Science and Systems Foundation, June 2018. ISBN 978-0-9923747-4-7. doi:10.15607/RSS.2018.XIV.065.

[188] Johansson, A., Helbing, D., and Shukla, P.K. Specification of the social force pedestrian model by evolutionary adjustment to video tracking data. *Advances in Complex Systems*, 10(supp02):271–288, December 2007. ISSN 0219-5259. doi:10.1142/S0219525907001355.

[189] Zanlungo, F., Ikeda, T., and Kanda, T. Social force model with explicit collision prediction. *EPL (Europhysics Letters)*, 93(6):68005, March 2011. ISSN 0295-5075. doi:10.1209/0295-5075/93/68005.

[190] Zanlungo, F., Feliciani, C., Yücel, Z., Nishinari, K., and Kanda, T. Macroscopic and microscopic dynamics of a pedestrian cross-flow: Part II, modelling. *Safety Science*, 158:105969, February 2023. ISSN 09257535. doi:10.1016/j.ssci.2022.105969.

[191] Totzeck, C. An anisotropic interaction model with collision avoidance. *Kinetic & Related Models*, 13(6):1219, 2020. doi:10.3934/krm.2020044.

[192] Yu, W., Chen, R., Dong, L., and Dai, S. Centrifugal force model for pedestrian dynamics. *Physical Review E*, 72(2):026112, August 2005. doi:10.1103/PhysRevE.72.026112.

[193] Chraibi, M., Seyfried, A., and Schadschneider, A. Generalized centrifugal force model for pedestrian dynamics. *Physical Review E*, 82:046111, 2010. doi:10.1103/PhysRevE.82.046111.

[194] Karamouzas, I., Sohre, N., Narain, R., and Guy, S.J. Implicit crowds: Optimization integrator for robust crowd simulation. *ACM Transactions on Graphics*, 36(4):1–13, July 2017. ISSN 0730-0301, 1557-7368. doi:10.1145/3072959.3073705.

[195] Szeri, A.Z. *Fluid Film Lubrication*. Cambridge University Press, Cambridge ; New York, 2nd ed edition, 2011. ISBN 978-0-521-89823-2.

[196] Parisi, D.R., Sartorio, A.G., Colonnello, J.R., Garcimartín, A., Pugnaloni, L.A., and Zuriguel, I. Pedestrian dynamics at the running of the bulls evidence an inaccessible region in the fundamental diagram. *Proceedings of the National Academy of Sciences*, 118(50), December 2021. ISSN 0027-8424, 1091-6490. doi:10.1073/pnas.2107827118.

[197] Parisi. Slow and fast pedestrian dynamics. *presentation at PED 2023, Eindhoven, Netherlands*, 2023.

[198] Silverberg, J.L., Bierbaum, M., Sethna, J.P., and Cohen, I. Collective Motion of Humans in Mosh and Circle Pits at Heavy Metal Concerts. *Physical Review Letters*, 110(22):228701, May 2013. doi:10.1103/PhysRevLett.110.228701.

[199] Negi, R.S., Iyer, P., and Gompper, G. Controlling Inter-Particle Distances in Crowds of Motile, Cognitive, Active Particles. *arXiv:2402.03851 [cond-mat, physics:physics]*, February 2024. doi:10.48550/arXiv.2402.03851.

[200] Fruchart, M., Hanai, R., Littlewood, P.B., and Vitelli, V. Non-reciprocal phase transitions. *Nature*, 592(7854):363–369, April 2021. ISSN 1476-4687. doi:10.1038/s41586-021-03375-9.

[201] Hannun, J., Dias, C., Taha, A.H., Almutairi, A., Alhajyaseen, W., Sarvi, M., and Al-Bosta, S. Pedestrian flow characteristics through different angled bends: Exploring the spatial variation of velocity. *PLOS ONE*, 17(3):e0264635, March 2022. ISSN 1932-6203. doi:10.1371/journal.pone.0264635.

[202] Ludlow, L.W. and Weyand, P.G. Energy expenditure during level human walking: Seeking a simple and accurate predictive solution. *Journal of Applied Physiology*, 120(5):481–494, March 2016. ISSN 8750-7587. doi:10.1152/japplphysiol.00864.2015.

[203] Chen, L., Bai, X.Z., Liang, Y.G., and Li, K.B. Calculation of Collision Probability. In Chen, L., Bai, X.Z., Liang, Y.G., and Li, K.B., editors, *Orbital Data Applications for Space Objects: Conjunction Assessment and Situation Analysis*, pages 135–183. Springer, Singapore, 2017. ISBN 978-981-10-2963-9. doi:10.1007/978-981-10-2963-9_5.

[204] Moussaïd, M., Helbing, D., Garnier, S., Johansson, A., Combe, M., and Theraulaz, G. Experimental study of the behavioural mechanisms underlying self-organization in human crowds. *Proceedings of the Royal Society B: Biological Sciences*, 276(1668):2755–2762, August 2009. ISSN 0962-8452, 1471-2954. doi:10.1098/rspb.2009.0405.
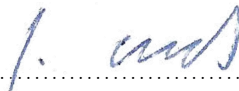
Erklärung

Hiermit versichere ich an Eides statt, dass ich die vorliegende Dissertation selbstständig und ohne die Benutzung anderer als der angegebenen Hilfsmittel und Literatur angefertigt habe. Alle Stellen, die wörtlich oder sinngemäß aus veröffentlichten und nicht veröffentlichten Werken dem Wortlaut oder dem Sinn nach entnommen wurden, sind als solche kenntlich gemacht. Ich versichere an Eides statt, dass diese Dissertation noch keiner anderen Fakultät oder Universität zur Prüfung vorgelegen hat; dass sie - abgesehen von unten angegebenen Teilpublikationen und eingebundenen Artikeln und Manuskripten - noch nicht veröffentlicht worden ist sowie, dass ich eine Veröffentlichung der Dissertation vor Abschluss der Promotion nicht ohne Genehmigung des Promotionsausschusses vornehmen werde. Die Bestimmungen dieser Ordnung sind mir bekannt. Darüber hinaus erkläre ich hiermit, dass ich die Ordnung zur Sicherung guter wissenschaftlicher Praxis und zum Umgang mit wissenschaftlichem Fehlverhalten der Universität zu Köln gelesen und sie bei der Durchführung der Dissertation zugrundeliegenden Arbeiten und der schriftlich verfassten Dissertation beachtet habe und verpflichte mich hiermit, die dort genannten Vorgaben bei allen wissenschaftlichen Tätigkeiten zu beachten und umzusetzen. Ich versichere, dass die eingereichte elektronische Fassung der eingereichten Druckfassung vollständig entspricht.

Teilpublikationen

- Cordes, J., Chraibi, M., Tordeux, A., and Schadschneider, A. Time-To-Collision Models for Single-File Pedestrian Motion. *Collective Dynamics*, 6(0):1–10, January 2022. ISSN 2366-8539. doi:10.17815/CD.2021.133.

- Cordes, J., Chraibi, M., Tordeux, A., and Schadschneider, A.. Single-File Pedestrian Dynamics: A Review of Agent-Following Models. In Nicola Bellomo and Livio Gibelli, editors, *Crowd Dynamics, Volume 4: Analytics and Human Factors in Crowd Modeling*, Modeling and Simulation in Science, Engineering and Technology, pages 143–178. Springer International Publishing, Cham, 2023. ISBN 978-3-031-46359-4. doi:10.1007/978-3-031-46359-4_6.

- Cordes, J., Schadschneider, A., and Nicolas, A. Dimensionless numbers reveal distinct regimes in the structure and dynamics of pedestrian crowds. *PNAS Nexus*, page pgae120, March 2024. ISSN 2752-6542. doi:10.1093/pnasnexus/pgae120.

- Cordes, J., Schadschneider, A., and Nicolas, A. Classification of Pedestrian Crowds by Dimensionless Numbers. *Collective Dynamics*, under Review, 2024.

Köln, 16.04.2024

....

(Ort, Datum, Unterschrift)

176

Schriften des Forschungszentrums Jülich
IAS Series

JÜLICH
Forschungszentrum